

STATUS OF THESIS

Title of thesis **The Effect of Flow Maldistribution on the Thermal Performance Degradation of Fin-tube Heat Exchangers**

I **CHIN WAI MENG**
(CAPITAL LETTERS)

hereby allow my thesis to be placed at the Information Resource Center (IRC) of Universiti Teknologi PETRONAS (UTP) with the following conditions:

1. The thesis becomes the property of UTP
2. The IRC of UTP may make copies of the thesis for academic purposes only.
3. This thesis is classified as

Confidential

Non-confidential

If this thesis is confidential, please state the reason:

The geometrical specifications of the fin patterns mentioned in the thesis are proprietary information of the sponsor for this research project, i.e. O.Y.L. Manufacturing Company Company Sdn. Bhd.

The contents of the thesis will remain confidential for 5 years.

Remarks on disclosure:

N/A

Endorsed by

Signature of Author

Signature of Supervisor

Permanent address:
19 Jalan SB Indah 1/13B
Taman Sg. Besi Indah
43300 Seri Kembangan

Name of Supervisor:
Prof. Dr. Vijay R. Raghavan

Date : _____

Date : _____

UNIVERSITI TEKNOLOGI PETRONAS
THE EFFECTS OF FLOW MALDISTRIBUTION ON THE THERMAL
PERFORMANCE DEGRADATION OF FIN-TUBE
HEAT EXCHANGERS

by

CHIN WAI MENG

The undersigned certify that they have read, and recommend to the Postgraduate Studies Programme for acceptance this thesis for the fulfilment of the requirements for the degree stated.

Signature: _____

Main Supervisor: Prof. Dr. Vijay R. Raghavan

Signature: _____

Co-Supervisor: -

Signature: _____

Head of Department: Assoc. Prof. Dr. Ahmad Majdi bin Abdul Rani

Date: _____

THE EFFECTS OF FLOW MALDISTRIBUTION ON THE THERMAL
PERFORMANCE DEGRADATION OF FIN-TUBE
HEAT EXCHANGERS

by

CHIN WAI MENG

A Thesis

Submitted to the Postgraduate Studies Programme

as a Requirement for the Degree of

DOCTOR OF PHILOSOPHY

DEPARTMENT OF MECHANICAL ENGINEERING

UNIVERSITI TEKNOLOGI PETRONAS

BANDAR SERI ISKANDAR,

PERAK

JUNE 2011

DECLARATION OF THESIS

Title of thesis

The Effect of Flow Maldistribution on the Thermal Performance Degradation of Fin-tube Heat Exchangers

I CHIN WAI MENG
(CAPITAL LETTERS)

hereby declare that the thesis is based on my original work except for quotations and citations which have been duly acknowledged. I also declare that it has not been previously or concurrently submitted for any other degree at UTP or other institutions.

Witnessed by

Signature of Author

Signature of Supervisor

Permanent address:
19 Jalan SB Indah 1/13B
Taman Sg. Besi Indah
43300 Seri Kembangan

Name of Supervisor:
Prof. Dr. Vijay R. Raghavan

Date : _____

Date : _____

DEDICATION

To my wife, **Sarina**, who has patiently endured my absence, and my frequent moments of preoccupation while at home, during the period of conducting this work. Thank you for your support and encouragement which has driven me to engage and complete the research.

To my kids, **Jonathan** and **Gillian**, who have given me so much joy in my life, and I hope this work will become a testament for you to “Always Try Your Best”.

More importantly, to **YHWH**, who have taught me: “Whatever you do, work at it with all your heart, as working for the Lord, not for men (Col. 3:23)”. All glory and praise be unto Him!

ACKNOWLEDGEMENTS

This research would not have been possible if not for the kind assistance rendered to me by O.Y.L. Research & Development Center Sdn. Bhd. Special thanks to the Operating Manager, Mr. Yeow Tee Siong, who has consented for me to conduct this research in the company and granting me access to the various test facilities available. I would also like to thank O.Y.L. Manufacturing Company Sdn. Bhd. who has provided me with the necessary fin-tube coils for my experiments.

Many people have come along my way and helped me during the course of this research. Among them, I would like to thank:

- Encik Rasulizam Hassan and Encik Nurul Hasrim, who have helped me with the experimental set-up
- Dr. Ng Khai Ching, who has guided me in the fundamentals of CFD
- Mr. Teng Yih Jeng and Ms. New Mei Yet, who have taught me the basics of GAMBIT and FLUENT

Last, but not least, my deepest gratitude to my supervisor, Professor Dr. Vijay R. Raghavan, from whom I have learnt so much. Thank you, sir, for your guidance, encouragement and counsel during these past few years. It has been a privilege and honour to work with you on this project.

ABSTRACT

Maldistribution of flow in a heat exchanger has an adverse effect on its thermal and hydraulic performance. Not only does the heat duty reduce but the fluid pressure drop across the exchanger increases too. The characteristics of a maldistribution profile are described by its four statistical moments of probability density function, viz. mean, standard deviation, skew and kurtosis. A novel mathematical analysis technique has been developed to demonstrate the influence of these statistical moments on the heat transfer and pressure drop performance of an exchanger.

The analysis has shown that both the mean and standard deviation have the highest degradation effect on the heat exchanger performance while subsequent higher moments have declining effects until the fourth moment kurtosis, which has no significant effect. A discretized numerical method was then used on the fin-tube heat exchanger coil to calculate the magnitudes of thermal degradation as the statistical moments of the air inlet velocity distribution and geometrical parameters of the exchanger are systematically changed. The results show that the degradation is not only dependent on the moments but also on the exchanger NTU , ratio of external to internal heat transfer coefficients, R , and the number of tube rows in the coil. Consequently, new correlation equations have been developed to predict the magnitude of deterioration from a known air velocity maldistribution profile, for a given heat exchanger geometry.

An experimental test rig was fabricated to validate the correlation equations. The same experimental data were then used to validate the Computational Fluid Dynamics (CFD) model of the fin-tube heat exchanger. With the same modelling technique, simulations with various exchanger geometry and layout designs can be performed to extract the statistical moments of the maldistribution and predict the heat exchanger performance. By doing so, the design could be optimized to find the lowest possible degradation effects. Maldistribution with low standard deviation and high positive skew is seen to give low thermal performance deteriorations.

ABSTRAK

Ketidakteraturan kelajuan aliran bendalir di dalam sebuah alat pemindah haba akan memberi kesan yang buruk ke atas prestasi pemindahan haba dan hidraulik alat tersebut. Bukan sahaja keupayaan pemindahan haba akan menurun, bahkan penurunan tekanan bendalir melalui alat itu akan meningkat. Profil ketidakseragaman tersebut boleh disifatkan melalui keempat-empat momen fungsi ketumpatan kebarangkaliannya, iaitu purata, sisihan piawai, skew dan kurtosis.

Hasil analisa telah menunjukkan bahawa purata dan sisihan piawai mempunyai kesan yang terbesar terhadap penurunan keupayaan pemindahan haba. Momen yang lebih tinggi mempunyai kesan yang semakin lemah sehingga kurtosis tidak memberi sebarang kesan langsung. Melalui satu kaedah pengiraan diskret ke atas sebuah pemindah haba sirip-tiub, penurunan keupayaan pemindahan haba telah didapati bergantung bukan sahaja kepada momen-momen tetapi juga kepada nilai NTU , nisbah koefisien pemindahan haba sebelah luar kepada sebelah dalam, R , dan bilangan baris tiub. Justera itu, satu set persamaan korelasi telah diterbitkan yang mampu mengira nilai penurunan keupayaan daripada momen-momen profil ketidakseragaman dan geometri pemindah haba.

Satu eksperimen telah dijalankan untuk memastikan kebetulan persamaan korelasi tersebut. Data eksperimen ini telah juga digunakan untuk memeriksa hasil simulasi CFD ke atas model pemindah haba sirip-tiub berkenaan. Melalui kaedah ini, simulasi untuk berbagai-bagai jenis geometri dan rekabentuk yang lain boleh dilakukan untuk mengenalpasti momen-momen ketidakseragaman dan dari itu mengira nilai penurunan keupayaan alat pemindah haba itu. Dengan itu, rekabentuknya boleh dioptimalkan untuk memberi penurunan keupayaan yang paling rendah. Ketidakteraturan yang memberi nilai sisihan piawai yang rendah dan nilai skew yang positif adalah diutamakan.

In compliance with the terms of the Copyright Act 1987 and the IP Policy of the university, the copyright of this thesis has been reassigned by the author to the legal entity of the university,

Institute of Technology PETRONAS Sdn Bhd.

Due acknowledgement shall always be made of the use of any material contained in, or derived from, this thesis.

© Chin Wai Meng, 2011

Institute of Technology PETRONAS Sdn Bhd

All rights reserved.

TABLE OF CONTENTS

DECLARATION OF THESIS	iv
DEDICATION	v
ACKNOWLEDGEMENT	vi
ABSTRACT	vii
TABLE OF CONTENTS.....	x
LIST OF TABLES	xiii
LIST OF FIGURES	xiv
LIST OF SYMBOLS	xvii

Chapter

1. INTRODUCTION	1
1.1 Overview	1
1.2 Description of fin-tube heat exchanger	1
1.3 Description of the flow maldistribution phenomenon	2
1.4 Adverse effects of maldistribution	9
1.5 Justification for the research	9
1.6 Objectives of research	10
1.7 Scope of research	11
1.8 Research methodology	11
1.9 Thesis outline	13
2. LITERATURE REVIEW	15
2.1 Overview	15
2.2 Review of findings	15
2.2.1 Air-side maldistribution	17
2.2.2 Tube-side maldistribution	26
2.3 Opportunities for research	30
2.4 Summary	36
3. MATHEMATICAL FORMULATION OF PERFORMANCE DEGRADATION DUE TO MALDISTRIBUTION.....	37
3.1 Overview	37
3.2 Fundamentals of statistical moments	37
3.3 Reasons for performance deterioration	42
3.4 Mathematical model	44
3.4.1 Thermal performance degradation	49
3.4.2 Hydraulic performance deterioration.....	51
3.5 Interpretation of the derivation	52
3.6 Normalization of moments.....	58

3.7	Physical reasoning of trends.....	61
3.8	Optimization of skew	62
3.9	Generality of results	64
3.10	Summary	67
4.	NUMERICAL ANALYSIS OF FLOW MALDISTRIBUTION ON THE THERMAL PERFORMANCE OF FIN-TUBE HEAT EXCHANGERS	69
4.1	Overview	69
4.2	Discretization model of the fin-tube heat exchanger	69
4.2.1	Psychrometrics	78
4.3	Generating velocity distribution.....	80
4.4	Calculation algorithm.....	84
4.5	Grid size independence	85
4.6	Results	89
4.7	Analysis and discussion	95
4.7.1	Effect of standard deviation	95
4.7.2	Effect of skew	95
4.7.3	Effect of NTU	96
4.7.4	Effect of h_i	97
4.7.5	Effect of air temperature.....	98
4.7.6	Effect of R	100
4.8	Comparison with other data	102
4.9	Implication of results.....	104
4.10	Summary	105
5.	INFLUENCE OF COIL GEOMETRY ON HEAT EXCHANGER THERMAL PERFORMANCE DEGRADATION	107
5.1	Overview	107
5.2	Fin-tube heat exchanger geometry	107
5.3	Influence of coil geometry	108
5.3.1	Numerical methodology	110
5.3.2	Row-by-row analysis	111
5.4	Results and discussion	115
5.4.1	Effect of number of tube rows, N_r	115
5.4.1.1	Row-by-row effect	118
5.4.2	Effect of tube diameter	121
5.4.3	Effect of fin pitch, F_p	123
5.4.4	Effect of tube pitch	125
5.4.5	Effect of fin pattern.....	127
5.5	Correlation development.....	129
5.6	Application of correlation	133
5.7	Summary	133
6.	EXPERIMENTAL STUDIES	135
6.1	Overview	135
6.2	Air-side heat transfer coefficient test	135
6.2.1	Specifications of test coils	136
6.2.2	Experimental set-up.....	138
6.2.3	Test conditions.....	144

6.2.4	Data reduction.....	144
6.2.5	Results and discussion.....	148
6.3	Flow maldistribution test rig.....	152
6.3.1	Experimental set-up.....	152
6.3.2	Air velocity measurement.....	157
6.3.3	Test procedure.....	160
6.3.4	Experimental results and discussion.....	163
6.4	Measurement uncertainty.....	172
6.5	Summary.....	175
7.	NUMERICAL SIMULATION STUDIES AND VALIDATION.....	177
7.1	Overview.....	177
7.2	CFD simulation for fin-tube heat exchangers.....	177
7.3	Governing equations.....	180
7.4	Geometrical modeling.....	182
7.5	Boundary conditions.....	182
7.5.1	Characterization of porous media.....	185
7.6	Grid independence test.....	186
7.7	Change of turbulence model.....	192
7.8	Effect of domain size.....	194
7.9	Velocity vectors at bell-mouth.....	196
7.10	Simulation of flow maldistribution.....	198
7.11	Simulation of thermal performance.....	208
7.11.1	Settings in Heat Exchanger Model.....	208
7.11.2	Results of simulation.....	213
7.12	Summary.....	220
8.	CONCLUSION.....	221
8.1	Review of findings.....	221
8.2	Recommendations for future research.....	224
	REFERENCES.....	227
	LIST OF PUBLICATIONS.....	241
	APPENDICES	
A.	Heat transfer Colburn j -factor correlation.....	243
B.	List of continuous probability density functions.....	245
C.	Specifications of flow nozzles.....	251

LIST OF TABLES

Table

2.1	Chronological summary of literature review	32
3.1	Summary of variations made to the statistical moments	53
3.2	Calculated normalized moments for resultant bimodal distribution	66
4.1	Value of constants for equation (4.25)	78
4.2	Results of grid independence test	85
5.1	Summary of results for coil geometry parametric study	115
5.2	Regression constants for equations (5.11) and (5.13)	131
6.1	Comparison of wavy fin pattern	136
6.2	Coefficient of discharge, C_d	146
6.3	Calculated uniform distribution heating capacity at 30.0°C inlet air temperature	164
6.4	Velocity data for uniform distribution at 0.324 m ³ s ⁻¹ [700 ft ³ min ⁻¹]	165
6.5	Statistical moments of measured maldistribution	165
6.6	Summary of experimental results	168
6.7	Uncertainty of instruments used in experiments	174
6.8	List of uncertainty relationships	174
7.1	Air properties used in simulation	183
7.2	Mesh schemes applied to model	187
7.3	Convergence time required for different mesh schemes	190
7.4	Summary of domain sizes compared	195
7.5	Comparison between simulated and experimental normalized moments for maldistribution Profile [Ⓜ]	205
7.6	Results of simulated outlet air temperature and D	217

LIST OF FIGURES

Figure

1.1	Example of fin-tube heat exchanger.....	3
1.2	Schematic diagram of fin-tube coil	4
1.3	Non-uniform air flow through a wall-mounted unit.....	5
1.4	Air diversion due to top and bottom panels.....	5
1.5	Air diversion due to drain pan	5
1.6	Examples of maldistributed air flow	7
1.7	Example of tube-side flow maldistribution	8
3.1	Representation of a distribution profile for a parameter ϕ	39
3.2	Examples of probability density functions which demonstrate the four statistical moments of a PDF.....	41
3.3	Example of heat transfer coefficient and pressure drop characteristics with velocity	46
3.4	Example of discretized fin-tube heat exchanger	47
3.5	Discretization of spatial and probability distributions.....	47
3.6	Transformation of discretized probability density function	48
3.7	Transformation of PDF for Case 1 with varying mean	55
3.8	Transformation of PDF for Case 2 with varying standard deviation (Mean = 1.00).....	56
3.9	Transformation of PDF for Case 3 with varying skew (Mean = 1.00)	57
3.10	Transformation of PDF for normalized moments with constant $s' = \left(\frac{s}{\bar{u}}\right)$ ratio of 0.38	60
3.11	Example plot of $(1-D) / (1+P_p)$ vs. skew showing optimum maximum point ($NTU = 0.40$ and standard deviation = 0.70).....	63
3.12	Bimodal distribution generated with a weightage factor of 0.55	66
4.1	Discretization of elements on a single row fin-tube heat exchanger.....	72
4.2	Profile of wavy, corrugated fin with staggered tubes.....	73
4.3	(a) Normal probability density function plot (mean = 1.00, standard deviation = 0.33, skew = 0.00, kurtosis = 0.00) showing the area under the curve for an interval of velocity ratio (b) Discretized velocity distribution derived from the normal PDF. The total $\Sigma N = 100$	82
4.4	Examples of velocity spatial distribution over the 10 x 10 (I -J) grid elements.....	83
4.5	Calculation algorithm to obtain cell element heating capacity	86
4.6	Overall calculation flowchart	87

4.7	Effect of kurtosis on D (Air inlet temperature = 20°C, water temperature = 45°C).....	90
4.8	D - NTU plot for skew = 1.00 with varying standard deviation.....	91
4.9	Effect of standard deviation on D	92
4.10	Effect of skew on D	92
4.11	Effect of h_i on D with varying NTU	93
4.12	Effect of h_i on D at fixed NTU and skew.....	94
4.13	Close-up view of D - NTU plot showing effect of inlet air temperature.....	99
4.14	Plot of D versus R	101
4.15	Digitized re-production of results from [38] for a one tube-row bundle (with $C_a/C_f = 0.1$).....	103
4.16	Digitized re-production of results from [19] (filled circles) for a one-pass tube bundle air-cooled heat exchanger and corresponding calculated performance degradation factor (non-filled circles). Air velocity 3.5 ms ⁻¹ , overall heat transfer coefficient 1,000 Wm ⁻² K ⁻¹	103
5.1	Schematic diagram of fin-tube heat exchanger.....	109
5.2	Profile of louvered fins, with staggered tubes.....	112
5.3	Intermediate temperatures for a discrete element (shaded) in a 3-row fin-tube coil.....	113
5.4	Effect of number of tube rows on D	117
5.5	Results of row-by-row analysis for (a) 3-row and (b) 4-row fin-tube heat exchanger.....	120
5.6	Effect of tube diameter on D	122
5.7	Effect of fin pitch on D	124
5.8	Effect of tube pitch on D	126
5.9	Effect of fin pattern on D	128
5.10	Parity plot for correlation equation.....	132
6.1	Circuiting of water flow in the 4-row fin-tube test coil.....	137
6.2	Schematic diagram of set-up for heat transfer coefficient test.....	139
6.3	Example of aspirating sampling device.....	140
6.4	Overall view of air loop in test rig.....	142
6.5	Centrifugal blower and air-conditioning equipment.....	142
6.6	Test duct with polyurethane insulation.....	143
6.7	Water inlet and outlet to test coil.....	143
6.8	Trend of experimental data (a) Inlet fluid temperatures (b) Water flow rate.....	145
6.9	j -factor plot for 2-row, $F_p = 1.270$ mm.....	149
6.10	j -factor plot for 4-row, $F_p = 1.814$ mm.....	149
6.11	Parity plot between experimental and predicted j -factor.....	150
6.12	Parity plot with correction factor, $C = 0.8816$, applied to j -Wang.....	151
6.13	Schematic diagram of test set-up for study of flow maldistribution.....	153
6.14	Overview of 2 nd test rig showing the U-shaped duct layout.....	155
6.15	Bell-mouth inlet.....	155
6.16	Sampling tree positioned in front of duct inlet.....	156
6.17	Water loop used in the experiment.....	156
6.18	Air velocity distribution measuring system.....	159
6.19	Pattern of paper block on coil face area. Dotted lines denote the 10x10 discretization grid.....	162
6.20	Results of heating capacity (water side) for uniform distribution.....	164
6.21	Velocity plot of uniform distribution at 0.324 m ³ s ⁻¹ [700 ft ³ min ⁻¹].....	165

6.22	Maldistribution velocity profile for (a) Set ② and (b) Set ③	167
6.23	Heating capacity degradation due to maldistribution Set ③	168
6.24	Plot of experimental D versus standard deviation	169
6.25	Plot of experimental D versus NTU	169
6.26	Parity plot between experimental and calculated D , and also between experimental and predicted D	171
7.1	Model of test duct in GAMBIT 2.4	184
7.2	Dimensions of model	184
7.3	Experimental data of air pressure drop through fin-tube coil	188
7.4	Demarcation of distinct volumes in the numerical model	189
7.5	Meshed geometry with Scheme 2	189
7.6	Velocity contours for mesh Scheme 2	191
7.7	Simulated velocity profile along z -axis ($y = 0$)	191
7.8	Comparison between turbulence models	193
7.9	Effect of domain size	195
7.10	Velocity vector plot along the duct centerline (Domain size 1 and mesh scheme 2; solution obtained with 1 st order upwind discretization and with RNG k - ϵ turbulence model)	197
7.11	Model generated in GAMBIT for flow blockage pattern Set ④	199
7.12	Simulated velocity contours for flow maldistribution	200
7.13	Comparison with experimental data for Profile Set ①	203
7.14	Comparison with experimental data for Profile Set ②	203
7.15	Comparison with experimental data for Profile Set ④	204
7.16	Parity plot comparing simulated and experimental velocity data	204
7.17	Experimental pressure drop data for other coil configurations	207
7.18	Examples of other flow blockage patterns (shaded)	207
7.19	Effectiveness of fin-tube coil	211
7.20	Plot of friction factor vs. Re_{Dh}	211
7.21	10 x 10 x 1 macros set in Heat Exchanger Model	212
7.22	Temperature contour of leaving air for uniform flow distribution	214
7.23	Temperature plot along the y -axis at $z = 0$ (Uniform flow distribution)	214
7.24	Temperature contour for maldistribution Profile ①	215
7.25	Temperature contour for maldistribution Profile ②	215
7.26	Temperature contour for maldistribution Profile ④	216
7.27	Comparison between simulated D and calculated/experimental D	217
7.28	Model of test duct with 4-row fin-tube coil	219
7.29	Parity plot between simulated and calculated D for 2-row and 4-row coils .	219

LIST OF SYMBOLS

The following list gives the meaning of symbols used in this thesis, unless otherwise defined in the text and appendices:

A	Heat transfer surface area [m^2]
A_c	Minimum cross-section flow area [m^2]
A_n	Nozzle throat area [m^2]
c_1, c_2	Constants [-]
c_p	Specific heat at constant pressure [$\text{Jkg}^{-1}\text{K}^{-1}$]
c_v	Specific heat at constant volume [$\text{Jkg}^{-1}\text{K}^{-1}$]
C	Correction factor [-]
\tilde{C}	Constant [-]
C_d	Coefficient of discharge [-]
C_I	Inertia coefficient [-]
C_k	Parameter defined in equation (7.4) [$\text{kgm}^{-2}\text{s}^{-2}$]
C_{min}	Minimum heat capacity rate [WK^{-1}]
C_{max}	Maximum heat capacity rate [WK^{-1}]
C_n	Parameter defined in equation (7.4) [kgm^{-3}]
C_r	Ratio of minimum to maximum heat capacity rate [-]
d	Tube diameter [m]
D	Thermal performance deterioration factor [-]
D_h	Hydraulic diameter [m]
D_n	Nozzle diameter [m]
D_c	Collar diameter [m]
D_r	Row thermal performance deterioration factor [-]
e	Turbulent dissipation energy [m^2s^{-3}]
E	Expectation function [-]
f	Probability density function [-], or friction factor [-]
F	Correction factor to account for deviation from pure counter-flow [-]
F_p	Fin pitch [mm]
g	Function, or acceleration due to gravity [ms^{-2}]
G	Mass flux [$\text{kgs}^{-1}\text{m}^{-2}$]
h	Heat transfer coefficient [$\text{Wm}^{-2}\text{K}^{-1}$]
H	Specific enthalpy of air [Jkg^{-1}]
i	Index [-]
I	Heat exchanger grid element number [-]
I	Hydraulic gradient [-]
j	Colburn j-factor [-]
J	Heat exchanger grid element number [-]
k	Thermal conductivity [$\text{Wm}^{-1}\text{K}^{-1}$], or non-dimensional moment defined in equation (3.16) [-], or turbulent kinetic energy [m^2s^{-2}]

K	Space-averaged root mean square velocity [ms^{-1}], or permeability [m^2]
K_c	Contraction loss coefficient [-]
K_e	Expansion loss coefficient [-]
l	Tube length [m]
L	Parameter defined in equation (4.14) [m], or flow length [m]
$LMTD$	Log-mean temperature difference [$^{\circ}\text{C}$]
m^2	Flow maldistribution parameter [-]
m	Parameter defined in equation (4.8) [m]
\dot{m}	Mass flow rate [kgs^{-1}]
n	Number of elements [-]
\vec{n}	Unit vector perpendicular to a surface [-]
N, NTU	Number of transfer units [-]
N_k	Number of discrete elements with value of k [-]
N_r	Number of tube rows [-]
N_t	Total number of discrete elements [-]
Nu	Nusselt number [-]
p	Parameter defined in equation (6.11), or pressure [Pa]
p_{ws}	Water vapour saturated pressure [Pa]
P	Probability of occurrence, or probability density function [-]
P_{atm}	Atmospheric pressure [Pa]
P_w	Pumping power [W]
P_p	Pumping power penalty factor [-]
Pr	Prandtl number [-]
q	Parameter defined in equation (6.12)
Q	Heat duty [W]
r	Parameter defined in equation (4.9) [m], or thermal resistance [KW^{-1}]
$r(\text{crossflow})$	Parameter defined in equation (6.10)
R	Ratio of external to internal heat transfer coefficient [-]
R_a	Gas constant [$\text{Jkg}^{-1}\text{K}^{-1}$]
R_e	Parameter defined in equation (4.11) [m]
R_I	Inertia resistance [m^{-1}]
R_{μ}	Viscous resistance [m^{-2}]
Re	Reynolds number [-]
s	Sample standard deviation
s_u	Sample standard deviation of velocity u [ms^{-1}]
S	PFHE channel flow standard deviation [-], or heat exchanger frontal area [m^2]
S_E	Energy source term [Wm^{-3}]
S_M	Momentum source term [$\text{kgm}^{-2}\text{s}^{-2}$]
t_{coil}	Depth of fin-tube coil [m]
T	Temperature [K]
u	Velocity distribution [ms^{-1}], or x -component of velocity vector \vec{u} [ms^{-1}]
\vec{u}	Velocity vector [m]
U	Overall heat transfer coefficient [$\text{Wm}^{-2}\text{K}^{-1}$], or uncertainty
v	y -component of velocity vector \vec{u} [ms^{-1}]
V	Velocity [ms^{-1}]

V_f	Face velocity [ms^{-1}]
V_{max}	Maximum velocity at minimum flow cross-section area [ms^{-1}]
V_n	Nozzle throat velocity [ms^{-1}]
V_r	Flow rate multiplication factor [-]
w	z -component of velocity vector \vec{u} [ms^{-1}]
W	Humidity ratio of air [kg/kg]
W_s	Humidity ratio of saturated air [kg/kg]
x	Cartesian coordinate, or velocity ratio [-], or variable
X_l	Transverse tube pitch [m]
X_t	Longitudinal tube pitch [m]
y	Cartesian coordinate, or fin thickness [m]
z	Cartesian coordinate
Z	Non-uniformity factor [-]

Greek symbols

α	Local flow non-uniformity parameter [-]
β	Parameter defined in equation (4.13) [-]
δ_c	Channel standard deviation parameter [-]
δ_r	Passage non-uniformity parameter [-]
Δ	Interval along the abscissa of discretized probability density plot [ms^{-1}]
Δp	Pressure drop [Pa],
$\Delta t_{m,cf}$	<i>LMTD</i> for pure counter-flow [$^{\circ}\text{C}$]
ε	Heat exchanger effectiveness [-]
ε_H	Turbulent momentum diffusivity [m^2s^{-1}]
ε_M	Turbulent thermal diffusivity [m^2s^{-1}]
γ	Population skew
γ_s	Sample skew
γ_u	Sample skew of velocity u [-]
κ	Population kurtosis
κ_s	Sample kurtosis
κ_u	Sample kurtosis of velocity u [-]
η_f	Fin efficiency [-]
η_s	Fin surface efficiency [-]
λ	Weightage factor [-]
ρ	Density [kgm^{-3}]
μ	Population mean, or dynamic viscosity [Pa.s]
σ	Population standard deviation
σ_b	Bulginess channel deviation [-]
σ_c	Fin spacing channel deviation [m]
σ_r	Ratio of minimum flow area to face area [-]
σ_t	Total channel deviation [-]
ϕ	Variable parameter, or parameter defined in equation (4.10) [-]
τ	Thermal performance deterioration factor [-]
\dot{v}	Volumetric flow rate [m^3s^{-1}]
ν	Specific volume of air [m^3kg^{-1}]
ν_f	Kinematic viscosity of fluid [m^2s^{-1}]

ψ	Non-uniformity factor [-]
ζ	Parameter defined in equation (4.12)
Ω	Variable parameter

Subscripts

a	Air-side
f	Fin, or fluid
i	Index, or internal
in	Inlet
k	Pertaining to variable k
m	Maldistributed, or average
n	Nozzle
o	External
out	Outlet
u	Uniform
w	Water-side

Superscripts

m	Exponent for pressure drop relationship in equation (3.13) [-]
n	Exponent for heat transfer coefficient relationship in equation (3.12) [-]
$'$	Normalized
$-$	Mean
$*$	Pertaining to air wet-bulb temperature

CHAPTER 1

INTRODUCTION

1.1 Overview

A general description of fin-tube heat exchangers commonly used in the industry is given in this chapter. The mechanism of flow non-uniformity occurring in these exchangers is introduced and its impact on the thermal and hydraulic performance is explained. The justification and objectives of the research are also outlined.

1.2 Description of fin-tube heat exchanger

Fin-tube heat exchangers, more commonly called *coils*, are used extensively in the heating, ventilation, air-conditioning and refrigeration (HVAC&R) and automotive industries as heat transfer elements to transport energy from a heat source or to a sink. There are two fluid streams flowing through the heat exchanger. Air flows over the fin surfaces and through the multiple passages created by the fins. Depending on the application of the heat exchanger, the fluid flowing in the tubes could be a liquid such as water, oil or refrigerant. The fluid could also be in single- or two-phase. Heat is then transferred between the two fluid streams, the amount of which is proportional to the temperature difference between the two fluids.

When the fluid in the tube is hotter than the entering air temperature, e.g. hot water or condensation of refrigerant, sensible heat is absorbed by the air which causes it to be heated up. On the other hand, when the fluid is colder, e.g. chilled water or evaporation of refrigerant, the air would be cooled due to the extraction of sensible heat. If the heat exchanger external surface temperature is lower than the air dew point temperature, latent heat would also be involved where condensation of water vapour from the air on the cooled surfaces will occur. In other words, simultaneous heat and mass transfer take place in such conditions.

The construction of such heat exchangers is a highly mechanized process. Aluminum fin strips, which have been stamped and punched with holes, are stacked together forming the exchanger core. Circular copper tubes (which are called “hairpins”) are then inserted through the holes and connected together forming a serpentine circuit within the core. By mechanically expanding the inner diameter of the tubes, the fins and tube are bonded together, creating an extended surface area for efficient heat transfer. An example of an assembled fin-tube heat exchanger is shown in Fig. 1.1(a) while Fig. 1.1(b) and 1.1(c) show the copper tubes and stamped fins, respectively. Fig. 1.2 shows a schematic diagram of the fins and tube showing the cross-flow configuration between the two fluid streams.

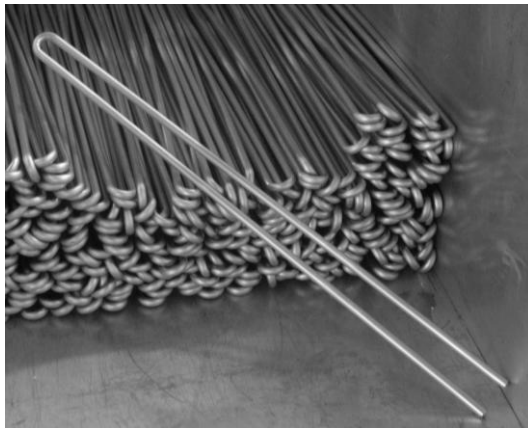
1.3 Description of the flow maldistribution phenomenon

The fin-tube heat exchanger is usually positioned within an enclosure together with the other components in a system. These will include the blower or propeller fan, motor and brackets. Due to the proximity of these items to the heat exchanger, some of the air flowing through the coil could be blocked or diverted. This contributes to the non-uniformity of air distribution flowing through the coil. With the design of systems becoming more compact in recent times, the volume space within the unit becomes smaller and the components are positioned ever closer to each other. The flow of air through the unit becomes more tortuous. Hence, the degree of air non-uniformity becomes higher.

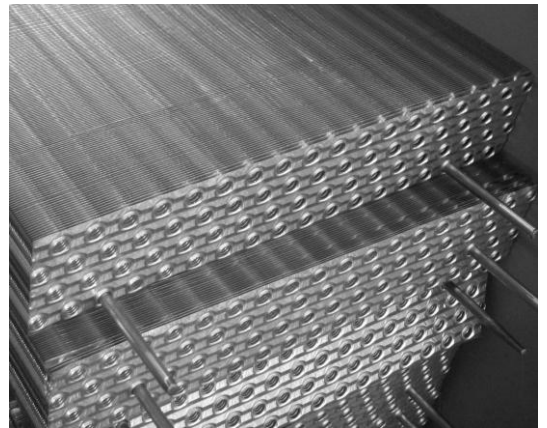
An example from an air-conditioning system is used to illustrate this situation. Fig. 1.3 is a sectional view of a wall-mounted residential air-conditioning fan coil unit, wherein the drive to make the unit more compact due to aesthetic reasons, has necessitated the heat exchanger to be “wrapped” around the blower within the plastic enclosure. As a result of this, the air flow gets distorted as it is aspirated by the blower.



(a)



(b)



(c)

Fig. 1.1: Example of fin-tube heat exchanger (a) Assembled fin-tube coil (b) Copper "hairpin" tubes (c) Stamped fins

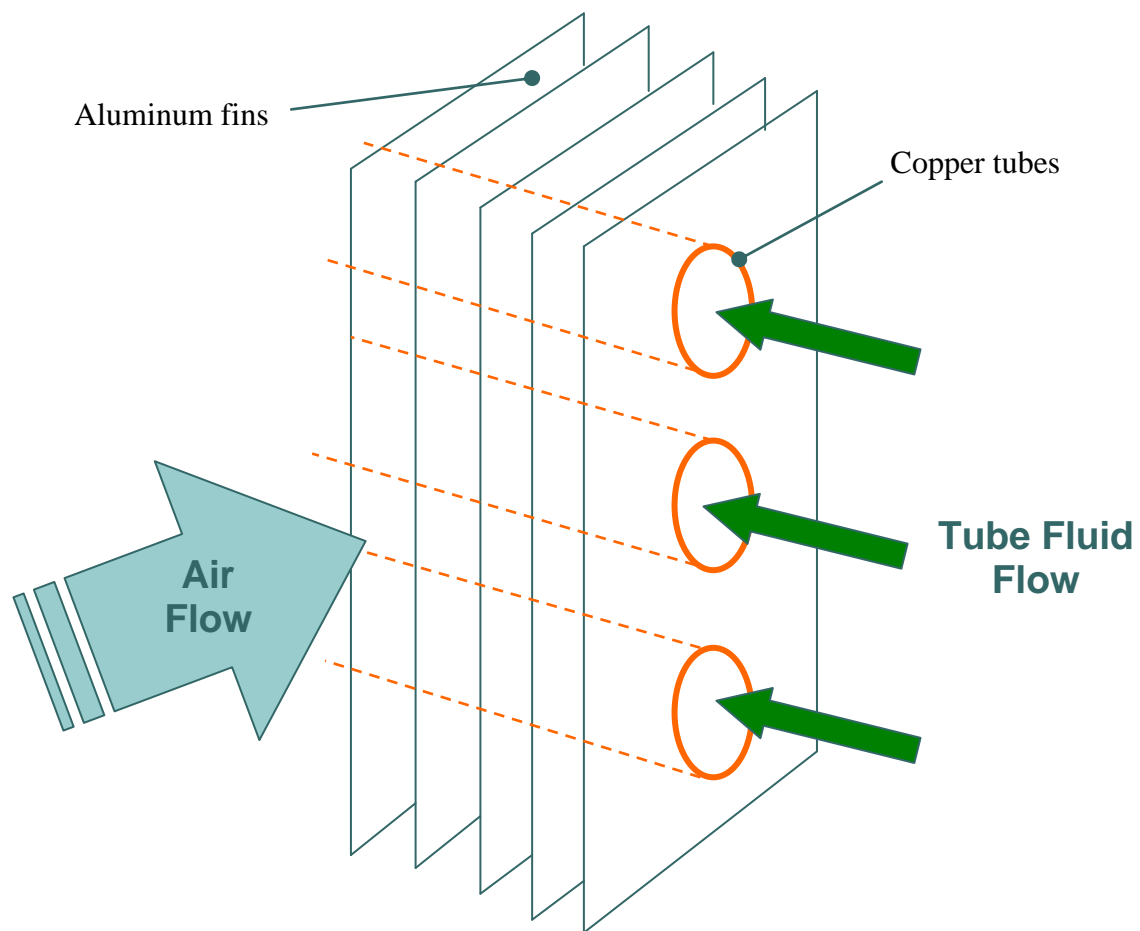


Fig. 1.2: Schematic diagram of fin-tube coil

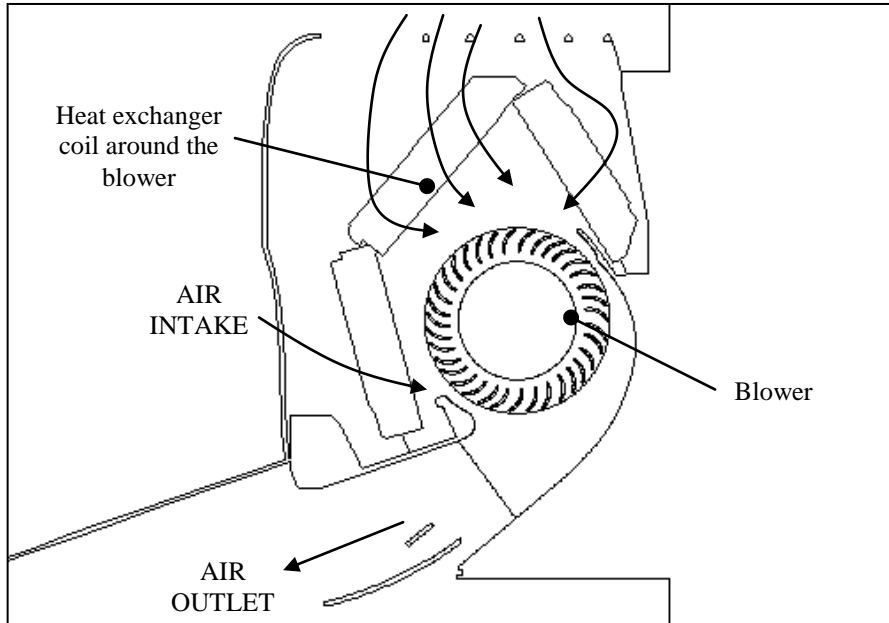


Fig. 1.3: Non-uniform air flow through a wall-mounted unit

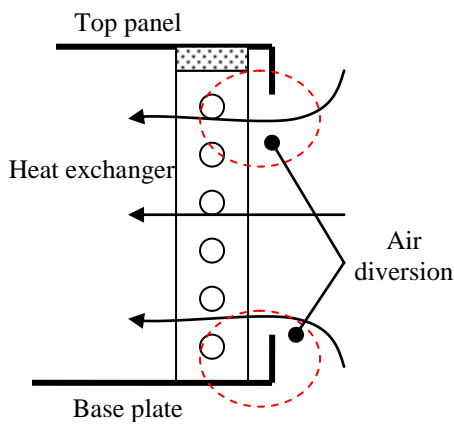


Fig 1.4: Air diversion due to top and bottom panels

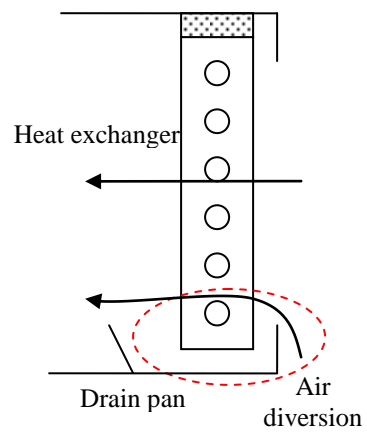


Fig. 1.5: Air diversion due to drain pan

Besides that, the structural design of the enclosure casing itself could give rise to problems of flow non-uniformity. For vertically mounted coils, the air velocity at the upper and lower portions of the coil adjacent to the top and bottom casing panels will be the slowest due to diversion and friction effects, as shown in Fig. 1.4. All evaporator coils also have condensate drain pans which will divert some air away from the lower portion of the coil. Fig. 1.5 illustrates this problem. Other examples of air non-uniformity occurring in a unit, as shown in Fig. 1.6, include:

- a) Slanting of the heat exchanger coil at an angle with respect to the air flow direction to reduce the overall height of the unit.
- b) Positioning the air moving propeller fan at the top of a tall heat exchanger coil.
- c) Bending of the heat exchanger coil into L-shape to maximize the coil face area for a given enclosure casing volume.
- d) Attachment of air ductwork to the unit which include bends, tees, fittings and transition pieces.

On the tube side of the coil, maldistribution occurs when uneven mass flow rates occur in each of the coil tube circuits, as illustrated in Fig. 1.7. This could come about as a result of:

- a) Improper header and distributor design, especially at the inlet pipe
- b) Unequal serpentine tube length among the circuits in the coil
- c) Positioning and orientation of the circuits within the coil with respect to the air flow which could induce temperature maldistribution in the tube-side

In general, two-phase refrigerant flows are more difficult to distribute uniformly among the circuits. Gravitational forces could also play a part in separating the phases, thereby aggravating the maldistribution.

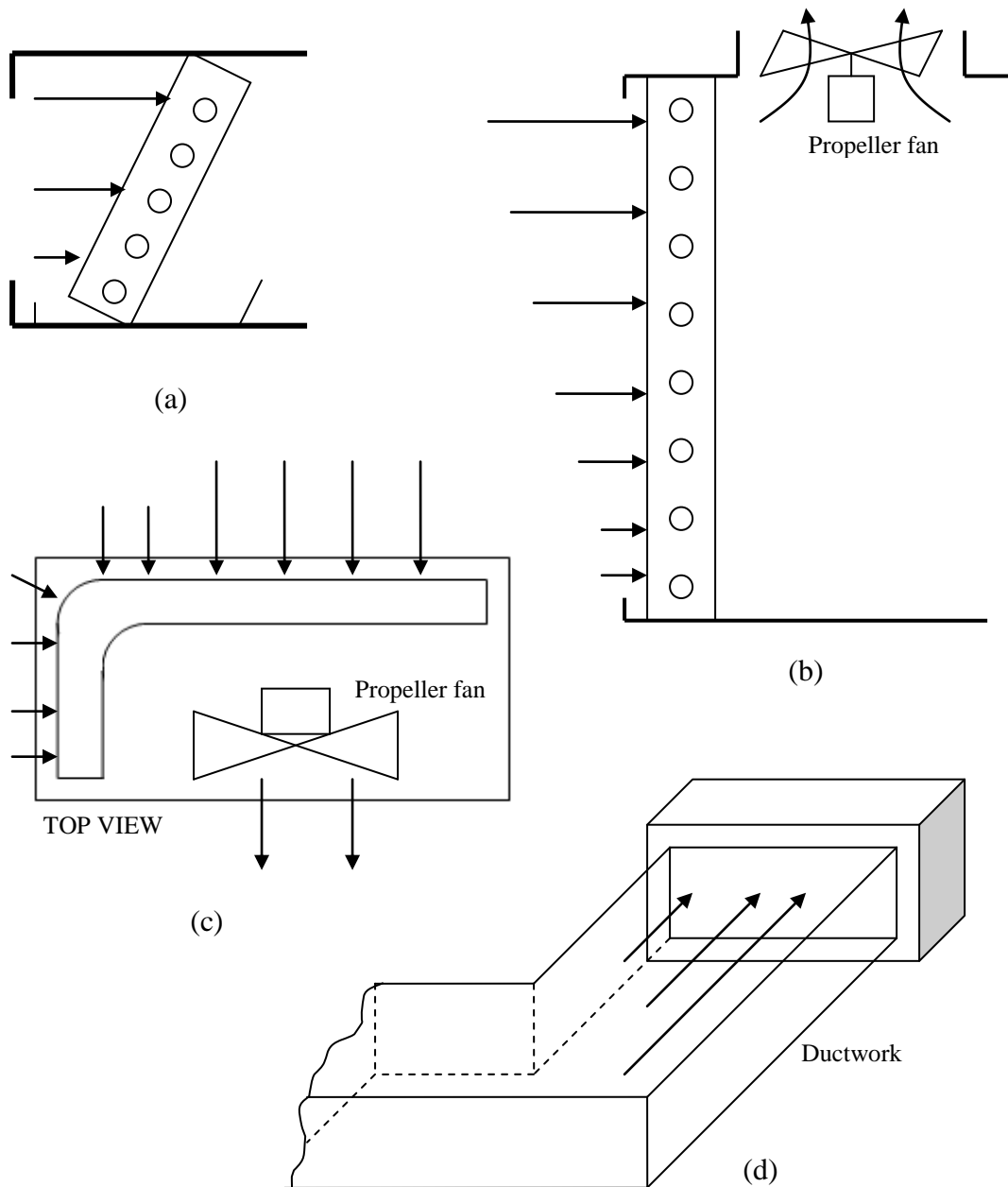


Fig. 1.6: Examples of maldistributed air flow (a) Slanted coil (b) Tall coil (c) L-shaped coil (d) Bend in return ductwork

Uneven mass flow rate in each circuit of the exchanger

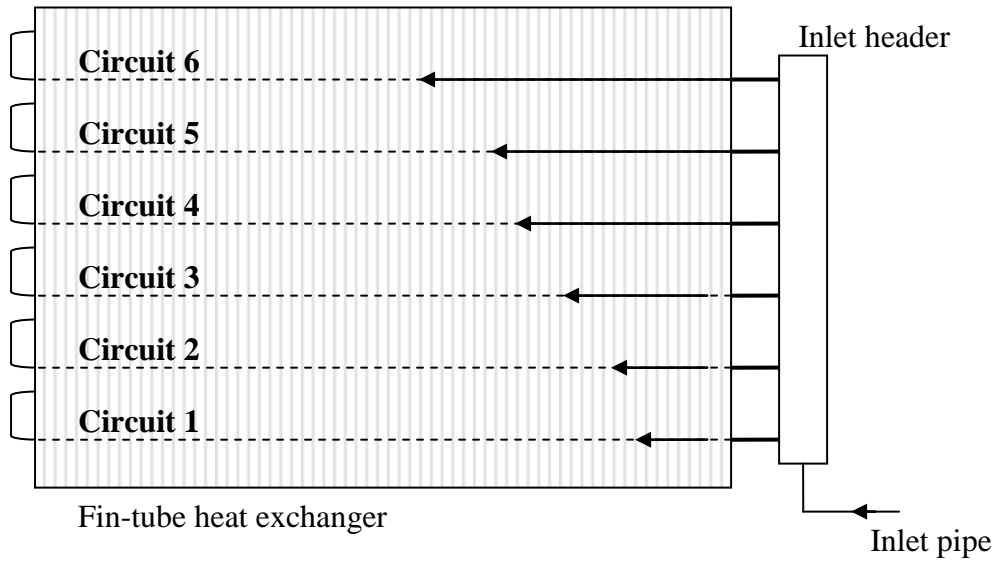


Fig. 1.7: Example of tube-side flow maldistribution

1.4 Adverse effects of maldistribution

The effects of maldistribution on a heat exchanger are well-known. It impacts performance in two ways. Not only does the heat transfer performance become poorer but the fluid pressure drop through the core will also increase due to the flow non-uniformity on either side of the exchanger. In spite of this, the design of heat exchangers is usually carried out by assuming uniform flow distribution on both fluid streams. The main reasons for doing so are:

- 1) The maldistribution profile in the exchanger is not known *apriori* during the design stage.
- 2) The performance degradation effects of maldistribution are perceived to be small which can be accounted for by applying safety factors.

Consequently, it is not uncommon to find that heat exchangers are over-sized for a particular duty. This practice not only makes the exchanger cost-ineffective but it causes the exchanger to operate at low energy efficiency levels, as the heat transfer capability drops while the energy input to pump the fluid increases.

1.5 Justification for the research

A study [1] has shown that Malaysia consumed approximately 89 billion kWh of electrical energy in 2008, where well over one-third was used in commercial buildings [2]. Perez-Lombard et al. [3] have shown that approximately 40 to 50% of the energy used in buildings is due to the installed refrigeration and HVAC systems which employ fin-tube heat exchangers extensively. If the cost of electricity is taken as RM0.27 per kWh, and if the energy consumption of these HVAC&R systems could be reduced by just 1%, energy cost reduction of approximately RM32 million per annum could be realized. Such a saving would be significant in view of the current global energy crisis which is seeing a potential reduction of world crude oil production [4]. Dwindling resources have also caused escalation of crude oil prices which had reached a record high of US\$146 per barrel on July 2008 [5].

It is because of the realization that HVAC&R systems are among the main consumers of energy that many countries have implemented regulatory controls to

ensure that this type of equipment operates at high energy efficiency levels. For example, the European Union has implemented an Energy Labeling programme for air-conditioning equipment with cooling capacity less than 12 kW, following the EU Council directive 92/75/EEC [6]. Similar programmes are also in place in Australia and New Zealand (Regulation AS/NZS 3823.2) [7], Hong Kong (Energy Labeling Ordinance 2009) [8] and Singapore (Mandatory Energy Labeling Scheme 2008) [9]. Closer to home, Malaysia has recently implemented a similar voluntary energy labeling in 2009 for air-conditioning products with cooling capacity up to 7.32 kW (25,000 Btu/hr) [10]. Consumers are continuously being educated and encouraged to purchase equipment which has the highest energy efficiency.

As a result of the demand for high energy efficiency, various design strategies have been used to increase the heat transfer performance while reducing the electrical power input of HVAC&R equipment. Some examples of these include using high efficiency compressors, improving the heat transfer characteristics of the heat exchanger and implementing frequency-inverter control systems. In this respect, the mitigation of flow maldistribution in heat exchangers would be another strategy to improve system energy efficiency. Even though past researches have indicated small magnitudes of thermal performance degradation due to maldistribution (e.g. 5-15% as reported by Mueller [11]), every percent of improvement in performance by reducing the flow non-uniformity would be significant for energy conservation.

1.6 Objectives of research

In view of the large consumption of energy by systems which employ such fin-tube heat exchangers, focus has been given in this research to quantify and reduce the degradation effects of flow maldistribution on the thermal performance of these exchangers. To start the research, an understanding of the characteristics of maldistribution and its effect on the performance of the heat exchanger is essential. Hence, the first objective identified for this work is to investigate and quantify the effects of the air flow maldistribution statistical moments of mean, standard deviation, skew and kurtosis on the thermal performance of a fin-tube heat exchanger.

Since the geometry of the heat exchanger affects its heat transfer performance, the effects of the geometrical parameters on the performance degradation must also be taken into consideration. Therefore, the second objective of this research is to investigate the influence of these fin-tube coil geometrical parameters on the thermal performance degradation arising from the flow maldistribution.

An examination of the *status quo* on the research conducted in the field of maldistribution shows no comprehensive methodology available to predict the performance degradation due to any flow non-uniformity. Consequently, a third objective has been formulated for this research, viz. to develop a mathematical model that allows prediction of the heat exchanger performance with respect to the flow maldistribution statistical moments. The developed correlation could then be used to modify the heat exchanger layout design to minimize the adverse maldistribution effects and optimizing the system for energy efficiency. As a result, the developed set of correlation equations becomes the novelty arising from this research work.

1.7 Scope of research

The research conducted in this work has investigated the maldistribution of velocity on the air-side of fin-tube heat exchangers. The temperature distribution of the inlet air was assumed to be uniform. Similarly, the flow and temperature distributions on the tube-side were also assumed to be uniform. Only the degradation of the heat exchanger thermal performance was studied in this work. Even though the results have been derived for fin-tube heat exchangers, the concepts and findings would still be applicable for other type of exchangers since the same fundamental heat transfer and fluid flow principles would be applied in the analysis.

1.8 Research methodology

In order to achieve the objectives stated in the preceding sub-section, the following methodology was adopted for the research:

1. Develop a mathematical treatment for a fin-tube heat exchanger from fundamental principles to explain the degradation phenomenon due to flow maldistribution.
2. Develop a numerical model to calculate the magnitude of thermal performance degradation with respect to variations in the four statistical moments of the flow maldistribution. The model makes use of available heat transfer coefficient correlations to model the fins and tubes in the exchanger. In addition, the temperatures of the tube fluid and the tube wall are assumed to be constant along the flow length. This assumption is necessary to isolate distortions due to local effects arising from variations in temperature and properties of the tube fluid. As a result, the findings of the research can be applied for fin-tube exchangers with single-phase flows in the tubes, e.g. water, having small temperature differentials, and with two-phase flows, e.g. refrigerants, with little or no superheat and sub-cooling.
3. In parallel with item 2, generate a set of air-side maldistribution profiles to systematically vary the four statistical moments of mean, standard deviation, skew and kurtosis. These are to be applied on the heat exchanger numerical model where the thermal performance degradation is to be calculated and analyzed.
4. Repeat items 2 and 3 for different coil geometries, e.g. number of rows, fin pitch, tube pitch and fin type.
5. Based on the calculated results, develop a correlation with respect to the moments and coil geometry.
6. Build a test rig to replicate air-side maldistribution profiles on a fin-tube heat exchanger. The air flow distribution profile and the exchanger thermal performance degradation are measured and compared with the predictions of the correlation developed in item 5 in order to validate the model, which may then be available for future work.
7. Simulate the fin-tube heat exchanger used in the experiment with Computational Fluid Dynamics (CFD). The CFD model is to be validated with the experiment data. With the validated model, simulation with various other geometries and

design layout could be performed to extract the statistical moments and to predict the performance degradation.

1.9 Thesis outline

The presentation of the thesis has been divided into a number of chapters. After the present introductory Chapter 1, the literature in the area of maldistribution in heat exchangers is reviewed in Chapter 2. A detailed mathematical treatment of the performance degradation due to maldistribution is reported in Chapter 3. The definition of statistical moments used to characterize the non-uniform distribution profile is also given in this chapter. Chapter 4 describes the numerical model which was used to calculate the performance degradation of a single-row fin-tube heat exchanger arising from a set of maldistribution profiles with varying moments. The influence of the exchanger coil geometrical parameters, e.g. tube rows, fin pitch, tube pitch, fin type, etc. are shown in Chapter 5.

In addition, Chapter 5 presents the new set of correlation equations developed to predict the thermal performance degradation due to maldistribution. Chapter 6 then describes the experiments performed to validate the analysis method and correlations while Chapter 7 reports the Computational Fluid Dynamics (CFD) simulation work done on fin-tube heat exchangers. The conclusions of the work are given in Chapter 8.

CHAPTER 2

LITERATURE REVIEW

2.1 Overview

This chapter documents the findings of the literature review to determine the state of the art in the field of flow maldistribution in heat exchangers. The review covers various types of heat exchangers with particular attention being given to fin-tube coils. The review also covers air-side as well as tube-side maldistribution in the coils.

2.2 Review findings

Much of the early research in this field had dealt with the maldistribution problem in shell-and-tube heat exchangers, probably because of their wide application in industries at that time. In the review paper by Mueller and Chiou [12], examples cited of such work include the study by Whistler [13] and Tinker [14] on the effects of fluid bypass and leakage through the baffled segments in the exchanger shell, and the experimental work done by Gotoda and Izumi [15] to measure the inlet velocity maldistribution at the tube sheet of the exchanger.

There has also been some research to investigate this phenomenon in many other types of heat exchangers. Chiou [16, 17] and Ranganayakulu et al. [18] have done extensive work to quantify the thermal degradation in both streams of cross-flow heat exchangers. Berryman and Russell [19] have studied flow maldistribution across tube bundles in air-cooled heat exchangers. In the work by Bassiouny and Martin [20], flow maldistribution in the channels of a plate heat exchanger was examined where the flow behaviour was characterized with a parameter, m . Sparrow and co-workers

[21, 22] did experiments on the heat transfer performance of tube banks using the naphthalene sublimation technique, to determine the effects of air non-uniformity due to blockages and right-angle bend in the duct.

However, the available literature on maldistribution is not extensive, as noted by Mueller [11]. The literature is widely dispersed, covering a large range of heat exchanger applications. Also, the detrimental effects of maldistribution are usually ignored. This apparent lack of concern is due to the relatively small reduction in thermal performance observed with turbulent and low NTU (i.e. high velocity) fluid flows. Consequently, conventional heat exchanger design procedures assume uniform distributions of flow and temperature, even though such uniform distributions are rare, and the base designs are usually combined with a safety factor to estimate the exchanger performance. Such practices have been found to be adequate for design but in reality the safety factors have concealed the true loss of performance due to the actual maldistribution profiles found in the exchanger core.

Kitto and Robertson [23] have identified two situations where the effects of maldistribution should not be ignored, i.e. when:

1. Design margins are being reduced
2. Thermal performance of the exchanger becomes very sensitive to flow changes

The first situation prevails when the heat exchanger performance must be balanced with the capital cost of equipment. The degradation effects of maldistribution must be known to prevent over-sizing of the heat exchanger which inflates the equipment final cost. This is even more critical with the design of compact fin-tube heat exchangers in air-conditioning products which face stiff price competition and rising raw material cost. The second situation relates to exchangers which have a two-phase fluid flowing in the core, in which there is always a natural tendency of the phases to separate. The variations of the fluid vapour quality in the different channels of the exchanger become sensitive to flow maldistribution on the other side which could induce secondary effects, such as causing large temperature differentials along the flow path, which aggravate the deterioration. Such situations are commonly encountered in air-

conditioning fin-tube heat exchangers which have refrigerants either in flow boiling or condensation.

In short, Kitto and Robertson [23] have emphasized that the effects of maldistribution should not be ignored, but instead require careful assessment. They have then reiterated the main causes of maldistribution, which were originally stipulated by Mueller and Chiou [12], i.e.:

- a) Mechanical design-induced
- b) Flow self-induced
- c) Two-phase flow separation and instabilities
- d) Fouling induced

Clearly, the examples shown in Fig. 1.3 to Fig. 1.7 belong to (a). The work presented in this thesis will not deal with problems related to (b), (c) and (d).

2.2.1 Air-side maldistribution

Perhaps one of the precursor studies which have motivated the research on air-side maldistribution for fin-tube heat exchangers was that by London [24] where the effect of non-uniform passages on the performance of plate-fin heat exchangers used as gas turbine regenerators was investigated. The non-uniformity of flow through the passages was induced due to the irregular spacing between corrugations produced during the manufacturing process. The analysis was performed under fully developed laminar flow for a two-passage model with rectangular and triangular flow channels arranged in parallel. The results of the analysis have shown that larger deviations in the channel sizes, which are quantified with a passage non-uniformity parameter (δ_r), will result in higher net loss in the effective NTU . The smaller passage will have a higher NTU due to the reduced mass velocity and higher heat transfer coefficient due to the reduced hydraulic diameter; and vice-versa.

This work was subsequently extended by Mondt [25] where the curvature and bulginess of the rectangular deep-fold fins were taken into consideration together with the uneven fin spacing. By using the concept of standard deviation, a fin spacing

channel deviation (σ_c) and a bulginess channel deviation (σ_b) were used to characterize the non-uniform flow passages. These were then combined to give a total channel deviation (σ_t). The measured heat transfer performance results for 4 sets of test specimens with varying channel deviations were then presented with Colburn j -factor plots versus the flow Reynolds number which clearly show deterioration with respect to the ideal uniform channel spacing. Larger total channel deviations resulted in higher magnitudes of NTU losses, thus confirming the model developed by London [24].

As a further extension, Shah and London [26] investigated the influence of passage-to-passage non-uniformity for an n -size passage model, instead of the two-size model used by London earlier [24]. A Gaussian passage size distribution (i.e. Normal distribution) was imposed for an 11-passage model and the Nusselt number for the exchanger was evaluated at varying channel deviations. As the channel standard deviation parameter (δ_c) increases, the Nusselt number reduces, indicating poorer heat transfer performance. However, this parameter was found inadequate when skewed distributions were used in the model.

Subsequent to this, Fagan [27] reported the first maldistribution work on fin-tube heat exchangers used in air-conditioning systems. The study covered one dimensional air flow maldistribution patterns flowing over single-row and multiple-row (i.e. up to 4 rows) fin-tube evaporators and condensers. An integration procedure was applied on a mathematical model of the heat exchanger to calculate the thermal performance deterioration with the non-uniform flow. The root mean square (RMS) of the difference between the local velocity and average velocity was used to characterize the non-uniform distribution profiles. The results from this work indicated that distributions with larger RMS have larger thermal performance deterioration. The highest capacity loss exceeding 14% was obtained with a step air distribution profile for a 3-row condenser coil.

Chiou [28] studied the effect of air flow non-uniformity on the performance of a fin-flat tube condenser coil used in the air-conditioning system of an automobile. By applying a similar mathematical discretization technique used in his previous work [16, 17], the thermal performance deterioration factor, τ , was calculated:

$$\tau = \frac{\mathcal{E}_{uniform} - \mathcal{E}_{nonuniform}}{\mathcal{E}_{uniform}} \quad (2.1)$$

A non-uniformity factor, Z , was introduced to characterize the degree of maldistribution on the air-side. The factor was developed based on the concept of standard deviation. For every flow distribution model, a unique characteristic $\tau - Z$ curve was plotted. As a result of incoherence of the $\tau - Z$ plots, the magnitude of deterioration could not be correlated satisfactorily. However, larger magnitudes of Z resulted in higher deterioration factors. Chiou later used the same technique to extend the work to cover evaporators [29] and radiator, heater and oil cooler [30] in automobiles. Similar graphical $\tau - Z$ curves have also been plotted for these applications.

Following the footsteps of Chiou, Kondo and Aoki [31] used the modified Fluid-In-Cell (FLIC) method to calculate the effect of two- and three-dimensional air flow profiles on an automobile evaporator. The flow domain was discretized into triangular finite element meshes and the governing mass, momentum and energy conservation equations were solved. The degree of flow non-uniformity was expressed by using the space-averaged root-mean-square velocity distribution factor, K , i.e.

$$K = \sqrt{\frac{1}{S} \int_s [v(s) - \bar{v}]^2 ds} \quad (2.2)$$

where S is the frontal area of the heat exchanger. The same thermal deterioration factor used by Chiou [28], i.e. equation (2.1), was also calculated, though defined differently, i.e.

$$D = \frac{Q_u - Q_m}{Q_u} \quad (2.3)$$

where Q is the exchanger heat duty. As a result, a simple quadratic relationship between D and K was developed to correlate the magnitude of degradation with the degree of maldistribution, i.e.

$$D = 14.8K^2 \quad (2.4)$$

In another mathematical modeling study, Domanski [32] developed a computer programme called EVSIM which calculated the evaporator cooling capacity based on a tube-by-tube approach and which takes into consideration the air-side and tube-side

maldistributions. Good agreement within $\pm 8\%$ for the total cooling capacity was achieved between the simulation results and reported experimental data. It was also reported that the air flow maldistribution was found to be the primary reason for the coil capacity degradation. It was further noted that the air-side non-uniformity altered the distribution of refrigerant in both symmetrical and non-symmetrical tube circuits as long as the design distribution did not match the air-side maldistribution.

As an extension to Domanski's work [32], Lee and Domanski [33] used an upgraded EVAP5M simulation program to evaluate the performance of fin-tube evaporators which had R-22 and zeotropic-mixture R-407C refrigerant flowing in the tubes. One-dimensional maldistributed air velocity profiles (i.e. step and triangular distributions) were then imposed on 3-row coils with three types of refrigerant circuit designs, i.e. cross-counter flow, cross-parallel flow and cross flow. Of the three, the cross flow circuiting gave the poorest performance. It was observed that triangular distribution profiles have the worst effect on the evaporator performance, e.g. up to 43% with R-407C refrigerant in the cross-flow circuit design. However, it was not possible to recommend a general rule for estimating capacity degradation for R-22 and R-407C. A combination of coil circuit design and fluid distribution (both air side and refrigerant side) affects the performance of the evaporator, and it must be evaluated case-by-case.

The work was then followed-up by Lee et al. [34] where the effects of two-dimensional maldistribution profiles on the thermal performance of fin-tube evaporator with zeotropic refrigerant R-407C was studied. Four velocity profiles were entered into the modified EVSIM programme developed previously [32], i.e. (a) uniform, (b) convex, (c) concave and (d) inclined. Of these, the concave distribution gave the worst degradation of 6%. The reason given for the degradation was the change of local transfer characteristics due to different air velocity on each section along the flow path which changes the heat flux, and therefore affects the heat transfer coefficients in the tube.

A more recent numerical study was conducted by Shao et al. [35] on serpentine microchannel heat exchangers which have propane refrigerant (R-290) condensing in tubes. Three types of air maldistribution profiles were imposed on the coil surface. As

expected, the highest capacity degradation up to 21% was obtained with a 2-dimensional non-uniform profile which exhibited the highest velocity variation. The magnitude of degradation for the 2-dimensional non-uniformity was larger than that for 1-dimension.

One of the earliest reported experimental studies of flow maldistribution on fin-tube heat exchangers was the study conducted by Chwalowski et al. [36]. In the experiment, the cooling capacity of evaporator coils was measured to verify three numerical algorithms developed to calculate and predict the thermal performance of the coils. Several sets of coils were tested, i.e. V-shaped and inclined flat coils. Due to the inclination, the air velocity was observed to be higher at the upper portion of the coil than the bottom. Actual velocity measurements were made with a pitot tube. The general trend of the results showed that the coil suffered higher capacity degradation as the inclination angle with respect to the flow direction reduces. With lower angles, the difference in the velocities between the top and bottom portions of the coil was more pronounced. For example, at 15° and with an air flow rate of $11.5 \text{ m}^3/\text{min}$ ($406 \text{ ft}^3/\text{min}$), the capacity was lower by 30% with respect to that at 90° , while at an angle of 25° , the degradation was 22%. Consequently, the measured cooling capacities did not match the predictions given by the numerical models which assumed uniform distribution.

The experimental results from this work have been used by Domanski [32] to verify his EVSIM program. The results also showed that the tube circuit in the evaporator coil which experienced higher air velocities had larger superheat at the circuit outlet. Larger differences in the amount of superheat between the circuits in the coil contributed to higher performance degradation. Therefore, the degradation was attributed to the combination of both the primary air-side and induced refrigerant-side maldistributions.

Timoney and Foley [37] have commented that there was a lack of experimental work to measure the effects of flow maldistribution on heat exchangers, especially the effects of the turbulent characteristics of the flow. Hence, a test facility was fabricated to measure the non-uniform air velocity over a compact evaporator fin-tube coil by means of Laser Doppler Anemometer (LDA). The method was able to measure the

air-side turbulence intensity at specific locations on the coil face. The heat exchanger had refrigerant R134A flowing in the tubes.

Initial air velocity distribution measurements exhibited good uniformity over the coil surface (i.e. average of 4.0 m/s). Air flow non-uniformity was then introduced by placing a perforated metal plate covering certain portions of the coil. In this work, both the mean and standard deviation were used to characterize the flow distribution. The heat duty of the exchanger was measured on the refrigerant side.

The results for the non-uniform distributions showed either the same or better heat duty than the case with uniform distribution. This was contrary to previous findings where non-uniform air flow distributions gave capacity degradation over uniform distribution. The measurements from the LDA showed that the non-uniform distribution had a higher velocity standard deviation and higher turbulence intensity. Hence, it was suggested that turbulence effects or favourable interaction between local convection coefficients inside and outside the tubes could be the reason for this observation. Similar results were later obtained by Ryan and Timoney [38] where 15% augmentation in heat transfer was obtained with non-uniform flows which have high induced turbulence.

Beiler and Kroger [39] examined the maldistribution problem for single and two rows of finned tube bundles in air-cooled heat exchangers (ACHE). The results of their forced-draft experiments clearly showed that the deterioration of the first row was less than that for the second row. This was expected because of the distortion of the temperature distribution after passing through the first row. Similar findings were also reported by Fagan [27]. Nevertheless, the value of thermal deterioration factor was low, i.e. less than 2%.

Further to that, experiments with induced-draft arrangements revealed that the effect of air flow maldistribution was more prominent with the forced-draft arrangement. However, the high turbulence in the wake of the forced-draft fan tends to enhance the heat transfer coefficient of the exchanger, thus counteracting the effect of the maldistribution to a large extent. Hence, the overall performance is less affected when compared with the induced-draft system. This meant that induced-draft systems will see larger performance deterioration due to non-uniformity of the air and

temperature. Therefore, the power required for the air-moving fan would be higher for an induced- than for a forced-draft system.

Kirby et al. [40] presented the effect of non-uniform air flow distribution on the performance of a window air-conditioner unit. Due to the compact arrangement of the unit, maldistribution on the evaporator coil was imposed by the placement of a squirrel cage blower close behind the coil. Maldistribution on the condenser coil was imposed by the propeller fan itself. Measured velocities were observed to vary by a factor of three among all the data over both coils. In the wind tunnel experiments used to mimic the non-uniform distribution on the evaporator, where a circular disk with the same diameter as the blower covered 16% of the coil face area, the measured cooling capacity degradation over a range of air flow rates did not exceed 2%. With the blocked evaporator coil, air velocity was higher on the un-blocked regions therefore increasing the heat transfer coefficient (which varied with the 0.7 power of velocity). But this increase was not sufficient to completely offset the effect of decreasing area of heat exchange, hence only giving a small percentage of degradation.

Furthermore, the point where superheat transition occurred in the tube circuit was moved downstream in the coil, i.e. nearer to the outlet. A larger percentage of the coil remained in the two-phase region (i.e. with a reduced superheat area) which has a lower thermal resistance. This helped to offset the inability of velocity to compensate fully for the loss of heat transfer surface area. The implication from this work was that the capacity losses due to air flow non-uniformity would be larger in evaporators with smaller two-phase area or with high superheat at the outlets. This would also mean that coils with single phase flows in the tubes will be more sensitive to air side maldistributions.

The detrimental effects of having large superheat variations at the tube outlets of the evaporator arising from the air-side maldistribution could be counteracted by means of smart distributors, as demonstrated by Choi et al. [41]. The experimental results indicated that by controlling the amount of superheat at the evaporator outlets, the penalty of cooling capacity could be reduced. This was achieved by adjusting the opening of expansion valves which regulate the refrigerant mass flow rate through

each of the three individual circuits in the coil. For example, with a velocity ratio of 1:2.59 between the upper and lower portions of the coil, the cooling capacity penalty was measured at 6% when the superheat is not controlled; which was then recovered to 2% when the superheat was adjusted to 5.6°C for all the circuits. Similar findings have been reported by Payne and Domanski [42].

In the same work [41], a standard deviation of the superheat values for all the circuits with respect to the overall main exit superheat was also used to analyze the problem. With higher velocity ratio, this standard deviation increased until a plateau was reached. This occurred when the superheated temperature approached the inlet air temperature.

The maldistribution problem in a large package rooftop air-conditioning unit was investigated by Aganda and co-workers in two papers [43, 44]. In the first paper, the air velocity distribution and turbulence were measured at a plane 25mm upstream of the evaporator. This was done by using a single hot-wire anemometer probe. The velocity mean and root-mean-square (RMS) of velocity fluctuations were used to characterize the non-uniformity. In the sequel, the velocities over each parallel circuit in the coil were normalized by dividing with the mean value. It was found that the air flow maldistribution over each circuit caused refrigerant maldistribution among the circuits. With a single thermal expansion valve controlling the refrigerant flow at the inlet, the worst performing circuit dictated the performance of the whole evaporator. The worst case scenario indicated a 38% loss in heat transfer performance due to the reduction of refrigerant mass flow rate as a result of the valve control sensor detecting the outlet temperature of the less effective circuit. Hence, the results of this work demonstrated the importance of locating correctly the control sensor of the expansion valve on the coil. In practice, the sensor would be placed in a position where the liquid from the non-effective circuits would have mixed with superheated vapour from the other circuits, thus mitigating this detrimental effect to some extent.

The work by Elgowainy [45] was probably the first to investigate air flow maldistribution on fin-tube heat exchangers by using a commercial Computational Fluid Dynamics (CFD) code. Unlike the previous analytical methods where 1-dimensional or 2-dimensional geometric regular maldistribution patterns (e.g.

triangular, parabolic, etc.) were used, CFD allows analysis of more realistic, 3-dimensional maldistribution profiles. In this work, simulation of air flow over a cylindrical-shaped heat exchanger in a heat pump unit was performed. The heat exchanger itself takes up 75% of the face area. A propeller fan was located on top of the unit. In the CFD model, the coil was treated as a porous medium. The simulation results showed the non-uniform air velocities over the coil face area with the maximum velocity occurring near the top and steadily declining to the bottom. The decline was attributed to the radial outward velocity component at the tip of the propeller fan blade which sucks up more air through the upper portion of the coil. This situation is similar to that shown in Fig. 1.6(b).

A tube-fin section, which has a single inter-fin spacing, was then simulated to determine the effects of the air velocity on the air pressure drop and heat transfer coefficient. The actual geometry of the fin pattern (i.e. smooth and louvered fin) was used in the simulation. The simulated air velocities on the full heat exchanger were then put in into the model and the mass-averaged pressure drop and area-averaged heat transfer coefficient were computed for the whole coil. The results showed an increase of pressure drop by 9% and 8% with smooth fin and louvered fin, respectively, as a result of the non-uniform distribution. However, the effect on the heat transfer coefficient was not as significant, i.e. with a reduction of 1.5% and 0.9% for the smooth and louvered fins, respectively. From the results of this study, Elgowainy has demonstrated that the effect of the maldistribution was more pronounced on the pressure drop than on the thermal performance of the heat exchanger.

More recently, studies in flow maldistribution has focused on determining the degradation effects on the formation of frost on fin surfaces. For example, Chen et al. [46] has studied the performance of a fin-tube evaporator with an oblique non-uniform frontal air velocity under frosting conditions. The numerical CFD study showed that smaller oblique angles caused larger degradation of refrigerating capacity, which was also reflected in the reduction of weight of frost formed on the fin surfaces. It was observed that the magnitude of deterioration was dependent on the variation of the velocity component perpendicular to the coil surface and the effect of flow vortices formed on the coil surface as the oblique angle changes. The effect on

the air-side pressure drop was also found to be more sensitive to the oblique angle than the capacity and frost weight. This observation is also consistent with the findings of Elgowainy [45]. From the analysis of the data, several correlation equations were developed to relate the refrigerating capacity, frost weight and pressure drop with the oblique angle.

In a similar experimental study by Gong et al. [47], the dynamic frosting characteristics of an air source heat pump chiller with 50kW nominal cooling capacity was investigated experimentally. Three air maldistribution profiles were imposed on the double-V fin-tube coils of the unit which acted as evaporators. An air flow maldistribution degree (AMD) was used to describe the maldistribution. An examination of the definition of AMD reveals similarities with the distribution standard deviation. For their work, the values of AMD used were 0.18, 0.49 and 0.93. The results clearly showed that as the AMD increased, the frost layer grew faster on the fin surfaces while the stable working time of the refrigeration system became shorter and hunting of the operating parameters (i.e. suction pressure and evaporation temperature) occurred. This was attributed to the induced refrigerant maldistribution in the evaporator circuits causing differences in the superheat at the circuit outlets. As the maldistribution increased, the differences became larger which reduced the heating capacity, refrigerant mass flow rate and evaporating temperature of the system. Hence, the temperature difference between the air and evaporator increased, leading to more rapid frosting.

2.2.2 Tube-side maldistribution

One of the earliest researches in the area of tube-side maldistribution was the work done by McDonald and Eng [48], where small magnitudes of heat transfer degradation of about 4% were obtained due to non-uniform distribution in the tubes of a cross-flow heat exchanger. Rabas [49] performed numerical calculations by discretizing the tubes of a shell-and-tube condenser into cells. With brine flowing in the tube for each cell as vapour condensed in the shell, the imposed tube-side maldistribution did not impair significantly the exchanger thermal performance due to the long tube lengths and low effectiveness value. The worst case of non-uniformity

would only cause a degradation of 10%. These results were similar to the other findings of relatively small effects of air-side maldistribution on exchangers with single-phase flows in the tubes.

Due to the difficulty in establishing mathematical models of two-phase flows in tubes, most researches on tube-side maldistribution have been done experimentally or by CFD simulations. Previous researches in this area have primarily focused on the design of headers and manifolds which distribute the fluid among the circuits in the exchanger core. For example, in a series of papers, Jiao and co-workers [50, 51, 52] investigated experimentally various designs of inlet header distributor for plate-fin heat exchangers (PFHE) and their effect on the flow maldistribution problem. The flow distribution through the channels of the exchanger was characterized by calculating the standard deviation, S . Both air and water had been used in their study. The header design parameters varied in the experiments include, among others, the inlet flow angle, inlet pipe diameter and header diameter. From the data, polynomial correlation equations with Reynolds number were developed for various header configurations to allow prediction of S . However, the analysis methodology and empirical equations are specific for the headers of PFHE and are not applicable for other types of heat exchangers.

As described in the preceding section, the maldistribution problem is more severe with two-phase fluids flowing in the tubes due to the gravitational effects which tend to stratify the vapour and liquid phases. Not only does maldistribution of mass flow occur among the tubes but the mass fraction of vapour and liquid in each tube may also be different. If the distribution header is not designed properly, these effects will be compounded. There have been quite a number of experimental studies to understand the two-phase flow mechanism in the headers and to determine the best geometry for the header to minimize the maldistribution effects.

An example of these is the work by Vist [53] who investigated the distribution of two-phase carbon dioxide (CO_2) refrigerant in a horizontal round manifold. The refrigerant enters the manifold at one end and exits at 10 parallel vertical tubes. The distribution of the refrigerant was characterized by using a flow ratio in each tube for both vapour and liquid phases. The experimental results showed that the vapour phase

was mainly distributed in the tubes closest to the manifold inlet while liquid was distributed mainly to the tubes at the other end. At low vapour fractions, vapour tends to flow into the tubes closest to the inlet. With high vapour fractions, the distribution of the vapour phase became more uniform among the tubes but the liquid tended to enter the tubes which were furthest away from the inlet. The distribution was also affected by the manifold diameter. The phase split in the local junctions of the manifold was very much dependent on the vapour fraction in the branch tube and the mass flux in the manifold itself.

A similar experimental work was done by Hwang et al. [54] with a horizontal manifold and vertically oriented flat mini-channel tubes. A flow visualization technique was employed to observe the flow pattern in the manifold. Refrigerant R-410A was used in the experiment while the normalized standard deviation (NSTD) of the liquid mass flow rate in the tubes described the non-uniform distribution in the tubes. Two inlet configurations were tested in the work, i.e. end-inlet (which was similar to the set-up used by Vist [53]) and side-inlet. The results of the NSTD indicated that the side-inlet configuration showed a better liquid flow distribution as compared with the end-inlet.

Flow visualization by videography was also used in the work by Ahmad et al. [55] to observe the two-phase flow characteristics in headers of plate heat exchangers. The type of flow pattern occurring in the header manifold, i.e. stratified, stratified jet, liquid jet and liquid film, was found to be dependent on the mass flux and quality of the fluid. High flow momentum of the liquid phase in the header was observed to be favourable for homogeneous distribution among the channels. It was also determined that a horizontal header orientation has better distribution characteristics than the vertical.

On the other hand, the study of flow maldistribution in headers by Habib et al. [56] was done with a commercial CFD code. Oil was used as the working fluid in the header assembly. The degree of flow maldistribution was characterized by using the normalized standard deviation of the mass flow and static pressure distribution in the header. For the study, the inlet nozzles and outlet tubes of the header were oriented perpendicularly. The results of the simulation have identified the geometrical

parameters of the header that affect the distribution among the outlet tubes, i.e. nozzle diameter, nozzle geometry, number of nozzles, incorporation of a secondary header and number of passes.

The commercial CFD code, FLUENT, was also used by Ismail et al. [57] to simulate air flow distribution through the header and tubes of three compact plate-fin heat exchangers. The headers for two of these exchangers have perforated baffle plates, which were similar to the ones studied by Wen and Li [58], inserted at specific distances from the pipe inlet. The comparison of performance between the real maldistributed case and the ideal uniform case was given in terms of pressure drop. It was clearly seen that the maldistributed flow experienced higher pressure drops by about 6% to 34%. However, with the presence of the baffle plates, the hike in pressure drop was reduced to some extent, due to the suppression of maldistribution.

It can be seen from all these results that the design of headers and distributors should be optimized on a case-by-case basis. In this respect, CFD is a useful design tool which can be used to reduce the tube-side maldistribution. There is no single header configuration which would be optimum for any heat exchanger application. This is not only dependent on the geometrical configuration of the heat exchanger but also on the mass flux of the fluid flowing in the header.

Lastly, Shao et al. [59] performed numerical calculations with a system balancing algorithm on a heat pump system, which has a fin-tube or micro-channel coil as the evaporator under frosting conditions. The evaporator was modeled with the tube-by-tube approach. The dynamic heating capacity of the system was solved in progressive time steps and compared with measurements made under controlled conditions of 2°C dry-bulb temperature and 1°C wet-bulb temperature. The results showed a decreasing trend of the heating capacity with time as the ice formed on the fin surfaces became thicker. Good agreement was obtained between the experimental and simulation results when the refrigerant maldistribution in the evaporator was taken into consideration in the algorithm. A uniform distribution model showed the heating capacity reducing at a slower rate. In other words, the maldistribution had an adverse effect on the heating performance of the system.

2.3 Opportunities for research

It is obvious from the literature reviewed that almost all the past researchers have reported deterioration of performance when the heat exchanger encountered flow maldistribution. The statistical parameters most commonly used to characterize the non-uniform flow distribution are the mean and standard deviation, or other parameters which have definitions similar to the standard deviation. These represent the first and second statistical moments of the probability density function (PDF) for the non-uniform distribution. However, no research has been found that investigates the effect of higher statistical moments, i.e. skew and kurtosis, on the maldistribution problem in heat exchangers. In the opinion of the author, these four moments define the characteristics of the maldistribution profile and hence the influence of all of them needs to be considered. The importance of these higher moments has been recognized in several other types of applications, e.g. in packed beds [60] where the pressure drop distribution skewness across the annular test section was determined, and in trickle beds [61] where all four moments were used to define the porosity distribution in the bed.

The review has also revealed that no comprehensive correlations are available which could successfully predict the heat exchanger performance for any given non-uniform flow distribution. A summary of the available correlations from all the literature surveyed has been compiled chronologically in Table 2.1 to demonstrate this situation. Among the few reported are the correlation equations developed by Kondo and Aoki [31] and Jiao et al. [50, 51, 52] which only relate the performance degradation with the flow distribution standard deviation, without taking into consideration the effect of higher moments. The same is also observed in the graphical results obtained by Chiou [16, 17, 28] where the absence of skew and kurtosis in the model could be the reason for the incoherent $\tau - Z$ (i.e. deterioration factor vs. non-uniformity factor) plots obtained for a particular heat exchanger with several maldistribution profiles.

It is from these identified research opportunities arising from the literature review that the research objectives presented in Chapter 1 have been established. It can also

be seen from the review that the maldistribution problem for the fin-tube heat exchanger could be examined from either the air-side or tube-side, or a combination of both. However, it has been highlighted that the air-side maldistribution has primary influence over that of the tube-side. Hence, the research undertaken in this work has focused on the maldistribution problem arising only from the effect of air-side flow non-uniformity. This study would then serve as the platform for continuing the research with tube-side and combined maldistributions.

Table 2.1: Chronological summary of literature review

Author(s)	Ref.	Year	Type of heat exchanger studied	Statistical moments or parameters used to quantify maldistribution	Is maldistribution correlation available?
London	[24]	1970	Plate-fin, triangular passages	Passage non-uniformity parameter, δ_r	Yes. But given in graphical plot: % change NTU and Δp vs. δ_r
Mondt	[25]	1977	Plate-fin	Total combined channel deviation, σ_t	Yes. But given in graphical plots: NTU decrease vs. σ_t
Chiou	[16]	1978	Cross-flow (single-pass)	Non-uniformity factor, ψ	Yes. But given in graphical plot: $\tau-\psi$
Fagan	[27]	1980	Fin-tube	Mean, RMS	No
Shah and London	[26]	1980	Flow passages (laminar flow)	Channel standard deviation parameter, δ_c	Yes. But given in graphical plot: $Nu-\delta_c$
Chiou	[17]	1982	Cross-flow	Mean	Yes. But given in graphical plot: $\tau-NTU$
Sparrow and Ruiz	[21]	1982	Tube banks (cross-flow)	None	No
Bassiouny and Martin	[20]	1983	Plate heat exchangers	m	No
Sparrow and Berman	[22]	1984	Tube banks (cross-flow)	None	No
Chiou	[28]	1984	Fin-tube (flat tube)	Non-uniformity factor, Z	Yes. But given in graphical plot: $\tau-Z$ plot
Chiou	[29]	1985	Fin-tube	Non-uniformity factor, Z	Yes. But given in graphical plot: $\tau-Z$ plot
Chiou	[30]	1985	Fin-tube	Non-uniformity factor, ψ	Yes. But given in graphical plot: $\tau-\psi$

Table 2.1: Chronological summary of literature review (continued)

Author(s)	Ref.	Year	Type of heat exchanger studied	Statistical moments or parameters used to quantify maldistribution	Is maldistribution correlation available?
Rabas	[49]	1985	Shell-and-tube	Mean, velocity ratio	No
Kondo and Aoki	[31]	1986	Fin-tube	RMS K -value	Yes
Mueller	[11]	1987	General (review paper)	-	No
Rabas	[63]	1987	Air-cooled condenser	Mean, % deviation from uniform values	No
Berryman and Russell	[19]	1987	Tube bundles	Mean, standard deviation	No
Mueller and Chiou	[12]	1988	General (review paper)	-	No
Chwalowski et al.	[36]	1989	Fin-tube	Average (mean)	No
Kitto and Robertson	[23]	1989	General (review paper)	-	No
Domanski	[32]	1991	Fin-tube	Mean	No
Timoney and Foley	[37]	1994	Fin-tube	Mean, standard deviation	No
Xu et al.	[64]	1996	Fin-tube	Mean, RMS	No
Beiler and Kroger	[39]	1996	Fin-tube bundle	Mean	No
Ranganayakulu et al.	[18]	1997	Plate-fin, cross-flow	Local flow non-uniformity parameter, α	No
Lee and Domanski	[33]	1997	Fin-tube	Average (mean)	No
Ryan and Timoney	[38]	1997	Fin-tube	Mean, RMS K -value	No
Kou and Yuan	[65]	1997	Cross-flow (single-pass)	Mean	No

Table 2.1: Chronological summary of literature review (continued)

Author(s)	Ref.	Year	Type of heat exchanger studied	Statistical moments or parameters used to quantify maldistribution	Is maldistribution correlation available?
Ratts	[66]	1998	Concentric-tube	None	No
Kirby et al.	[40]	1998	Fin-tube	None	No
Meyer and Kroger	[67]	1998	Finned-tube	Mean, kinetic energy correction factor	No
Lalot et al.	[68]	1999	Heater bank	Mean, ratio of highest to lowest velocities	No
Ranganayakulu and Seetharamu	[69]	1999	Cross-flow	Mean, local non-uniformity parameter, α	No
Aganda et al.	[43]	2000	Fin-tube	Mean	No
Aganda et al.	[44]	2000	Fin-tube	Mean, RMS, turbulence intensity	No
Lee et al.	[34]	2003	Fin-tube	Average (mean)	No
Choi et al.	[41]	2003	Fin-tube	Velocity ratio, standard deviation	No
Elgowainy	[45]	2003	Fin-tube	Average (mean)	No
Payne and Domanski	[42]	2003	Fin tube	Mean, standard deviation	No
Yuan	[70]	2003	Cross-flow (3-fluids)	Local non-uniformity parameter, α	No
Jiao et al.	[50]	2003	Plate-fin (header)	Standard deviation	Yes
Jiao et al.	[51]	2003	Plate-fin (header)	Standard deviation	Yes
Vist	[53]	2004	Round tube manifold	Flow ratio	No

Table 2.1: Chronological summary of literature review (continued)

Author(s)	Ref.	Year	Type of heat exchanger studied	Statistical moments or parameters used to quantify maldistribution	Is maldistribution correlation available?
Wen and Li	[58]	2004	Plate-fin (header)	Absolute and relative maldistribution parameter	Yes (for baffle punch ratio)
Rao and Das	[71]	2004	Plate	m	No
Rao et al.	[72]	2005	Plate	m	No
Chen et al.	[46]	2005	Fin-tube	Oblique angle	Yes
Jiao and Baek	[52]	2005	Plate-fin (header)	Standard deviation	Yes
T'Joean and De Papepe	[73]	2006	Fin-tube	None	No
Wen et al.	[62]	2006	Plate-fin (header)	Velocity ratio, flow maldistribution parameter	Yes (for baffle punch ratio)
Hwang et al.	[54]	2007	Mini-channel manifold	Flow ratio, normalized standard deviation	No
Gong et al.	[47]	2008	Fin-tube	Mean, standard deviation (AMD)	No
Mishra et al.	[74]	2008	Cross-flow	Local non-uniformity parameter, α	No
Shao et al.	[35]	2009	Micro-channel	None	No
Ahmad et al.	[55]	2009	Plate heat exchanger manifold	Flow ratio	No
Habib et al.	[56]	2009	Header	Normalized standard deviation	No
Ismail et al.	[57]	2010	Plate-fin header	None	No
Shao et al.	[59]	2010	Fin-tube	None	No

2.4 Summary

A comprehensive literature review has been done to determine the *status quo* of research in the area of flow maldistribution in heat exchangers. The review has given particular attention to both air-side and tube-side maldistributions on fin-tube heat exchangers. From this, several opportunities for research have been identified. Due to its primary influence on the heat exchanger thermal performance, the effects of air-side flow maldistribution are investigated in this work. Since no prior work has been done to evaluate the effects of skew and kurtosis on the maldistribution problem, this research examines the combined effect of all four statistical moments of probability density function on the heat transfer performance degradation.

CHAPTER 3

MATHEMATICAL FORMULATION OF PERFORMANCE DEGRADATION DUE TO MALDISTRIBUTION

3.1 Overview

In this chapter, the characteristics of a distribution profile are examined. The profile is defined with the four statistical moments of probability density function, i.e. mean, standard deviation, skew and kurtosis. A Taylor series expansion of the fundamental relationship for heat transfer and pressure drop with the fluid velocity has revealed the contributions of each maldistribution statistical moment to the thermal and hydraulic performance degradation of a heat exchanger. The mathematical derivation is done by discretizing both the continuous non-uniform velocity distribution and the heat exchanger itself into a number of cell elements. From these, the sample estimates of the distribution moments are calculated. The findings of this analysis have provided the basic understanding of the maldistribution degradation phenomenon.

3.2 Fundamentals of statistical moments

In statistics, a random variable may be categorized as discrete, if it can be counted, or continuous, if it is measured [75]. Since both fluid velocity and temperature require measurements to quantify their magnitudes, these variables will describe continuous distribution profiles in a heat exchanger. The distribution itself can be expressed either spatially, i.e. within a space defined with a suitable coordinate system (e.g. Cartesian, x - y - z), or in a frequency distribution plot. In the former, the varying velocity or temperature in the distribution occurs at different locations on the exchanger; while in the latter, the frequency of occurrence for a particular velocity or temperature is given as a probability. For this purpose, a probability density curve is

used, as illustrated in the following Fig. 3.1. Therefore, the equation which describes this density curve is called the **probability density function** (PDF).

It is this probability density function which determines the set of statistical moments for a non-uniform distribution. The concept of moment in mathematics has evolved from the concept of moment in physics. By definition, the r^{th} moment of a real-value function $g(x)$ about a value c is given as:

$$\mu_r = \int_{-\infty}^{\infty} (x-c)^r g(x) dx \quad (3.1)$$

Therefore, the first moment of a probability density function, $f(\phi)$, for a parameter ϕ about the origin is the expectation of ϕ , i.e. the mean of the distribution, μ :

$$\mu_1 = \int_{-\infty}^{\infty} \phi f(\phi) d\phi = E(\phi) = \mu \quad (3.2)$$

The r^{th} **central moment** of the probability distribution function around the mean is given as:

$$\mu_r = \int_{-\infty}^{\infty} (\phi - \mu)^r f(\phi) d\phi = E(\phi - \mu)^r \quad (3.3)$$

Thus, the second central moment gives the variance, from which the positive square root is the standard deviation, σ :

$$\mu_2 = E(\phi - \mu)^2 = \text{Var}(\phi) = \sigma^2 \quad (3.4)$$

The **normalized** r^{th} central moment or standardized moment is the r^{th} central moment divided by σ^r , i.e. μ_r / σ^r . The third normalized central moment is called the skew, γ :

$$\gamma = \mu_3 / \sigma^3 \quad (3.5)$$

A distribution with positive skew will have an elongated tail to the right; and vice-versa. A normal distribution curve has a skew of zero.

The fourth normalized central moment, or kurtosis, is a measure of how tall and skinny or short and squat a distribution is, which is given as:

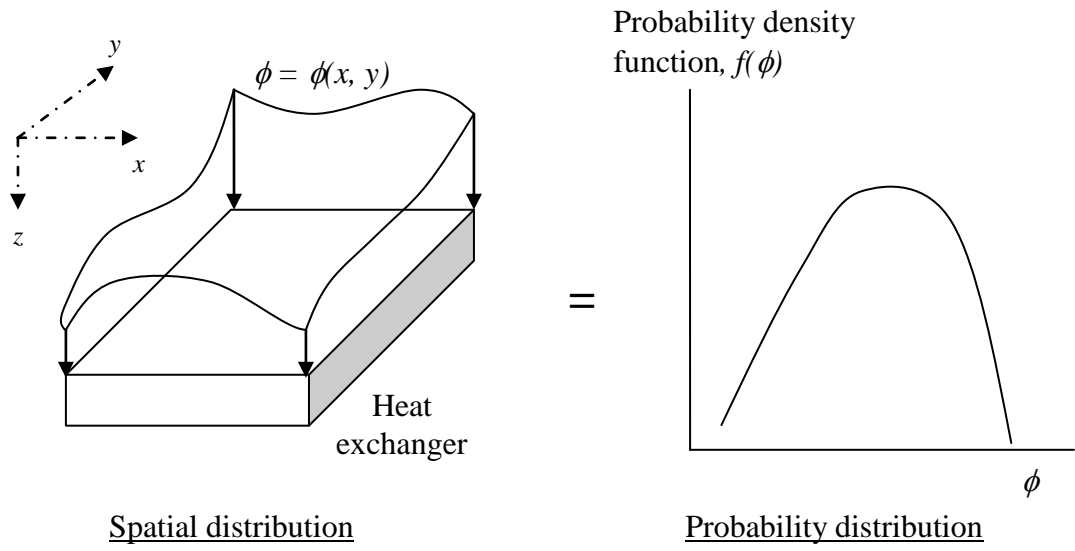


Fig. 3.1: Representation of a distribution profile for a parameter ϕ

$$\kappa = \mu_4 / \sigma^4 \quad (3.6)$$

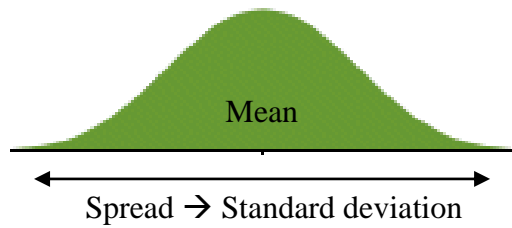
Positive kurtosis distribution, called leptokurtic, indicates a relatively peaked distribution while a negative kurtosis distribution, called platykurtic, corresponds to a flat distribution. If the kurtosis is equal to zero, the frequency distribution is called mesokurtic.

The definitions of equations (3.1) to (3.6) have been obtained from [76, 77]. An alternative definition of kurtosis is also given in [78], which is often referred to as “excess kurtosis”:

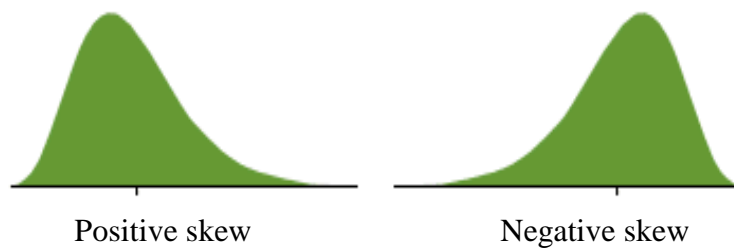
$$\kappa = \mu_4 / \sigma^4 - 3 \quad (3.7)$$

The reason for using this definition is because the kurtosis proper for a standard normal distribution is 3, i.e. by using equation (3.6). With this alternative convention, the normal distribution will have an excess kurtosis of zero, making it convenient to compare the peakedness of a distribution with the normal distribution. In the Microsoft EXCEL software, the excess kurtosis definition is used.

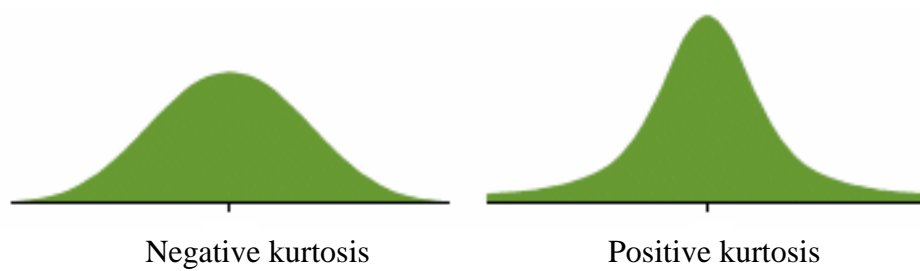
In short, the mean gives the location of the central value for the distribution while standard deviation defines the variability, or spread, of the distribution. The skew is a measure of the lopsidedness of the distribution and the kurtosis is a measure of the degree of flattening of the frequency curve. The following Fig. 3.2 illustrates examples of probability distribution curves which demonstrate these four statistical moments.



(a)



(b)



(c)

Fig. 3.2: Examples of probability density functions which demonstrate the four statistical moments of a PDF: (a) Location and spread of distribution (b) Lopsidedness of distribution (c) Degree of flattening or peakedness

The definitions of moments given above are valid for a large population size, e.g. for the continuous velocity distribution profile which theoretically has an infinite number of velocities. When the profile is approximated by discretization, there will be a small, finite number of velocity elements. In such an instance, it is more appropriate that the sample moments are estimated. In this work, the unbiased sample estimator equations for mean, standard deviation, skew and kurtosis, with a sample size of n , are given as the following [79]:

a) Sample mean, $\bar{\phi}$

$$\bar{\phi} = \frac{\sum_{i=1}^n \phi_i}{n} \quad (3.8)$$

b) Sample standard deviation, s

$$s^2 = \frac{\sum_{i=1}^n (\phi_i - \bar{\phi})^2}{(n-1)} \quad (3.9)$$

c) Sample skew, γ_s

$$\gamma_s = \frac{n}{(n-1)(n-2)} \sum_{i=1}^n \left(\frac{\phi_i - \bar{\phi}}{s} \right)^3 \quad (3.10)$$

d) Sample kurtosis, κ_s

$$\kappa_s = \frac{n(n+1)}{(n-1)(n-2)(n-3)} \sum_{i=1}^n \left(\frac{\phi_i - \bar{\phi}}{s} \right)^4 - \frac{3(n-1)^2}{(n-2)(n-3)} \quad (3.11)$$

3.3 Reason for performance deterioration

The fundamental reason for the performance degradation of a heat exchanger arising from the maldistribution is due to the relationship of the convective heat transfer coefficient and fluid pressure drop in the exchanger to the fluid velocity flowing through it, which can be expressed in the form:

$$h = c_1 \cdot V^n \quad (3.12)$$

$$\Delta p = c_2 \cdot V^m \quad (3.13)$$

where the exponent $n < 1$ and $m > 1$. These relationships can be deduced from well-established heat transfer and friction factor correlations for turbulent flows [80]. This behaviour is illustrated as shown in Fig. 3.3. The magnitude of the constants, c_1 and c_2 , and exponents, n and m , will thus define the heat transfer and fluid flow characteristics in the exchanger which takes into consideration the effect of the shape, size and spacing of the flow channels and the geometry of the channel surfaces. The attachment of headers, nozzles and fittings used to divert or converge the flow through the exchanger core can also be accounted for by these constants in certain types of heat exchangers; for example, cross-flow and fin-tube heat exchangers.

In other words, the gross maldistribution that takes place on the heat exchanger is defined by the resultant approach fluid velocity. On the other hand, the approach velocity distribution would also be affected by the downstream flow behaviour through the exchanger core itself due to friction effects, passage-to-passage variations and re-laminarization in the flow passages. In this respect, higher flow resistance in the exchanger core will tend to attenuate the inlet maldistribution profile.

When the distribution is uniform, all the velocities will be the same, say $V = 1.0$. In a maldistributed profile, there will be certain portions in the exchanger core which experience both higher and lower velocities than the mean value. Due to n being < 1 , the portions with the lower velocities have a larger influence in reduction of heat transfer coefficient than the increase for the higher velocities. Similarly, with $m > 1$, higher velocities have a more significant effect on the increase of pressure drop than its reduction at lower velocities. For example, consider $n = 0.8$ and $m = 1.8$ (i.e. typical for fully developed turbulent pipe flows, as can be seen from the Dittus-Boelter Nu correlation and Blasius f -factor correlation [80]), and for simplicity, half of the exchanger has 50% higher velocity than the mean, i.e. $V_{high} = 1.5$, whereas the other half has 50% lower velocity, i.e. $V_{low} = 0.5$.

By using equation (3.12), the reduction in heat transfer coefficient for the lower velocity is calculated as 42.6% while the increase for the higher velocity is 38.3%. Since the heat transfer rate is proportional to the heat transfer coefficient, this would mean that there is a net reduction of 2.2% in thermal performance arising from this maldistribution with respect to the case of uniform distribution, i.e.

$$\frac{Q_{maldistributed}}{Q_{uniform}} = \frac{[(0.5 * 0.5^{0.8}) + (0.5 * 1.5^{0.8})]}{1} = 0.978 \quad (3.14)$$

Simultaneously, the changes in the fluid pressure drop arising from this situation are calculated as 107.5% increase and 71.3% reduction for the higher and lower velocities, respectively. This results in a 62.8% net increase of mass-averaged pressure drop, i.e.

$$\frac{\Delta p_{m,avg-maldistributed}}{\Delta p_{m,avg-uniform}} = \frac{[(0.5 * 0.5^{1.8}) * 0.5 + (0.5 * 1.5^{1.8}) * 1.5]}{1} = 1.628 \quad (3.15)$$

3.4 Mathematical model

In this study, the influence of the flow distribution statistical moments on the heat exchanger performance is investigated on only one fluid stream of the exchanger. To facilitate this, a cross-flow heat exchanger is modeled where the flow maldistribution is imposed on one side of the exchanger while the flow is uniform on the other side. In addition, the fluid inlet temperature on both fluid streams is held uniform and constant so as to isolate the flow maldistribution effects from any local temperature distortions.

Let the continuous velocity distribution on the inlet face area of a heat exchanger be expressed, within a spatial Cartesian coordinate system similar to that of Fig. 3.1, as $u = u(x, y)$. This will give rise to a PDF curve, $P(u)$. The area under this curve denotes the probability of occurrence for the velocity u in the distribution profile.

For the analysis, the cross-flow heat exchanger is discretized into smaller elements. This methodology is similar to that used by Chiou [17] and Ranganayakulu et al. [18]. The inlet face area is discretized into an arbitrary number of cells, N_f . An example is shown in Fig. 3.4 for a fin-tube cross-flow heat exchanger. A specific velocity is then assigned to each cell while another fluid flows with uniform velocity on the other side of the exchanger. The combination of these velocities for all the cells will give the velocity maldistribution profile on the exchanger. Essentially, both the

spatial distribution and probability distribution of velocity are correspondingly discretized with this process. This is illustrated in Fig. 3.5.

By using the same definition of equations (3.8) to (3.11), the sample estimates of the moments for the velocity distribution are calculated to give the mean, \bar{u} , standard deviation, s_u , skew, γ_u , and kurtosis, κ_u .

A new variable, k , is now defined, such that:

$$k = \frac{u - \bar{u}}{s_u} \quad (3.16)$$

This parameter can be viewed as a dimensionless moment.

The velocity in the abscissa of the discretized probability density function shown in Fig. 3.5 is then re-plotted as Fig. 3.6. The values of k will range from negative to positive while it is zero when the velocity u is the mean. Such a transformation allows a linkage between the spatial and probability fields of the distribution.

On the ordinate of Fig. 3.6, P_k is the discrete probability for k , which is actually an approximation of $P(u)$ for the continuous distribution. The number of elements having the magnitude of k in the distribution, N_k , is then approximately equal to the area under the probability density function curve at k for an interval of Δ_k multiplied by the total discrete elements, N_t . This can be expressed as:

$$P_k = \frac{N_k}{N_t} \cdot \frac{1}{\Delta_k} \quad (3.17)$$

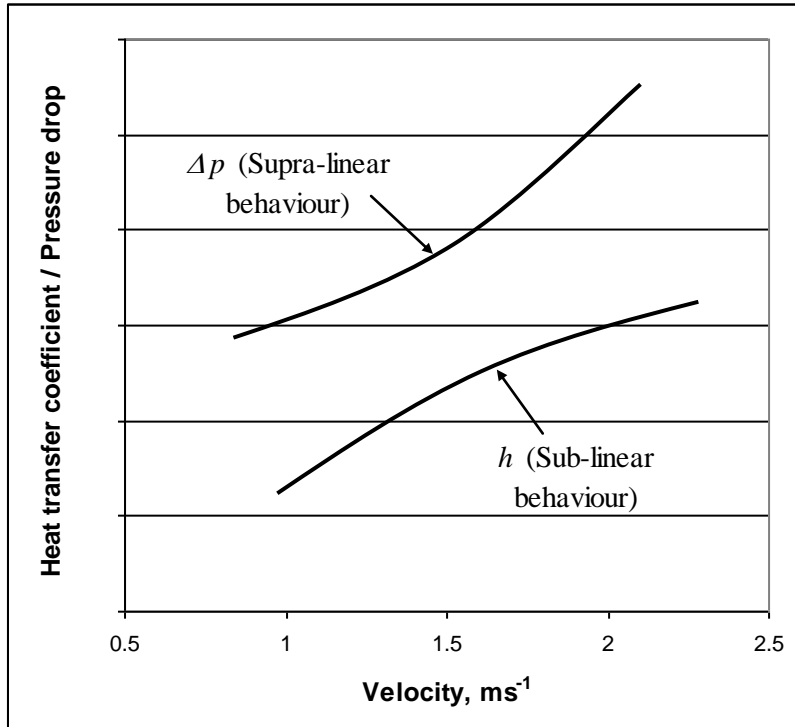


Fig. 3.3: Example of heat transfer coefficient and pressure drop characteristics with velocity

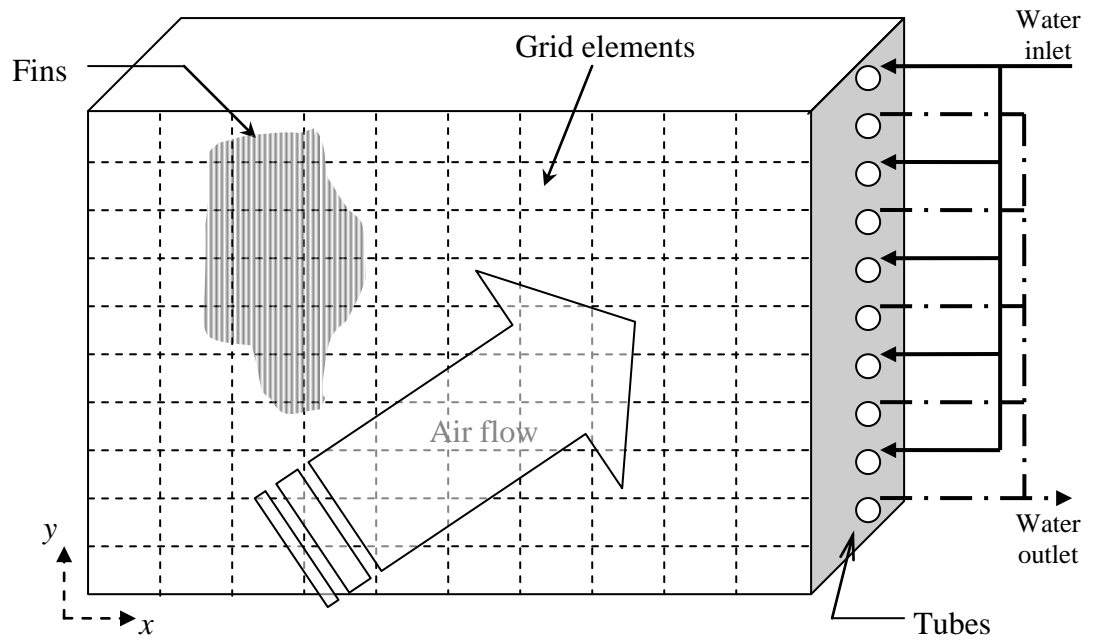


Fig. 3.4: Example of discretized fin-tube heat exchanger

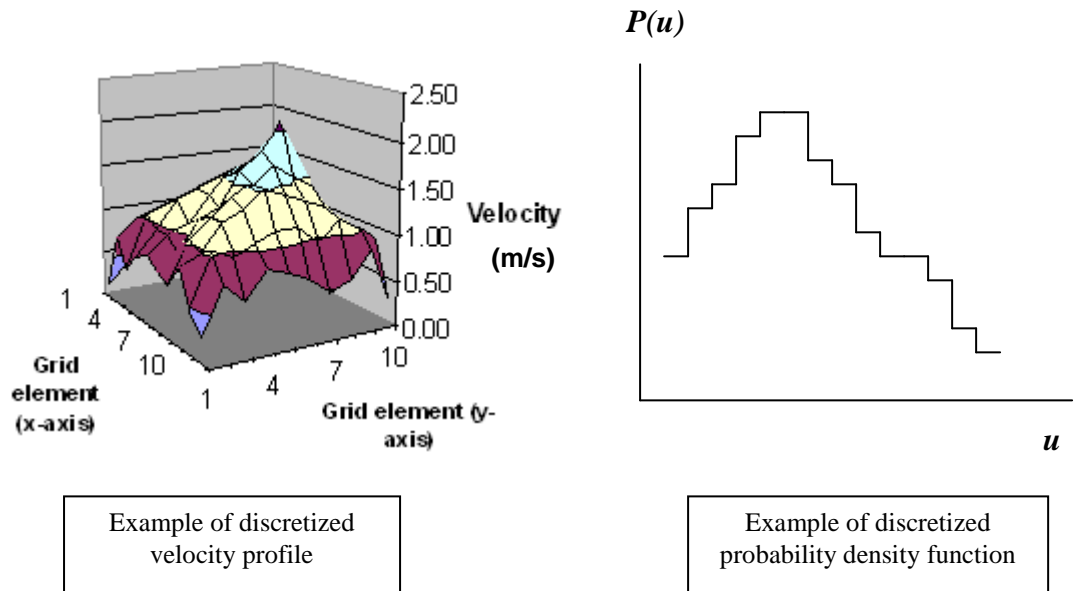


Fig. 3.5: Discretization of spatial and probability distributions

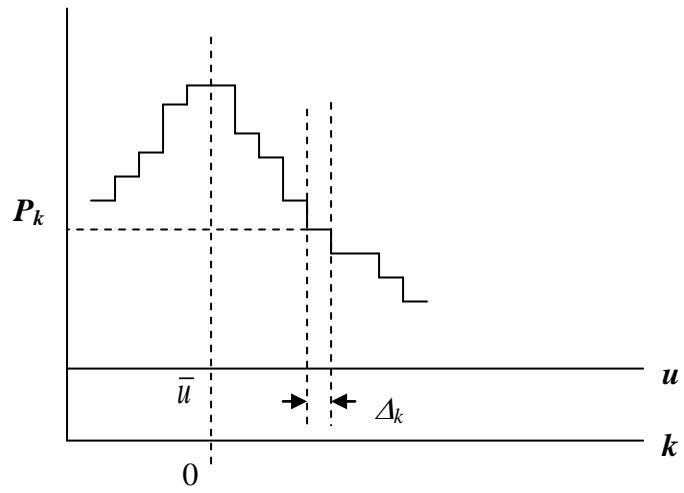


Fig. 3.6: Transformation of discretized probability density function

3.4.1 Thermal performance degradation

If A_o is the total external surface area for one discrete element of the exchanger, the total heat transfer of each element is given as:

$$q = h \cdot A_o \cdot \eta_s \cdot \Delta T \quad (3.18)$$

The fin surface efficiency, η_s , appears on the right-hand side of the equation to take into consideration the effects of fins on the heat transfer surfaces. If the exchanger does not have fins, then $\eta_s = 1$.

By using (3.12) and (3.16), and assuming a constant tube wall temperature, equation (3.18) can be re-written as:

$$q = \Phi \eta_s (\bar{u} + ks_u)^n \quad (3.19)$$

where $\Phi = c_1 \cdot A_o \cdot \Delta T$ is a constant

Hence, the total heating capacity for all elements which have the same magnitude of k is:

$$q_k = \Phi \eta_{s,k} (\bar{u} + ks_u)^n \cdot N_k \quad (3.20)$$

The total heating capacity of the heat exchanger is the summation of the elemental capacities q_k for all values of k . Substituting equation (3.17) into (3.20) for a fixed interval of Δ_k , the following equation is obtained:

$$Q_m = \Phi \Delta_k N_t \sum_k \eta_{s,k} \cdot P_k \cdot (\bar{u} + ks_u)^n \quad (3.21)$$

With a uniform distribution, $s_u = 0$ and all elements have the same fin efficiency, $\eta_{s,u}$.

Also $\sum_k P_k \Delta_k = 1$, and thus the uniform heating capacity is written as:

$$Q_u = \Phi N_t \cdot \eta_{s,u} \cdot \bar{u}^n \quad (3.22)$$

A Taylor series expansion of (3.21) will then give the following:

$$Q_m = \Phi \Delta_k N_t \sum_k \eta_{s,k} P_k \left[\bar{u}^n + ns_u k \bar{u}^{n-1} + \frac{n(n-1)}{2!} s_u^2 k^2 \bar{u}^{n-2} + \frac{n(n-1)(n-2)}{3!} s_u^3 k^3 \bar{u}^{n-3} + \frac{n(n-1)(n-2)(n-3)}{4!} s_u^4 k^4 \bar{u}^{n-4} + O^5 \right] \quad (3.23)$$

The thermal performance degradation factor, D , is defined as:

$$D = \frac{Q_u - Q_m}{Q_u} \quad (3.24)$$

With $Q_m < Q_u$, higher magnitudes of D have the meaning of higher deterioration of thermal performance.

Subtracting (3.23) from (3.22), and by assuming that $\eta_{s,u} \approx \eta_{s,k}$ for the same \bar{u} with both the maldistributed and uniform cases, equation (3.24) simplifies to:

$$D \approx -\Delta_k \left[n \left(\frac{s_u}{\bar{u}} \right) \sum_k k P_k + \frac{n(n-1)}{2!} \left(\frac{s_u}{\bar{u}} \right)^2 \sum_k k^2 P_k + \frac{n(n-1)(n-2)}{3!} \left(\frac{s_u}{\bar{u}} \right)^3 \sum_k k^3 P_k + \frac{n(n-1)(n-2)(n-3)}{4!} \left(\frac{s_u}{\bar{u}} \right)^4 \sum_k k^4 P_k + O^5 \right] \quad (3.25)$$

Now, from equation (3.10), the skew can be expressed as:

$$\gamma_u = \frac{\sum_{i=1}^{N_t} (u_i - \bar{u})^3}{N_t s^3} = \frac{\sum_i i^3}{N_t} = \frac{\sum_k k^3 N_k}{N_t} = \sum_k k^3 P_k \Delta_k \quad (3.26)$$

Similarly, from equation (3.11), kurtosis can be written as:

$$\kappa_u = \frac{\sum_{i=1}^{N_t} (u_i - \bar{u})^4}{N_t s^4} = \sum_k k^4 P_k \Delta_k \quad (3.27)$$

Inserting (3.26) and (3.27) into (3.25), and ignoring higher order terms ($O \geq 5$):

$$D \approx -\Delta_k \left[n \left(\frac{s_u}{\bar{u}} \right) \sum_k k P_k + \frac{n(n-1)}{2!} \left(\frac{s_u}{\bar{u}} \right)^2 \sum_k k^2 P_k + \frac{n(n-1)(n-2)}{3!} \left(\frac{s_u}{\bar{u}} \right)^3 \left(\frac{\gamma_u}{\Delta_k} \right) + \frac{n(n-1)(n-2)(n-3)}{4!} \left(\frac{s_u}{\bar{u}} \right)^4 \left(\frac{\kappa_u}{\Delta_k} \right) \right] \quad (3.28)$$

3.4.2 Hydraulic performance deterioration

A similar approach is applied to the air pressure drop for all the elements in the exchanger, i.e. from equation (3.13):

$$\Delta p = c_2 \cdot (\bar{u} + ks_u)^m \quad (3.29)$$

To quantify the degree of hydraulic performance deterioration, the mass-averaged pressure drop is used, i.e. for a constant inlet temperature:

$$\Delta p_{m,avg} = \frac{\sum_i \dot{v}_i \Delta p_i}{\dot{v}} \quad (3.30)$$

Equation (3.30) can also be viewed as a summation of all the elemental pumping power to give the total exchanger pumping value, P_w :

$$P_w = \sum_i \dot{v}_i \Delta p_i \quad (3.31)$$

The pumping power penalty factor, P_p , as a result of maldistribution is then defined as:

$$P_p = \frac{P_{w,m} - P_{w,u}}{P_{w,u}} \quad (3.32)$$

Higher values of P_p signify higher deterioration of hydraulic performance. By applying the same Taylor series expansion to equation (3.29) and with the same algebraic manipulation, equation (3.32) can be expressed as:

$$P_p \approx \Delta_k \left[(m+1) \left(\frac{s_u}{\bar{u}} \right) \sum_k k P_k + \frac{(m+1)m}{2!} \left(\frac{s_u}{\bar{u}} \right)^2 \sum_k k^2 P_k + \frac{(m+1)m(m-1)}{3!} \left(\frac{s_u}{\bar{u}} \right)^3 \left(\frac{\gamma_u}{\Delta_k} \right) + \frac{(m+1)m(m-1)(m-2)}{4!} \left(\frac{s_u}{\bar{u}} \right)^4 \left(\frac{\kappa_u}{\Delta_k} \right) \right] \quad (3.33)$$

3.5 Interpretation of the derivation

It is obvious from equation (3.28) and (3.33) that the thermal degradation factor, D , and pumping power penalty factor, P_p , are, in principle, functions of all four statistical moments. A recurring parameter in all the terms in the equations is the ratio $\left(\frac{s_u}{\bar{u}}\right)$.

The third term in the equation is related to the distribution skew while the fourth term is related to kurtosis. This implies that the mean and standard deviation have a dominant influence on the performance degradation. Also, since the equations are derived from a convergent Taylor series, the magnitudes of the subsequent higher order terms will become progressively smaller. Therefore, this implies that the skew and kurtosis have declining influence on D and P_p . With its larger denominator, the kurtosis term will have a weak, if not insignificant, effect.

Further examination of the equations shows that the magnitude of D and P_p are dependent not only on the statistical moments but also on the k - P_k characteristics of the PDF curves. However, due to the range of k from negative to positive, the magnitude of $\sum_k kP_k$ will be small, or zero for distributions with skew equal to zero.

Thus, the contribution from the first term in the two equations (3.28) and (3.33) is small. However, the second term is dominant due to the contribution of $\sum_k k^2 P_k$ and

it can be shown that this term is a constant with N_t :

$$\Delta_k \sum_k k^2 P_k = \sum_k \frac{N_k k^2}{N_t} = \sum_i \frac{k^2}{N_t} = \sum_i \frac{(u_i - \bar{u})^2}{N_t s_u^2} = \frac{N_t - 1}{N_t} \quad (3.34)$$

In addition, with $n < 1$ and $m > 1$, D and P_p are effectively always positive.

To further elucidate the dependency of the moments and k - P_k characteristics, equations (3.28) and (3.33) are examined by varying one moment at a time, while keeping the others constant, as can be seen in the following few cases, as summarized in Table 3.1. For simplicity, normal distribution curves are used in the discussion.

Table 3.1: Summary of variations made to the statistical moments

	Mean	Standard deviation	Skew	Kurtosis
<i>Case 1</i>	Varied	Fixed	Fixed	Fixed
<i>Case 2</i>	Fixed	Varied	Fixed	Fixed
<i>Case 3</i>	Fixed	Fixed	Varied	Fixed

Case 1

This situation is illustrated in Fig. 3.7(a) where the PDF curve of the distribution is translated as the mean varies. With the k notation transformation, all the PDF curves will have one common k - P_k characteristic, as shown in Fig. 3.7(b), i.e. $\sum_k kP_k$ will be the same. Therefore, equations (3.28) and (3.33) indicate that for this case, D and P_p vary inversely with the square or cube of the mean (i.e. ignoring the terms higher than O^4 in equations (3.28) and (3.33)).

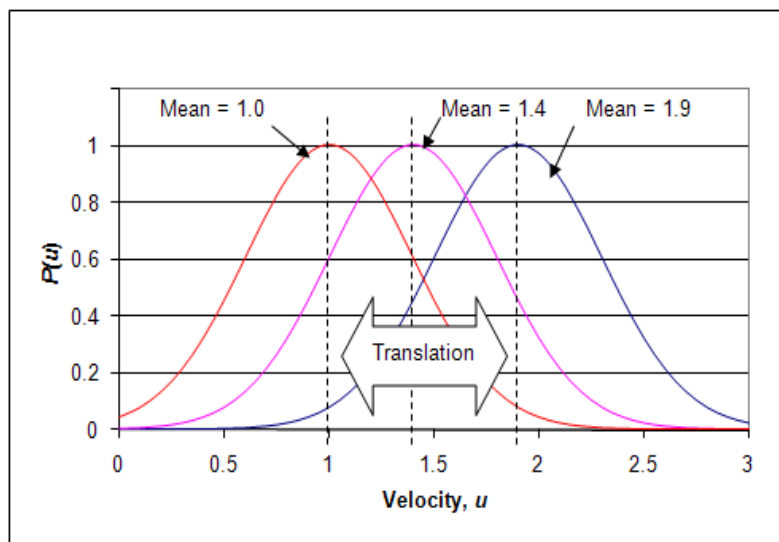
It is also observed in Fig. 3.7(b) that the transformed P_k curve has shifted slightly to the right. This is due to the forward differencing scheme used in the discretization procedure to calculate P_k . Similar observations will be seen in the following cases.

Case 2

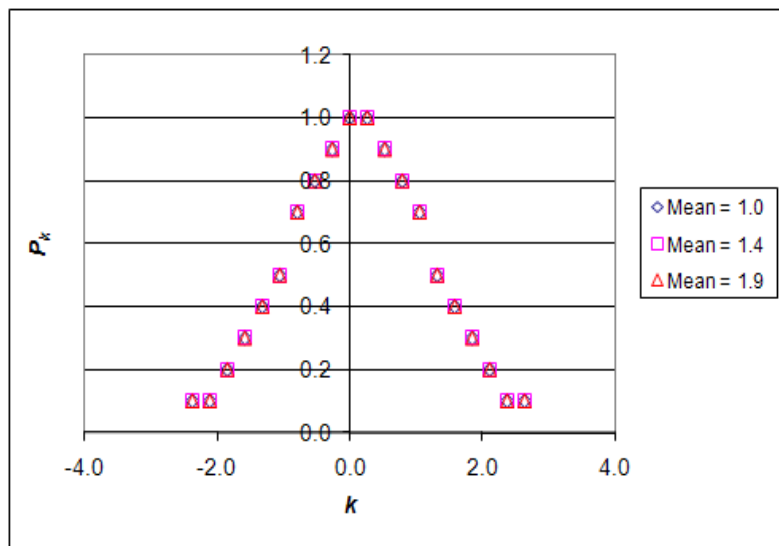
An example of the variation in standard deviation in this situation is illustrated in Fig. 3.8(a). Transformation to the k notation revealed that there is not much change in the distribution spread along the abscissa as shown in Fig. 3.8(b). With the first term having a small contribution, it is therefore seen that D and P_p will vary to the order of s_u^2 or s_u^3 as the contribution from the fourth terms is small. Higher magnitudes of standard deviation, s_u , will have higher deterioration effect.

Case 3

Fig. 3.9(a) gives an example of this situation where the skew varies between negative and positive values. The k transformation again show that the distribution spread along the abscissa is the almost the same, as indicated in Fig. 3.9(b). Hence, it is obvious from equation (3.28) and (3.33) that for this case, D and P_p varies linearly with skew. Also, with $n < 1$, negative values of skew will cause increasing deterioration effect as D becomes more positive, and vice-versa. Conversely, with $m > 1$, negative skews will cause P_p to be lower.

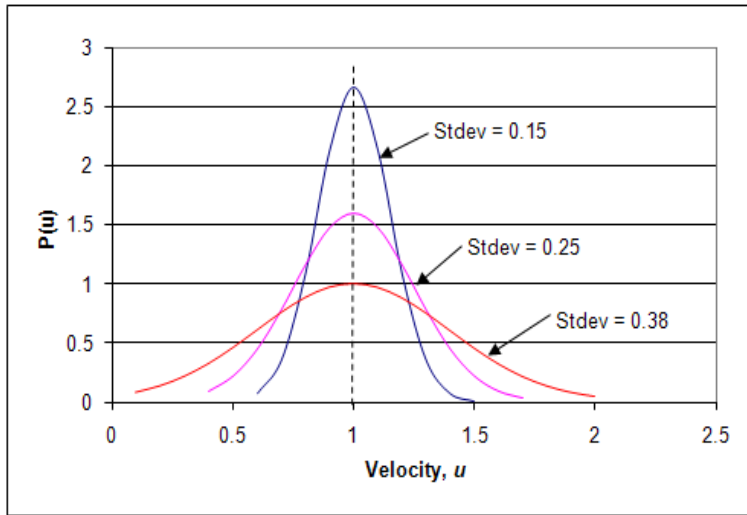


(a)

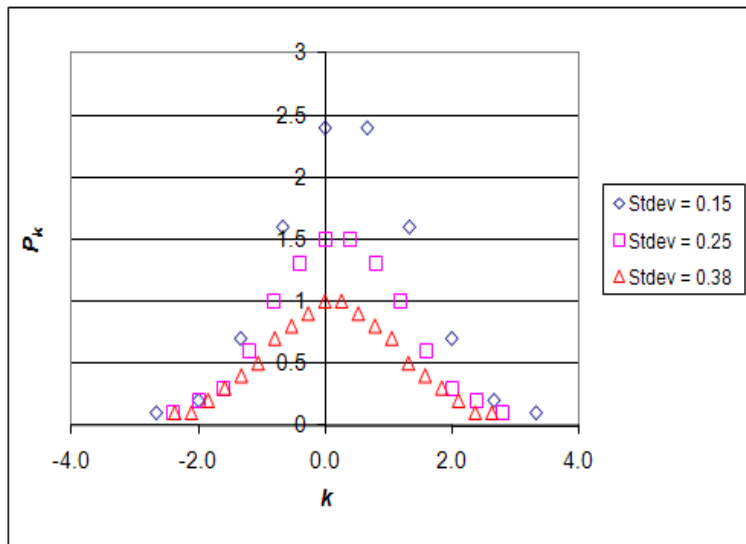


(b)

Fig. 3.7: Transformation of PDF for Case 1 with varying mean: (a) Translation of PDF (b) Transformation to k - P_k

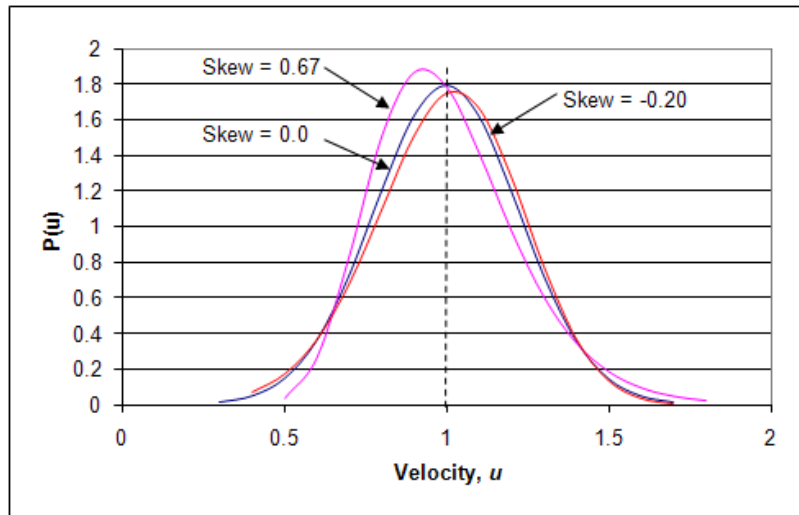


(a)

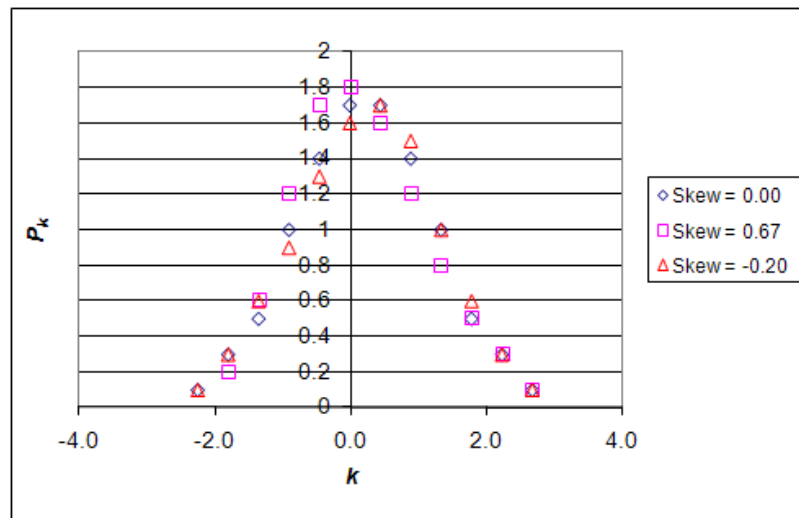


(b)

Fig. 3.8: Transformation of PDF for Case 2 with varying standard deviation (Mean = 1.00): (a) PDF curves (b) Transformation to k - P_k



(a)



(b)

Fig. 3.9: Transformation of PDF for Case 3 with varying skew (Mean = 1.00): (a) PDF curves (b) Transformation to k - P_k

3.6 Normalization of moments

The appearance of the $\left(\frac{s_u}{\bar{u}}\right)$ ratio in equations (3.28) and (3.33) suggests the possibility of analyzing the maldistribution problem with a normalized velocity profile. With this normalization, the mean would then become unity, i.e. $\bar{u}' = 1$. The following relationships are also derived from definitions (3.8) – (3.11):

$$\begin{aligned} s' &= s_u / \bar{u} \\ \gamma' &= \gamma_u \\ \kappa' &= \kappa_u \end{aligned} \quad (3.35)$$

And

$$k' = \frac{u' - 1}{s'} \quad (3.36)$$

Equation (3.28) is therefore re-written in the normalized form as:

$$\begin{aligned} D \approx -\Delta_k \left[ns' \sum_k k' P_k + \frac{n(n-1)s'^2}{2!} \sum_k k'^2 P_k + \frac{n(n-1)(n-2)s'^3}{3!} \left(\frac{\gamma'}{\Delta_k} \right) + \right. \\ \left. \frac{n(n-1)(n-2)(n-3)s'^4}{4!} \left(\frac{\kappa'}{\Delta_k} \right) \right] \end{aligned} \quad (3.37)$$

And similarly,

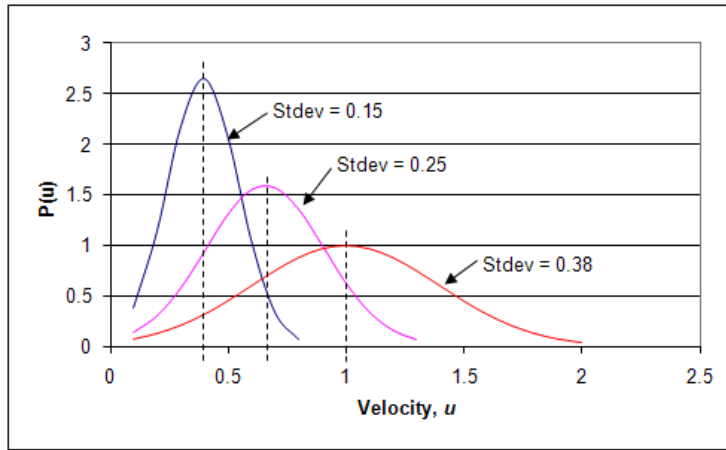
$$\begin{aligned} P_p \approx \Delta_k \left[(m+1)s' \sum_k k' P_k + \frac{(m+1)ms'^2}{2!} \sum_k k'^2 P_k + \frac{(m+1)m(m-1)s'^3}{3!} \left(\frac{\gamma'}{\Delta_k} \right) + \right. \\ \left. \frac{(m+1)m(m-1)(m-2)s'^4}{4!} \left(\frac{\kappa'}{\Delta_k} \right) \right] \end{aligned} \quad (3.38)$$

With this form, the trends of D and P_p with respect to the standard deviation, skew and kurtosis as discussed in the preceding cases are equally applicable to the respective normalized counterparts.

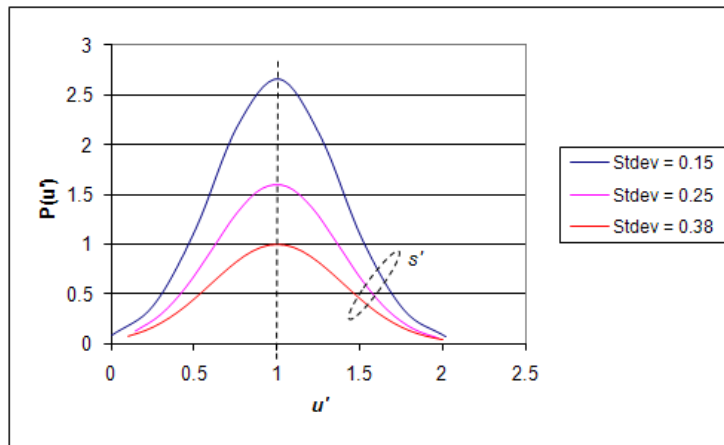
However, since the normalized $\bar{u}'=1$, the effect of the flow mean will need to be examined by using the non-dimensional NTU value:

$$NTU = \frac{UA}{C_{\min}} \quad (3.39)$$

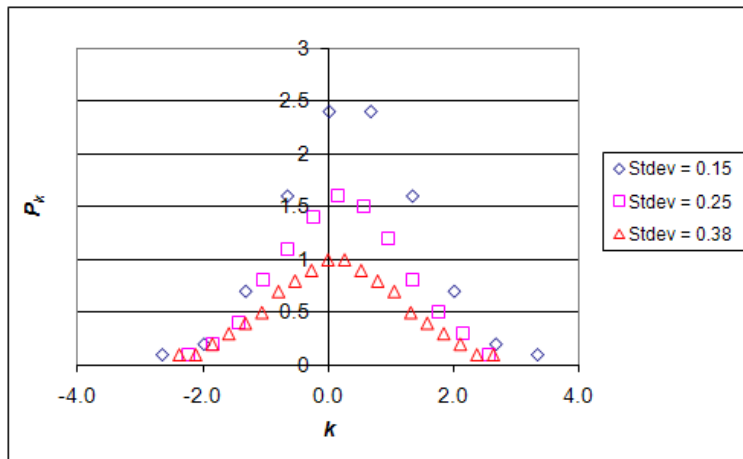
To do this, the flow mean velocities are multiplied with the normalized velocity distribution (i.e. $u = u' \bar{u}$) and the exchanger total NTU is evaluated. By doing so, the normalized standard deviation, s' , skew, γ' , and kurtosis, κ' , will be constant. An example is seen in Fig. 3.10(a) and 3.10(b) where the normalized standard deviation is kept the same, i.e. $s' = 0.38$. With this, as the mean increases, the standard deviation will also increase to maintain the same s' ratio. By applying the k notation, all the transformed PDF will also have a mean, $\bar{k} = 0$, as can be seen in Fig. 3.10(c). Since the NTU is inversely proportional to the mass flow rate, higher mean velocities will result in lower NTU values.



(a)



(b)



(c)

Fig. 3.10: Transformation of PDF for normalized moments with constant $s' = \left(\frac{s}{\bar{u}}\right)$ ratio of 0.38: (a) PDF curves (b) Normalized PDF curves (c)

Transformation to k - P_k

3.7 Physical reasoning of trends

It has been shown in the preceding section that as the distribution standard deviation increases, the magnitude of thermal and hydraulic deterioration increases. The reason for this occurrence is that the larger variation of velocities in the distribution cause a larger difference between the lowest, V_{low} , and highest, V_{high} , velocity magnitudes, and hence larger performance losses due to the same phenomenon as described in Section 3.3.

Distribution with positive skews will have a larger proportion of higher velocities. These higher velocities will tend to counteract the adverse thermal effects of the lower velocities which then reduce the heat transfer performance degradation. Conversely, distribution with negative skews will experience higher thermal deterioration due to the larger proportion of lower velocities. On the other hand, the higher velocities in a positive skewed distribution will tend to increase the pressure drop in the exchanger core which therefore increases the pumping power penalty, and vice-versa.

With fixed standard deviation and skew, the proportion of the higher and lower velocities in the distribution remains approximately the same with changes in the kurtosis, or peakedness of the distribution. Hence, the kurtosis does not play a part in determining the magnitude of performance degradation.

As described earlier, a higher mean corresponds to higher fluid velocities which results in lower NTU values. There are two mechanisms through which the mean affects the magnitude of D and P_p .

- a) Firstly, higher flow rates have larger inertias which are less susceptible to maldistribution effects.
- b) However, higher flow rates will give higher velocities over the fin surfaces which increase the heat transfer coefficient and pressure drop, as can be seen in equations (3.12) and (3.13), thus rendering the exchanger more sensitive to maldistribution effects.

The first effect is seen in *Case I* and Fig. 3.7, where the shape of the maldistribution profile remains unchanged as the mean varies. This explains the

reciprocal relationships between D and P_p with the mean for this situation. For other cases where the standard deviation and skew changes simultaneously together with the mean, both of these effects will occur. Obviously, these have opposing effects. However, the dominating effect will dictate the trend of D and P_p . This phenomenon is described in further detail in the next chapter.

3.8 Optimization of skew

Up to this point, the thermal and hydraulic degradations have been de-coupled in the analysis. However, the coupling of these effects can be examined by using the ratio of heat transfer per unit input power (Q/P_w), described as follows:

From (3.24), the maldistributed heating capacity is expressed as:

$$Q_m = Q_u (1 - D) \quad (3.40)$$

Similarly, from (3.32), the maldistributed pumping power would be:

$$P_{w,m} = P_{w,u} (1 + P_p) \quad (3.41)$$

Hence, the ratio between these two would give:

$$\frac{Q_m}{P_{w,m}} = \frac{Q_u}{P_{w,u}} \frac{(1 - D)}{(1 + P_p)} \quad (3.42)$$

From the interpretation of *Case 3*, it was shown that for a specific NTU and standard deviation, increasing the skew will cause D to decrease while P_p increases. Therefore, this suggests that an optimum skew exists where the ratio $(1-D) / (1+P_p)$ would be a maximum. An example of such a plot for the ratio is shown in Fig. 3.11.

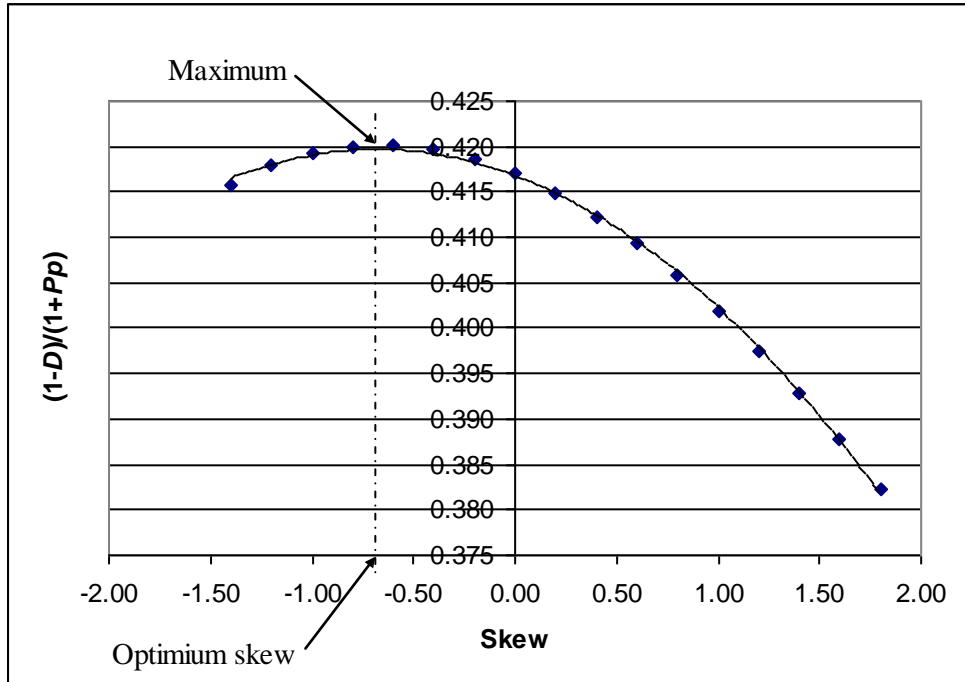


Fig. 3.11: Example plot of $(1-D) / (1+P_p)$ vs. skew showing optimum maximum point ($NTU = 0.40$ and standard deviation = 0.70)

3.9 Generality of results

Although a cross-flow heat exchanger has been used as an example in the analysis, the findings would still be applicable for other types of exchangers. For this, the exchanger must be discretized on the fluid inlet face area across the flow channels. In the case of a fin-tube heat exchanger, as shown in Fig. 3.4, this was done on the air inlet coil face area. For a shell-and-tube heat exchanger, each tube inlet on the tube sheet could form an individual cell element for the analysis. Similarly, divisions could be made along the inlet header of a plate heat-exchanger to discretize the flow among the plate channels. Smaller discretized cell sizes would reflect a closer approximation of the real exchanger application. In any case, the common fundamental governing equations used in deriving the degradation effects would ensure the generality of the model.

It is observed that all the probability density functions used in the analysis above are uni-modal. However, the derivation would also be valid for multimodal distributions as long as the overall distribution moments are used. From a practical view point, it is possible for a heat exchanger to encounter multimodal velocity distributions. A case of bimodal distribution can occur when the fluid flows through two consecutive bends in orthogonal planes before reaching the heat exchanger inlet. Another example would be an air-cooled fin-tube condenser which has multiple fans, rotating at different speeds, drawing air through the exchanger core.

As a further elaboration, a bimodal distribution which is derived from a combination of two individual uni-modal distributions is considered. The first distribution has a mean of \bar{u}_1 and standard deviation of s_1 , while the second distribution has a mean of \bar{u}_2 and standard deviation of s_2 . If λ is weightage factor used between these two distributions to generate the bimodal probability density function, the overall mean and variance for the resultant distribution would be given as [81]:

$$\bar{u} = \lambda\bar{u}_1 + (1 - \lambda)\bar{u}_2 \quad (3.43)$$

$$s^2 = \lambda(s_1^2 - (\lambda - 1)(\bar{u}_1 - \bar{u}_2)^2) - (\lambda - 1)s_2^2 \quad (3.44)$$

These could then be used in equations (3.10), (3.11) and (3.16) without losing the generality of the derivation.

A worked example is illustrated in Fig. 3.12 for two normal distributions (skew = 0.0) with $\bar{u}_1 = 1.0$, $\bar{u}_2 = 2.0$, $s_1 = 0.223$ and $s_2 = 0.40$. With a weightage factor of 0.55, the mean and standard deviation of the bimodal distribution are calculated as 1.45 and 0.589, respectively. The resultant distribution also has a positive skew. The following Table 3.2 shows the calculated normalized standard deviation and skew of these three distributions. It is observed that the resultant bimodal distribution has the highest normalized standard deviation, with normalized mean = 1.00, where in accordance to equations (3.37) and (3.38), it will have the highest magnitude of thermal and hydraulic performance deterioration. Even though the results are for a bi-modal distribution, the developed theory is also valid, by extension, for multimodal distributions.

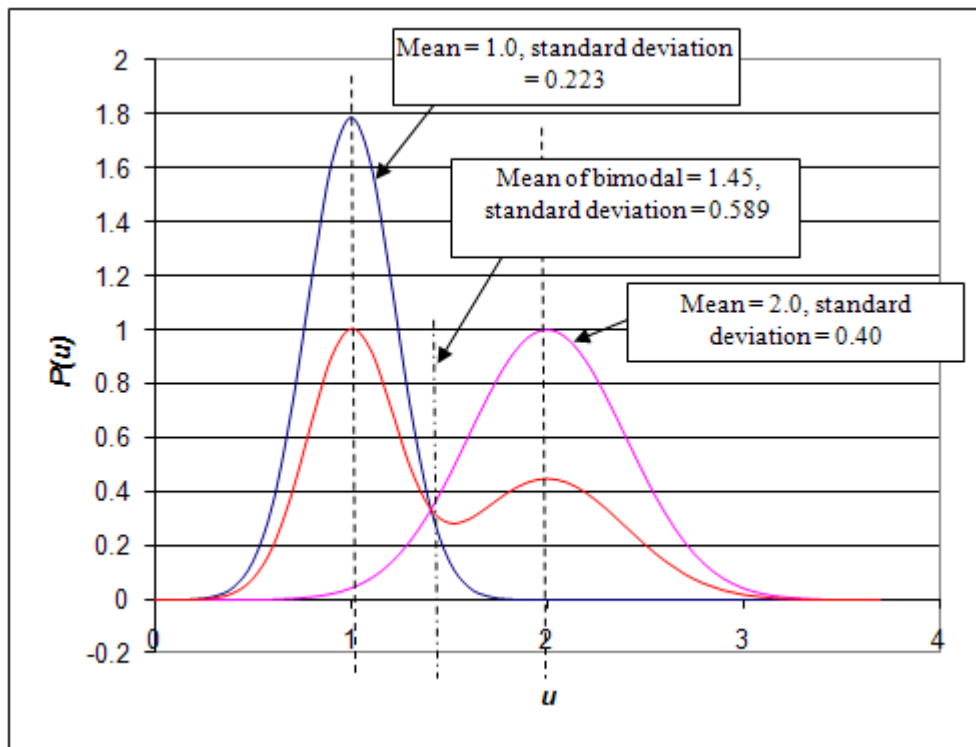


Fig. 3.12: Bimodal distribution generated with a weightage factor of 0.55

Table 3.2: Calculated normalized moments for resultant bimodal distribution

	Normalized	
	Standard deviation	Skew
1st distribution (Normal)	0.214	0.000
2nd distribution (Normal)	0.194	0.000
3rd distribution (Bimodal)	0.387	0.453

3.10 Summary

In this chapter, the definitions of the four statistical moments of probability density function, i.e. mean, standard deviation, skew and kurtosis, which characterize a maldistribution velocity profile, were defined. A new mathematical derivation, based on Taylor series expansion, was developed to bring out the contribution of each moment to the magnitude of thermal and hydraulic performance degradation. Of the four, the first and second moments, i.e. mean and standard deviation, have dominant effects on the heat exchanger performance. The subsequent higher moments were shown to have declining influence. For a known mean and standard deviation, positive skews was observed to give favourable low thermal degradation effects, but on the other hand, negative skews have low hydraulic performance penalties. Consequently, there exists an optimum magnitude of skew where the ratio of heat transfer per unit input power is a maximum.

The results of the derivation have also shown the possibility of analyzing the maldistribution problem by using normalized moments. With this method, the effect of the mean is captured by using the heat exchanger NTU value. Higher mean corresponds to lower values of NTU . Since the non-dimensional NTU takes into consideration other important parameters which affect the heat exchanger performance, i.e. the external and internal heat transfer coefficients and fluid temperatures, this normalization technique is preferred for further studies of the maldistribution problem.

Lastly, the generality of the derivation method for all types of heat exchangers was discussed. The applicability of the method for any multimodal distribution was also established, so long as the overall moments of the distribution are used in determining the degradation factors.

CHAPTER 4

NUMERICAL ANALYSIS OF FLOW MALDISTRIBUTION ON THE THERMAL PERFORMANCE OF FIN-TUBE HEAT EXCHANGERS

4.1 Overview

The effect of velocity maldistribution on the thermal performance of a single row fin-tube heat exchanger is examined numerically in this chapter. A discretization technique has been applied to the air inlet face area of the heat exchanger, which has been divided into 100 elements, with each element being assigned a specific velocity magnitude. As a result, all the elemental velocities on the coil face area define the statistical moments of the velocity distribution in the heat exchanger.

The velocity maldistribution used in the analysis was generated by manipulating the probability density functions of several well-defined distributions. The heat transfer performance for each element was then calculated by using the ε - NTU method with the known inlet fluid temperatures. By summing all the elemental performances, the thermal performance degradation factor for the entire exchanger was determined and the results analyzed with respect to the normalized moments, NTU and R , the ratio between the external and internal heat transfer coefficients.

4.2 Discretization model of the fin-tube heat exchanger

The methodology reported in Chapter 3 has demonstrated how the maldistribution degradation problem in an arbitrary heat exchanger could be analyzed by means of discretizing the exchanger into smaller elements. The same approach is now applied to fin-tube heat exchanger coils to quantify the magnitude of the thermal degradation factor, D , i.e. equation (3.24), as the statistical moments vary systematically.

However, examination of the derivation used in the previous chapter, which is based upon Newton's law of cooling, i.e. equation (3.18), shows that the normalized equation (3.37) is only an estimation for the thermal degradation factor, D . Several assumptions have been made in the derivation, i.e.

- a) Constant tube wall temperature.
- b) Constant temperature difference (ΔT) between the inlet air and fin surfaces.
- c) Ignoring variations in fin surface efficiency and approximating it with the efficiency under uniform distribution ($\eta_{s,k} \approx \eta_{s,u}$).

It is known that in reality, the fin surface temperature is dependent on the inlet air velocity itself, and also on the tube internal heat transfer coefficient. The fin surface efficiency is also dependent on the surface temperature. However, in spite of the assumption, the derivation was found adequate to demonstrate the contribution of each statistical moment to the magnitude of D . As a result of this assumption, the derived equation (3.37) would not be able to calculate and quantify exactly the magnitude of D .

Subsequently, a more robust discretization technique based on the ε - NTU approach was used for the analysis. This approach was found to be more suitable as the fin surface temperature is not required to be known to calculate the heat exchanger thermal performance. To facilitate this, a numerical model of a single row fin-tube heat exchanger, similar to that shown in Fig. 3.4, was established as a baseline for the study. The coil has 10 tubes which forms 5 identical circuits through the exchanger core, as shown in Fig. 4.1. The tube diameter was 9.52mm with a tube pitch of 25.4 mm and row pitch of 22.0 mm. The coil also has wavy fins, as shown in Fig. 4.2, with a fin pitch of 1.411mm (i.e. 18 fins per inch). Such coil specifications would be commonly encountered in air-conditioning and refrigeration equipment. As the size of the coil face area would not affect the results of the analysis, the coil length was arbitrarily chosen as 600 mm with a height of 254 mm. The entire coil face area was then discretized into a 10 x 10 grid to give 100 elements. Each element was treated as an individual cross-flow heat exchanger with the tube in the center, as illustrated in Fig. 4.1.

Following the observations from Chapter 3, every individual element on the coil was assigned a normalized velocity ratio. The combination of these elemental velocity ratios will therefore define the maldistribution profile which has a normalized mean of 1.00. The normalized sample standard deviation, skew and kurtosis could also be determined from these values. The methodology used to generate and assign the distribution to the individual elements is discussed in the next section.

For the numerical simulation, the air volume flow rate through the exchanger ranged from 0.11 to 0.45 m³s⁻¹ (240 – 960 ft³min⁻¹), which corresponds to an average face velocity range of 0.70 to 3.00 ms⁻¹ covering a typical range of velocities used in practice. This average face velocity was then multiplied with the normalized velocity ratios assigned on the 10 x 10 grid to give the actual velocity maldistribution in the heat exchanger. The inlet air temperature was also ranged from 15°C to 45°C during the simulation, which reflects typical application range in air-conditioning systems.

Water was considered as the working fluid in the tubes to keep the heat transfer analysis less complicated. Hot water was used where the inlet temperature ranged from 40°C to 70°C, i.e. air was heated as it flowed through the fin passages. By imposing a high flow rate through the tubes, the water temperature through the coil remained essentially the same. The water flow rate ranged from 0.14 to 10.74 m³hr⁻¹ so as to give a minimum $Re_w = 10,000$ at the lowest flow rate, which corresponded to turbulent flow in the tubes. With the controlling thermal resistance residing on the air-side, the high water flow rate mimicked the high heat transfer coefficient in the tube-side arising from flow boiling or condensation, as typically encountered in the evaporators and condensers of HVAC&R equipment. For the numerical simulation, the range of internal heat transfer coefficients used in the calculation was from 4,540 to 147,000 Wm⁻²K⁻¹.

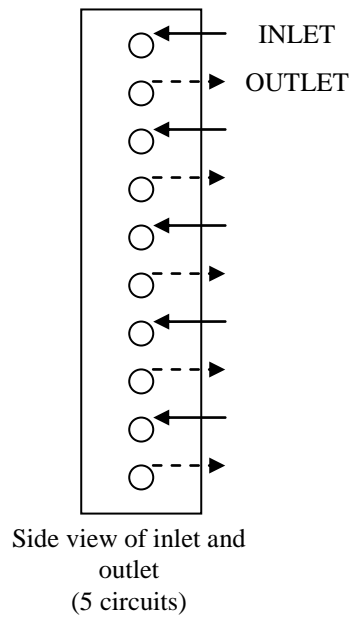
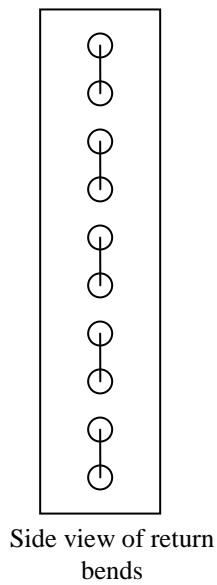
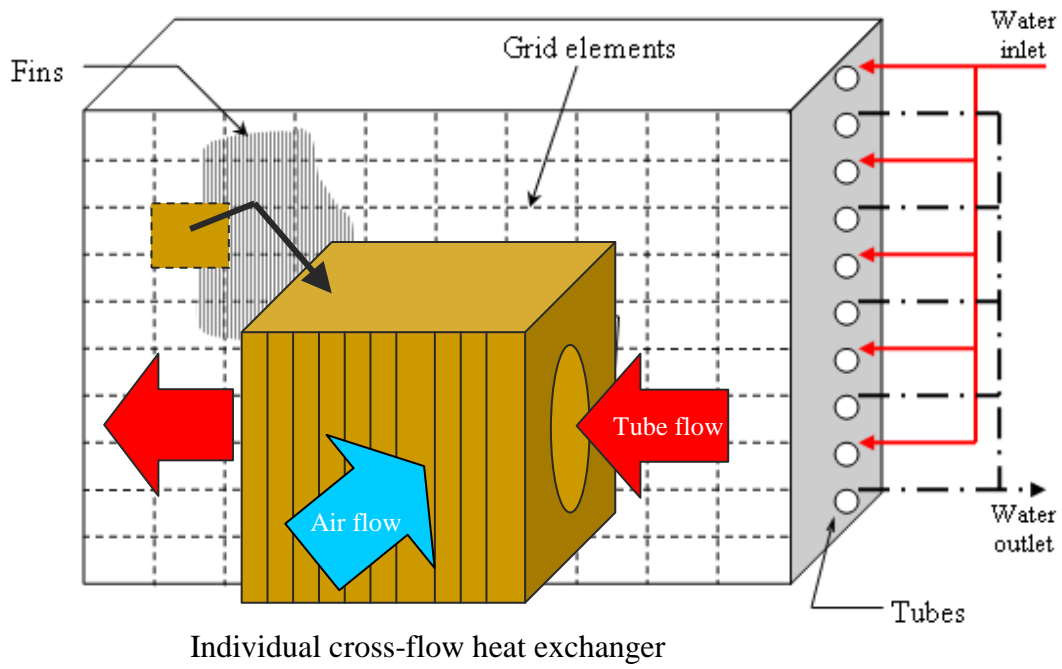
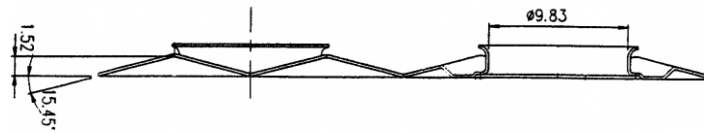


Fig. 4.1: Discretization of elements on a single row fin-tube heat exchanger



Section A-A

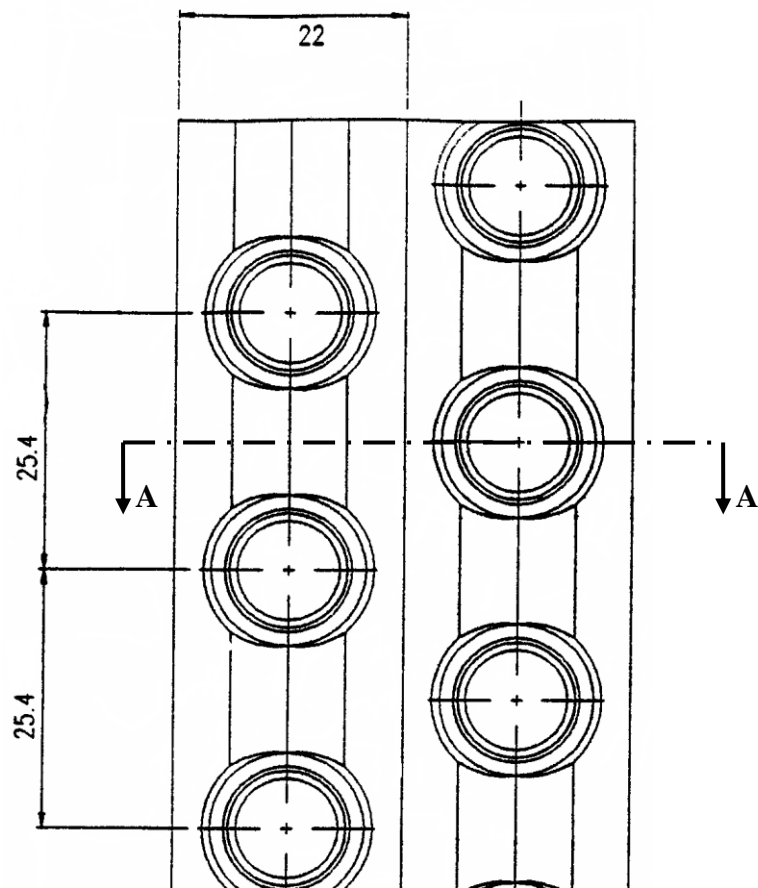


Fig. 4.2: Profile of wavy fin with staggered tubes

For each i^{th} discrete element, the thermal resistance equation was applied to determine the overall heat transfer coefficient, $U_{o,i}$:

$$\frac{1}{U_{o,i}A_o} = \frac{1}{\eta_s h_{o,i}A_o} + \frac{\ln(d_o/d_i)}{2\pi k_{wall}lA_o} + \frac{1}{h_i A_i} \quad (4.1)$$

where A_o and A_i are the total external and internal surface areas of the element, d_o and d_i are the tube external and internal diameters, respectively, $h_{o,i}$ and h_i are the external and internal heat transfer coefficients, respectively, η_s is the fin surface efficiency, l is the element tube length and k_{wall} is the tube wall thermal conductivity. The effect of tube fouling is ignored in the thermal resistance equation above.

There are two possible ways to determine the external heat transfer coefficient, $h_{o,i}$, for each element. The first is to use the j -factor correlation developed by other researchers, for example the correlation developed by Wang et al. [82] for wavy fins. This correlation is reproduced in Appendix A. Correlations are available in literature for other fin patterns, e.g. louvered fins and slit fins. From the j -factor, $h_{o,i}$ is calculated with the following equation:

$$\frac{h_{o,i}D_c}{k_a} = j \text{Re}_{Dc} \text{Pr}_a^{1/3} \quad (4.2)$$

where Re_{Dc} is the air-side Reynolds number based on the fin collar diameter. The main advantage of this method is the ease of using the general form of the correlation for similar fin patterns within the range of geometrical parameters specified by the correlation. However, this method lacks accuracy for a specific manufactured fin pattern which may differ from that used during the development of the correlation. The correlation itself has a margin of deviation to fit the data scatter. Wang et al. [82] have reported a margin of $\pm 15\%$ for their correlation.

The second method is to use actual h_o experimental data of fin-tube coils to generate the j -factor correlation. This method is preferred, and has been adopted in the present research, as the actual fins used for the work are characterized, which allows a greater degree of accuracy. To do this, the experiment must cover a range of geometrical parameters for the fin-tube heat exchanger which has the same fin

pattern, e.g. number of rows and fin pitch. The details of this experiment are described in Chapter 6.

In this work, the wavy fin-tube heat exchangers used have been obtained from O.Y.L. Manufacturing Company Sdn. Bhd., the sponsor for this research. For ease of handling the data, the calculated j -factors obtained from the experiment were correlated by applying a correction factor, C , to the Wang et al. correlation [82], as follows:

$$j_{OYL} = C \cdot j_{Wang} \quad (4.3)$$

The magnitude of this correction factor is dependent on the fin surface geometry. The value of the factor has been determined experimentally in Chapter 6. With the j -factor known, h_o can then be calculated from equation (4.2).

On the other side of the exchanger, the determination of the internal heat transfer is much easier. In the simulation, this was done by applying the Pethukov-Kirilov-Popov correlation for turbulent flows [80]:

$$Nu_w = \frac{h_i d_i}{k_w} = \frac{(f_w / 2) Re_w Pr_w}{\tilde{C} + 12.7(f_w / 2)^{1/2} (Pr_w^{2/3} - 1)} \quad (4.4)$$

where k_w and f_w are the thermal conductivity of water and tube-side friction factor, respectively,

and

$$\tilde{C} = 1.07 + 900 / Re_w - [0.63 / (1 + 10 Pr_w)] \quad (4.5)$$

The tube-side friction factor was calculated by using the Blasius correlation [80], i.e.

$$f_w = 0.0791 Re_w^{-0.25} \quad (4.6)$$

The fin efficiency, η_f , was calculated by using the Schmidt sector method for continuous fins [83] with hexagonal, or staggered, tube array:

$$\eta_f = \frac{\tanh(mr\phi)}{mr\phi} \quad (4.7)$$

where

$$m = \sqrt{\frac{2h_o}{k_f y}} \quad (4.8)$$

$$r = d_o/2 \quad (4.9)$$

$$\phi = \left(\frac{R_e}{r} - 1 \right) [1 + 0.35 \ln(R_e/r)] \quad (4.10)$$

and

$$\frac{R_e}{r} = 1.27 \zeta \sqrt{(\beta - 0.3)} \quad (4.11)$$

$$\zeta = \frac{X_t}{2r} \quad (4.12)$$

$$\beta = \frac{2L}{X_t} \quad (4.13)$$

with

$$L = \frac{1}{2} \sqrt{(X_t/2)^2 + (X_t/2)^2} \quad (4.14)$$

From the fin efficiency, the overall fin surface efficiency was calculated with the following equation:

$$\eta_s = 1 - \frac{A_f}{A_o} (1 - \eta_f) \quad (4.15)$$

where A_f is the surface area of the fins alone, without the fin base area.

With the U_o calculated for each coil element, the heat transfer (Q_i) for each element was then determined from:

$$Q_i = \varepsilon_i C_{\min,i} (T_{w,in} - T_{a,in}) \quad (4.16)$$

where $T_{w,in}$ and $T_{a,in}$, respectively are the water and air temperatures entering the element and $C_{\min,i}$ is the element minimum heat capacity rate which is defined as:

$$C_{\min,i} = \dot{m}_{a,i} c_{p,a} \quad (4.17)$$

The element heat exchanger effectiveness, ε_i , is a function of the element number of transfer units, NTU_i , which, following the definition of equation (3.39), is given as:

$$NTU_i = U_{o,i} A_o / C_{\min i} \quad (4.18)$$

The effectiveness is also a function of the heat capacity rate ratio, C_r , which is defined as:

$$C_r = C_{\min i} / C_{\max} \quad (4.19)$$

With water flowing in the tube side of the heat exchanger, the maximum heat capacity rate, C_{\max} , is given as:

$$C_{\max} = \dot{m}_w c_{p,w} \quad (4.20)$$

For an unmixed – unmixed cross-flow configuration for both the air and water fluid streams, the relationship for the effectiveness, ε_i , is given as [84]:

$$\varepsilon_i = 1 - \exp \left[\left(\frac{1}{C_r} \right) NTU^{0.22} \{ \exp[-C_r NTU^{0.78}] - 1 \} \right] \quad (4.21)$$

The sum of all the elemental heat transfer rates, $\sum_i Q_i$, was calculated to give the total heat exchanger heating capacity. The total NTU for the exchanger was calculated from:

$$NTU = \frac{\sum_i U_{o,i} A_o}{\sum_i C_{\min i}} \quad (4.22)$$

The air outlet temperature from each element was calculated from:

$$T_{a,out,i} = \frac{Q_i}{C_{\min i}} + T_{a,in} \quad (4.23)$$

From these, the mass-averaged outlet air temperature was calculated as:

$$T_{a,out} = \frac{\sum_i (C_{\min i} \cdot T_{a,out,i})}{\dot{m}_a c_{pa}} \quad (4.24)$$

The above calculation procedure was performed for both cases of maldistributed and uniform velocity distributions to obtain the corresponding thermal performances, Q_m and Q_u , respectively. These were then used to obtain the thermal performance degradation factor, D , as defined in equation (3.24).

4.2.1 Psychrometrics

The air properties required for the computation, i.e. within 15°C to 45°C, were calculated based upon the inlet temperature. The calculation of moist air properties, i.e. density and specific heat, was done by using psychrometric equations formulated by ASHRAE [85]. For this, the air dry-bulb and wet-bulb temperatures were used to determine the water vapour saturation pressure (p_{ws}). The equation used to calculate this, which is valid between 0°C to 200°C, is given as:

$$\ln(p_{ws}) = C_1/T + C_2 + C_3T + C_4T^2 + C_5T^3 + C_6 \ln(T) \quad (4.25)$$

With p_{ws} expressed in Pa, and the air temperature, T , in Kelvin, the values of the constants are given in the following table:

Table 4.1: Value of constants for equation (4.25)

	Constants
C_1	-5.8002206E+03
C_2	1.3914993E+00
C_3	-4.8640239E-02
C_4	4.1764768E-05
C_5	-1.4452093E-08
C_6	6.5459673E+00

The humidity ratio of saturated air (W_s) at a given barometric pressure P_{atm} (which was taken as 101.325 kPa) and temperature, T , can be calculated as:

$$W_s = 0.62198 \frac{P_{ws}}{P_{atm} - P_{ws}} \quad (4.26)$$

If the air wet-bulb temperature (T^*) is used in the calculation of equations (4.25) and (4.26), the corresponding p_{ws}^* and W_s^* are obtained. With these, the air humidity ratio, W , was calculated from:

$$W = \frac{(2501 - 2.381T^*)W_s^* - 1.006(T - T^*)}{2501 + 1.805T - 4.186T^*} \quad (4.27)$$

Then, the water vapour partial pressure for the moist air, p_w , was obtained from:

$$p_w = \frac{P_{atm}W}{0.62198 + W} \quad (4.28)$$

The air humidity ratio can also be calculated by using the value of p_w from this equation:

$$W = 0.62198 \frac{p_w}{P_{atm} - p_w} \quad (4.29)$$

Hence, the air specific volume was calculated from:

$$\nu = \frac{R_a T}{P_{atm}} (1 + 1.6078W) \quad (4.30)$$

where R_a is the gas constant (dry-air) = 287.055 Jkg⁻¹K⁻¹. The inverse of the specific volume is the air density. The air specific heat capacity was calculated from:

$$c_{p,a} = 1.0056 + 1.86W \quad (4.31)$$

Other transport properties of air required for the calculation, i.e. dynamic viscosity and thermal conductivity, were obtained by fitting the data published by ASHRAE [85] with a third order polynomial equation. The data used for the fitting was sufficient to cover the range of air temperatures studied in this work.

4.3 Generating velocity distributions

Each discrete cell on the coil was assigned an inlet air velocity value. To determine these velocities and their required quantity to make up the distribution, calculations with continuous probability density functions (PDF) were used. There are many PDF available which can be used to fit the required combination of mean, standard deviation, skew and kurtosis. Most of these distributions have well-defined equations established for these four moments. By manipulating the parameters in these equations, it is possible to generate a distribution with the required moments.

To illustrate this methodology, a worked example with Normal distribution is described as follows. The PDF for this distribution is given as:

$$P(x) = \frac{1}{\sigma\sqrt{2\pi}} \exp\left(-\frac{(x-\mu)^2}{2\sigma^2}\right) \quad (4.32)$$

This distribution has a skew of 0.00 and kurtosis of 0.00. To simulate a normalized distribution profile, the mean, μ , is set at 1.00. A standard deviation (normalized), σ , of 0.33 is specified for the example. The discretized values of $P(x)$ can then be calculated for a range of velocity ratios, x , for example 0.1 to 2.0, at intervals of 0.1. The plot of this PDF is shown in Fig. 4.3. This distribution will be imposed on the same 10 x 10 grid as shown in Fig. 4.1. It is noted that for the simulation, the values of x are non-negative.

The total area under this probability distribution curve is equal to 1. Hence, multiplying the area under the curve for any interval of velocity ratio with the number of discrete elements, i.e. 100, will give the approximate quantity required for a given velocity ratio. Since the PDF is continuous, a rounding to the nearest integer is required.

The same procedure was then applied for other PDF choices. A PDF was selected based on the skewness of the density function plot. Zero skew distributions can be generated not only with the Normal distribution but also from the Pearson Type VII and Wigner semi-circle distributions. The Skew Normal distributions can give both positive and negative skews. Positive skew distributions were generated with the Log Normal and Chi distributions. Beta distributions were used to generate negative

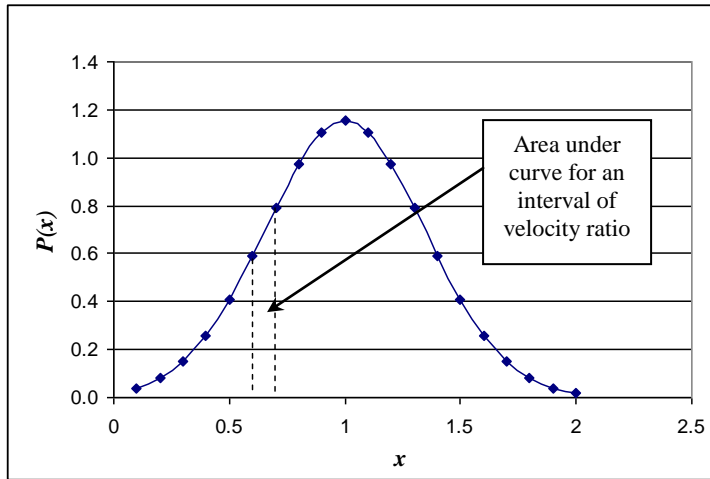
skews. A listing of all the distributions used in this study, compiled from several sources, is given in Appendix B [86 - 90].

The velocities and their corresponding quantities generated from the discretized distribution, e.g. from Fig. 4.3(b), were then assigned to the individual coil discrete elements. There are many possible arrangements of the velocities on the grid. Two methods have been used in this work, i.e. by manual and by random assignment.

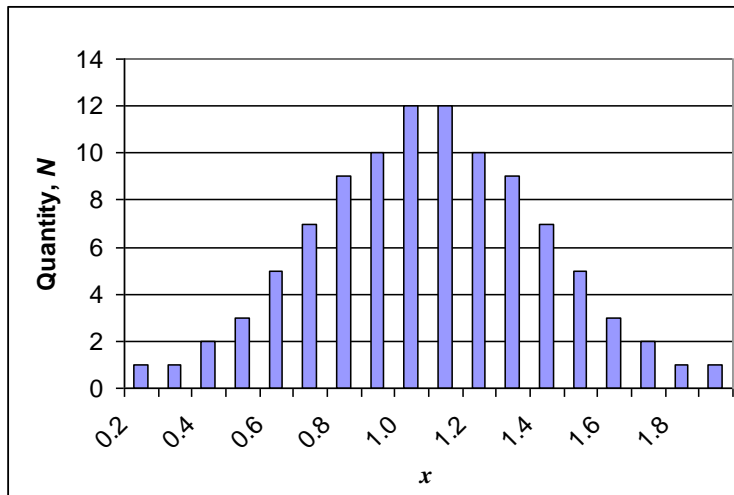
For the first case, the velocity spatial distribution was manually arranged to give pre-determined non-uniform spatial distribution shapes, e.g. dome, planar, double-humped, etc. Some examples of these are shown in Fig. 4.4. In the second case, the location for each velocity was randomly assigned by means of a random number generator. This was implemented with the Rnd function in Visual Basic, as shown below, which generates a random integer (x2) between 1 and 100 to indicate the cell location.

```
Randomize  
x1 = Rnd  
x2 = Int(100 * x1 + 1)
```

Consequently, the resultant spatial distribution does not have any fixed or distinct shape profile.



(a)



(b)

Fig. 4.3: (a) Normal probability density function plot (mean = 1.00, standard deviation = 0.33, skew = 0.00, kurtosis = 0.00) showing the area under the curve for an interval of velocity ratio (b) Discretized velocity distribution derived from the normal PDF. The total $\Sigma N = 100$.

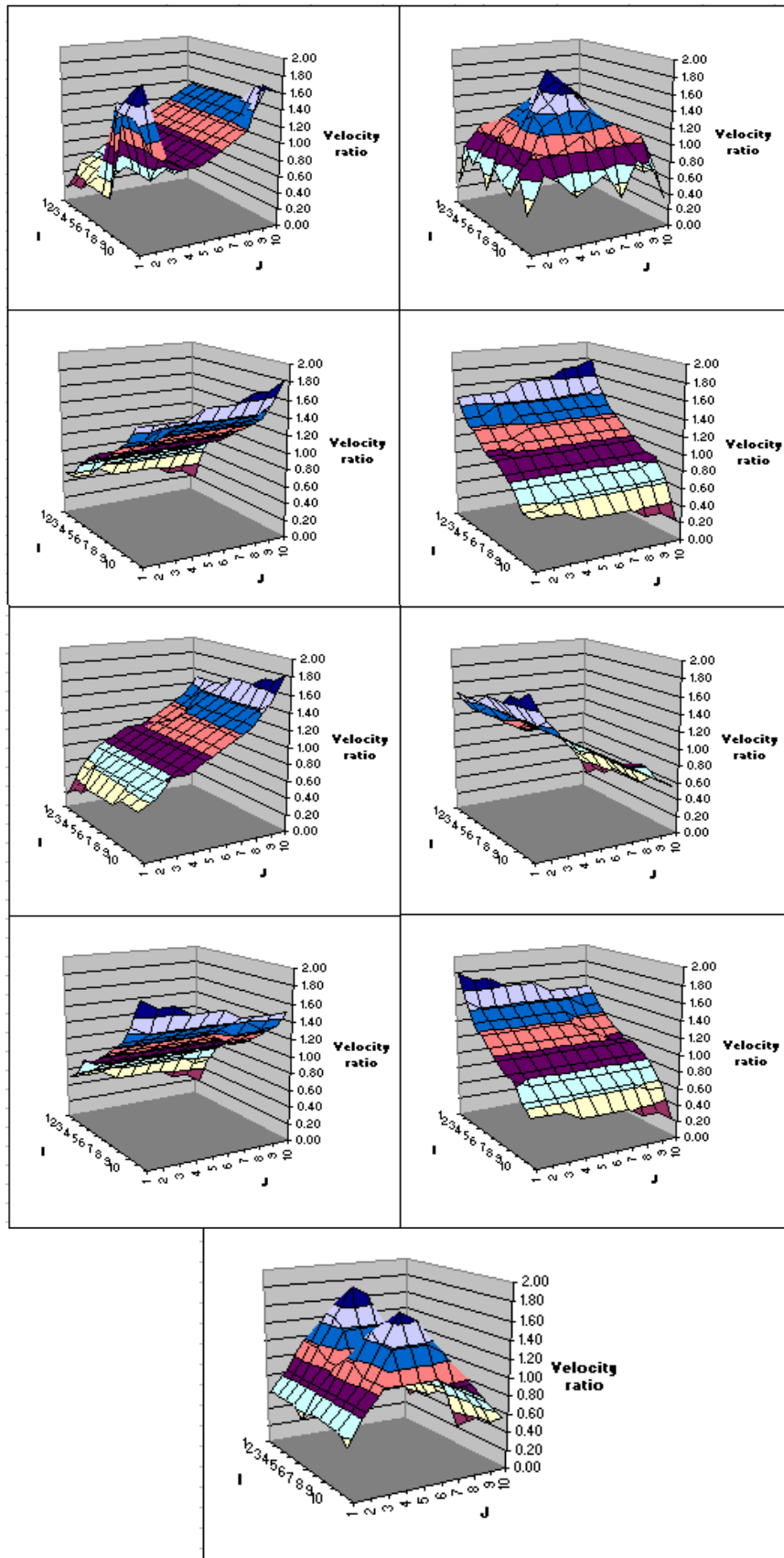


Fig. 4.4: Examples of velocity spatial distribution over the 10 x 10 (I -J) grid elements

In either case, the shape of the spatial distribution will not affect the magnitude of heating capacity. This is because of the constant water temperature, and hence constant tube wall temperature, along the tube length. In view of this, the random assignment is preferred due to the ease of implementation in the calculation algorithm. With the velocity ratios assigned, the last step in the procedure to generate the velocity distribution on the heat exchanger was to multiply all the ratios with the average coil face inlet velocity.

4.4 Calculation algorithm

The computation of the heat exchanger heating capacity was done by using Microsoft EXCEL. From the velocity maldistribution input, the performance of each element was calculated line-by-line on the spreadsheet where all the required equations, as described in the previous section, have been assembled. The main reason for using EXCEL was due to the availability of in-built statistical functions to calculate standard deviation [STDEV()], skew [SKEW()] and kurtosis [KURT()] for a set of data.

A total of 20 velocity maldistribution profiles, with random spatial distributions, were generated for the analysis. The range of normalized statistical moments covered by these maldistributions is as follows:

1. Standard deviation: 0.10 to 0.70
2. Skew: -1.0 to +1.0
3. Kurtosis: -1.0 to +1.0

These profiles are stored as a database list on the spreadsheet itself.

For each maldistribution profile and a set of air flow rates and fluid inlet temperatures, the calculation steps to determine the heating capacity of each cell element are shown in a flowchart as illustrated in Fig. 4.5. These were then repeated iteratively as the air flow rate, air and water inlet temperatures and internal heat transfer coefficients were systematically changed.

The overall calculation procedure is shown in Fig. 4.6. In this work, the internal heat transfer coefficient was changed in 5 steps, i.e. ranging from 4,540 to 147,000 $\text{Wm}^{-2}\text{K}^{-1}$. The temperatures were increased in steps of 5°C while the air flow rate multiplication factor (V_r) was increased in steps of 0.2. To perform this iteration procedure, a macro programme written in Visual Basic (VBA) was embedded into the EXCEL spreadsheet.

4.5 Grid size independence

The 10x10 grid size used in the simulation was chosen based upon the experience from other researchers, e.g. Ranganayakulu et al [18]. However, to further justify the use of this grid, a grid sensitivity test was performed. For this purpose, a set of calculations were performed on the single row fin-tube heat exchanger which has the same air-side maldistribution, but with four different grid sizes, i.e. 10 x 10, 10 x 11, 10 x 15 and 10 x 20. The normalized statistical moments which define this maldistribution were standard deviation = 0.32, skew = 0.00 and kurtosis = -0.30. The magnitude of degradation factor, D , was calculated for all four cases with an inlet air flow rate of $0.283 \text{ m}^3\text{s}^{-1}$. The inlet temperatures of the air and water were at 20°C and 50°C , respectively.

The results of this test are given in Table 4.2 which shows that D is not affected significantly by the grid size. Consequently, maintaining a coarser 10x10 grid was more practical for computation without any significant impact on the calculation results.

Table 4.2: Results of grid independence test

Grid size	D	Deviation with respect to 10x10 grid
10x10	2.07%	-
10x11	2.08%	0.48%
10x15	2.07%	0.00%
10x20	2.06%	-0.48%

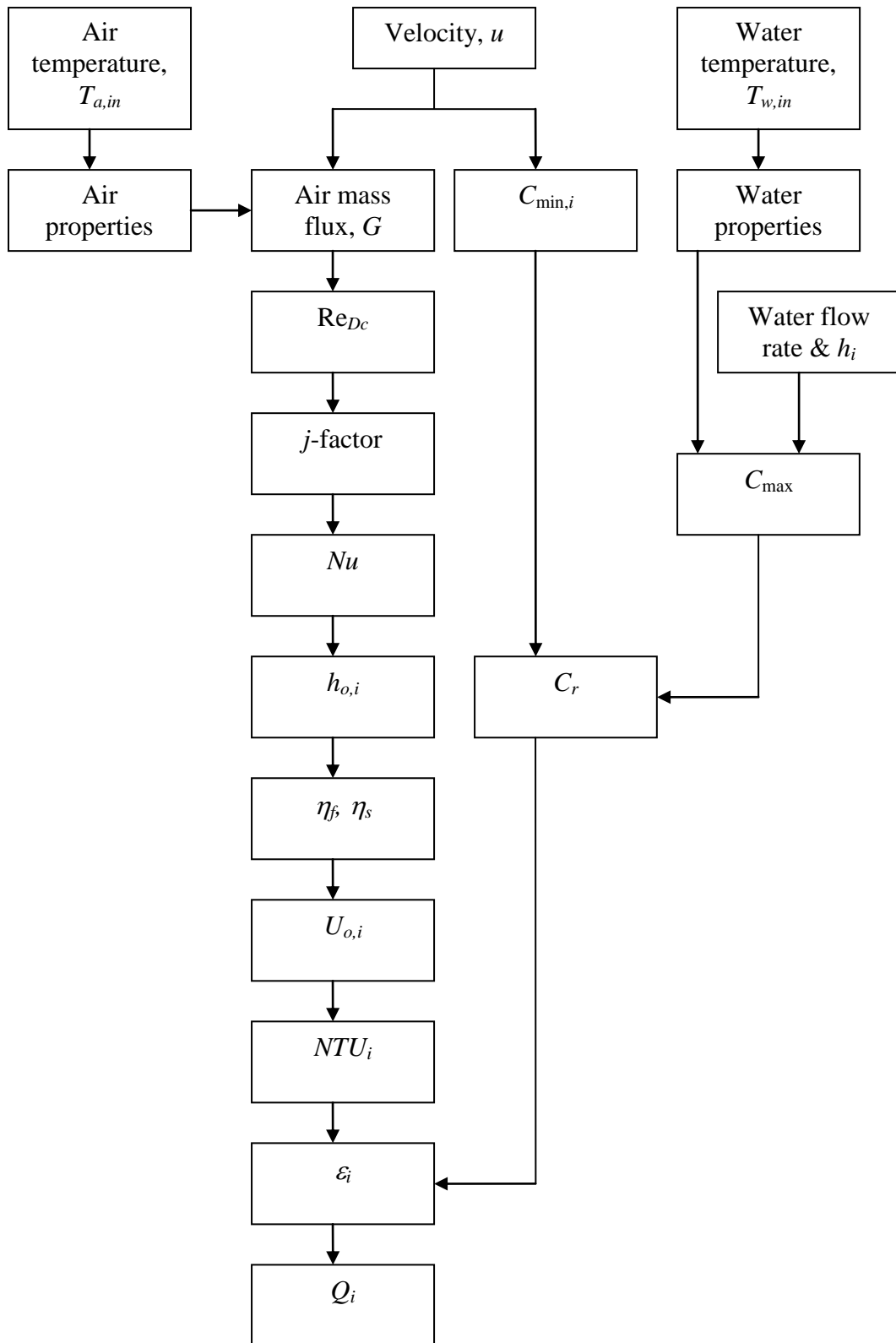


Fig. 4.5: Calculation algorithm to obtain cell element heating capacity

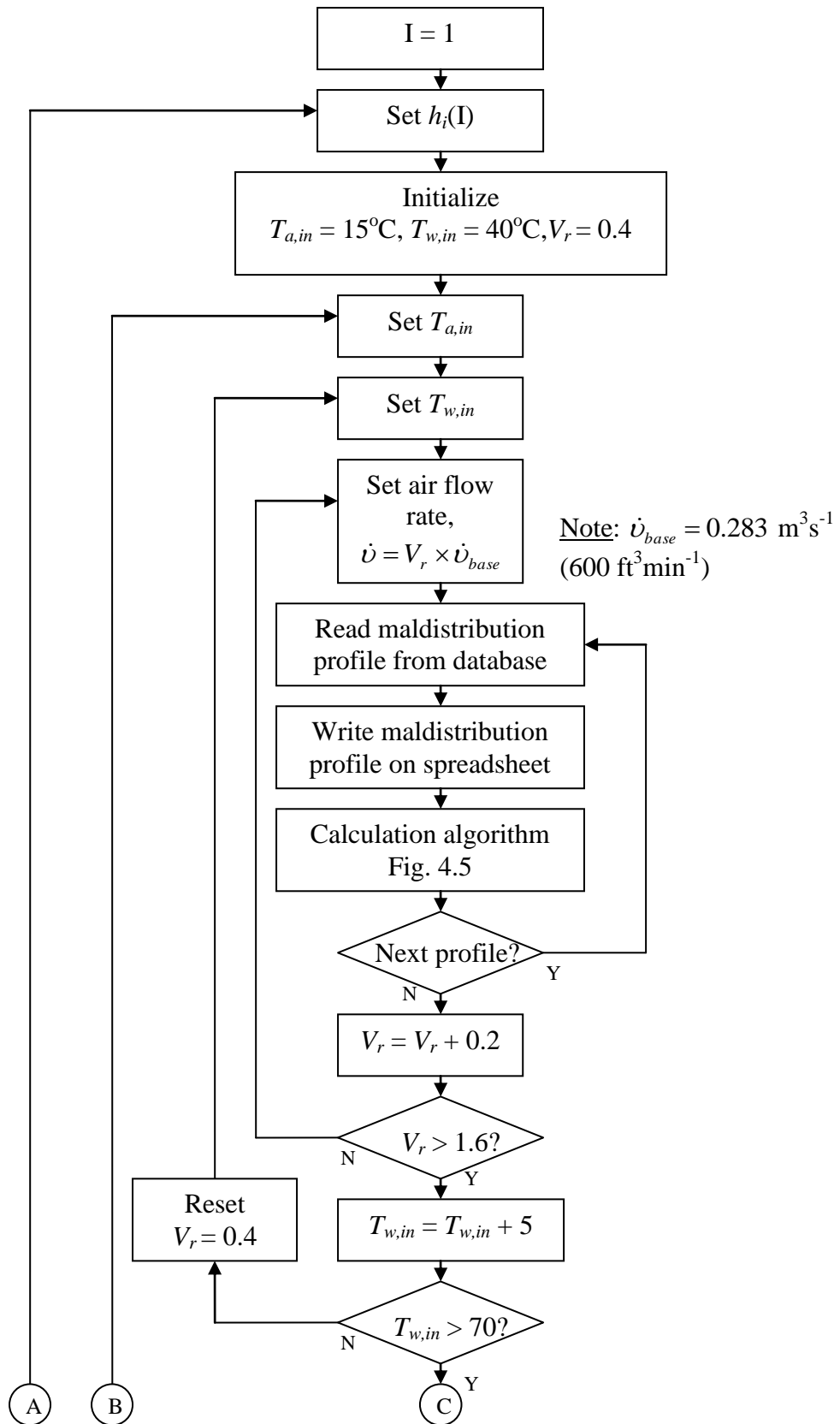


Fig. 4.6: Overall calculation flowchart

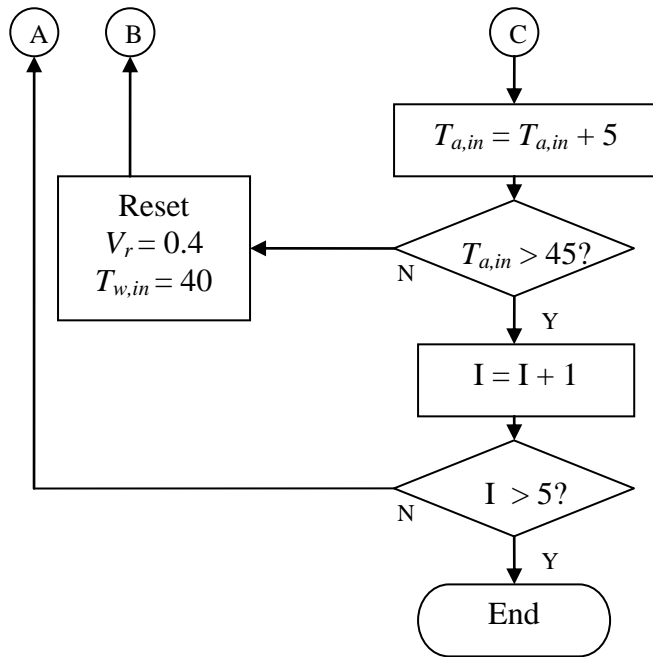


Fig. 4.6: Overall calculation flowchart (continued)

4.6 Results

The simulation was initially done by calculating the heat exchanger heating capacity with varying kurtosis while the mean, standard deviation and skew were held constant. Fig. 4.7 illustrates examples of the calculated D of the exchanger coil for normalized standard deviation of 0.10, 0.36 and 0.44, and normalized skew of 0.00 and 0.72. The air face velocity was set at 1.85 ms^{-1} .

In general, the trend lines are flat which indicates that kurtosis does not have a significant effect on the heat exchanger thermal performance. This is in agreement with the observations from the analysis in Chapter 3. As a result of this, kurtosis was not controlled further when generating the maldistribution profiles for subsequent simulation calculations.

The results of the calculation as the moments, fluid temperatures and air flow rates change are presented with plots of D vs. NTU . Fig. 4.8 shows such an example of a D - NTU plot for normalized skew of 1.00 with $h_i = 4,540 \text{ Wm}^{-2}\text{K}^{-1}$. The calculation data were then re-plotted to describe the effect of standard deviation and skew on D . This was done for specific NTU values. Figs. 4.9 and 4.10 illustrate these effects with $NTU = 1.0$.

The effects of the maldistribution on the exchanger performance were then compared with respect to higher magnitudes of h_i . The trend of the calculated D could be seen in Fig. 4.11 for a specific set of moments. These effects could also be presented alternatively by plotting D versus h_i , at a specific NTU and skew, as shown in Fig. 4.12.

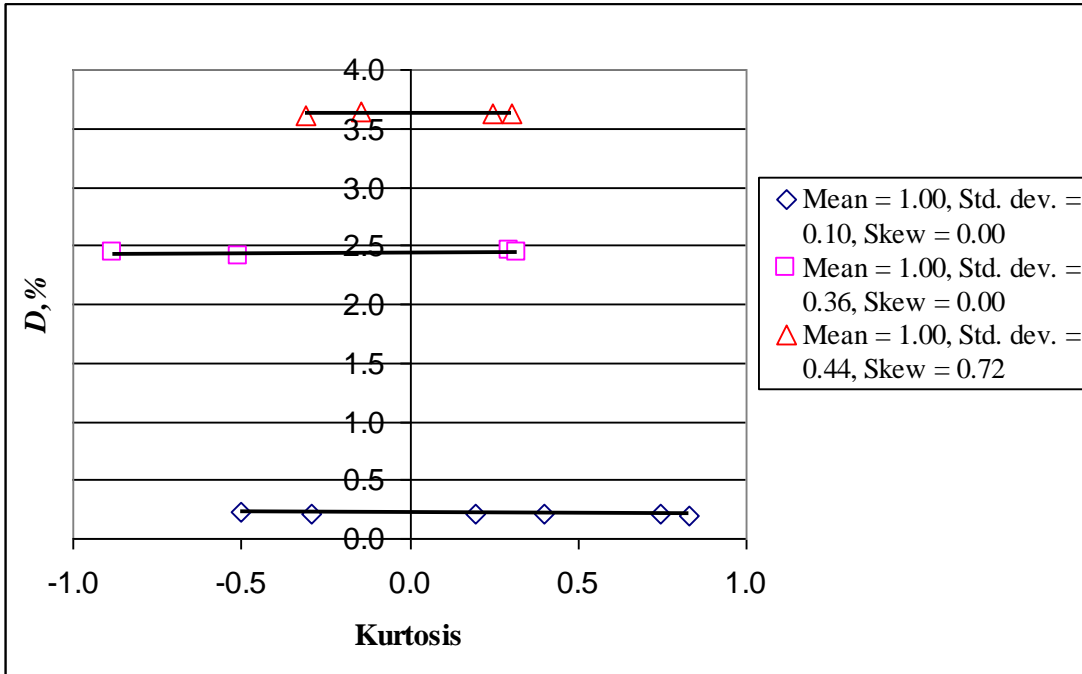
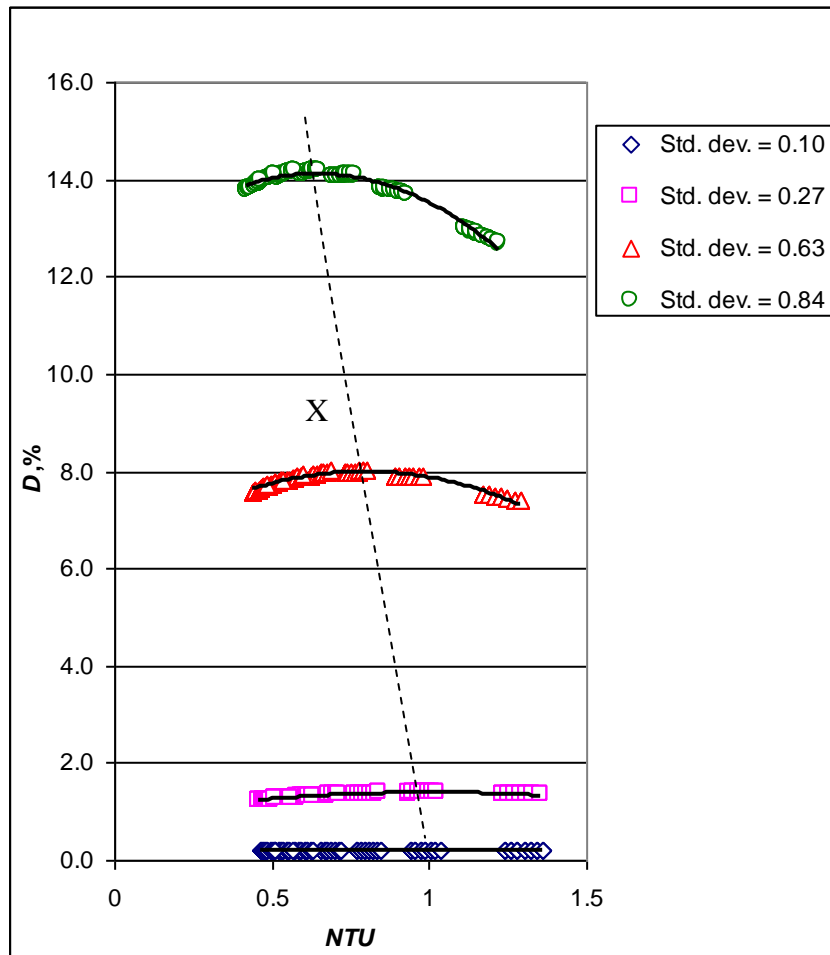


Fig. 4.7: Effect of kurtosis on D
 (Air inlet temperature = 20°C, water temperature = 45°C)



**Fig. 4.8: D - NTU plot for skew = 1.00 with varying standard deviation
(Mean = 1.00, $h_i = 4,540 \text{ Wm}^{-2}\text{K}^{-1}$)**

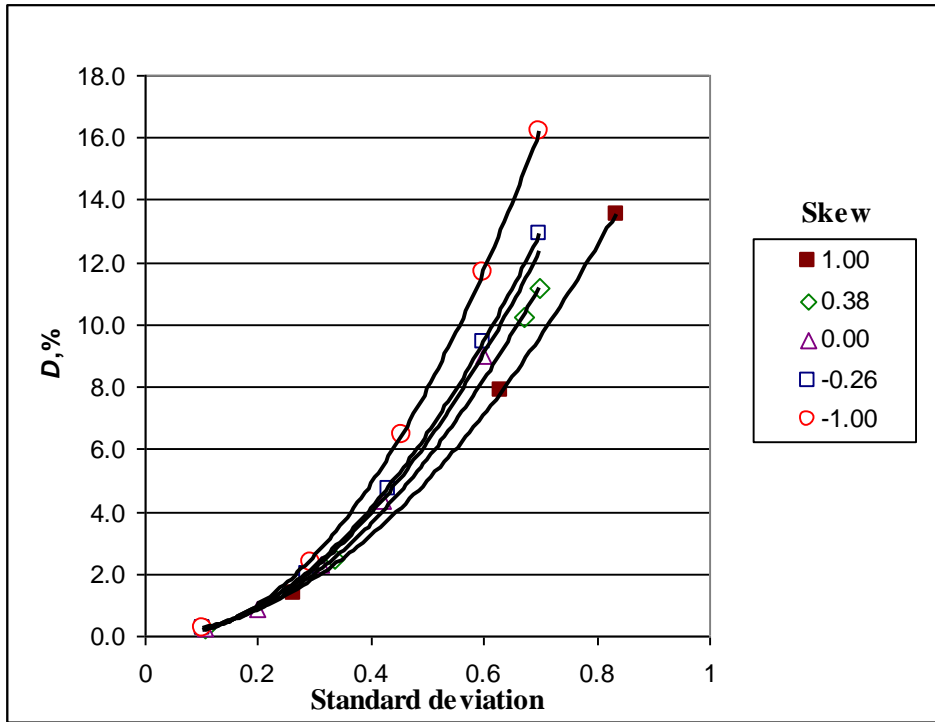


Fig. 4.9: Effect of standard deviation on D
 (Mean = 1.00, $NTU = 1.0$, $h_i = 4,540 \text{ Wm}^{-2}\text{K}^{-1}$)

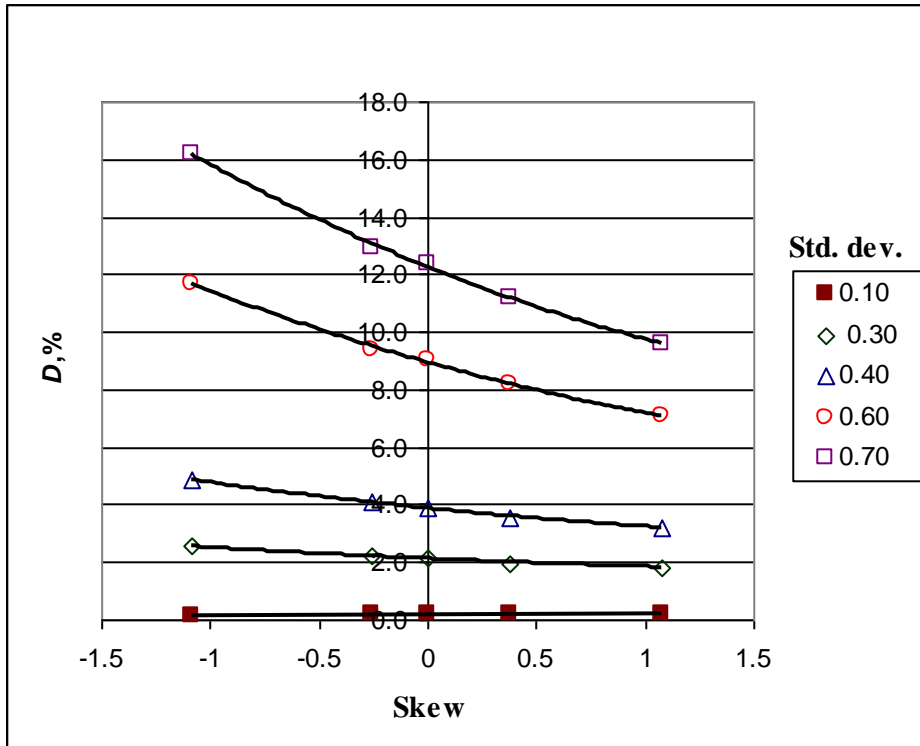
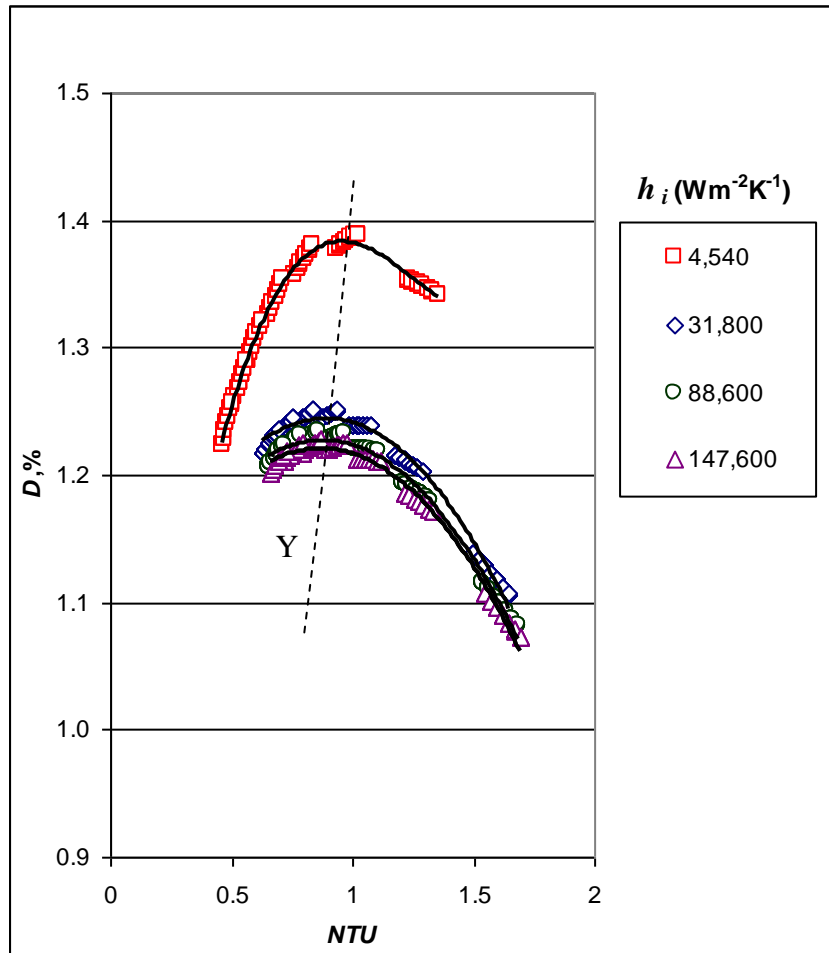
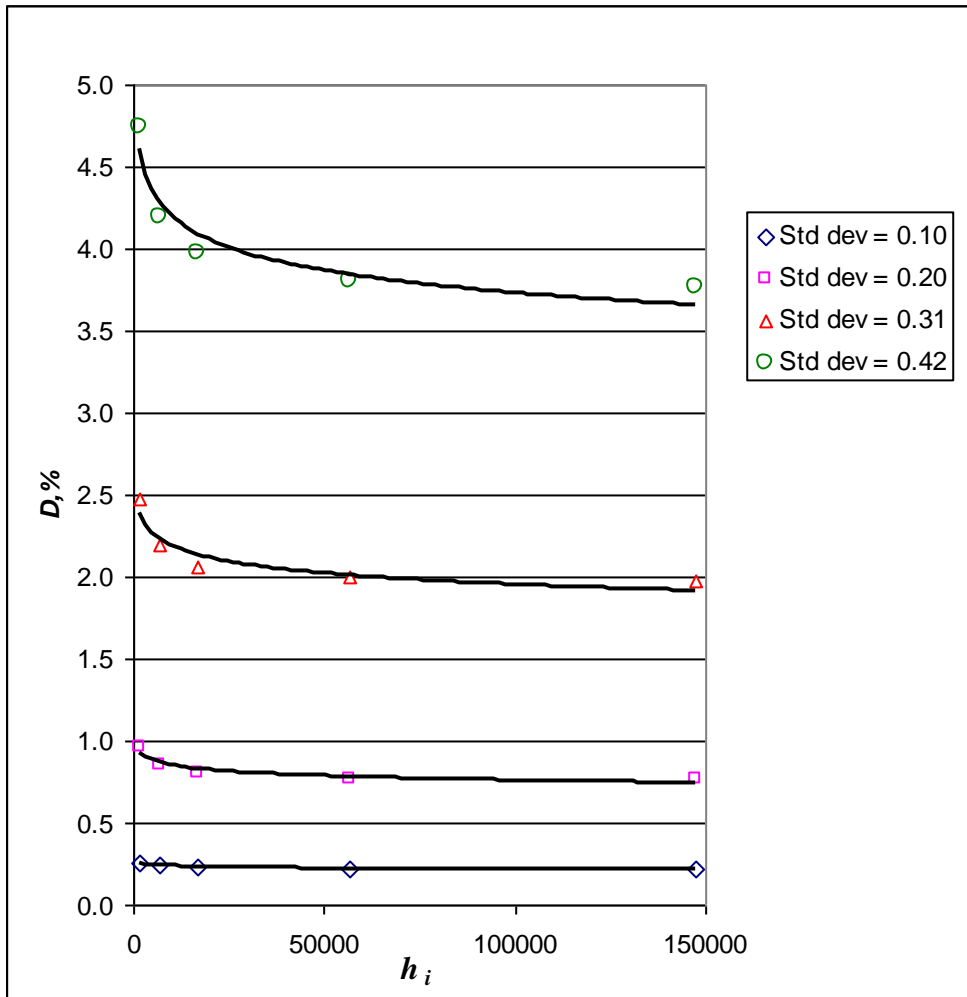


Fig. 4.10: Effect of skew on D
 (Mean = 1.00, $NTU = 1.0$, $h_i = 4,540 \text{ Wm}^{-2}\text{K}^{-1}$)



**Fig. 4.11: Effect of h_i on D with varying NTU
(Mean = 1.00, standard deviation = 0.27, skew = 1.00)**



**Fig. 4.12: Effect of h_i on D at fixed NTU and skew
(Mean = 1.00, NTU = 1.0, skew = 0.00)**

4.7 Analysis and discussion

The results of the numerical study have clearly shown confirmation of the theoretical findings obtained in Chapter 3 which states that the first three statistical moments of the maldistribution, i.e. mean, standard deviation and skew, affect the heat exchanger thermal performance. The effect of the mean was represented in the calculation by the non-dimensional parameter NTU . Also, as observed in the preceding section, the fourth moment, kurtosis, did not show a perceptible effect on the magnitude of D . The effects of these moments are now described in greater detail in the following subsections.

4.7.1 Effect of standard deviation

Corresponding to the findings from previous research, e.g. [27, 32], the calculation results show that higher standard deviation will cause a larger performance deterioration. The deterioration factor, D , is found to increase supralinearly with normalized standard deviation. D increases at a faster rate as the standard deviation increases. The trend lines of Fig. 4.9 show that a third degree polynomial equation can be used to fit the data points, which is in agreement with equation (3.28), for a known skew and NTU . When the velocity distribution is uniform, the standard deviation will equal zero, and hence $D = 0$. Nevertheless, the magnitude of D calculated is also low, e.g. only 2% when the normalized standard deviation is about 0.30. With higher standard deviation of 0.70, D is between 12% and 16%. This corresponds well with the findings of Mueller [12].

4.7.2 Effect of skew

The results in Fig. 4.10 show that skew has no significant effect when the standard deviation is lower than 0.10. When the normalized standard deviation is between 0.10 and 0.40, the performance deterioration varies linearly with skew, i.e. following the theoretical trend observed in Chapter 3. However, with higher standard deviations, D tends to vary in the order of the square of skew. This deviation from the linear trend could be due to the amplification of the differences, at higher standard deviations,

with the theoretical derivation arising from the assumptions made, as highlighted in Section 4.2.

Nevertheless, the results also confirm that at higher positive skews, the performance deterioration is less, and vice-versa. As explained in the previous chapter, this is because the positive skew distribution has a larger proportion of higher velocities which reduce the adverse effects of the lower velocities.

4.7.3 Effect of NTU

The results shown in Fig. 4.8 demonstrate the trend of performance deterioration with respect to the magnitude of NTU . High values of NTU correspond to low air flow rates (i.e. lower mean) and with high inlet temperatures. As the air flow rate increases, i.e. NTU decreases, the magnitude of D will initially increase. The reason for this phenomenon is that the higher air velocities will cause the external heat transfer coefficient, h_o , on the fin surfaces to increase. With the reduction of thermal resistance from the external convective surfaces, the exchanger coil becomes more susceptible to the detrimental effects of maldistribution.

Essentially, the air-side maldistribution will only affect the external thermal resistance, r_o . Here r_o is the controlling component in the total thermal resistance network which, ignoring the tube wall conduction resistance, is expressed as:

$$r_t = r_o + r_i \quad (4.33)$$

As the NTU continues to reduce, a peak for D is reached, where a further increase of air flow rate will cause the deterioration to diminish. With further reduction of NTU , the external resistance will continue to decrease while the internal resistance remains the same (i.e. fixed h_i). The magnitude of r_o will now approach r_i , whence it will no more be controlling and the influence of r_i becomes more significant in determining the total heat transfer through the exchanger. Since the degradation effect is only dependent on r_o and since the ratio of r_o/r_t becomes smaller, the degradation effect of maldistribution becomes less, i.e. D reduces. This declining trend at high flow rates concurs with the findings of Fagan [27]. Furthermore, this also corresponds

to a larger mass flow rate through the exchanger which becomes less susceptible to the degradation effect caused by maldistribution.

Consequently, the two opposing effects due to increasing h_o , which leads to a reducing r_o/r_i ratio, and increasing flow inertia, as the NTU reduces, describes the parabola-like curves of the $D-NTU$ plot seen in both Figs. 4.8 and 4.11. As the standard deviation increases, the domes of the curves become more prominent. This corresponds to the larger deterioration effects suffered by the exchanger. A fitting of these curves indicates that a quadratic or cubic relationship with NTU is adequate to characterize the phenomenon.

It is further observed that as the normalized standard deviation increases, the peak points of these curves will describe a *locus maxima* line to the left as NTU decreases (dotted line marked 'X' in Fig. 4.8). The wider spread of velocities in the maldistribution profile causes h_o , or r_o , to be more controlling over the deterioration effect, and hence it will need a much higher air flow rate (i.e. lower NTU) for h_i , or r_i , to become effective in reducing D .

A cursory examination of equation (3.37) seems to indicate that a fixed normalized standard deviation and skew for a maldistribution would not affect the degradation factor, D , even though the mean or NTU changes. The apparent contradiction with the observations from this numerical study is a result again of the assumptions used in the theoretical model which did not account for the tube-side convective heat transfer resistance in determining the overall degradation effect.

4.7.4 Effect of h_i

As an extension to this, the analysis of the effects of internal heat transfer coefficient, h_i , on the degradation factor, D is illustrated in Fig. 4.11. It is clearly seen that as h_i becomes higher, the magnitude of D reduces. This is due to the higher heat flux through the tube walls causing the exchanger to be less sensitive to the adverse effects of maldistribution. It can also be seen from the plot that the maximum peaks of these curves falls on another *locus maxima*, as indicated by the dotted line 'Y'. These maximum points shift to the left as h_i increases.

A possible explanation for this is that as h_i increases, $r_i \rightarrow 0$. The external resistance, r_o , becomes more influential. It needs a much higher air flow rate, i.e. lower NTU , to bring the magnitude of r_o to approach r_i and for the internal resistance to have a significant effect on the heat transfer.

The plot shown in Fig. 4.12 further reinforces the observation that higher magnitudes of h_i reduces the adverse effect. However, when $h_i > 17,000 \text{ Wm}^{-2}\text{K}^{-1}$ the rate of reduction in D is lower and tends to an asymptotic value. The trend of these results also suggests a reciprocal relationship between D and h_i .

4.7.5 Effect of air temperature

A closer inspection of Figs. 4.8 and 4.11 shows that there is a pattern in the data scatter along the D - NTU trend lines. Analysis of the data has revealed that this scatter is due to the air inlet temperature. To illustrate this, Fig. 4.13 gives a close-up view of the D - NTU plot for standard deviation of 0.63, skew of 1.00 and h_i of $4,540 \text{ Wm}^{-2}\text{K}^{-1}$. The two lines indicate the range of air temperature limits (i.e. $15^\circ\text{C} - 45^\circ\text{C}$) used in the calculations.

The results indicate that higher inlet air temperatures will cause the deterioration to increase though the change is small ($< 0.1\%$). This occurrence is due to the change in air properties where a higher temperature not only gives a lower density but also lowers the viscosity and increases the thermal conductivity. All of these will cause the fin surface to become more sensitive to the maldistribution.

The temperature effects tend to diminish at lower magnitudes of NTU , i.e. at higher air velocities. This observation corresponds with the previously described result where the external thermal resistance loses its dominance at higher air velocities, and the effect of the internal resistance is to reduce D .

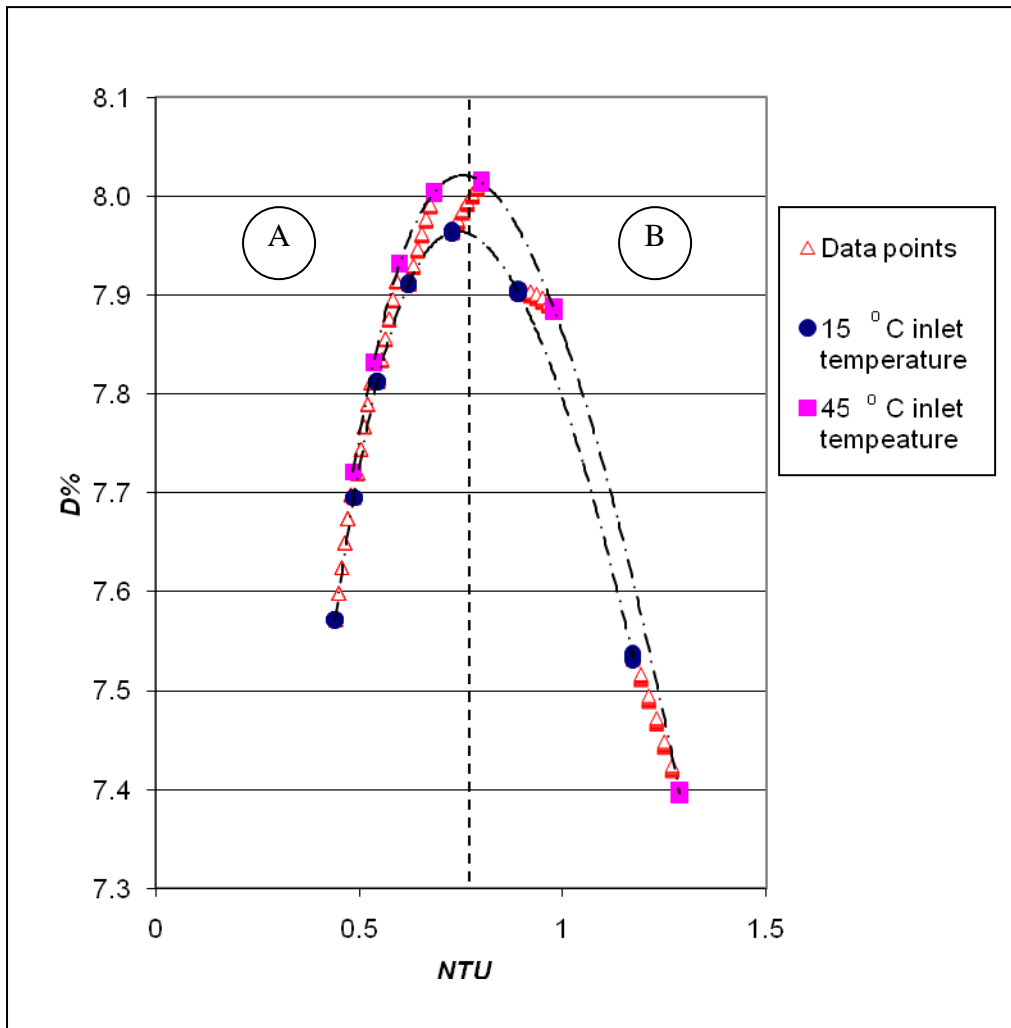


**Fig. 4.13: Close-up view of D - NTU plot showing effect of inlet air temperature
(Mean = 1.00, standard deviation = 0.63, skew = 1.00)**

4.7.6 Effect of R

It is evident from the results that the magnitude of thermal degradation is very much dependent on the ratio between the external and internal thermal resistances. To analyze this effect in more detail, a graph of D vs. R is also plotted, where R is the ratio between the external and internal heat transfer coefficients, i.e.

$$R = \frac{h_o}{h_i} \quad (4.34)$$

An example is shown in Fig. 4.14 for the same normalized moments of Fig. 4.13. Higher R values correspond to higher air flow rates, and vice-versa. The parabola-like curve is similar to the D - NTU plot. The D - R plot shows that a second or third order polynomial equation could characterize the trend between these two parameters. It is obvious that there is a relationship between Fig. 4.13 and Fig. 4.14 where the area “A” to the left of the peak in the former diagram corresponds to the area “E” to the right of the peak in the latter diagram; and similarly with “B” and “F”.

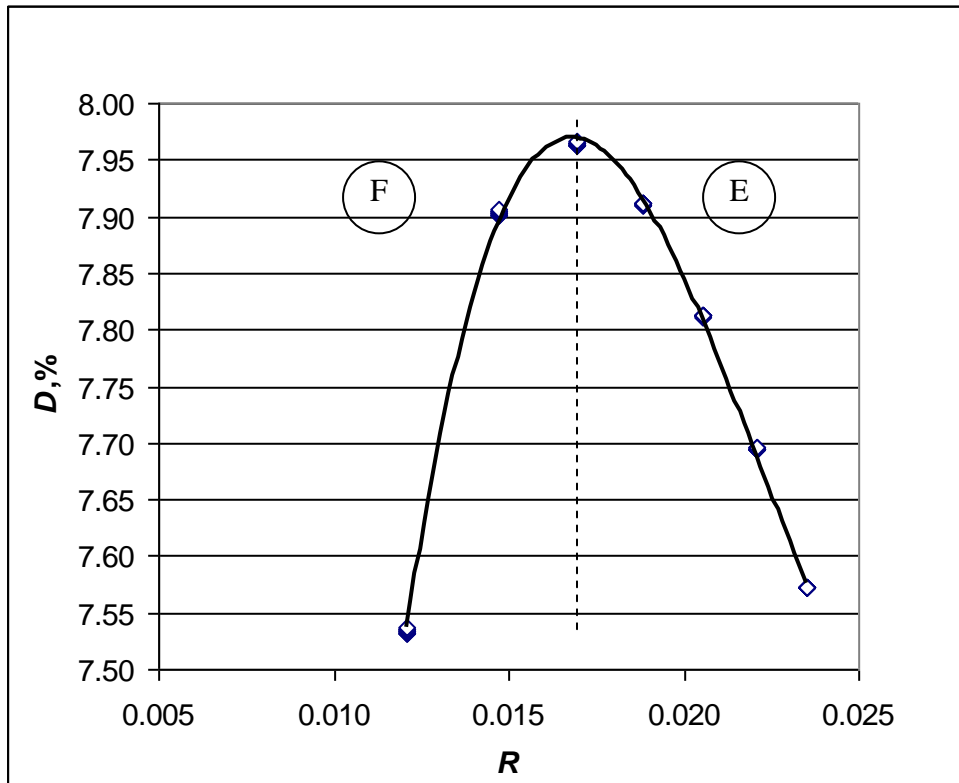


Fig. 4.14: Plot of D versus R

(Mean = 1.00, standard deviation = 0.63, skew = 1.00, $h_i = 4,540 \text{ Wm}^{-2}\text{K}^{-1}$, $T_{a,in} = 15^\circ\text{C}$)

4.8 Comparison with other data

As a further verification for the trends observed, comparisons were also made with other data obtained from literature. For this purpose, published experimental results were used to demonstrate the trend of performance degradation.

Beiler and Kroger [39] have published their experimental results of thermal performance deterioration factor arising from an air flow maldistribution on a finned tube bundle heat exchanger. Fig. 4.15 is a re-production of the published data for one-row of tubes which clearly shows the parabola-like D - NTU curve for the exchanger. At $NTU = 1.0$, D is approximately 1.2% which is similar to the results in Fig. 4.11 though the span of NTU values for this exchanger is larger. However, information of the distribution moments is not available in the paper.

In the work by Berryman and Russell [19], air flow maldistribution profiles on the tube bundles of an air-cooled heat exchanger with standard deviation up to 0.30 were measured. The results of the effect on the thermal performance efficiency are reproduced in Fig. 4.16 for a one-pass configuration. The thermal performance degradation factor is thus obtained by subtracting this reduction in efficiency from unity. The resulting plot clearly shows the cubic relationship between the degradation factor and standard deviation.

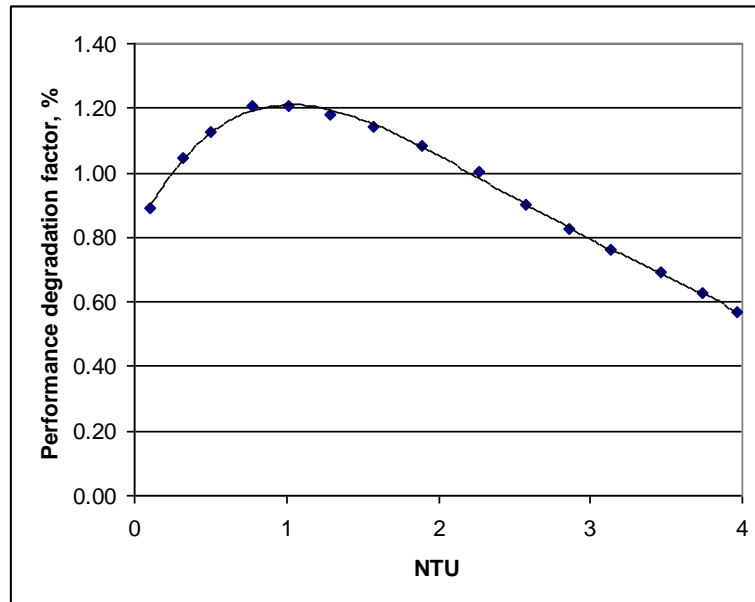


Fig. 4.15: Digitized re-production of results from [39] for a one tube-row bundle (with $C_a/C_f = 0.1$)

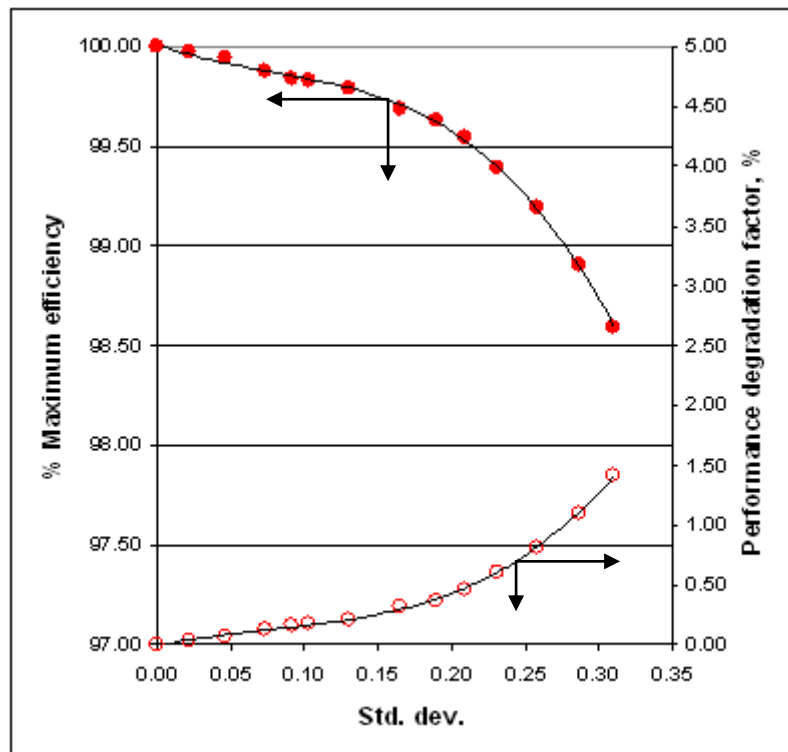


Fig. 4.16: Digitized re-production of results from [19] (filled circles) for a one-pass tube bundle air-cooled heat exchanger and corresponding calculated performance degradation factor (non-filled circles). Air velocity 3.5 ms^{-1} , overall heat transfer coefficient $1,000 \text{ Wm}^{-2}\text{K}^{-1}$.

4.9 Implication of the results

In general, the air velocity maldistribution on a fin-tube heat exchanger in a system is mainly due to the geometrical layout of the heat exchanger with respect to other components. The findings from this work indicate that the fin-tube exchanger should be positioned in such a way that the inlet air velocity profile will have the lowest possible standard deviation and the highest possible skew. Apart from that, the exchanger should be designed to operate at air flow rates which avoid the peak of the D - NTU curve for a specific maldistribution profile. Since operating at low flow rates (i.e. high NTU) would have a heating capacity disadvantage, the exchanger should operate, where possible, at sufficiently high air flow rates, i.e. to the left of the D - NTU peak, to reduce the maldistribution effects.

If the degree of maldistribution could be determined during the design stage, the penalty on the thermal performance could be predicted. This could be done by direct measurements of the velocity profile on the prototype exchanger face area itself, or by means of numerical simulation, e.g. Computational Fluid Dynamics (CFD), for a conceptual heat exchanger. In this respect, CFD simulations would be more practical to extract the moments with various types of design. The simulation process could be repeated until an optimum design is obtained.

Since higher magnitudes of h_i have lower deterioration factors, it follows that fin-tube exchangers with viscous flows, e.g. oil, will suffer a larger degradation effect as compared to those with water. Thus, application of fin-tube exchangers as oil coolers will be more susceptible to maldistribution effects. With the same reasoning, heat exchangers which have high tube fluid flow rates will be less sensitive to maldistribution degradation.

4.10 Summary

A numerical scheme, based on the ε - NTU method, has been implemented on the discretized model of a single-row fin-tube heat exchanger to determine the effect of flow maldistribution on its thermal performance. The results of the numerical calculation are in agreement with the theoretical results obtained in Chapter 3, i.e. equation (3.28), which has established the relationship between the thermal performance degradation with the four statistical moments.

The following general relationships between D and the four independent variables of standard deviation, skew, NTU and R were obtained from the results:

- a) D varies as the cube of standard deviation
- b) D is not affected by skew when standard deviation is lower than 0.10
- c) D varies linearly with skew for standard deviation between 0.10 and 0.40 but to the square of skew for higher values
- d) D varies as the cube of NTU
- e) D varies as the square of R

The inlet air temperature will also affect the magnitude of D due to changes of the transport properties; however the effect is small, i.e. $< 0.1\%$.

A maldistribution profile with low standard deviation and high positive skew is preferred so as to give low thermal performance penalty. Heat exchangers with high internal heat transfer coefficients are less sensitive to the maldistribution degradation effects.

CHAPTER 5

INFLUENCE OF COIL GEOMETRY ON HEAT EXCHANGER THERMAL PERFORMANCE DEGRADATION

5.1 Overview

The geometrical parameters of a fin-tube heat exchanger are defined in this chapter and the influence of these parameters on the thermal performance degradation factor, D , of the fin-tube heat exchanger is studied numerically. The geometrical parameters examined in this work include the number of tube rows, tube diameter, fin pitch, transverse tube pitch, longitudinal tube pitch and fin pattern. A row-by-row analysis is also performed to investigate the effects of the flow maldistribution on subsequent tube rows in the exchanger. Finally, a new set of correlation equations is proposed which would allow prediction of the performance degradation for design purposes.

5.2 Fin-tube heat exchanger geometry

Fig. 5.1 illustrates a schematic diagram of a fin-tube heat exchanger with staggered tubes, typically used in the air-conditioning, refrigeration and automotive industries. The common parameters used to describe the heat exchanger coil are the number of tube rows, tube diameter, fin pitch, transverse tube pitch and longitudinal tube pitch. The coil height and width are determined by the two tube pitches while the coil length determines the total number of fins in the coil stack.

The heat exchanger is also characterized by the pattern on the fin surfaces. These surfaces are usually pressed or punched to give wavy corrugations, slits or louvers to augment the heat transfer rate. They work by interrupting and breaking up the air boundary layer on the fin surfaces. Consequently, the air side heat transfer coefficient is higher with these surface patterns.

A substantial amount of work has been done by past researchers to quantify the effects of these geometrical parameters on the air-side heat transfer coefficient. Correlation equations have been developed for specific fin patterns covering a range of parameters which allow predictions of the heat transfer performance. An example of such correlations developed by Wang et al. [82] is reproduced in Appendix A. Other examples include the works done by Xie et al. [91] and Kim et al. [92].

5.3 Influence of coil geometry

It is obvious from these previous studies that the heat exchanger geometrical parameters have a significant effect on the heat transfer performance of the exchanger. Consequently, the geometry of the fin-tube coil is expected to affect the magnitude of the thermal performance degradation factor, D (i.e. equation (3.24)), due to flow maldistribution.

To investigate these geometrical effects, the discretized fin-tube heat exchanger model described in the previous chapter was used. The effects of the geometrical parameters, the maldistribution statistical moments and the internal and external heat transfer coefficients on the value of D were calculated and the results analyzed.

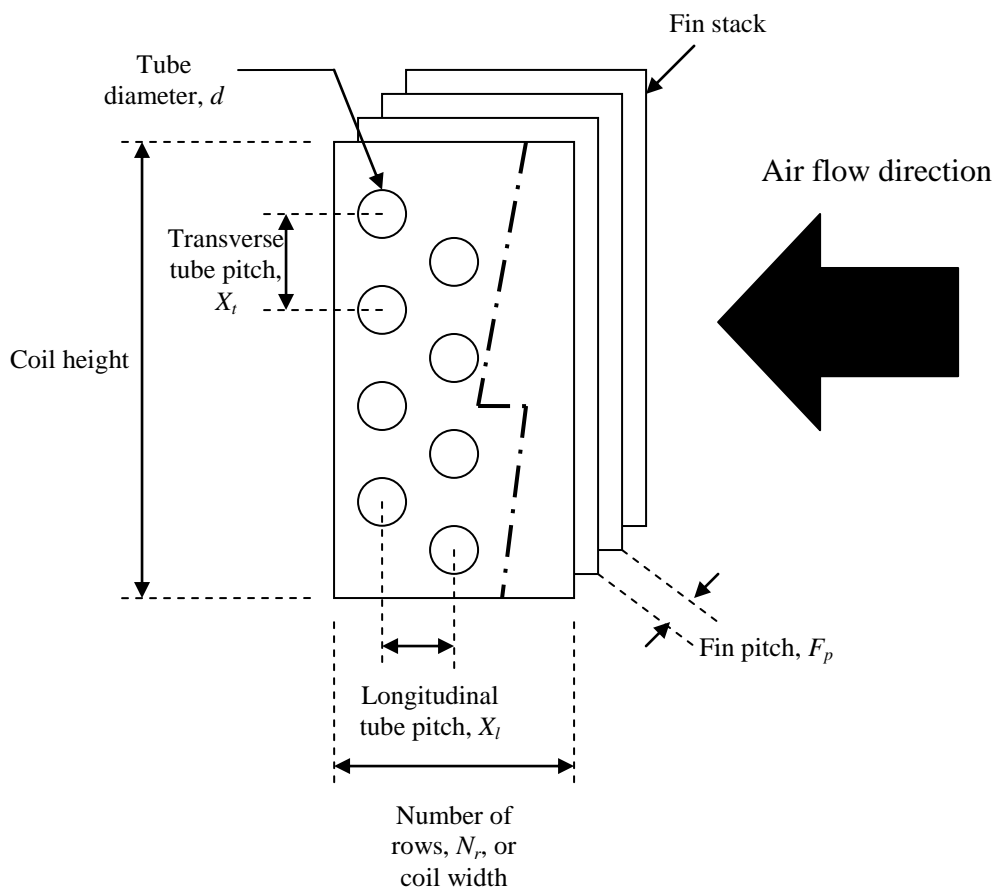


Fig. 5.1: Schematic diagram of fin-tube heat exchanger

5.3.1 Numerical methodology

The numerical simulation was performed on a fin-tube coil model which has the same face area, i.e. 600mm coil length x 254mm coil height. The same 10 x 10 discretization grid was also applied to the coil face. As the coil geometry parameters vary, the total external surface area and heat transfer coefficient for each of the elements changes accordingly.

With this model, the same calculation algorithm described in Chapter 4 was applied for each cell element. In contrast to that work where a single coil geometry specification was used throughout the calculation, the present simulation was applied to different coil geometries. The effect of the geometrical parameters was taken into consideration through the air-side j -factor correlation. This can be seen from the correlation example in Appendix A where these parameters are variables in the set of equations.

The ranges of the geometrical parameters used in the model are given as follows, which reflect typical values used in the industry:

1. N_r : 1 to 4
2. d : 8.71mm to 10.33mm
3. F_p : 1.154mm to 1.588mm
4. X_i : 19.0mm to 25.4mm
5. X_o : 22.9mm to 27.9mm

The air flow maldistribution statistical moments used in the present simulation were the same as applied earlier. Also, the same range of air and water inlet temperatures were used, i.e. 15°C to 45°C and 40°C to 70°C, respectively, while the tube wall temperature was maintained constant in the calculation.

Typically, fin-tube heat exchangers with larger number of tube rows have higher heat transfer capabilities and are used with higher air flow rates. In view of that, a wider range of average coil face velocity was used in calculation, i.e. 0.6 to 7.0 ms^{-1} . The same range of internal heat transfer coefficients was also used, i.e. from 4,540 to 147,000 $\text{Wm}^{-2}\text{K}^{-1}$. As a result, the NTU varies between 0.20 and 4.50 while the ratio R varies from 0.00030 to 0.055.

In addition to the wavy, corrugated fin pattern, the simulation was also performed with louvered fins. The j -factor correlation for louvered fins developed by Wang et al. [93] was used in the calculation to determine the external heat transfer coefficient, h_o . Fig. 5.2 shows the profile of the louvered fins studied in this work.

5.3.2 Row-by-row analysis

The study on the effect of multiple tube rows on the degradation factor, D , was further extended to analyze the influence of upstream tube rows to the subsequent downstream rows. This row-by-row analysis was done by evaluating the thermal degradation factor of each tube row, D_r , where $r = 1$ to N_r .

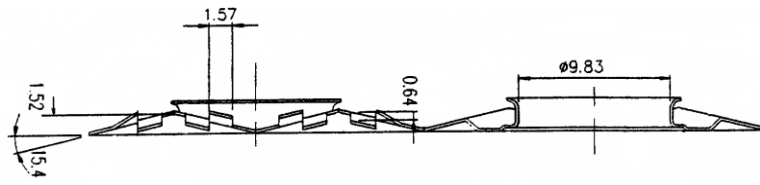
To do this, the intermediate air temperature between successive rows must be known for every discrete element of the exchanger coil. The intermediate temperature was solved with an iterative Log Mean Temperature Difference (*LMTD*) procedure, which is described as follows.

For illustration purposes, a discrete element of a 3-row fin-tube heat exchanger is used, as shown in the Figure 5.3. The element has an inlet air velocity, u and an inlet temperature, $T_{a,in}$. The tubes in the heat exchanger have hot water flowing inside with a constant temperature of T_w . The total external surface area of the element is A_o . With the same algorithm shown in Fig. 4.5, the heating capacity of the element, Q_i , is calculated by using the ε -*NTU* method, and the outlet air temperature, $T_{a,out}$, is known from equation (4.20).

If Q_{i-1} , Q_{i-2} and Q_{i-3} denote the elemental heating capacity contributed by each of the three tube rows in the element (which is identified with the subscripts 1, 2 and 3), then:

$$Q_i = Q_{i-1} + Q_{i-2} + Q_{i-3} \quad (5.1)$$

The temperature T_{1-2} is defined as the average intermediate temperature leaving the first row which enters the second row. Similarly, T_{2-3} is the average intermediate temperature between the second and third rows.



Section B-B

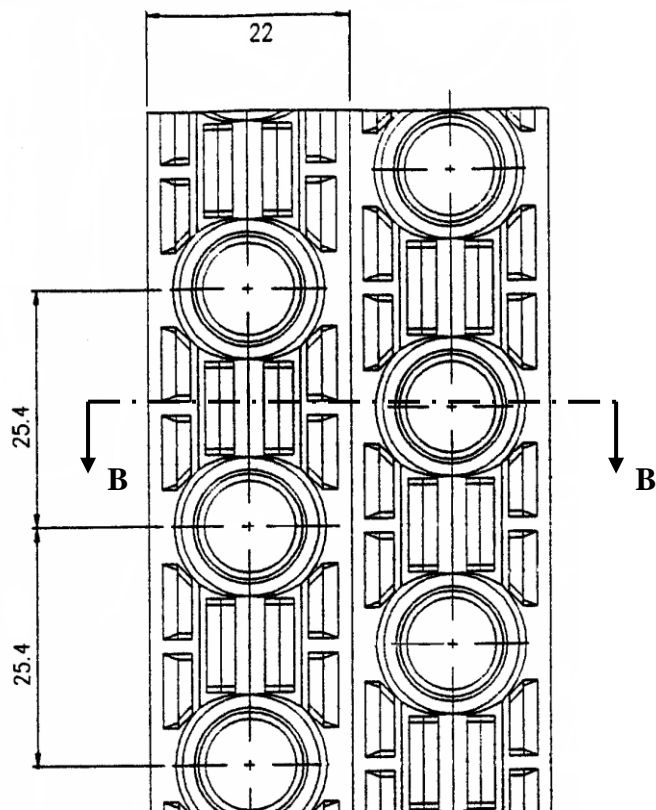


Fig. 5.2: Profile of louvered fins, with staggered tubes

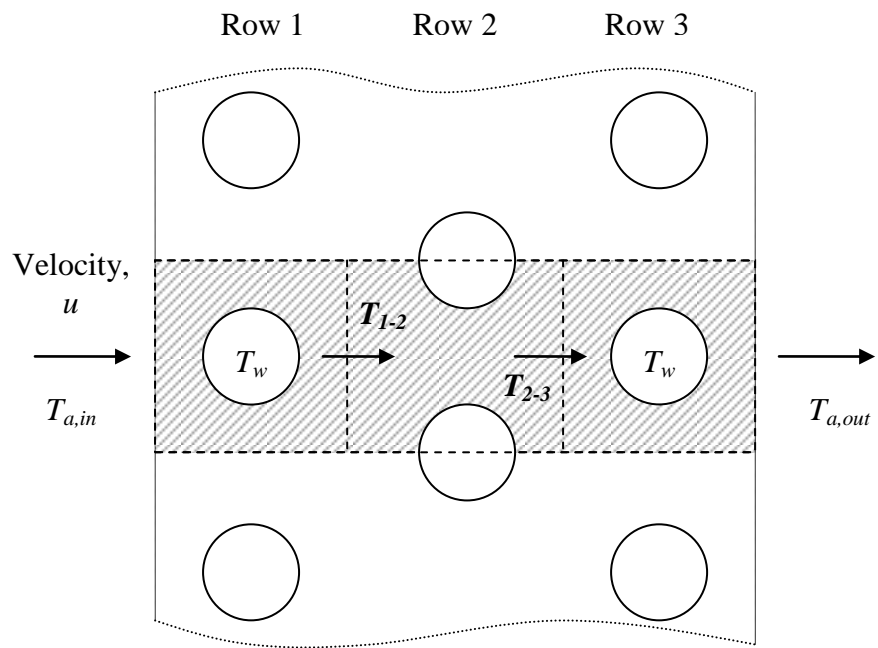


Fig. 5.3: Intermediate temperatures for a discrete element (shaded) in a 3-row fin-tube coil

If $U_{o,i}$ is the overall heat transfer coefficient of the element, the heating capacity of each row of the element can be expressed as:

$$Q_{i-1} = U_{o,i} A_o LMTD_1 \quad (5.2)$$

$$Q_{i-2} = U_{o,i} A_o LMTD_2 \quad (5.3)$$

$$Q_{i-3} = U_{o,i} A_o LMTD_3 \quad (5.4)$$

where

$$LMTD_1 = \frac{(T_w - T_{a,in}) - (T_w - T_{1-2})}{\ln\left(\frac{T_w - T_{a,in}}{T_w - T_{1-2}}\right)} \quad (5.5)$$

$$LMTD_2 = \frac{(T_w - T_{1-2}) - (T_w - T_{2-3})}{\ln\left(\frac{T_w - T_{1-2}}{T_w - T_{2-3}}\right)} \quad (5.6)$$

$$LMTD_3 = \frac{(T_w - T_{2-3}) - (T_w - T_{a,out})}{\ln\left(\frac{T_w - T_{2-3}}{T_w - T_{a,out}}\right)} \quad (5.7)$$

The heating capacities are also given as:

$$Q_{i-1} = \dot{m}_a c_{p,a} (T_{1-2} - T_{a,in}) \quad (5.8)$$

$$Q_{i-2} = \dot{m}_a c_{p,a} (T_{2-3} - T_{1-2}) \quad (5.9)$$

$$Q_{i-3} = \dot{m}_a c_{p,a} (T_{out} - T_{2-3}) \quad (5.10)$$

The intermediate temperature T_{1-2} is solved iteratively with equations (5.2) and (5.8) by incrementing T_{1-2} in steps of 0.01 from $T_{a,in}$ until Q_{i-1} converges. With T_{1-2} known, the iterative procedure is then repeated with equations (5.3) and (5.9) where T_{2-3} is changed incrementally from T_{1-2} until Q_{i-2} converges. The procedure is again repeated to obtain T_{out} and Q_{i-3} with equations (5.4) and (5.10), where T_{out} would converge to the value obtained from the earlier discretized ε - NTU algorithm.

The summation of all the elemental Q_{i-1} , Q_{i-2} and Q_{i-3} will give the total heating capacity for Row 1, Row 2 and Row 3. This is done for both uniform and

maldistributed flows and the thermal performance degradation factors for each row can then be worked out.

For the analysis, fin-tube heat exchangers with 3 and 4 tube rows were selected where a flow maldistribution with normalized standard deviation of 0.31 and zero skew was imposed on the coil face area. The simulation was done at specific flow rates between 0.28 and 0.94 m³s⁻¹ (600 – 2,000 ft³min⁻¹), which corresponds to a range of face velocity 1.83 ms⁻¹ to 6.10 ms⁻¹. The inlet air and water temperatures were 20°C and 50°C, respectively.

5.4 Results and discussion

The findings of the simulation with different coil geometry parameters are summarized in the following Table 5.1. The results are further discussed in the following sub-sections.

Table 5.1: Summary of results for coil geometry parametric study
(For NTU: 0.4~4.8, Inlet air and water temperatures: 20°C & 50°C, respectively)

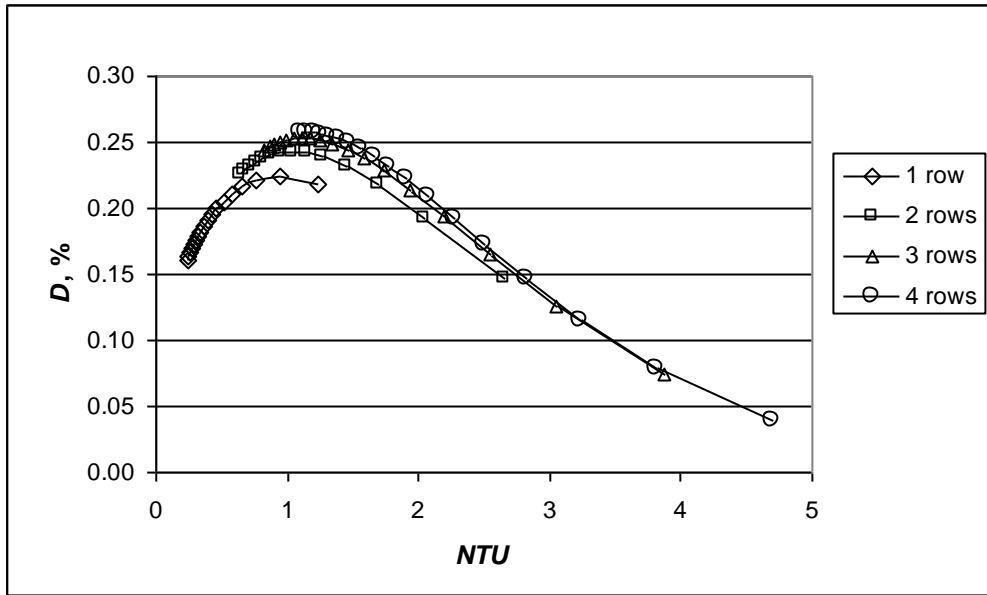
Parameter	Effect on D
Number of tube rows, N_r	D increases as N_r increases
Tube diameter, d	D increases as d reduces
Fin pitch, F_p	D increases as F_p reduces
Transverse tube pitch, X_t	D increases as X_t reduces
Longitudinal tube pitch, X_l	D increases as X_l increases
Fin pattern	D louver fin > D wavy fin

5.4.1 Effect of number of tube rows, N_r

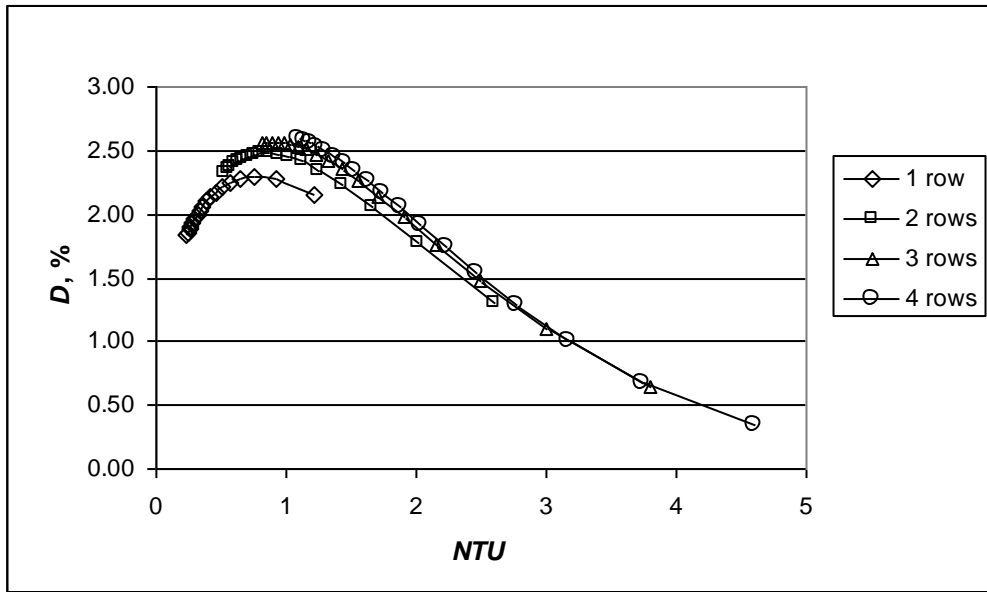
For the same wavy fin pattern, tube diameter, fin pitch and tube pitch, the results of thermal degradation effect for 1, 2, 3 and 4 tube rows are shown in Fig. 5.4(a) and 5.4(b) with two different sets of moments. The plot for each number of tube rows describes the same parabola-like D - NTU characteristic curve as reported for a single row in the previous chapter. It is clearly seen that as the number of rows increases, the

thermal deterioration becomes larger, i.e. the peak of the parabola is higher with increasing number of rows. Since the fin surface area increases with more tube rows, the exchanger NTU also increases.

The physical reasoning for this phenomenon is that as the air moves from the first row to the second row, a maldistributed temperature is induced in the air leaving the first row due to its maldistributed flow. The interaction of these two maldistribution profiles of velocity and temperature in the second row results in the amplification of the deterioration effects. With each successive row added in the coil, the degree of amplification increases. This effect has also been pointed out by both Fagan [27] and Rich [94].



(a)



(b)

Fig. 5.4: Effect of number of tube rows on D : (a) $s' = 0.10$, $\gamma' = 1.08$ (b) $s' = 0.31$, $\gamma' = 0.00$ [$F_p = 1.411\text{mm}$, $d = 9.52\text{mm}$, $X_t = 22.0\text{mm}$, $X_t = 25.4\text{mm}$, wavy fins]

The plots in Fig. 5.4 also show that as the number of tube rows increases, the incremental effect on degradation weakens, as can be seen from the lines collapsing together for $N_r \geq 3$. This is expected because the amplification effect due to temperature maldistribution begins to diminish at the third and fourth tube rows as the leaving air temperature approaches that of the water temperature.

It is also observed that as the number of tube rows increases, the peaks of the D - NTU curves shift to the right towards higher NTU values. As reported in Chapter 4, the decreasing trend with lower NTU values after the peak is due to the decreasing external thermal resistance, r_o , with respect to the fixed internal resistance, r_i . As r_o approaches the value of r_i , r_i becomes more dominant in controlling the degradation effect. With the increase of turbulence arising in the heat exchanger core from the higher number of tube rows having the effect of reducing the resistance r_o , the peak shifts to a lower air flow rate (i.e. higher NTU) and causes the internal resistance to become dominant.

5.4.1.1 Row-by-row effect

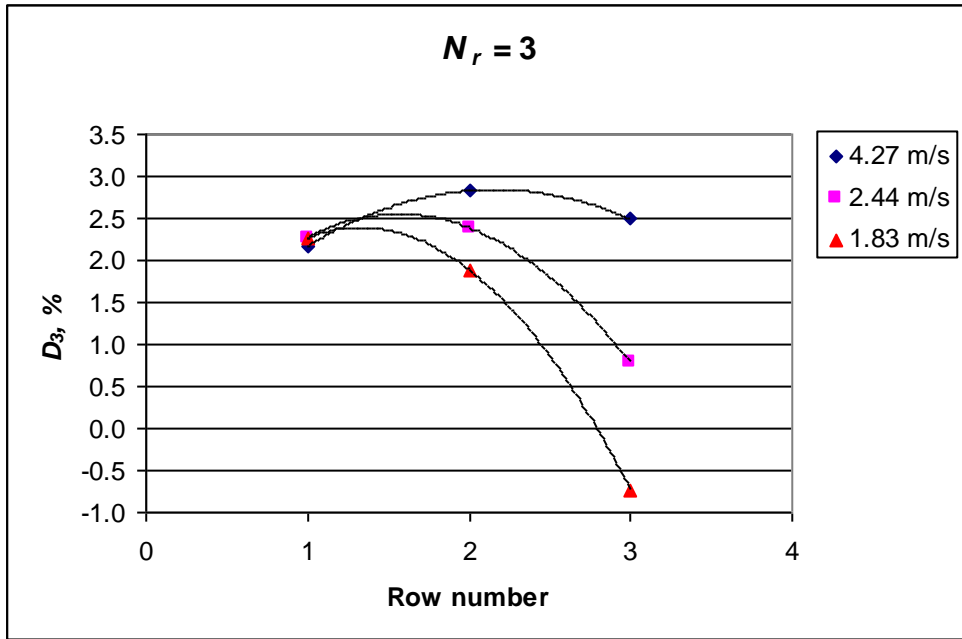
The results of the row-by-row analysis are shown in Fig. 5.5(a) and 5.5(b) for the 3-row and 4-row coils, respectively. The graphs clearly show the dependence of the row-by-row degradation trend on the approach air velocity. At higher velocities, the row degradation factor, D_r , increases from the first row, to the second or third row, before it begins to decrease. As mentioned in the preceding section, this is due to the amplification of deterioration effects due to the induced temperature maldistribution by the flow maldistribution on the first row. As a result of the reduced heating capacity in the upstream rows, the local temperature difference between water and air in the downstream tubes becomes larger as compared to the case with a uniform flow distribution. Hence, this offsets the deteriorating effects partially in the subsequent third and fourth rows, thereby causing D_r to reduce.

However, the trend is different at lower velocities (e.g. 1.83 ms^{-1}) where D_r is seen to decline steadily from the first row as the flow progresses downstream.

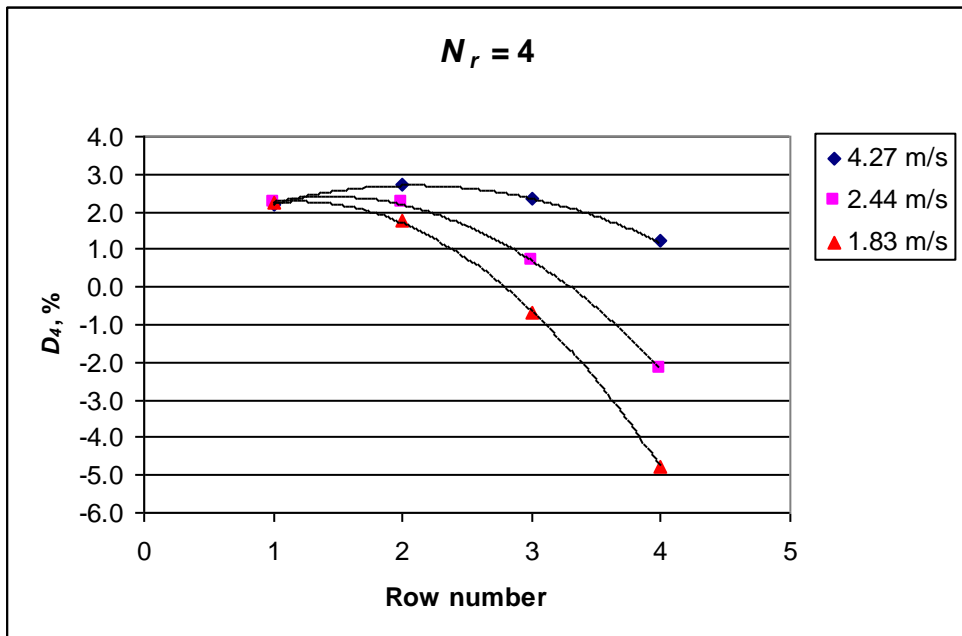
Interestingly, a heat transfer augmentation, i.e. negative magnitudes of D_r , is observed in the third or fourth row.

With a reduction in flow velocity, the external heat transfer coefficient reduces which therefore causes lower degradation effects arising from the flow maldistribution. Consequently, the augmentation effect from the larger local temperature differences in the latter rows between water and air becomes more dominant in reducing the row degradation factor, D_r , as the flow progresses through the coil depth. This continues until the heating capacity of the downstream rows become even higher than that with uniform flow distribution. Nevertheless, the magnitude of this augmentation would be small as the air temperature approaches the water temperature in the latter rows.

The results of this row-by-row calculation have shown that higher air flow rates are able to “propagate” the deterioration effects deeper into the fin-tube coil, causing higher degradation factor, D , for coils with higher number of tube rows. In contrast, lower air velocities can be seen as having weaker ability to cause degradation effects in deeper coils.



(a)



(b)

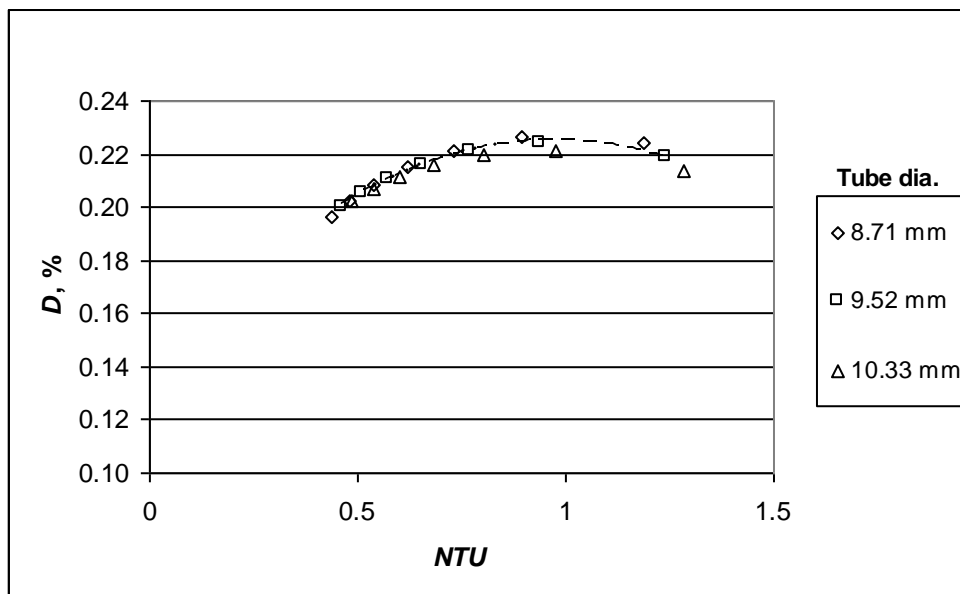
Fig. 5.5: Results of row-by-row analysis for (a) 3-row and (b) 4-row fin-tube heat exchanger [Standard deviation = 0.31, skew = 0.00, $h_i = 4,540 \text{ Wm}^{-2}\text{K}^{-1}$]

5.4.2 Effect of tube diameter

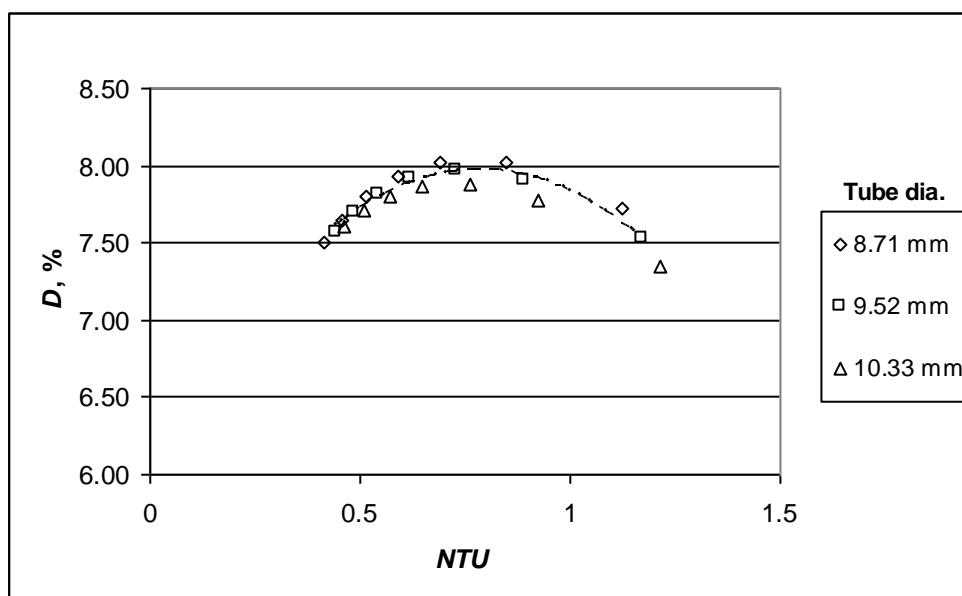
The results of the calculation by changing the tube diameter for a single row heat exchanger are given in Fig. 5.6(a) and 5.6(b). Two sets of data with different standard deviations but with the same skew are presented. With the other geometrical parameters remaining the same, three typical diameters used in the industry, 8.71mm, 9.52mm and 10.33mm were chosen.

The D - NTU plots show that as the tube diameter increases, the magnitude of degradation reduces. However, the change in D is small. This indicates that the tube diameter has a weak influence on the maldistribution degradation effect.

The reason for the observed trend is due to the size of the wake formed behind the tube. The recirculation flow in this region will cause the fin surface area directly behind the tubes to become less effective for heat transfer. As pointed out by Wang and Chi [95], this ineffective area increases when the tube diameter is larger. Consequently, the mean heat transfer coefficient reduces. Hence, this makes the exchanger less susceptible to maldistribution effects.



(a)



(b)

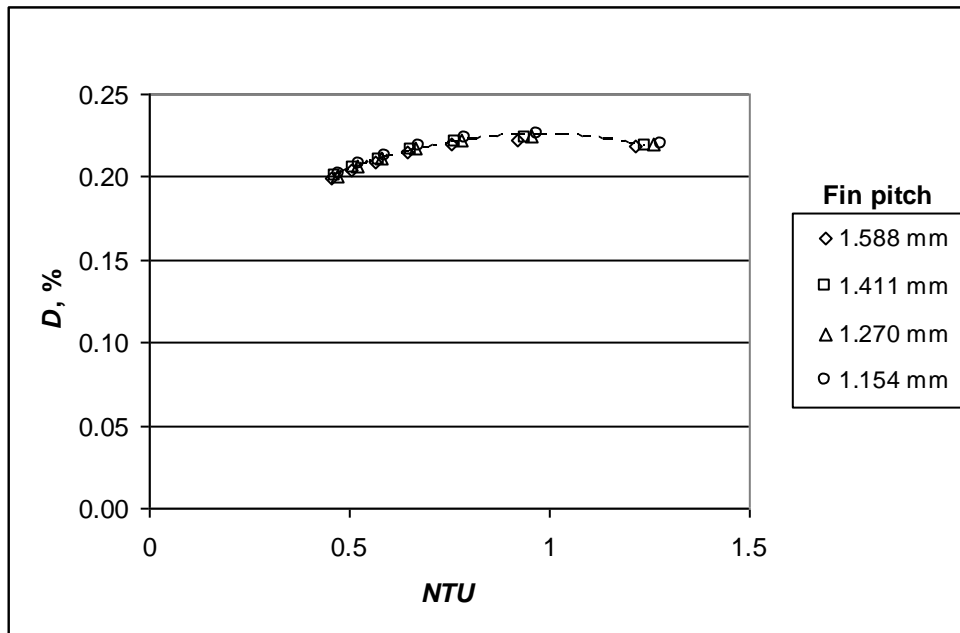
Fig. 5.6: Effect of tube diameter on D : (a) $s' = 0.10$, $\gamma' = 1.08$ (b) $s' = 0.63$, $\gamma' = 1.08$ [$N_r = 1$, $F_p = 1.411\text{mm}$, $X_t = 22.0\text{mm}$, $X_t = 25.4\text{mm}$, wavy fins]

5.4.3 Effect of fin pitch, F_p

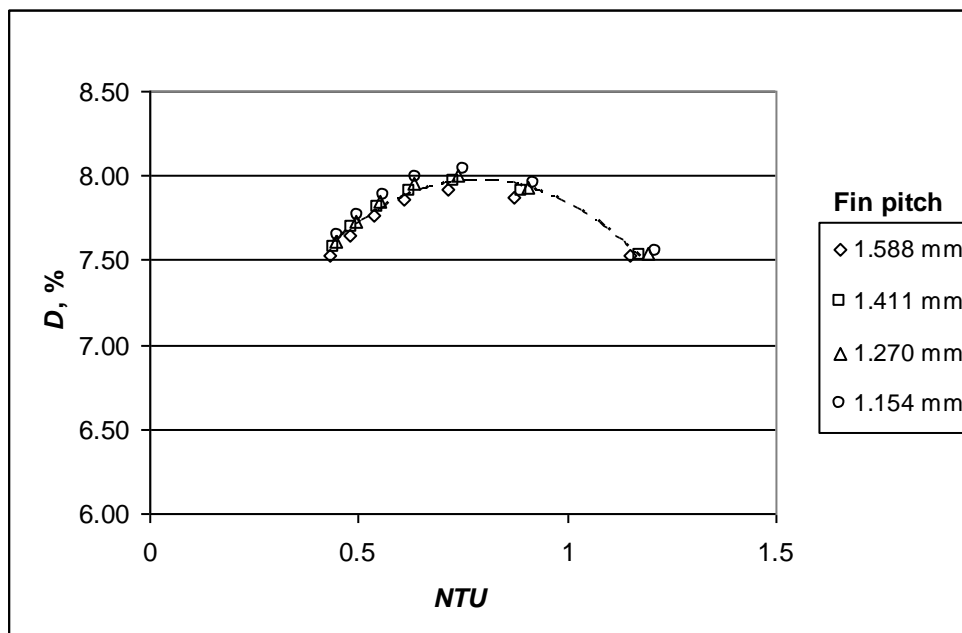
The effect of the exchanger fin pitch is shown in Fig. 5.7(a) and 5.7(b) for 2 different sets of moments. The fin pitch for the single row coil was varied from 1.154mm to 1.588mm while the other parameters remain the same.

The results clearly show that the fin pitch has a weak effect on the degradation factor, D . At low standard deviation, the effect is insignificant. Nevertheless, the trend shows that lower fin pitches exhibit slightly higher degradation effects.

These observations are in agreement with the findings reported by Wang et al. [95] which state that the j -factor (and hence h_o) for typical plain and wavy fin-tube heat exchangers is nearly independent of fin pitches. Wang has also drawn similar conclusions for louvered fins [93]. An explanation for this, as given in [96], is that the closer fin passages tend to stabilize the vortices formed behind the tubes. Larger fin pitches will cause larger vortex sizes which lead to a decrease in heat transfer performance. Hence, this reduces the heat transfer coefficient which de-sensitizes the exchanger to maldistribution effects.



(a)



(b)

**Fig. 5.7: Effect of fin pitch on D : (a) $s' = 0.10$, $\gamma' = 1.08$ (b) $s' = 0.63$, $\gamma' = 1.08$
 $[N_r = 1, d = 9.52\text{mm}, X_t = 22.0\text{mm}, X_t = 25.4\text{mm}, \text{wavy fins}]$**

5.4.4 Effect of tube pitch

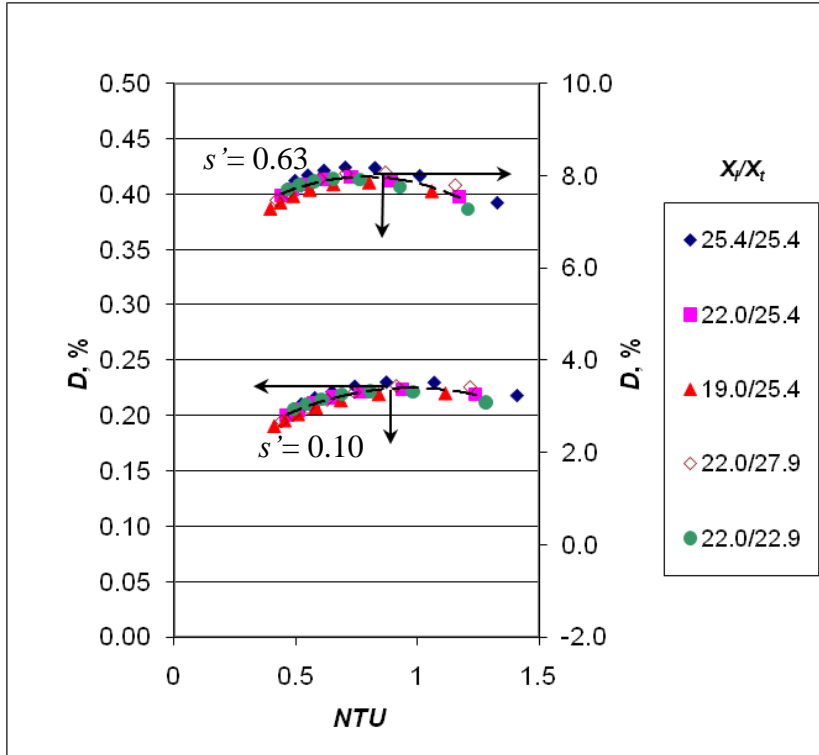
To investigate the effect of tube pitch, both the longitudinal (X_l) and transverse (X_t) tube pitches are changed together in pairs to reflect typical patterns used in the industry. For this study, 5 pairs of values are used, i.e.

1. $X_l/X_t = 25.4\text{mm}/25.4\text{mm}$
2. $X_l/X_t = 22.0\text{mm}/25.4\text{mm}$
3. $X_l/X_t = 19.0\text{mm}/25.4\text{mm}$
4. $X_l/X_t = 22.0\text{mm}/27.9\text{mm}$
5. $X_l/X_t = 22.0\text{mm}/22.9\text{mm}$

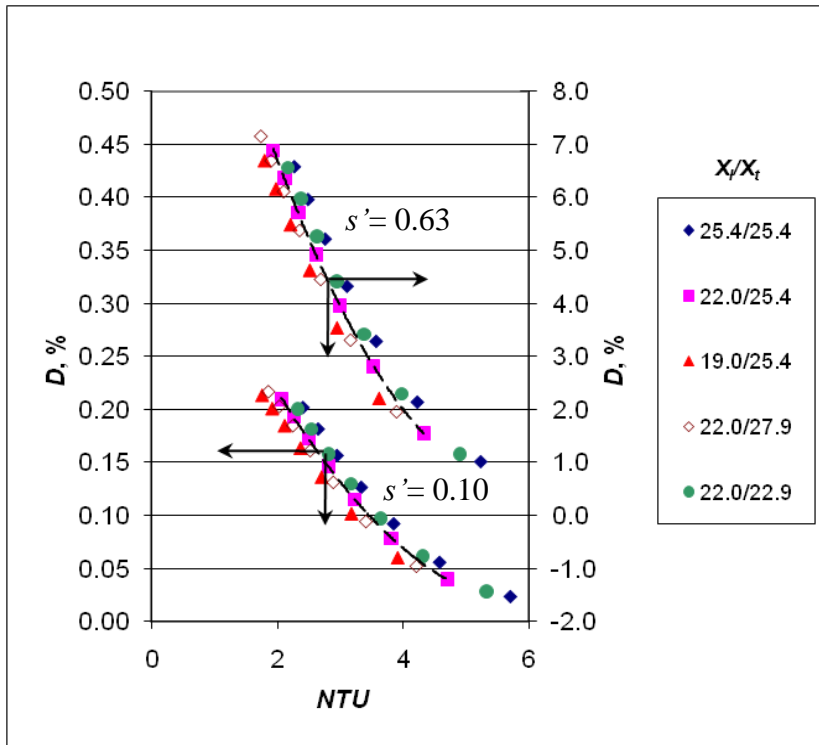
The results of the calculation are shown in Fig. 5.8(a) and 5.8(b) for 1 tube row and 4 tube rows, respectively.

The plots for the various combinations of tube pitch show that the tube pitch has a weak influence on the degradation factor, D . With the 1-row configuration, the data points fall within $\pm 3\%$ while for the 4-row coil, the scatter is approximately $\pm 6\%$. However, it can be generally seen that larger longitudinal tube pitches will suffer higher degradation penalties. This could be due to the longer flow path downstream between each successive tube rows which allows a better mixing of the air stream. The resulting higher heat transfer coefficient thus causes the exchanger to be more susceptible to maldistribution effects.

On the other hand, a narrower transverse tube pitch is observed to have higher degradation factors with the multi-row exchanger. A possible explanation for this is that as the transverse tube pitch decreases, the maximum air velocity through the minimum cross-section area of the fin passage, V_{max} , becomes higher which therefore increases the heat transfer coefficient. As is to be expected, this phenomenon is not significant with the single row exchanger.



(a)



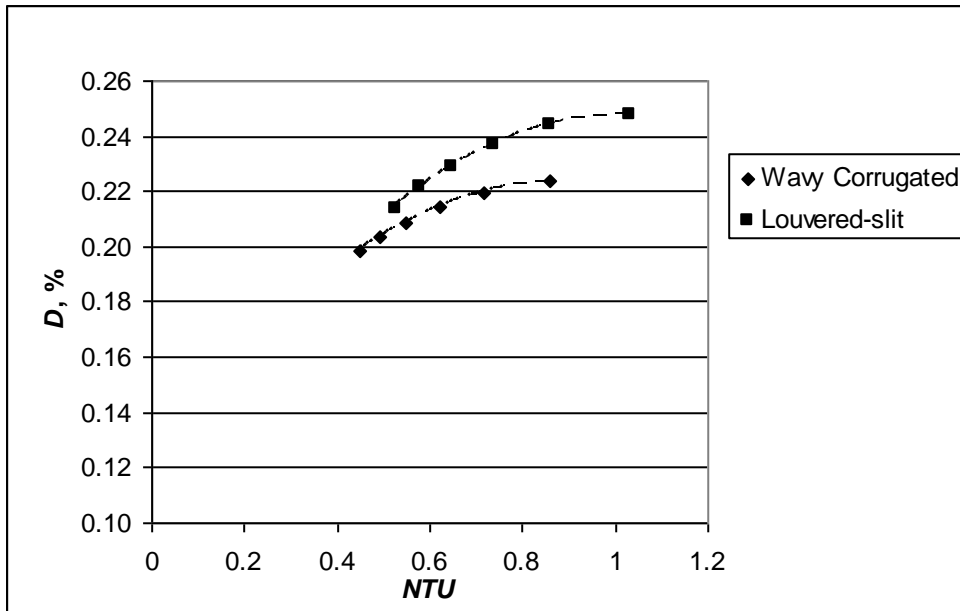
(b)

**Fig. 5.8: Effect of tube pitch on D : (a) $N_r = 1$, $\gamma' = 1.08$ (b) $N_r = 4$, $\gamma' = 1.08$
[$d = 9.52\text{mm}$, wavy fins]**

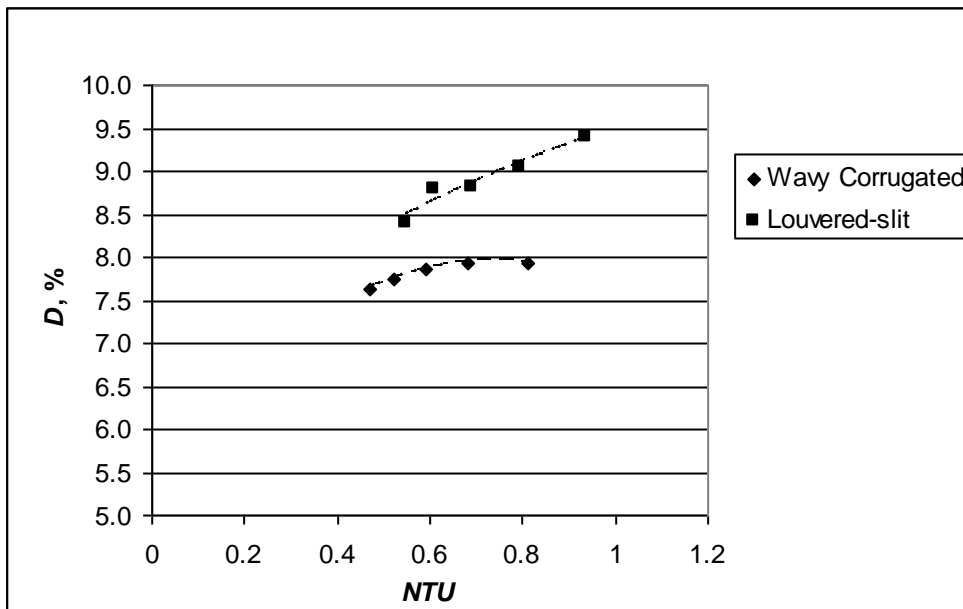
5.4.5. Effect of fin pattern

The results of the comparison between the corrugated and louvered fins for a single row coil configuration are given in Fig. 5.9(a) and 5.9(b). The simulation was done with all other geometrical parameters remaining the same.

It is well-known that the heat transfer coefficient of louvered fins is higher than that of wavy fins. Therefore, it is not surprising that the D factor for the louvered fins is significantly higher than that of wavy fins. It is expected that other fin patterns, e.g. slots, cuts and dimples, will also have significant effect on the magnitude of degradation as compared to wavy fins.



(a)



(b)

Fig. 5.9: Effect of fin pattern on D : (a) $s' = 0.10$, $\gamma' = 1.08$ (b) $s' = 0.63$, $\gamma' = 1.08$

[$d = 9.52\text{mm}$, $N_r = 1$, $F_p = 1.411\text{mm}$, $X_t = 22.0\text{mm}$, $X_t = 25.4\text{mm}$]

5.5 Correlation development

The relationship between the degradation factor, D , and the maldistribution statistical moments has been identified in the previous chapter. The influence of the exchanger NTU and the ratio of external to internal heat transfer coefficients, R , have also been established. Since only the number of tube rows has a significant effect on D , it was taken into consideration to develop a set of correlation equations to predict the thermal performance degradation factor due to flow maldistribution.

Referring back to Fig. 4.10, it is observed that D varies linearly with skew when standard deviation is less than 0.40, whereas it varies as the square of skew for standard deviation between 0.40 and 0.70. Therefore, two separate correlation equations are proposed for the two ranges to reflect the differences in D vs. skew dependence:

1) For $s' \leq 0.40$

$$D = F_1 \times [(a_1 s'^3 + b_1 s'^2 + c_1 s')(d_1 \gamma' + e_1)(f_1 N^2 + g_1 N + h_1)(i_1 R^2 + j_1 R + k_1) + s'^3 (l_1 \gamma' + m_1 N^2 + n_1 R^2) + s'^2 (o_1 \gamma' + p_1 N^2 + q_1 R^2)] \quad (5.11)$$

where

$$F_1 = \alpha N_r^\beta \quad (5.12)$$

2) For $0.40 < s' < 0.70$

$$D = F_2 \times [(a_2 s'^3 + b_2 s'^2 + c_2 s')(d_2 \gamma'^2 + e_2 \gamma' + f_2)(g_2 N^2 + h_2 N + i_2)(j_2 R^2 + k_2 R + l_2) + s'^3 (m_2 \gamma'^2 + n_2 N^2 + o_2 R^2 + p_2 \gamma'^2 N^2 + q_2 \gamma'^2 R^2 + r_2 N_r^2 R^2) + s'^2 (t_2 \gamma'^2 + u_2 N^2 + v_2 R^2 + w_2 N_r^2)] \quad (5.13)$$

where

$$F_2 = \omega N_r^\psi N^\theta R^\xi \quad (5.14)$$

In the two correlations above, a_1, \dots, q_1 and a_2, \dots, w_2 and $\alpha, \beta, \dots, \xi$ are constants; and for brevity, $N = NTU$.

Even though D was shown to vary either as the square or cube of NTU in Chapter 4, a quadratic relationship was chosen in the two correlations above in view of the slight difference in the D - NTU curve fit with NTU raised to the power of two. A regression analysis with a second-order term will entail fewer constants than with a third-order term which simplifies the correlation.

The constants were solved by means of non-linear regression analysis. A dataset of 4,200 calculation results were made available for the regression. By using the Datafit software [97], the solutions for the constants, rounded to 4 significant figures, are given in Table 5.2. The coefficients of multiple determination, R^2 , for both fits of data are given as 0.99 and 0.95, respectively.

The parity plot comparing the calculated and predicted values of D is given in Fig. 5.10. The plot shows reasonable agreement between these two within $\pm 15\%$. The results of this regression are valid within the limits of parameters indicated in Section 5.3.1. The correlations are also only valid for wavy corrugated fins. Since the magnitude of degradation is significantly affected by the fin pattern, a new set of correlations must be developed with the same methodology for each type of fin pattern.

Table 5.2: Regression constants for equations (5.11) and (5.13)

a_1	0.1761	a_2	-1.574
b_1	4.172	b_2	2.721
c_1	-0.02860	c_2	-0.547
d_1	-0.6221	d_2	-0.3175
e_1	1.756	e_2	-0.6981
f_1	0.1380	f_2	2.364
g_1	-1.148	g_2	0.1532
h_1	3.660	h_2	-3.313
i_1	-252.5	i_2	8.179
j_1	4.877	j_2	-198.7
k_1	1.136	k_2	0.8141
l_1	-3.164	l_2	1.827
m_1	-0.2161	m_2	7.298
n_1	-564.2	n_2	-0.4669
o_1	5.261	o_2	-1618
p_1	-0.3446	p_2	-0.5642
q_1	4142	q_2	-724.0
α	0.008608	r_2	31.41
β	0.2465	t_2	-1.302
		u_2	1.023
		v_2	3941
		w_2	-0.01205
		ω	0.01557
		Ψ	-0.01263
		θ	0.1226
		ξ	0.04200

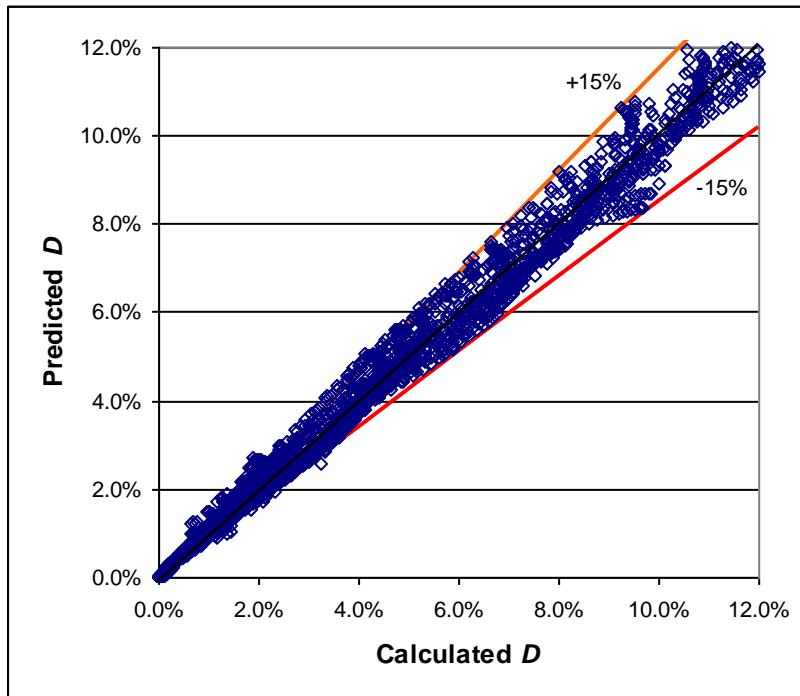


Fig. 5.10: Parity plot for correlation equation

5.6 Application of the correlation

The simple form of the correlation equations allows a quick calculation of the exchanger thermal performance degradation once the flow maldistribution profile is known. This makes the model suitable to use with Computational Fluid Dynamics (CFD) simulations which enable predictions of the air flow profile on the coil due to its layout design in a system. The positioning of the coil with other components in the system could be varied to give a more favorable distribution of moments, e.g. with low standard deviation and high skew. With each design modification, the moments are extracted from the simulation and entered into the correlation to give estimates of the thermal performance penalty. This is then repeated until the best possible design with maximum heat duty is obtained.

However, for this purpose, calculation of the exchanger heat duty under uniform flow distribution is required. This can be done by using readily available software packages, for example, NIST Evap-Cond [98] and CoilDesigner [99], which also discretize the coil face area into smaller elements for analysis.

In as much as these software packages and other distributed parameter models (e.g. Jia et al. [100]) are capable of predicting the exchanger heat duty under air flow maldistribution, the calculation procedure is more cumbersome. On the other hand, the proposed correlations in this study offer a faster and simpler method to analyze the maldistribution problem. Nevertheless, it is acknowledged that the present form of the correlations does not take into consideration the effects of tube-side maldistribution and varying tube wall temperature. These could be the subject of subsequent research work.

5.7 Summary

A parametric study has been performed to analyze the influence of the fin-tube heat exchanger geometry on the thermal performance degradation factor, D , due to air flow maldistribution. All the common exchanger coil geometrical parameters, except for the number of tube rows, have either a weak or an insignificant effect on the degradation factor. As the number of tube rows increases, the heat exchanger

experiences larger deterioration in thermal performance. It is also observed that the fin surface pattern has a significant effect on the magnitude of D . Patterns which give higher heat transfer augmentation tend to suffer higher degradation due to the flow maldistribution. Although the other geometrical parameters, i.e. tube diameter, fin pitch and tube pitch, have insignificant effect on the degradation factor, a similar trend is observed where higher heat transfer coefficients cause the heat exchanger to be more sensitive to the maldistribution.

With these findings, a set of correlation equations is proposed to predict the degradation factor from the maldistribution statistical moments, i.e. mean, standard deviation and skew, and where the effect of the number of tube rows is also taken into consideration. The developed correlation is able to give predictions which agree reasonably well with calculated data within $\pm 15\%$. However, the correlation is only valid with wavy corrugated fins. New correlations are required for other types of fin pattern, for example louvered and slit fins.

CHAPTER 6

EXPERIMENTAL STUDIES

6.1 Overview

This chapter reports the details of two sets of experimental studies conducted in support of this research. In the first series of experiments, the air-side heat transfer coefficients for a set of fin-tube heat exchanger coils covering a range of coil geometrical parameters were determined. The purpose of this experiment was to determine the j -factor correlation for the actual wavy fin pattern analyzed in this research. In the second experiment, the effects of non-uniform air velocity distribution on the thermal performance degradation of fin-tube coils were measured. At the same time, the statistical moments of the flow maldistribution were also obtained by measuring the velocity profile across the coil face area. The results of this second experiment were used to validate the correlation equations developed in Chapter 5.

6.2 Air-side heat transfer coefficient test

As explained in Chapter 4, the purpose of these experiments is to characterize the external heat transfer coefficient (h_o) of the actual fins used in this work. This would allow a greater degree of accuracy for h_o as compared to the predictions from published correlations. For the case of wavy fins, Table 6.1 lists the main differences in the fin geometry between that studied in this work and that used by Wang et al. for a group of 27 test coils [82]. It is these dissimilarities that cause variations in h_o between the present work and that of Wang et al. Hence, the present experiments were intended to largely eliminate these uncertainties from the analysis. The details of the present set of experiments are given in the following sub-sections.

6.2.1 Specifications of test coils

A total of 8 fin-tube heat exchangers with wavy fins were fabricated and used for the experiment. The ranges of geometrical parameters covered by these coils, which reflect typical values used in the air-conditioning industry, are given as follows:

- a) Number of tube rows, N_r : 1 to 4
- b) Fin pitch, F_p : 1.27mm to 2.12mm
- c) Tube pitch, $X_t = 25.4$ mm and row pitch, $X_l = 22.0$ mm
- d) Tube diameter, $d = 9.52$ mm, i.e. with fin collar diameter $D_c = 9.83$ mm

Each coil has a face area of 0.171m^2 with 10 tubes for each row. The tubes in each coil have been connected to give 5 identical serpentine circuits where the flow of hot water in the circuits was in a cross-counter flow direction to the air flow. An example of the tube circuits for a 4-row coil is shown in the following Fig. 6.1.

Table 6.1: Comparison of wavy fin patterns

Actual fin studied in this work	Fin pattern used by Wang et al. [82]
Row pitch = 22.0 mm	96% of test samples have row pitch = 19.05 m
Fin collar diameter = 9.83 mm	78% of test samples have collar diameter ≤ 8.62 mm
Corrugation waffle height = 1.52 mm	63% of test samples have waffle height ≤ 1.32 mm

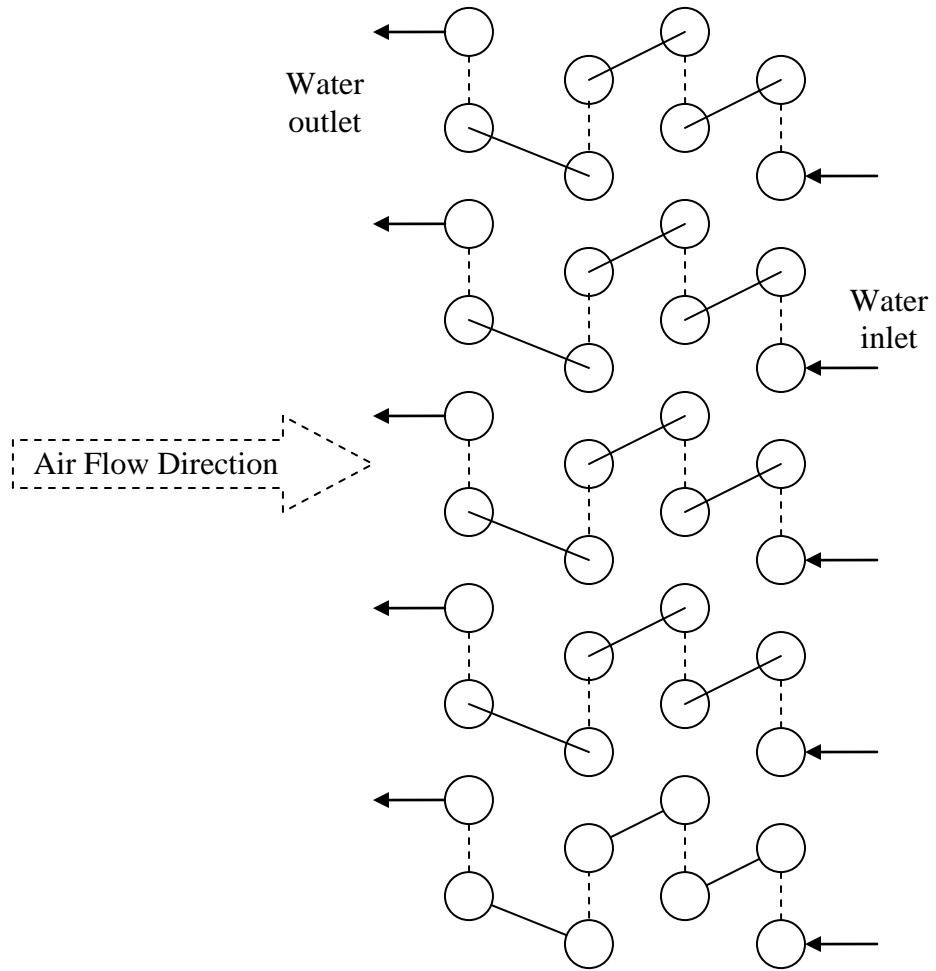


Fig. 6.1: Circuiting of water flow in the 4-row fin-tube test coil

6.2.2 Experimental set-up

The experimental study used in this work to measure the external heat transfer coefficient was based upon the methodology prescribed by Shah and Sekulic [101]. A schematic diagram of the test set-up is shown in Fig. 6.2. In general, it can be seen that the test rig has two loops, i.e. the air loop and the water loop. In the air loop, air was drawn by a centrifugal blower through the fin-tube test coil and through a nozzle chamber. The pressure drop across the nozzle was measured with a differential pressure manometer (YOKOGAWA EJX-110), from which the air flow rate was calculated. By regulating the speed of the blower with an inverter, the flow rate in the loop was controlled.

Air from the blower was then delivered to an air-conditioning equipment which has a chilled water heat exchanger and an electric heater. The air dry-bulb temperature entering the fin-tube test coil was controlled by a PID heater controller which regulates a solid state relay to vary the electric heater output. At the same time, the chilled water flow rate in the heat exchanger was also regulated by adjusting the opening of a control valve. Both the dry-bulb (DB) and wet-bulb (WB) temperatures of the entering and leaving air of the test coil were measured by using Pt-100 Resistance Temperature Detector (RTD) sensors. In accordance with ASHRAE standard [102], this was done by extracting a sample of the air at the entering and leaving locations with an aspirating air sampler device where the RTD sensors were inserted to measure the temperatures. A sampling tree positioned across the cross-section of the test duct was also connected to the sampler unit to obtain the cross-section average temperature at each location. Fig. 6.3 illustrates this sampling device.

In the water loop, a pump was used to circulate hot water in the tube circuit. A magnetic flow meter (YOKOGAWA AXF-015) was used to measure the water flow rate. Another frequency inverter was used to regulate the speed of the pump in order to vary the flow rate. The water itself was heated up with an electric heater. The entering water temperature was controlled with a PID controller, via a solid state relay, to the heater in a water tank. Both the inlet and outlet water temperatures of the test coil were also measured with RTD sensors.

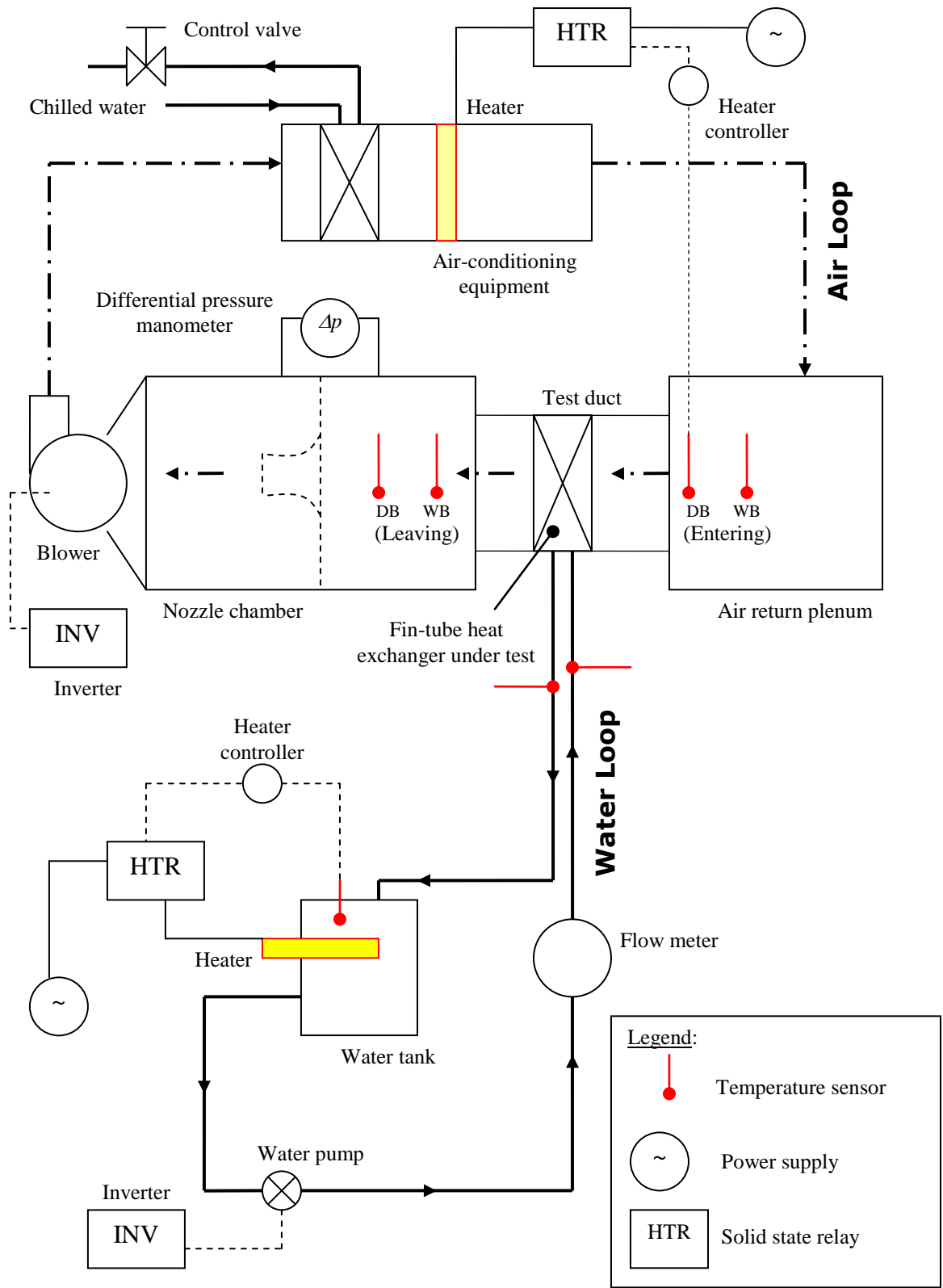


Fig. 6.2: Schematic diagram of set-up for heat transfer coefficient test

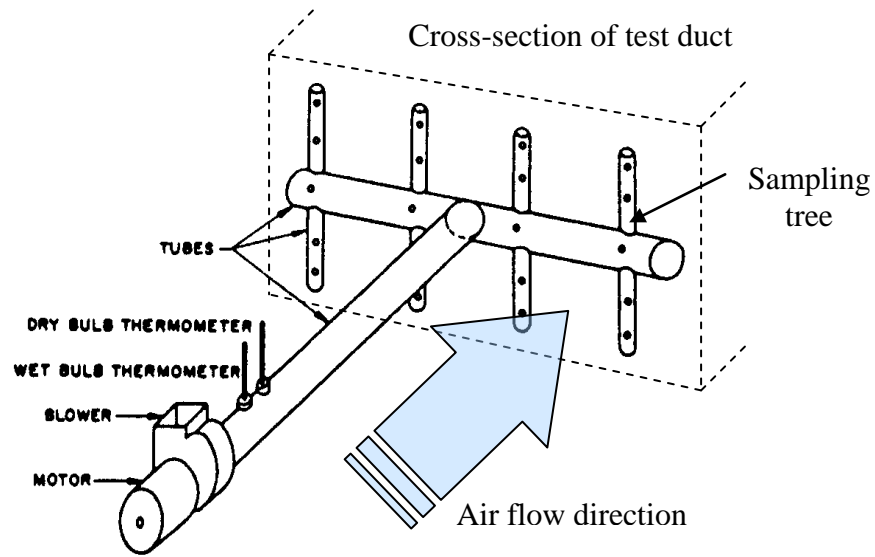


Fig. 6.3: Example of aspirating sampling device [102]

To prevent heat gain or heat loss, all the air duct and water pipes in the test rig were insulated. With careful experimentation, the air-side heating capacity of the test coil agreed with the water-side within $\pm 5\%$, as prescribed by [103].

All the data from the instruments were acquired with a YOKOGAWA MX-100 recorder. A customized LabView programme was used to communicate and transfer data from the recorder to a computer, which were then displayed on the monitor screen. The temperature and air flow rate readings were monitored and controlled for stabilization before readings were taken. The criteria for deciding this steady state condition include:

1. A continuous operation of at least 30 minutes
2. Air and water temperatures to be within $\pm 0.1^\circ\text{C}$ of set-point
3. Water flow rate to be within $\pm 0.01 \text{ m}^3\text{hr}^{-1}$ of set-point
4. Air flow rate to be within $\pm 0.0014 \text{ m}^3\text{hr}^{-1}$ ($\pm 3 \text{ ft}^3\text{min}^{-1}$) of set-point
5. Difference between air-side and water-side heating capacity to be lower than $\pm 5\%$

Upon stabilization, an averaging process was initiated where the acquired data were downloaded and saved onto a Microsoft EXCEL template spreadsheet at 5 seconds interval for duration of 5 minutes, i.e. a total of 60 data points.

The photographs in Fig. 6.4 to 6.7 show the actual test rig used in the experimentation.

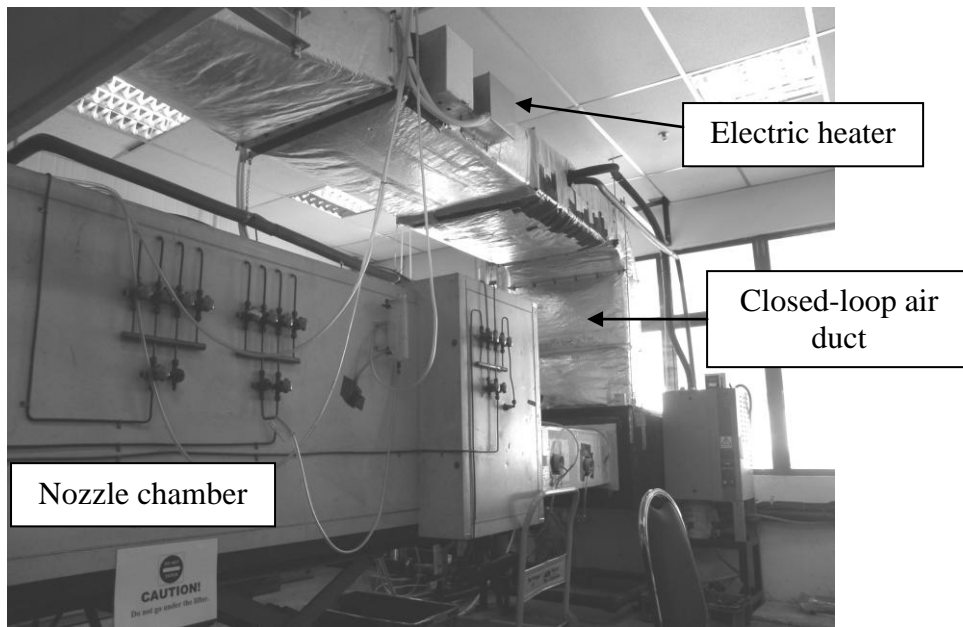


Fig. 6.4: Overall view of air loop in test rig

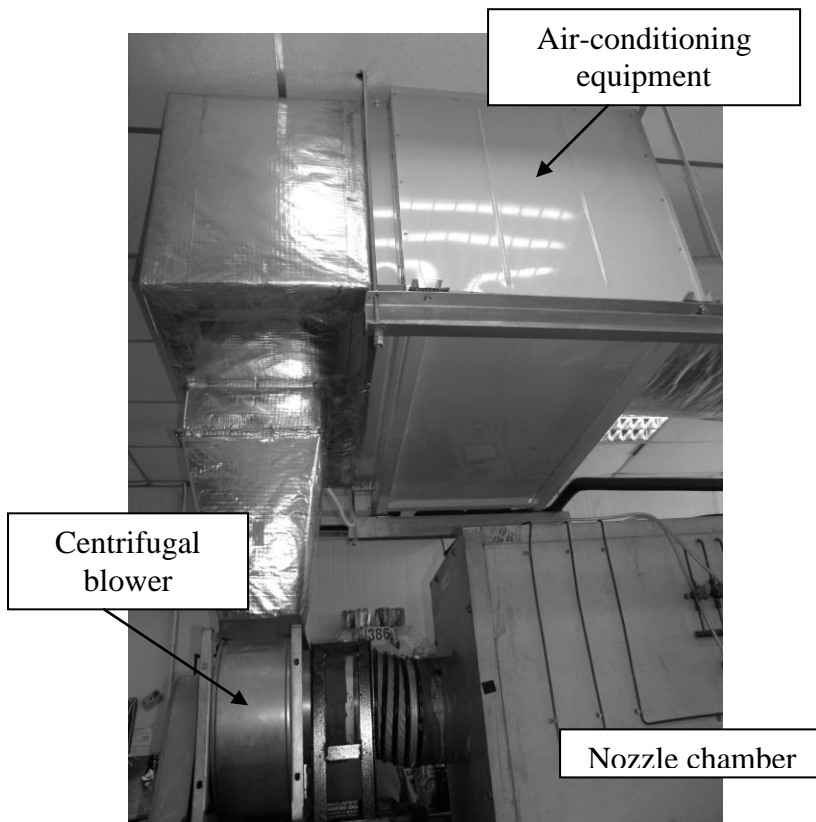


Fig. 6.5: Centrifugal blower and air-conditioning equipment

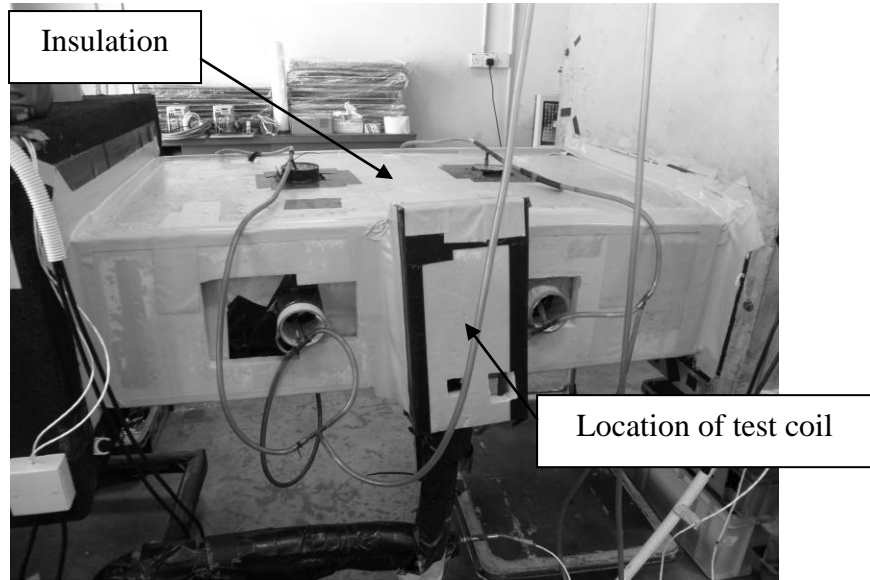


Fig. 6.6: Test duct with polyurethane insulation

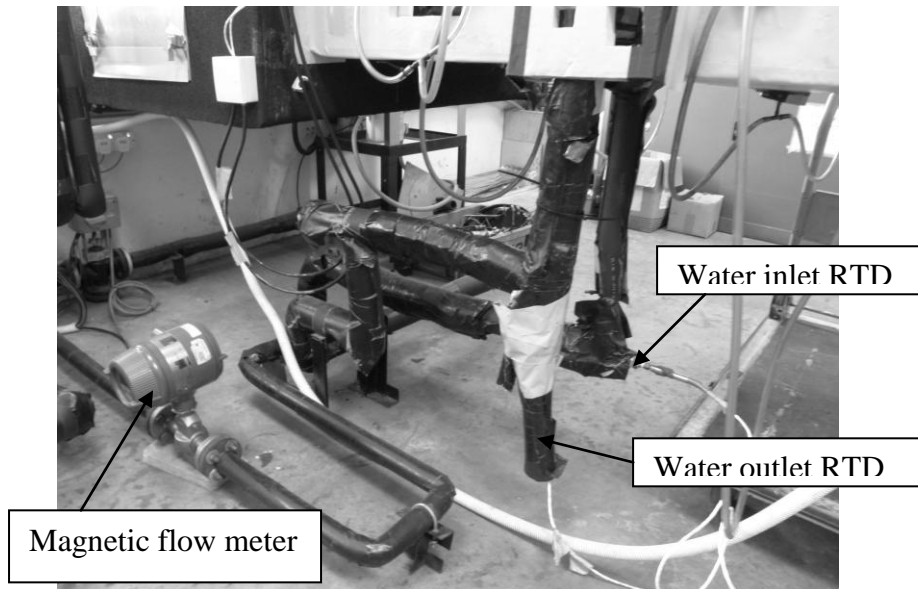


Fig. 6.7: Water inlet and outlet to test coil

6.2.3 Test conditions

Each fin-tube coil was tested at the following conditions:

- 1) Inlet air temperature = 28°C
- 2) Inlet water temperature = 50°C
- 3) Air flow rate: 0.189 – 0.425 m³s⁻¹ (400 - 900 ft³min⁻¹)
- 4) Flow rate of water = 2600 kg hr⁻¹

The water flow rate used was high in order to maintain a low temperature differential between the inlet and outlet of the coil (i.e. < 3°C). Fig. 6.8 illustrates an example of the trend over time for the temperatures of the two fluids at inlet and water flow rate.

6.2.4 Data reduction

The air volume flow rate through a single nozzle, \dot{v} , was calculated from the pressure drop across the nozzle, Δp_n , with the following equation:

$$\dot{v} = C_d A_n V_n = C_d A_n \sqrt{2g\Delta p_n v_n} \quad (6.1)$$

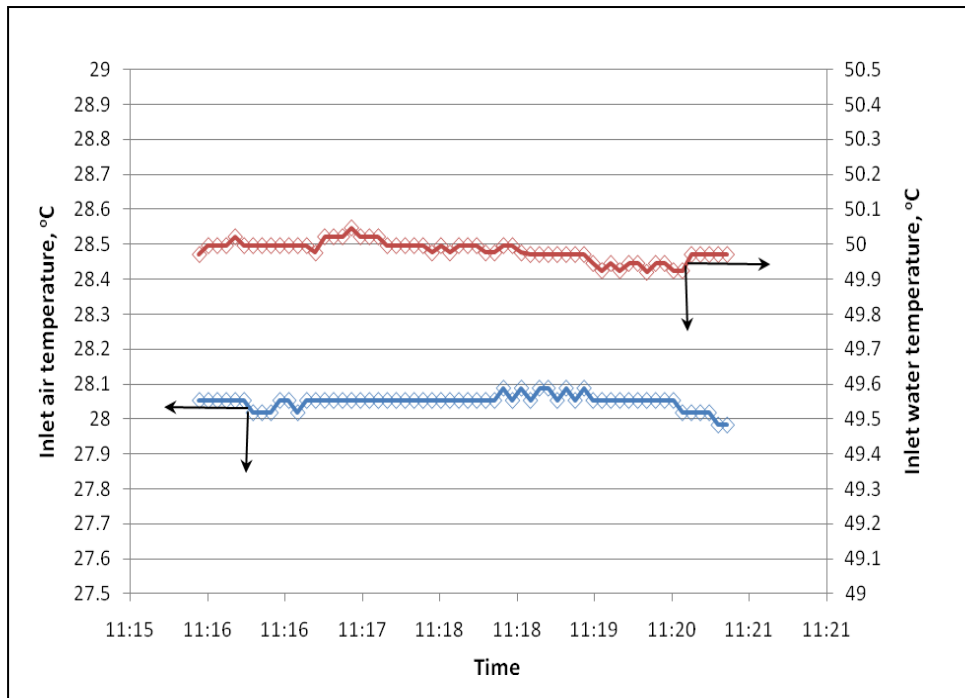
where A_n = nozzle throat area, V_n = throat velocity, g = acceleration due to gravity = 9.81 ms⁻² and v_n = air specific volume calculated from the leaving dry-bulb and wet-bulb temperatures, i.e. from equation (4.30).

The nozzle coefficient of discharge, C_d , was obtained from the following Table 6.2, where the nozzle Reynolds number, Re_n , was calculated from:

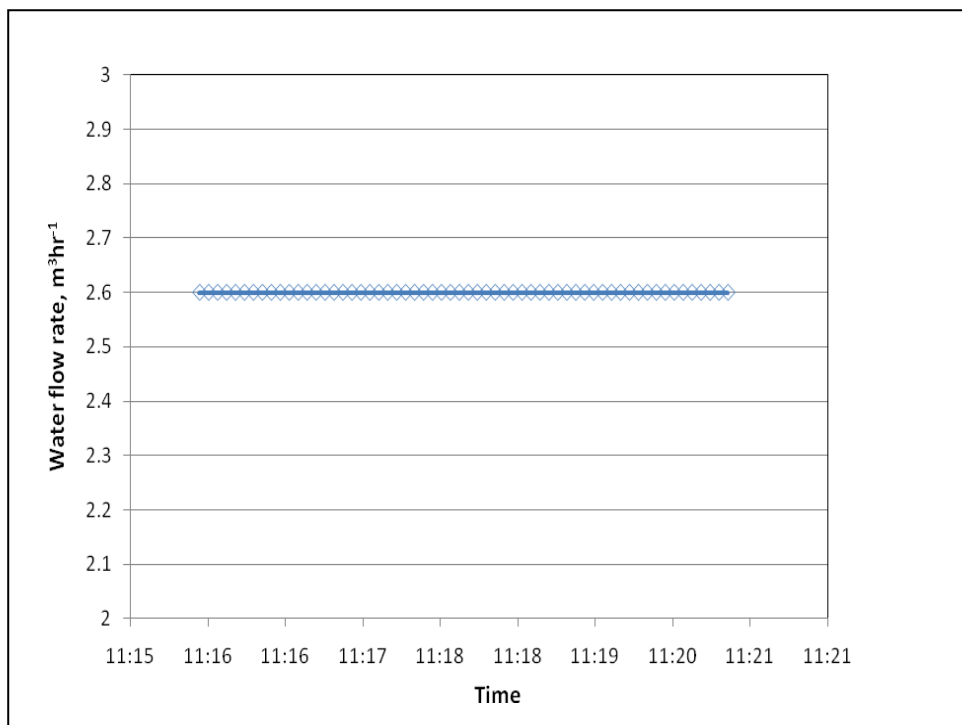
$$Re_n = \frac{\rho_a V_n D_n}{\mu_a} \quad (6.2)$$

and where D_n = nozzle throat diameter and μ_a is the air leaving dynamic viscosity. The nozzle was certified by the equipment supplier as fabricated according to the specifications detailed by ASHRAE [104], which are given in Appendix C. The standard itself has stated that no calibration was required for such nozzles [104].

For the case of multiple nozzles, equations (6.1) and (6.2) are computed for each nozzle and the flow rates summed together.



(a)



(b)

Fig. 6.8: Trend of experimental data (a) Inlet fluid temperatures (b) Water flow rate

Table 6.2: Coefficient of discharge, C_d [104]

Reynolds number, Re_n	C_d
50,000 – 100,000	0.97
100,000 – 150,000	0.98
200,000 – 500,000	0.99

From the dry-bulb and wet-bulb temperatures measured at both the entering and leaving air locations, the corresponding air enthalpy was calculated. By using the same psychrometric equations described in Section 4.2.1, the specific enthalpy, H , was calculated with the following equation [85]:

$$H = 1.006T + W(2501 + 1.86T) \quad (6.3)$$

where T = dry-bulb temperature, W = humidity ratio

With these, the coil heating capacity was then calculated as:

$$Q = \dot{v}(H_{leaving} - H_{entering}) / \nu_n \quad (6.4)$$

Alternatively, this is also expressed as:

$$Q = \dot{v}_{pa} c_{p,a} (T_{leaving} - T_{entering}) / \nu_n \quad (6.5)$$

On the water side, the heating capacity is calculated as:

$$Q_w = \dot{m}_w c_{p,w} (T_{w,in} - T_{w,out}) \quad (6.6)$$

For a valid test, the difference between Q and Q_w , i.e. the heat balance, must be lower than 5%.

This heating capacity was then used to obtain the heat exchanger overall heat transfer coefficient, U_o . Since all the four terminal temperatures of the two fluid streams were known, the LMTD approach was used for the analysis. This can be expressed as:

$$Q = U_o A_o F \Delta t_{m,cf} \quad (6.7)$$

where A_o = external heat exchanger surface area and $\Delta t_{m,cf}$ = log-mean temperature difference for a pure counter-flow configuration, which is given as:

$$\Delta t_{m,cf} = \frac{(T_{w,out} - T_{a,in}) - (T_{w,in} - T_{a,out})}{\ln \left(\frac{T_{w,out} - T_{a,in}}{T_{w,in} - T_{a,out}} \right)} \quad (6.8)$$

Since the actual fin-tube heat exchanger has a counter-cross flow configuration, a correction factor, F , is required. From the work by Bowman [105], the following equation can be used to calculate this factor for a two-pass, counter-cross flow configuration:

$$F = \frac{r(\text{crossflow})}{\Delta t_{m,cf}} \quad (6.9)$$

where

$$r(\text{crossflow}) = \frac{q}{2 \ln \left(\frac{1}{1 - \frac{q}{p} \ln \left(\frac{\sqrt{1-p} - \frac{q}{p}}{1 - \frac{q}{p}} \right)} \right)} \quad (6.10)$$

and

$$p = \frac{T_{w,in} - T_{w,out}}{T_{w,in} - T_{a,in}} \quad (6.11)$$

$$q = \frac{T_{a,out} - T_{a,in}}{T_{w,in} - T_{a,in}} \quad (6.12)$$

With U_o known, the air-side heat transfer coefficient, h_o , was then calculated from the thermal resistance equation (4.1). The same equations (4.4) to (4.15) were used to determine the fin surface efficiency and internal heat transfer coefficient. Lastly, the non-dimensional j -factor was obtained by equation (4.2).

6.2.5 Results and discussion

The results of the j -factor are plotted with respect to the Reynolds number, Re_{Dc} . Two examples are shown in Fig. 6.9 and 6.10 for 2-row and 4-row coils with specific fin pitches. The trend of the plot clearly shows that as the Reynolds number increases, the j -factor reduces. This is in keeping with the form of equation (4.2) where Re_{Dc} becomes the denominator on the left hand side of the equation.

The results also show that the experimental j -factor (j -exp) is consistently lower than the value predicted from the Wang correlation (j -Wang) [82], which is presented in Appendix A. In other words, the air-side heat transfer coefficient of the actual fins used to fabricate the test coils is lower than that for the wavy fin pattern used by Wang et al. As pointed out in the preceding section, this is due to the dissimilarities in the fin pattern geometry. This observation is further illustrated in the parity plot of Fig. 6.11 which compiles the results of the experimental j -factor for all the test coils. All the experimental data points obtained are lower than the prediction within a band of -23.6%.

To improve the agreement between the experiment results and correlation prediction, a correction factor, C , is applied to the Wang correlation, as described in equation (4.3). From the spread of the data points, a value of 0.8816 is proposed for this factor. The parity plot of the data points when this factor is used with j -Wang shows a good agreement within $\pm 9\%$, as illustrated in Fig. 6.12. Hence, the modified correlation for the wavy fins used in this work becomes:

$$j_{OYL} = 0.8816 \times j_{Wang} \quad (6.13)$$

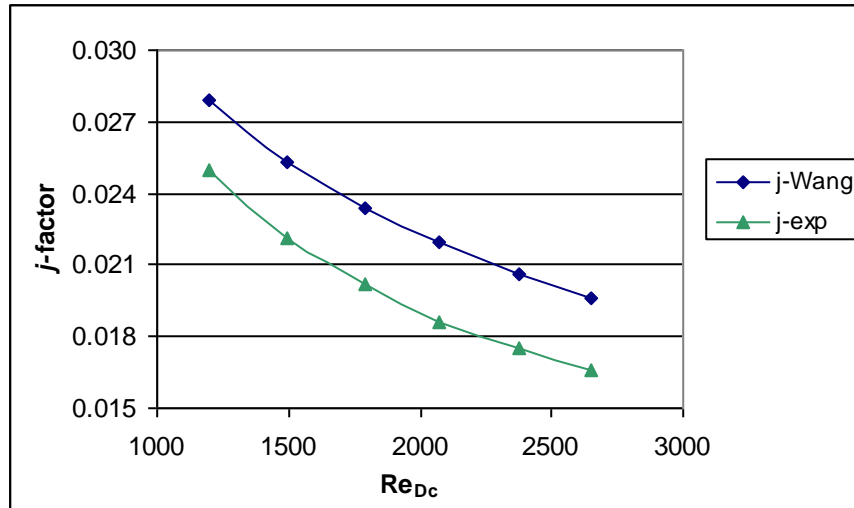


Fig. 6.9: j -factor plot for 2-row, $F_p = 1.270$ mm

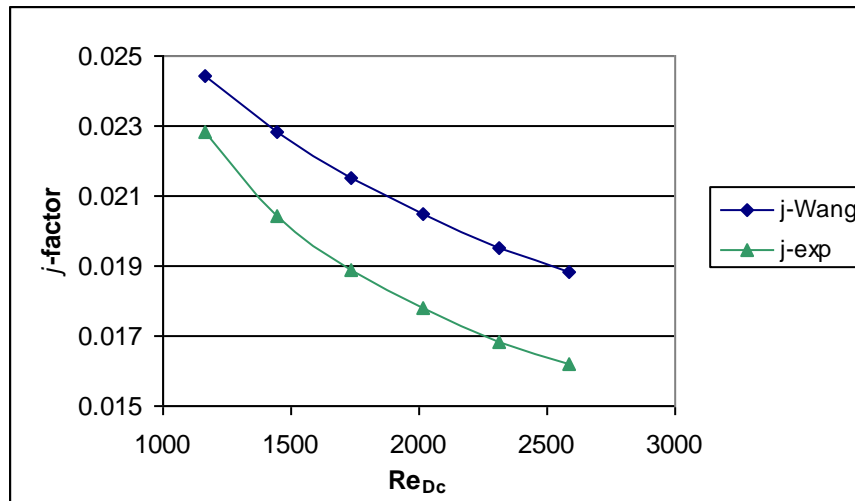


Fig. 6.10: j -factor plot for 4-row, $F_p = 1.814$ mm

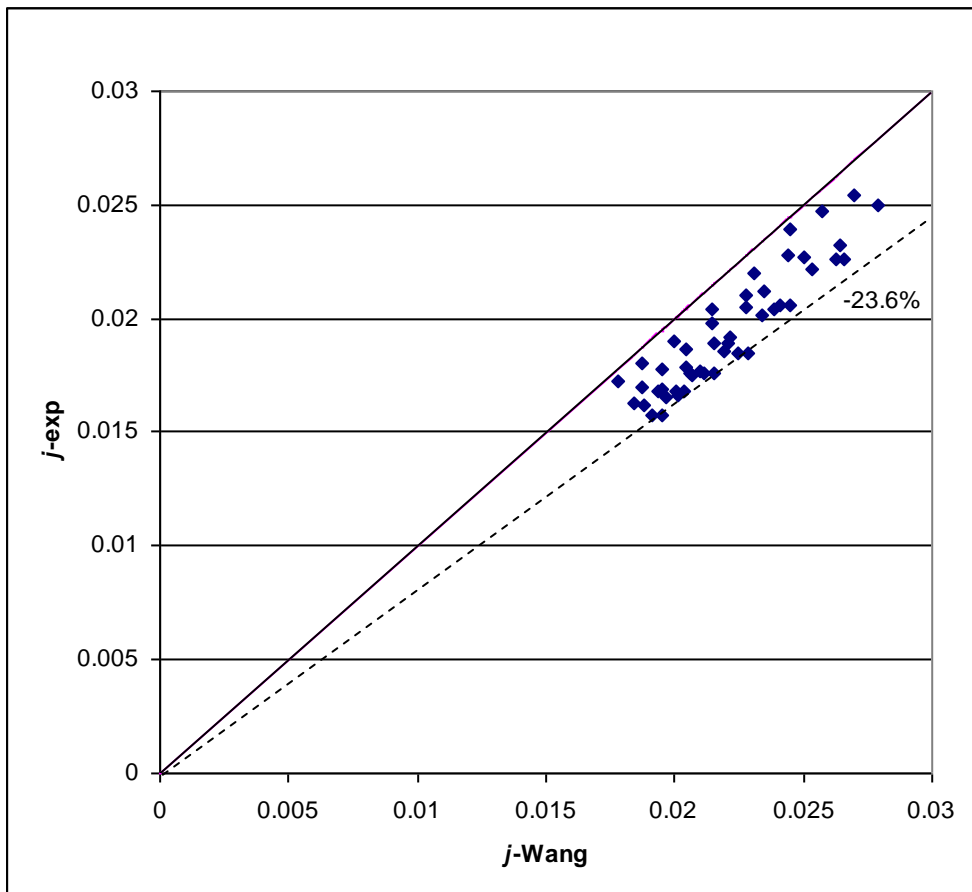


Fig. 6.11: Parity plot between experimental and predicted j -factor

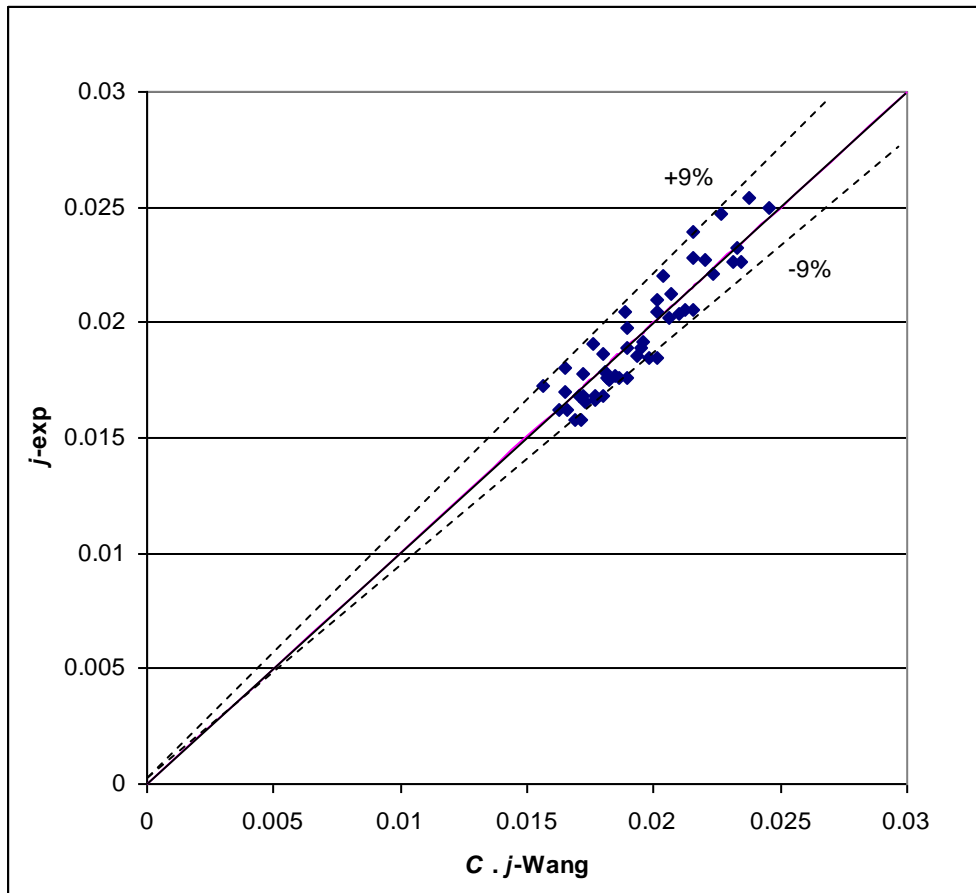


Fig. 6.12: Parity plot with correction factor, $C = 0.8816$, applied to $j\text{-Wang}$

6.3 Flow maldistribution test rig

The second test rig was designed and fabricated for the purpose of measuring the effect of flow maldistribution on the thermal performance of fin-tube heat exchangers. The data from this experiment was used to validate the theoretical basis of this research and the correlation equations developed in Chapter 5.

6.3.1 Experimental set-up

The set-up for this experiment was similar to the first test rig. The air stream flowing through the fin-tube test coil was heated up by a stream of hot water which flowed in a closed-loop through the tubes in the coil. However, the air was not re-circulated in a closed-loop, but rather was drawn from the atmosphere, through the test coil and discharged back into the atmosphere. Fig. 6.13 shows the schematic diagram of this test rig.

A description of the test rig is given as follows:

1. For consistency with the simulation results, the fin-tube test coil used in this experiment has the same cross-sectional face area, i.e. 600 mm length x 254 mm height. The equivalent hydraulic diameter for this is 377 mm.
2. Hot water was pumped through the coil with an inverter driven centrifugal pump. The water was heated with an electric immersion heater in an enclosed tank where the temperature was controlled with a PID controller linked to a solid state relay. A temperature sensor located in the pump return line provided the input to the PID controller. A magnetic water flow meter (YOKOGAWA AXF-015) was used to measure the volume flow rate of the water.
3. The water temperatures entering and leaving the coil were measured by two Pt-100 RTD sensors. The water flowed through the coil in a single downward serpentine circuit.

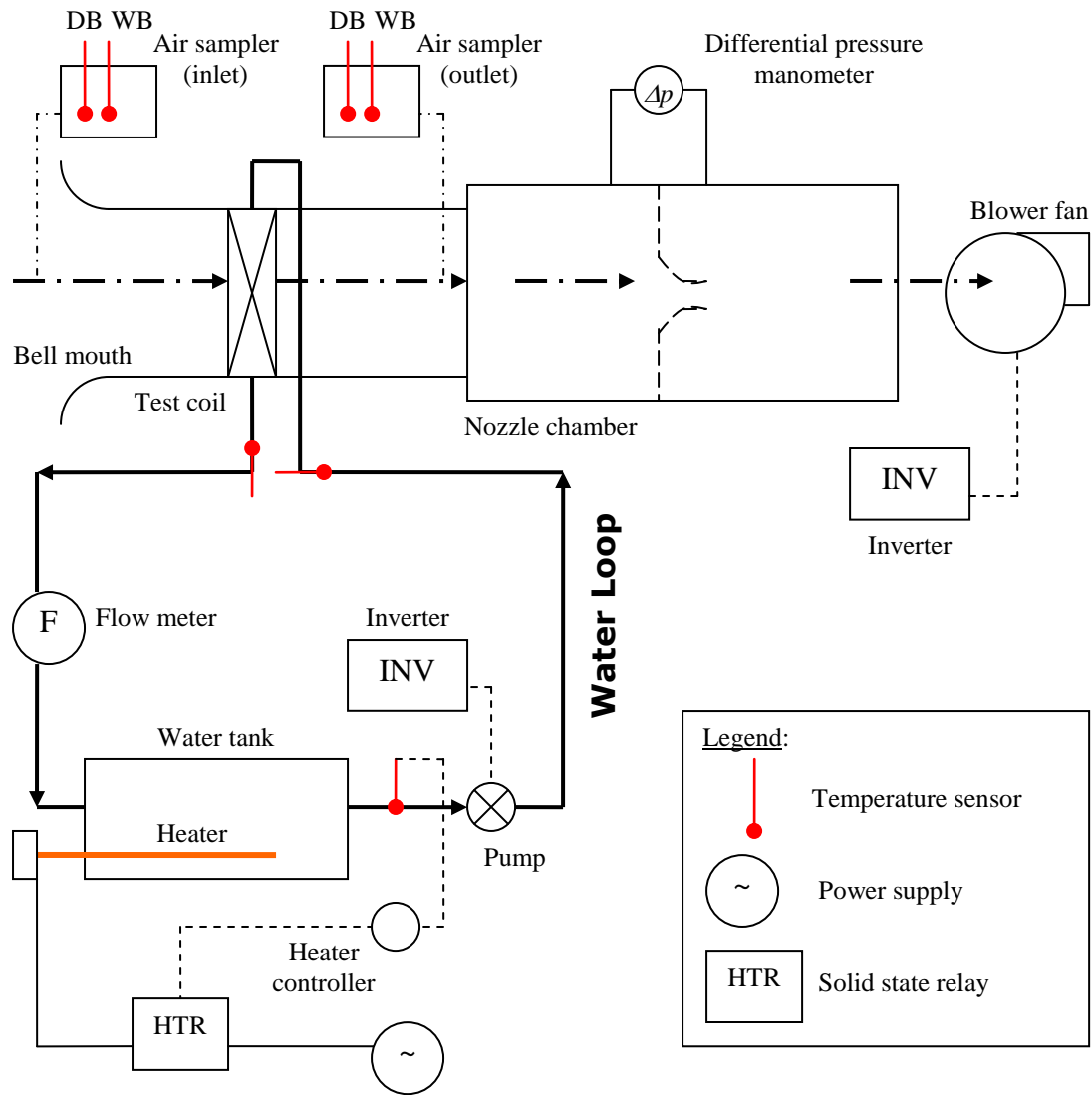


Fig. 6.13: Schematic diagram of test set-up for study of flow maldistribution

4. The fin-tube test coil was placed in a test duct which has a bell-mouth inlet section, and with the same cross-section area as the coil, to provide a convergent flow as air was drawn from the atmosphere into the duct. The bell-mouth design also prevented flow separation along the edges of the duct walls and ensured a uniform inlet air velocity on the coil without any free-stream turbulence. The length of this inlet section was 420 mm.
5. On the leaving side of the coil, an extended outlet duct, approximately 2.4 meters in length (i.e. about 6.5 times the hydraulic diameter), with the same cross section area as the test coil, was provided to prevent any downstream flow disturbances from propagating upstream to the coil. This outlet section was made from rigid 25 mm thick polyurethane (PU) sections which are taped together with cloth tape.
6. Downstream of this test duct assembly, an air nozzle chamber was connected. Air was drawn through the entire assembly by an inverter driven centrifugal blower attached at the end of the chamber. The air was discharged to the atmosphere. The static pressure drop across the nozzle in the chamber was measured with a differential pressure manometer (YOKOGAWA EJX-110), which allowed determination of the air volumetric flow rate. As stated earlier, the same equations (6.1) and (6.2) were used to calculate this flow rate.
7. The air inlet temperatures (dry-bulb and wet-bulb) were measured with an air sampler device (i.e. similar to Fig. 6.3), where a sampling tree was placed across the air inlet bell-mouth. Two Pt-100 RTD sensors located within the sampler box were used to measure these temperatures.
8. Similarly, another air sampler device was placed within the test duct just at the entrance of the nozzle chamber to measure the air leaving temperatures (dry-bulb and wet-bulb). Two other RTD sensors were used for this purpose.
9. With the air dry-bulb and wet-bulb temperatures known for both the entering and leaving air streams, the heating capacity of the heat exchanger was determined with the same calculation equations (6.3) and (6.4). The water-side capacity was also determined from equation (6.6).

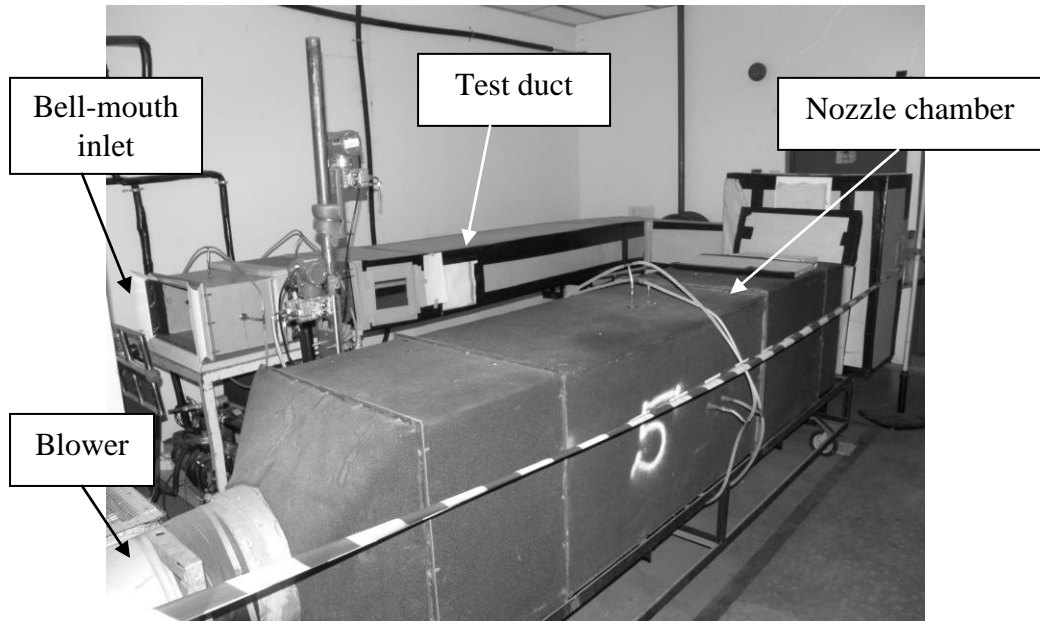


Fig. 6.14: Overview of 2nd test rig showing the U-shaped duct layout

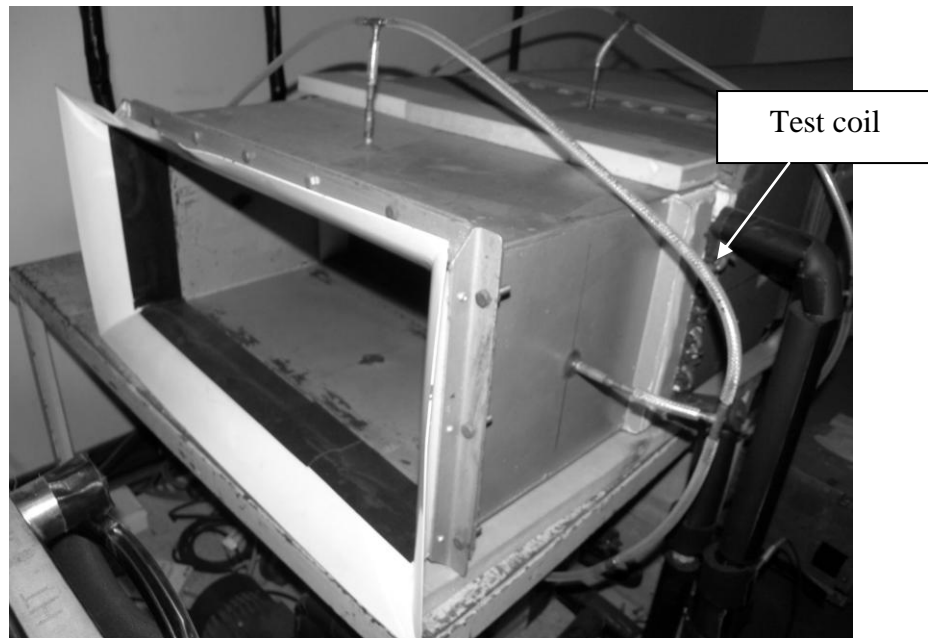


Fig. 6.15: Bell-mouth inlet

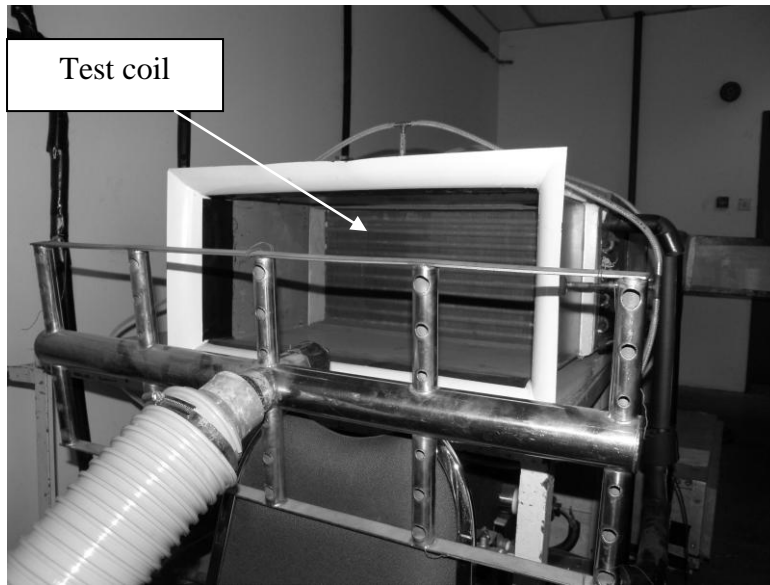


Fig. 6.16: Sampling tree positioned in front of duct inlet

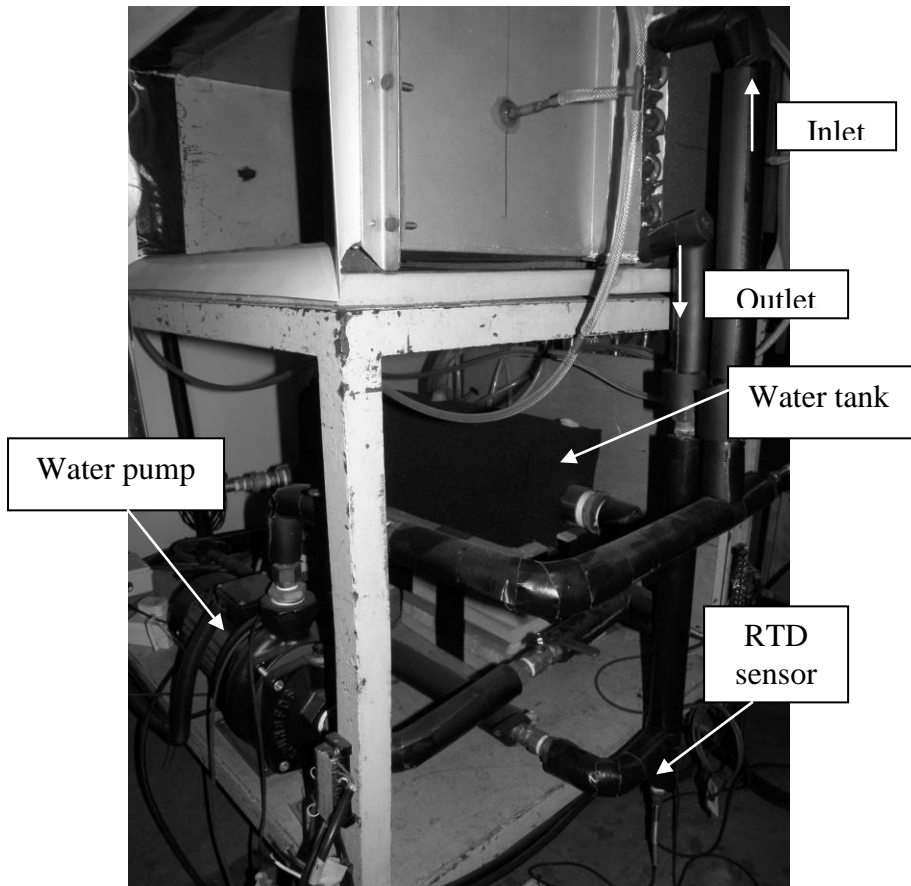


Fig. 6.17: Water loop used in the experiment

Due to the constraint of space availability for the test rig, the test duct and air nozzle chamber were arranged in a U-shaped assembly. Figures 6.14 to 6.17 show photographs of the actual test rig fabricated for this experiment.

All the readings from the instruments were acquired with the YOKOGAWA MX-100 recorder. A customized Labview software was then used to communicate with the recorder and display the data on the computer screen. Upon stabilization of test conditions, the data was sent to a Microsoft EXCEL spreadsheet where an averaging was done for each set of data captured every two seconds covering a 2 minute interval.

6.3.2 Air velocity measurement

Since the research on flow maldistribution for heat exchangers has not been extensive, the information available regarding the method of measuring the non-uniform velocity distribution is limited. In general, anemometers are used for such purposes. These will include the vane anemometer, turbine flow meter, hot-wire anemometer and the more sophisticated laser Doppler anemometer [106].

In the work done by Chwalowski et al. [36], a pitot-tube was used to traverse over the coil face to measure the non-uniform velocity distribution due to the coil slanting angle. As mentioned in Chapter 2, Timoney and Foley [37] used a traversing laser Doppler anemometer to measure the air flow maldistribution profile over a fin-tube evaporator while Aganda et al. [44] employed a single hot-wire anemometer for the same purpose. T'Joel et al. [73] used a heated sphere anemometer for their velocity measurements. Particle Image Velocimetry (PIV) has also been used by some researchers to measure flow maldistribution, for example by Wen et al. [62]. More recently, infra-red thermal imaging has also been attempted, i.e. by Caffagni et al. [107]. Inasmuch as these modern non-intrusive measurement methods are able to provide fast measurement readings, in the present case, there are no specific advantages to justify the higher cost techniques.

A simple and cost-effective approach has been selected for this experimentation where a heated thermistor anemometer was used, i.e. EXTECH Model 407123. The

thermistor itself consists of a glass-coated bead attached at the end of a telescopic probe. The anemometer works by measuring the cooling effect of air flowing across the thermistor which is supplied with constant electrical current input. The reading will therefore represent the average air velocity at the probe location, though the flow direction would not be known. However, since the theoretical analysis was done with a discretizing method where specific velocities have been assigned for each heat exchanger element, the measurement of the average velocities for each of these discrete elements would be adequate for comparison purposes.

The anemometer probe was manually traversed over the inlet coil face area within a 10 x 10 measuring grid, similar to that used during the discretization procedure. To facilitate this, 10 holes were made along the coil length, at the top of the test duct, approximately 4cm in front of the coil. The telescopic probe, which was held with a retort stand, was inserted through each hole successively. Ten equal-spaced markings were also made on the retort stand to indicate the locations to position the probe along the coil height. The readings displayed on the LCD screen of the anemometer were then transferred, via RS-232 serial interface and USB port, to a computer by using a customized data acquisition software provided by EXTECH (Model 40701).

At each location, velocity data for a period of 1 minute, with a scan interval of 2 seconds, were acquired and saved as a Microsoft EXCEL spreadsheet. The average of the data for each location was then calculated. Fig. 6.18 illustrates this measuring method.

In the experiment, the measurement location on the coil face was indicated with a row number (1 – 10) and column number (1 – 10). The element at the bottom-right corner, as viewed from the front of the inlet, has been assigned as Row 1 and Column 1. This is indicated in Fig. 6.18.

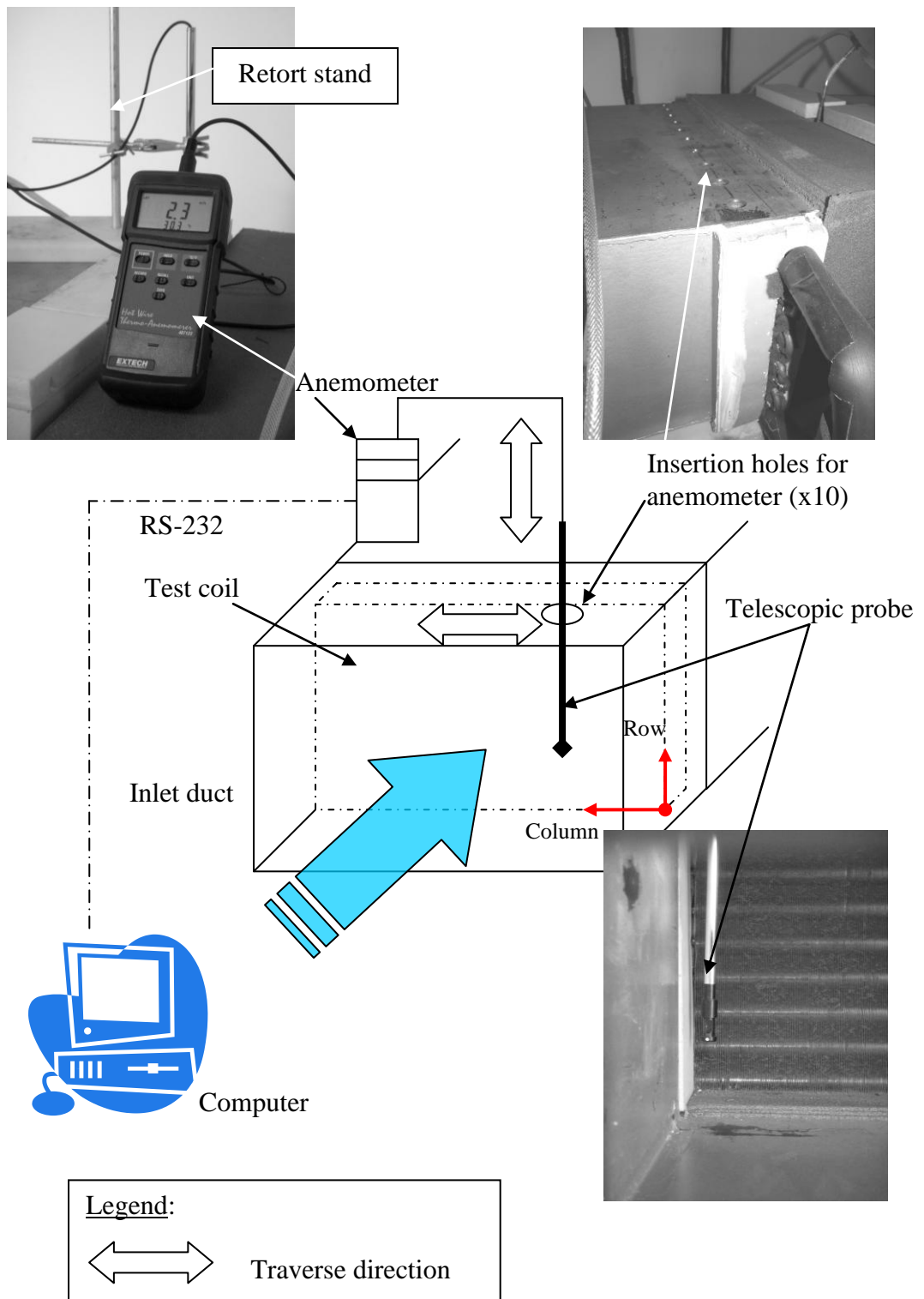


Fig. 6.18: Air velocity distribution measuring system

6.3.3 Test procedure

The fin-tube test coil used in this experiment has the following specifications:

- a) Single-row, with wavy fin pattern
- b) Fin pitch, F_p : 1.411 mm
- c) Tube pitch, $X_t = 25.4\text{mm}$ and row pitch, $X_l = 22.0\text{mm}$
- d) Tube diameter, $d = 9.52\text{mm}$
- e) Coil length = 590mm and coil height = 250mm

The first series of tests at uniform flow distribution was performed at several air mass flow rates, without any blockage on the coil, i.e.

1. 0.26 kgs^{-1} , or $0.236\text{ m}^3\text{s}^{-1}$ [$500\text{ ft}^3\text{min}^{-1}$] at 30°C
2. 0.31 kgs^{-1} , or $0.283\text{ m}^3\text{s}^{-1}$ [$600\text{ ft}^3\text{min}^{-1}$] at 30°C
3. 0.36 kgs^{-1} , or $0.324\text{ m}^3\text{s}^{-1}$ [$700\text{ ft}^3\text{min}^{-1}$] at 30°C
4. 0.42 kgs^{-1} , or $0.378\text{ m}^3\text{s}^{-1}$ [$800\text{ ft}^3\text{min}^{-1}$] at 30°C

The water flow rate was set at $1.1\text{ m}^3\text{hr}^{-1}$ with an inlet temperature of 50°C during the test.

For each air flow rate, the water-side heating capacities at several inlet air temperatures were obtained, within a range of 28.0°C to 33.0°C . The data required for the calculation was taken upon stabilization of the test condition, which was determined based on the same criteria listed in Section 6.2.2.

The heating capacity was then plotted against the inlet air temperature and a least-square regression curve was fitted through the data points. From the equation of the curve, the heating capacity at a nominal air temperature of 30.0°C was calculated.

To generate a flow maldistribution on the heat exchanger, six blockage patterns were imposed on the coil face area. This was achieved by placing sheets of paper

covering specific areas of the coil face. These patterns are shown in Fig. 6.19. Consequently, areas which were blocked will not have any air flowing through them, i.e. with zero velocity.

The velocity profile on the coil was measured with the anemometer for each of the six blockage patterns which gave the statistical moments of the flow maldistribution. The experiment was then repeated to determine the heating capacity and heat transfer performance degradation at 30.0°C for each maldistribution profile. This was done only with an air flow rate of 0.324 m³s⁻¹ [700 ft³min⁻¹].

With the first maldistribution profile (Set ①), the experiment was also repeated for the four air flow rates, covering a range of *NTU* from 0.58 to 0.85. Similarly, the thermal performance degradation factor was calculated at 30.0°C for each flow rate.

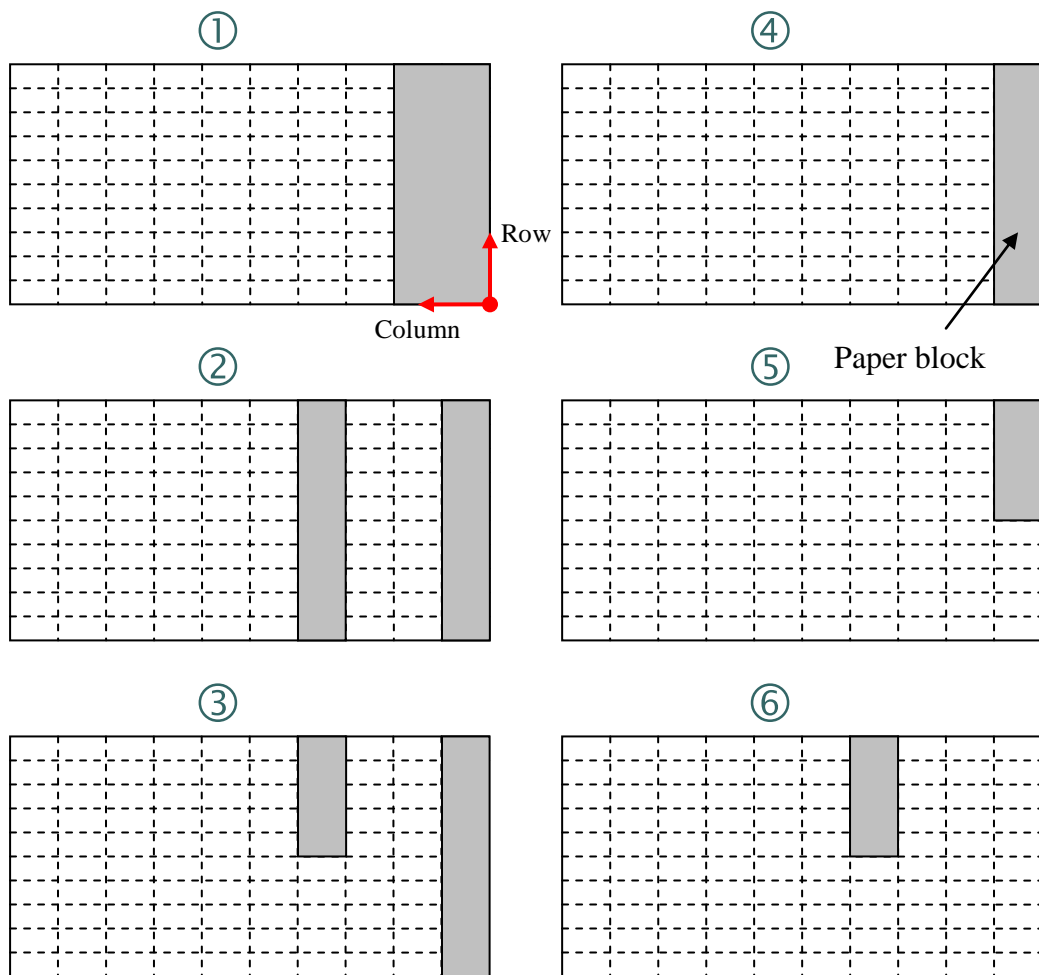


Fig. 6.19: Pattern of paper block on coil face area. Dotted lines denote the 10x10 discretization grid.

6.3.4 Experimental results and discussion

The results of the heating capacity with uniform flow distribution are shown in Fig. 6.20 for all the four air flow rates. The data points show that a linear fit could be made, covering the range of inlet air temperatures, for each set of data points. The computed heating capacities at 30.0°C are correspondingly shown in Table 6.3. It is obvious from the results that as the inlet air temperature increases, the heating capacity reduces due to the reducing temperature differential between the air and water in the tubes.

To verify the uniform distribution, a measurement of the velocity profile was made. The result of this measurement at a flow rate of $0.324 \text{ m}^3\text{s}^{-1}$ [$700 \text{ ft}^3\text{min}^{-1}$] is shown in Fig. 6.21. The actual measured inlet velocity data are shown in Table 6.4, which indicate a mean velocity of 2.44 ms^{-1} . By dividing the flow rate with the coil face area (i.e. 0.148m^2), the calculated average coil face velocity is obtained as 2.21 ms^{-1} , which is approximately 10% lower than the average anemometer reading. This small deviation is expected since the discretized velocity measurements did not take into consideration the decreasing velocities at locations nearer the wall of the test duct. Nevertheless, the data shown in Table 6.4 exhibits a reducing trend along the perimeter of the duct wall.

Normalization of the velocities in Table 6.4 reveals the following statistical moments for the distribution: mean = 1.00, standard deviation = 0.06, skew = -0.11, kurtosis = 0.52. Since the standard deviation is small, i.e. close to zero, the distribution was verified as uniform.

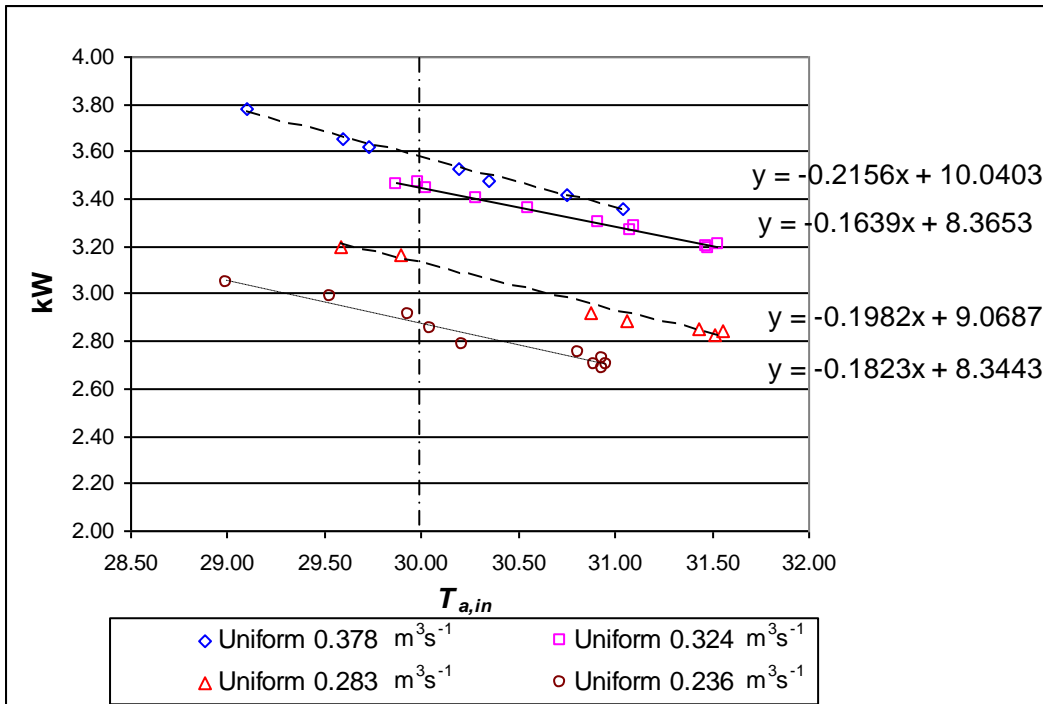


Fig. 6.20: Results of heating capacity (water side) for uniform distribution

Table 6.3: Calculated uniform distribution heating capacity at 30.0°C inlet air temperature

Air flow rate m^3s^{-1}	Heating capacity kW
0.378	3.57
0.324	3.45
0.283	3.12
0.236	2.88

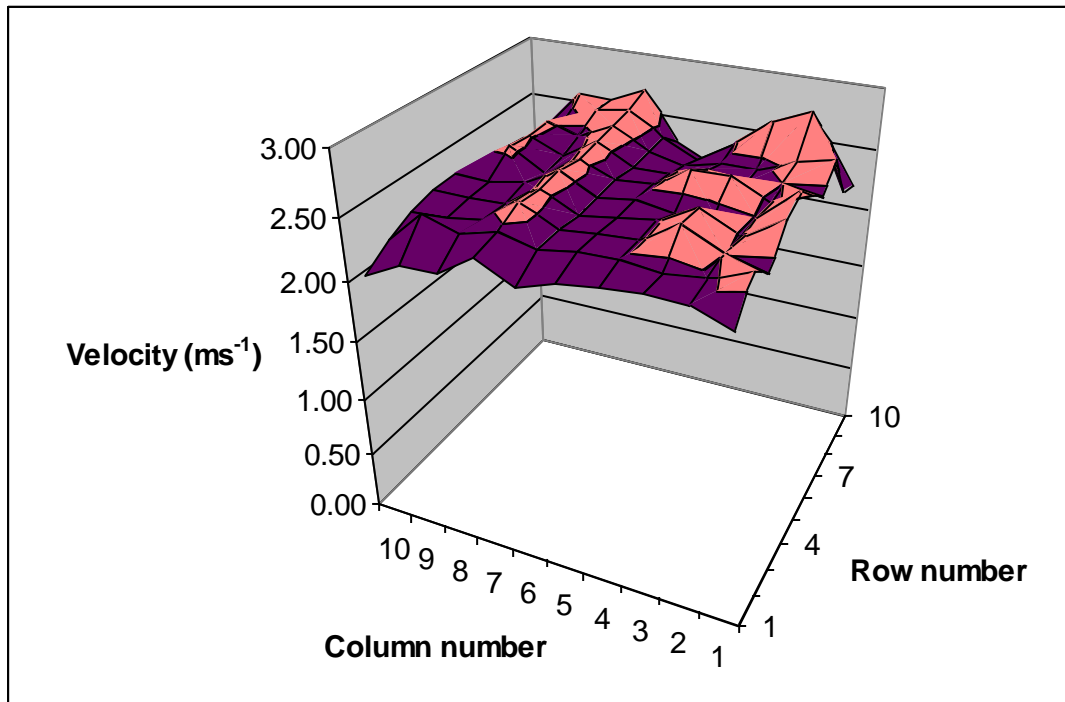


Fig. 6.21: Velocity plot of uniform distribution at $0.324 \text{ m}^3\text{s}^{-1}$ [$700 \text{ ft}^3\text{min}^{-1}$]

Table 6.4: Velocity data for uniform distribution at $0.324 \text{ m}^3\text{s}^{-1}$ [$700 \text{ ft}^3\text{min}^{-1}$]

		Column number									
		1	2	3	4	5	6	7	8	9	10
Row number	10	2.17	2.63	2.54	2.36	2.15	2.28	2.69	2.57	2.57	2.25
	9	2.24	2.83	2.72	2.48	2.29	2.44	2.62	2.58	2.43	2.09
	8	2.62	2.55	2.43	2.44	2.36	2.43	2.59	2.45	2.52	2.19
	7	2.45	2.50	2.44	2.50	2.41	2.40	2.57	2.40	2.51	2.25
	6	2.59	2.47	2.63	2.61	2.44	2.43	2.53	2.37	2.54	2.34
	5	2.74	2.49	2.44	2.40	2.45	2.40	2.57	2.41	2.36	2.37
	4	2.68	2.49	2.64	2.48	2.43	2.39	2.54	2.36	2.36	2.36
	3	2.43	2.51	2.65	2.47	2.45	2.42	2.57	2.37	2.33	2.31
	2	2.59	2.47	2.43	2.47	2.46	2.40	2.48	2.39	2.48	2.23
	1	2.33	2.43	2.45	2.42	2.38	2.27	2.42	2.24	2.23	2.09

Table 6.5: Statistical moments of measured maldistribution

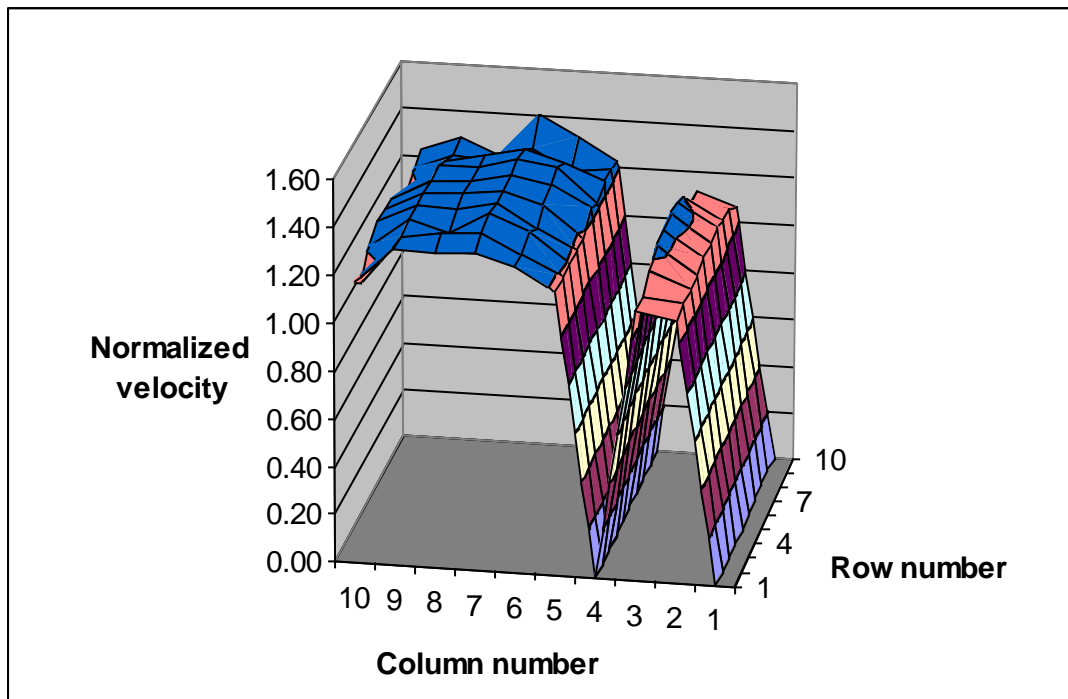
Set	Standard deviation	Skew
①	0.508	-1.452
②	0.5088	-1.437
③	0.443	-1.802
④	0.341	-2.522
⑤	0.237	-3.851
⑥	0.242	-3.588

The results of the measured normalized moments for the six maldistribution profiles generated by the blockage patterns shown in Fig. 6.19 are summarized in Table 6.5. Two examples of these maldistribution profiles are shown in Fig. 6.22 for Set ② and ③.

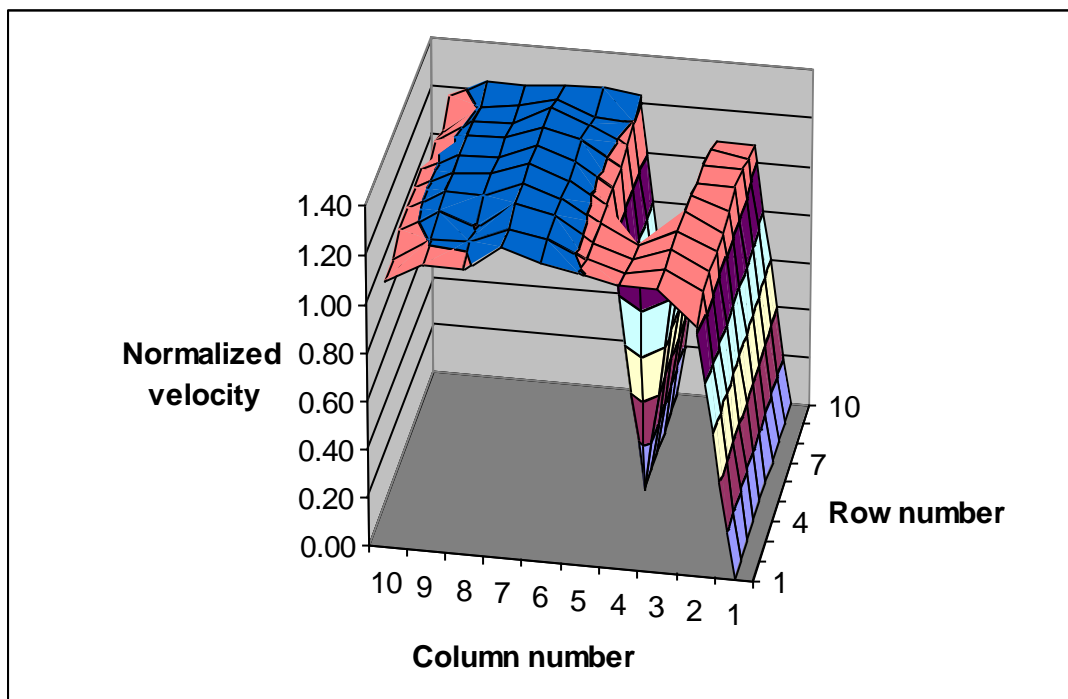
To illustrate the calculation procedure for the thermal performance degradation factor, D , the example of maldistribution Set ③ is used. The measured heating capacity with the maldistribution blockage is plotted versus the inlet air temperature, together with the corresponding uniform distribution, as shown in Fig. 6.23. It is clear from the results that the maldistribution has reduced the heating capacity of the coil. From the linear trend line equations, the heating capacities at 30.0°C for both cases have been calculated and D computed from equation (3.24).

From the measured discrete velocities on the coil face, the magnitude of D was calculated with the same discretization technique described in Chapter 4. At the same time, the heat exchanger NTU and ratio R were also calculated.

Table 6.6 summarizes the experimental results of D , NTU and R for all six maldistribution profiles. The calculated values of D are also given. Correspondingly, the predictions of D by using the correlation equations (5.11) and (5.13) are also tabulated together. From these data, D is plotted with respect to the varying standard deviation, as shown in Fig. 6.24. In the same figure, two prediction lines calculated from the developed correlations have also been plotted for similar values of NTU , skew and R as the standard deviation changes. Line A is for $NTU = 0.77$, skew = -3.5 and $R = 0.0044$, while line B is $NTU = 0.70$, skew = -1.5 and $R = 0.0040$. From these lines, the cubic trend of the experimental D with respect to the maldistribution standard deviation can be seen.



(a)



(b)

Fig. 6.22: Maldistribution velocity profile for (a) Set ② and (b) Set ③

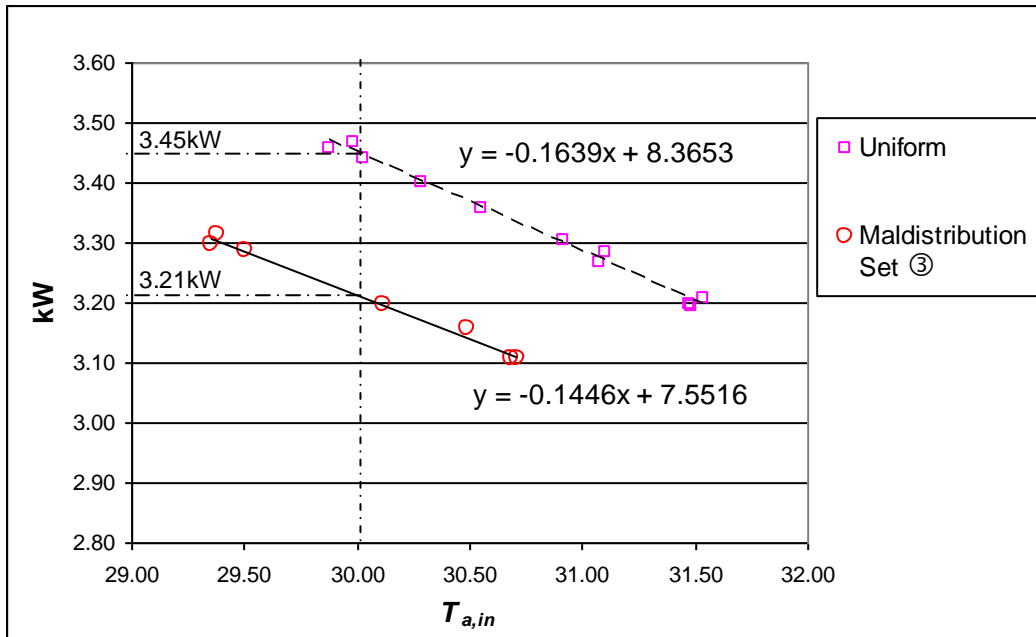


Fig. 6.23: Heating capacity degradation due to maldistribution Set ③

Table 6.6: Summary of experimental results

	Set ①	Set ②	Set ③	Set ④	Set ⑤	Set ⑥
Standard deviation	0.508	0.508	0.443	0.341	0.236	0.242
Skew	-1.452	-1.437	-1.802	-2.522	-3.851	-3.588
NTU	0.693	0.693	0.716	0.749	0.776	0.775
R	0.00406	0.00405	0.00416	0.00431	0.00444	0.00444
D , experiment	9.62%	9.38%	6.81%	4.19%	3.01%	2.54%
D , calculation	9.67%	9.67%	7.58%	4.64%	2.28%	2.34%
D , prediction	9.16%	9.17%	6.59%	3.51%	1.85%	1.90%

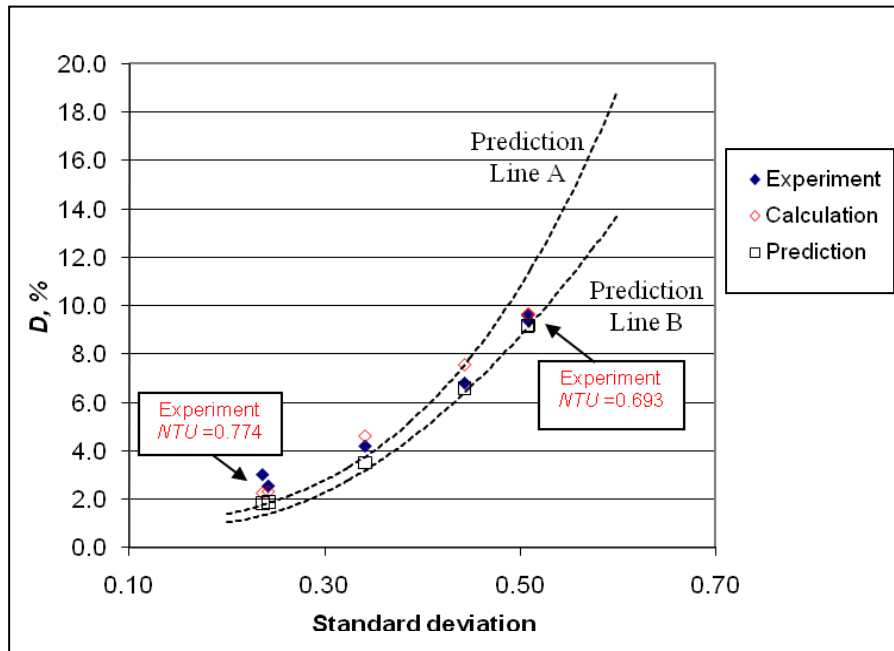


Fig. 6.24: Plot of experimental D versus standard deviation

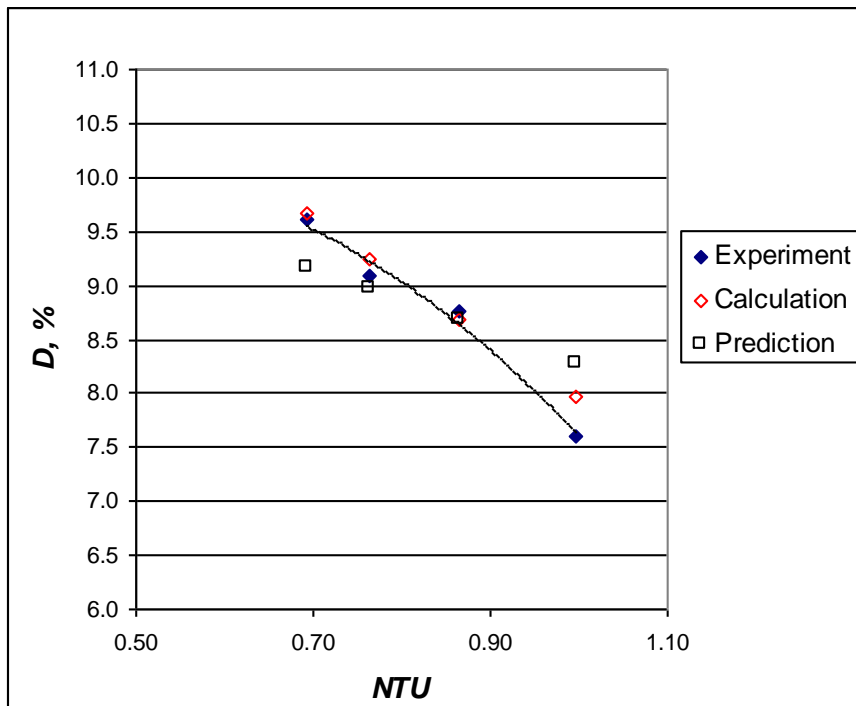


Fig. 6.25: Plot of experimental D versus NTU

Next, the results of experiment for maldistribution Set ① when the air flow rate varies through the test coil are presented in Fig. 6.25. Within the range of tested NTU , the results show that D increases as NTU decreases. The calculation results and predictions from the correlation equations are also superimposed on the same figure.

To compare the agreement between the experimental and calculated values of D , the data from both Fig. 6.24 and 6.25 are plotted together in a parity plot, as shown in Fig. 6.26. Similarly, the comparison between the experimental and prediction values is also shown in the same plot. The plot shows a good agreement within $\pm 10\%$ between the experiment and calculation results. However, a few points lie on the $\pm 15\%$ range for the prediction data. Obviously, this is due to the $\pm 15\%$ deviation observed for the correlation equations, as reported in Chapter 5.

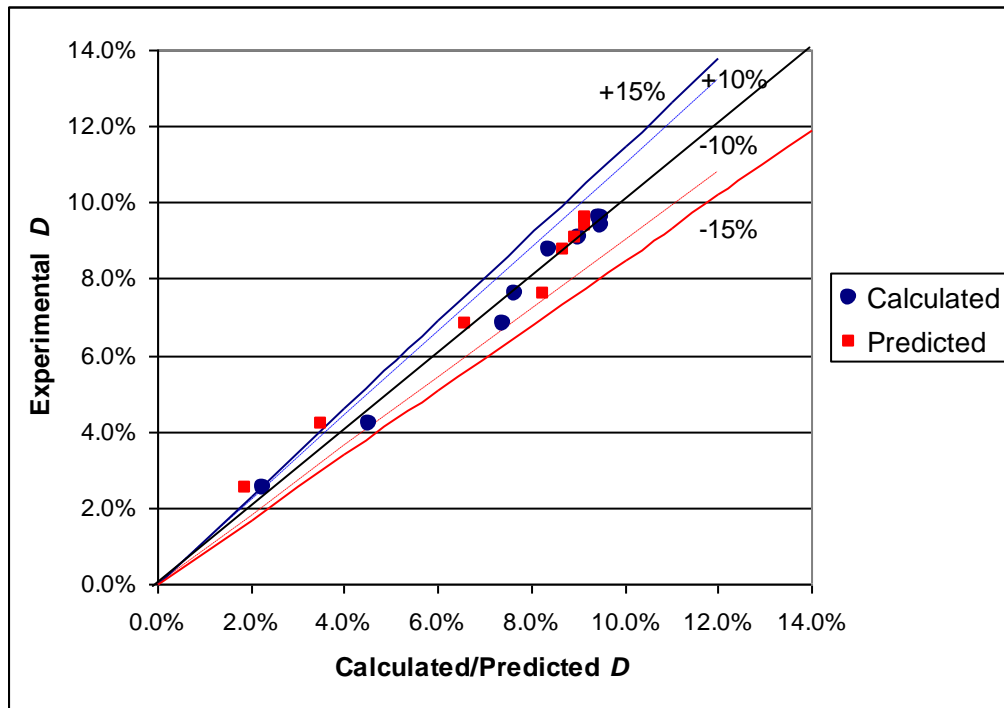


Fig. 6.26: Parity plot between experimental and calculated D , and also between experimental and predicted D

6.4 Measurement uncertainty

Uncertainties in the experimental measurement data were calculated with the error propagation method developed by Kline and McClintok [108]. To do this, the uncertainties of the instruments used in the experiments were obtained from the corresponding accuracy specifications and calibration certificates. Table 6.7 summarizes this information for the instruments used in both test rigs.

In general, the uncertainty of a measurement comprises of two components, i.e. the random variation of repetitive measurements and the bias or systematic errors of the instruments due to the test environment. In the guidelines given by UKAS [109], the analysis of random uncertainties by statistical means is called Type A evaluation. The analysis of systematic errors is included in the Type B uncertainty evaluation. The combination of both types will give the combined uncertainty of the measurement.

For a parameter which is derived from a set of measurements obtained during experimentation, the uncertainty of the parameter is calculated from the uncertainty of each individual measurement. Suppose this parameter, Ω , is a function of several independent variables, $x_1, x_2, x_3, \dots, x_n$, i.e.

$$\Omega = \Omega(x_1, x_2, x_3, \dots, x_n) \quad (6.13)$$

If U_i is the uncertainty of the measurement for variable x_i , and by assuming that the uncertainty of each variable has the same probability of occurring, the uncertainty of Ω , U_Ω , will be given as:

$$U_\Omega^2 = \left(\frac{\partial \Omega}{\partial x_1} U_1 \right)^2 + \left(\frac{\partial \Omega}{\partial x_2} U_2 \right)^2 + \left(\frac{\partial \Omega}{\partial x_3} U_3 \right)^2 + \dots + \left(\frac{\partial \Omega}{\partial x_n} U_n \right)^2 \quad (6.14)$$

As an example, consider equation (6.6) which is used to determine the water-side heating capacity. By applying equation (6.14), the uncertainty of the heating capacity, U_{Q_w} , is expressed as:

$$\left(\frac{U_{Q_w}}{Q_w}\right)^2 = \left(\frac{U_v}{\dot{v}_w}\right)^2 + \left(\frac{U_{T_i}}{\Delta T_w}\right)^2 + \left(\frac{U_{T_o}}{\Delta T_w}\right)^2 \quad (6.15)$$

where U_v , U_{T_i} and U_{T_o} are the uncertainties for the measured water volume flow rate, water outlet temperature and water inlet temperature respectively, i.e. as shown in Table 6.7. In the equation, ΔT_w is the water temperature differential.

In calculating the uncertainty of a parameter, Ω , which may be expressed as algebraic combination of several variables A, B and C, the relationships shown in Table 6.8 have been used. With this, the calculated expanded uncertainties from the experimental data, for a 95% confidence level, are given as follows:

a) Heat transfer coefficient test

Uncertainty of air-side heating capacity: $\pm 1.4\%$

Uncertainty of j -factor: $\pm 1.2\%$

b) Maldistribution test

Uncertainty of water-side heating capacity: $\pm 0.4\%$

Uncertainty of thermal degradation factor, D : $\pm 0.2\%$

Table 6.7: Uncertainty of instruments used in experiments

Instrument	Uncertainty
RTD temperature sensor	$\pm 0.03^\circ\text{C}$
Differential pressure manometer	$\pm 0.05 \text{ mmH}_2\text{O}$
Barometer	$\pm 0.50 \text{ mmHg}$
Water flow meter	$\pm 0.02 \text{ m}^3\text{hr}^{-1}$
Heated thermistor anemometer	$\pm 0.20 \text{ ms}^{-1}$

Table 6.8: List of uncertainty relationships

Expression for parameter Ω	Uncertainty relationship
$\Omega = A \pm B \pm C$	$U_\Omega^2 = U_A^2 + U_B^2 + U_C^2$
$\Omega = \frac{A \cdot B}{C}$	$\left(\frac{U_\Omega}{\Omega}\right)^2 = \left(\frac{U_A}{A}\right)^2 + \left(\frac{U_B}{B}\right)^2 + \left(\frac{U_C}{C}\right)^2$
$\Omega = \ln A$	$U_\Omega = \frac{U_A}{A}$
$\Omega = A^n$	$\frac{U_\Omega}{\Omega} = n \frac{U_A}{A}$

6.5 Summary

The first test rig has successfully characterized the heat transfer coefficient for the actual wavy fins used in the research. A correction factor of 0.8816 was applied to the existing j -factor correlation which has been developed by Wang et al. [82]. This modified correlation was then used in the analysis of the maldistribution problem for fin-tube heat exchangers in this work.

The results from the maldistribution experimental test rig has also successfully verified the discretization analysis technique used in this research. A good agreement for the thermal degradation factor, D , within $\pm 10\%$ was obtained between the experimental results and the theoretical calculated data. At the same time, a reasonable agreement within $\pm 15\%$ was obtained between the experimental results and the values predicted by the developed correlations. The larger deviation is expected because of the inherent uncertainties in the correlation equations themselves.

CHAPTER 7

NUMERICAL SIMULATION STUDIES AND VALIDATION

7.1 Overview

In this chapter, the results of Computational Fluid Dynamics (CFD) simulation for flow maldistribution in a fin-tube heat exchanger are reported. A commercial CFD software, FLUENT, was used for the study. The geometry of the maldistribution experimental test rig described in Chapter 6 was generated in GAMBIT. The simulation results of the inlet velocity profile and thermal performance degradation factor were validated with actual experimental data. The validated CFD model could then be used for various combinations of fin-tube geometrical parameters and layout.

7.2 CFD simulation for fin-tube heat exchangers

There is an extensive amount of literature available which describes Computational Fluid Dynamics (CFD) simulation work for fin-tube heat exchangers. In general, these simulations can be categorized into:

- 1) Simulation of a section of the fin surfaces
- 2) Simulation of the entire fin-tube heat exchanger

In the first category, the objective of the simulations is to examine the heat transfer and friction characteristics as air flows over the fin surfaces. A small section of the fin is typically modeled where periodic and symmetric boundary conditions are applied. This simulation is useful to determine the effect of fin surface patterns, e.g. louvers, slits and slots, on the heat transfer coefficient and friction factor of the fins. An example of such simulation includes the work done by Erekan et al. [110] where a 2-fin model with an elliptical tube and with air flowing in between the fin passage

was studied. It was found from the simulation that increasing the ellipticity of the tube would increase the heat transfer from the fins. A similar model of fins with elliptic tubes was also studied by Sahin et al. [111] with hot flue gas and water flowing in between the passage and in the tube, respectively. An enhancement of heat transfer was observed with the increase of fin inclination angle with respect to the approach flue gas direction. In a more recent work, Borrajo-Pelaez et al. [112] used the commercial CFD code, FLUENT, to perform a 3-D finite volume simulation for a plain fin-tube heat exchanger. With a similar 2-fin and round tube model, a parametric study was performed where the effect of several geometrical parameters on the Nusselt number and friction factor was investigated. The simulation was performed by taking into consideration the internal heat transfer coefficient due to water flowing in the tubes and heat conduction through the tube walls and fins.

A detailed, comprehensive modeling of an entire roof-top package air-conditioning unit was performed by Moukalled et al. [113]. Full-size models of the evaporator and condenser coils, with the exact number of fins, were included in the model. The rationale for doing so was to eliminate the need for approximate models to account for air drag through the fins. This resulted in an excessive number of mesh cells which required a large computing cost to solve. Nevertheless, an excellent agreement within $\pm 3\%$ between simulation and experimental data was obtained for the cooling capacity.

Due to the extreme difficulty in modeling the exact geometry of the exchanger, CFD simulation of the entire coil is usually performed by using an approximate porous media approach. The fin-tube heat exchanger is replaced with an isotropic and homogenous porous medium which is characterized with an equivalent core pressure drop relationship. This is done by using the Forchheimer equation, which is cited in [114] as:

$$I = aV + bV^2 \quad (7.1)$$

where I is the hydraulic gradient and V is the approach velocity. a and b are coefficients which are dependent on the properties of fluid and the porous medium.

Further work by Ward, cited in [114], has expanded equation (7.1) for both laminar and turbulent flows in the porous medium as:

$$I = \frac{\mu_f V}{\rho_f g K} + \frac{C_I V^2}{g \sqrt{K}} \quad (7.2)$$

Expressing in terms of pressure drop:

$$\Delta p = \frac{\mu_f L V}{K} + \frac{\rho_f C_I L V^2}{\sqrt{K}} \quad (7.3)$$

In both the equations above, K is the permeability of the porous medium and C_I is the inertia coefficient. L is the flow length of the porous medium. By defining

$C_k = \mu_f L / K$ and $C_n = \rho_f C_I L / \sqrt{K}$, equation (7.3) is re-written as:

$$\Delta p = C_k V + C_n V^2 \quad (7.4)$$

By relating the fin-tube heat exchanger pressure drop and velocity data to the quadratic equation above, the equivalent porous media characteristics could be obtained for the CFD model. In most instances, these data are obtained experimentally.

Examples of simulation done with this porous medium approach were the studies by Elgowainy [45] and Ismail et al. [57]. In both cases, the results of the simulation gave the air velocity distribution on the heat exchanger. The velocities within the range of the resulting Reynolds numbers were then applied on separate fin models to calculate the f - and j -factors of the fins, i.e. very much like the simulation of the first category. A mass-averaged overall j -factor was then computed over the entire core length.

Similarly, Hayes et al. [115] used the porous media approach to calculate the heat transfer and pressure drop performance of a matrix heat exchanger. In their model, a known constant heat flux was defined at the lower side of the porous medium. Consequently, the air temperature was highest along the bottom of the exchanger and decreased as the distance from the bottom wall increased.

7.3 Governing equations

The CFD simulation performed in this work was used to solve for the velocity, pressure and temperature fields for an incompressible, Newtonian fluid stream flowing through the fin-tube heat exchanger. The professional version of the commercial CFD code, FLUENT 6.3, was used as the solver. The following set of equations for incompressible turbulent flows was applied on the heat exchanger which describes the three physical conservation laws within a Cartesian coordinate system [116]:

a) Conservation of mass

$$\frac{\partial u}{\partial x} + \frac{\partial v}{\partial y} + \frac{\partial w}{\partial z} = 0 \quad (7.5)$$

Expressing in vector notation:

$$\nabla \cdot \vec{u} = 0 \quad (7.6)$$

b) Conservation of momentum

- In the x -direction:

$$\frac{\partial u}{\partial t} + u \frac{\partial u}{\partial x} + v \frac{\partial u}{\partial y} + w \frac{\partial u}{\partial z} = -\frac{1}{\rho_f} \frac{\partial p}{\partial x} + (\nu_f + \varepsilon_M) \left(\frac{\partial^2 u}{\partial x^2} + \frac{\partial^2 u}{\partial y^2} + \frac{\partial^2 u}{\partial z^2} \right) + S_{M,x} \quad (7.7a)$$

- In the y -direction:

$$\frac{\partial v}{\partial t} + u \frac{\partial v}{\partial x} + v \frac{\partial v}{\partial y} + w \frac{\partial v}{\partial z} = -\frac{1}{\rho_f} \frac{\partial p}{\partial y} + (\nu_f + \varepsilon_M) \left(\frac{\partial^2 v}{\partial x^2} + \frac{\partial^2 v}{\partial y^2} + \frac{\partial^2 v}{\partial z^2} \right) + S_{M,y} \quad (7.7b)$$

- In the z -direction:

$$\frac{\partial w}{\partial t} + u \frac{\partial w}{\partial x} + v \frac{\partial w}{\partial y} + w \frac{\partial w}{\partial z} = -\frac{1}{\rho_f} \frac{\partial p}{\partial z} + (\nu_f + \varepsilon_M) \left(\frac{\partial^2 w}{\partial x^2} + \frac{\partial^2 w}{\partial y^2} + \frac{\partial^2 w}{\partial z^2} \right) + S_{M,z} \quad (7.7c)$$

These three equations can also be expressed in compact vector form as:

$$\left[\frac{\partial u_i}{\partial t} + \nabla \cdot (u_i \vec{u}) \right] = -\frac{1}{\rho_f} \frac{\partial p}{\partial x_i} + (\nu_f + \varepsilon_M) \nabla \cdot (\nabla u_i) + S_{M,i} \quad (7.8)$$

for $i = 1, 2, 3$, representing the three coordinate directions.

c) Conservation of energy

$$\frac{\partial T}{\partial t} + u \frac{\partial T}{\partial x} + v \frac{\partial T}{\partial y} + w \frac{\partial T}{\partial z} = (\alpha_f + \varepsilon_H) \left(\frac{\partial^2 T}{\partial x^2} + \frac{\partial^2 T}{\partial y^2} + \frac{\partial^2 T}{\partial z^2} \right) + S_E \quad (7.9)$$

In vector notation:

$$\left[\frac{\partial T}{\partial t} + \nabla \cdot (T\vec{u}) \right] = (\alpha_f + \varepsilon_H) \nabla \cdot (\nabla T) + S_E \quad (7.10)$$

In all three equations above, ρ_f is the fluid density while p is the pressure at a particular node. u , v and w are the velocity components in the x , y and z directions, respectively, which defines the velocity vector \vec{u} , while T is the node temperature. The symbols ν_f and α_f are the molecular momentum and thermal diffusivity of the fluid, respectively, while ε_M and ε_H are the turbulent momentum and thermal diffusivity, respectively. S_M and S_E are the momentum and energy source terms, respectively. It is noted that the equations (7.7a), (7.7b) and (7.7c) above are also known as the Reynolds-averaged Navier-Stokes (RANS) equations.

To solve the above set of equations, volume integration, covering all the discretized meshes within the system control volume, is applied to each PDE. Volume integration of the divergence terms (∇) in the equations will require transformation to surface integrals by using the Gauss divergence theorem, i.e.

$$\int_{dV} (\nabla \cdot \vec{u}) dV = \int_{dA} (\vec{n} \cdot \vec{u}) dA \quad (7.11)$$

where \vec{n} is a unit vector normal to the surface element dA . The solution will give the velocity, pressure and temperature field of the fluid within the system.

Following the footsteps of previous researchers, viz. Carluccio et al. [117] and Moukalled et al. [113], the k - e turbulence model was initially selected in this work to determine the turbulent diffusivities ε_M and ε_H . Two additional partial differential equations must be solved to obtain the turbulent kinetic energy (k) and turbulent dissipation rate (e) [118]. The default values for the adjustable constants in the k - e model, as described in [118], have been set in FLUENT.

7.4 Geometrical model

The geometry of the flow maldistribution test rig described in Chapter 6 was generated in GAMBIT 2.4. Since it was the air flow distribution on the fin-tube heat exchanger that was of importance in this study, the flow measuring nozzle chamber and centrifugal fan far downstream were not included in the model. Only the bell-mouth inlet section upstream of the coil and a short downstream section of the outlet test duct were modeled.

Fig. 7.1 illustrates the completed model of the test duct. The model was enclosed within a domain which included the atmosphere. The discharge of the test duct was positioned to coincide with the outlet of the domain volume. This would mean that in the model, the air flowing through the test duct would be discharged out of the domain itself, though in fact, the discharge was to the nozzle. The overall external dimensions of the model are shown in Fig. 7.2. The domain has a size of 2m x 1m x 1m. The model also required that an extension block be added upstream of the inlet bell-mouth. This was necessary to ensure good quality of mesh elements of the bell-mouth section. Other than that, a single row fin-tube coil was modeled in between the inlet and outlet sections of the test duct. The origin of the coordinate system was located in the center of this fin-tube coil with the x , y and z -directions shown in Fig. 7.1.

7.5 Boundary conditions

The boundary conditions set in FLUENT for the model are summarized as the following:

- a) Wall boundary condition: All the duct surfaces of the bell-mouth inlet, outlet section and around the fin-tube coil perimeter were assigned as no-slip walls, i.e. with zero velocity ($\vec{u} = 0$) on the wall surfaces.
- b) Mass flow rate boundary condition: The discharge of the outlet section was set with a specified mass flow rate (\dot{m}_a) in the positive x -direction.

- c) Pressure inlet boundary condition: The boundaries of the domain round the duct model were set with a zero total gauge pressure. The atmospheric pressure, P_{atm} , of the fluid was also set at 101.325 kPa.
- d) Porous media: The fin-tube heat exchanger was assigned as a porous medium with an equivalent fluid pressure drop characteristic.

Air was chosen as the fluid within the computational domain. With the assumption of incompressible flow, the air density was assigned a constant value at a specific temperature. The values of air properties shown in Table 7.1 have been used in the simulation. The densities were calculated by using the psychrometric equations obtained from ASHRAE [85] while the viscosity data were taken from [119]. The temperatures chosen for the simulation reflect typical design values used in the industry.

Table 7.1: Air properties used in simulation

Temperature	Density (kgm^{-3})	Dynamic viscosity ($\mu\text{Pa.s}$)
20°C	1.182	18.2
30°C	1.137	18.6

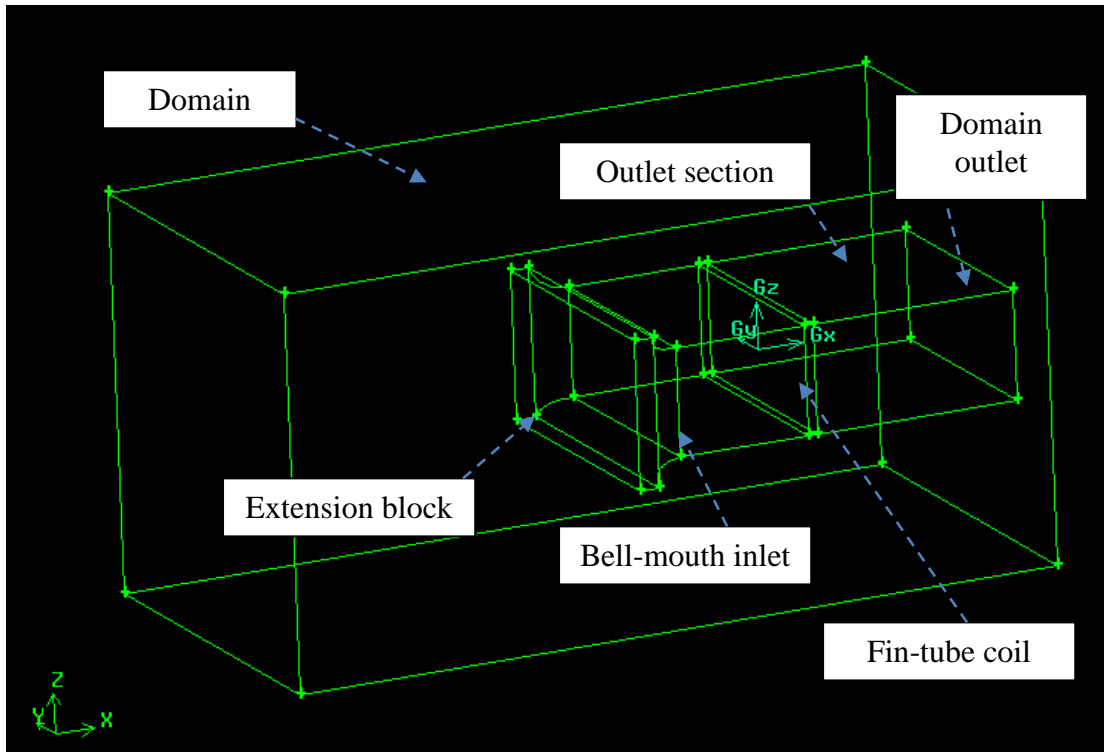


Fig. 7.1: Model of test duct in GAMBIT 2.4

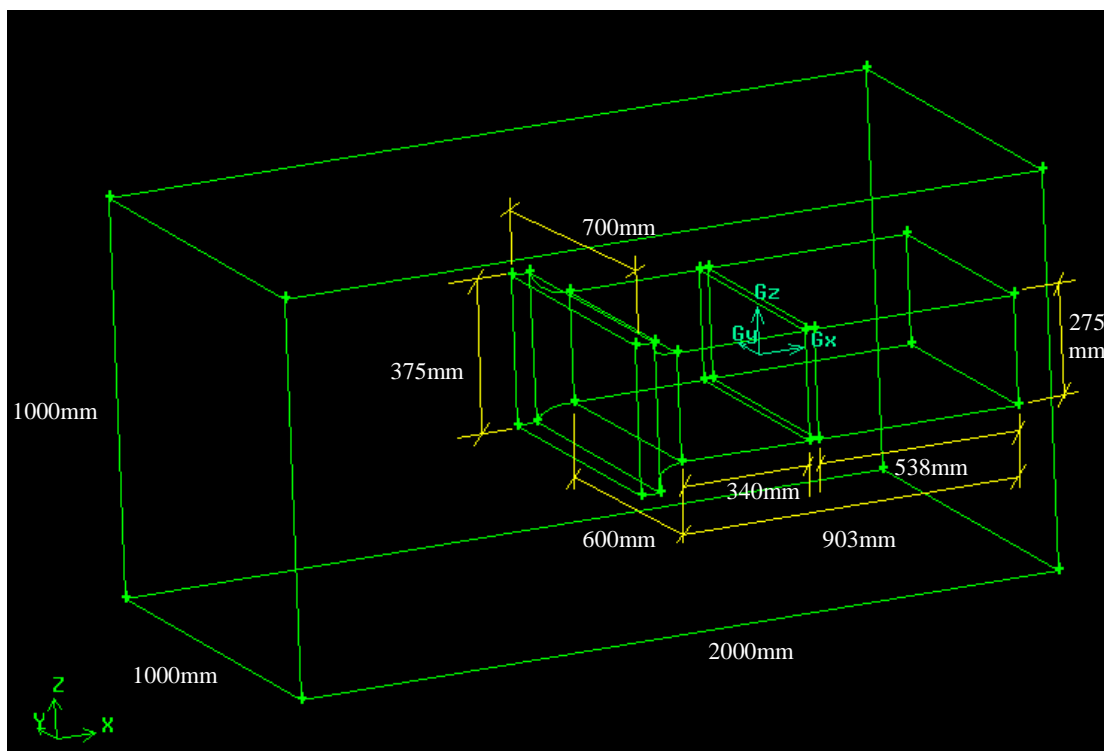


Fig. 7.2: Dimensions of model

7.5.1 Characterization of porous media

The air pressure drop characteristics of the fin-tube heat exchanger used in this study were obtained experimentally with the methodology stipulated in [103]. This was done with the same thermal experimental test rig described in Chapter 6. Two sets of static pressure holes (~ 1mm diameter) were drilled on the centerlines of the four test duct walls, upstream and downstream of the fin-tube coil. Each set of four static pressure holes were then connected together with plastic hose to give the average static pressure at that particular section. A differential pressure manometer was then used to measure the pressure drop between the entering and leaving planes.

The results of the measured pressure drop with varying air flow face velocity are plotted as shown in Fig. 7.3. A second order polynomial equation is used to correlate the experimental data. Since the pressure drop is zero when there is no flow, the fitted line is anchored at the origin. From this equation, the coefficients C_k and C_n for equation (7.4) can be obtained.

The porous media viscous (R_μ) and inertia resistance (R_I) coefficients are defined in FLUENT as follows [120] :

$$\Delta p = R_\mu V + \frac{1}{2} \rho_f R_I L V^2 \quad (7.12)$$

In FLUENT, R_I is also known as the form coefficient. By comparing equation (7.12) with (7.3) and (7.4), one would then arrive at the following relationships:

$$R_\mu = \frac{1}{K} = \frac{C_k}{\mu_f t_{coil}} \quad (7.13)$$

$$R_I = \frac{2C_n}{\rho_f t_{coil}} \quad (7.14)$$

where t_{coil} is the depth of the coil.

From the experimental pressure drop data, the calculated values for the porous media resistances in the x -direction are $R_{\mu} = 462,349 \text{ m}^{-2}$ and $R_I = 27.27 \text{ m}^{-1}$. These values have been entered into the FLUENT porous media model as boundary conditions.

Since there is no flow in the y -direction due to the fins, the resistances would be infinite. Similarly, the flow is constrained in the z -direction due to duct walls at the top and bottom of the coil. As a result, both the viscous and inertia resistances in the y - and z -directions have been artificially set in FLUENT as 1,000 times the magnitudes in the x -direction.

7.6 Grid independence test

The entire computational domain can be seen comprising of 5 distinct volumes, A to E, as indicated in Fig. 7.4. Each volume was discretized with volume meshes in GAMBIT. Due to the rectangular block shape of the model, structured hexahedral volume meshes were used on volumes A, B, C and D. However, since the bell-mouth of volume A has four curved surfaces, the volume discretization was preceded by surface meshing with quadrilateral elements on these curvatures. This was necessary to ensure good quality of meshes generated within the volume A. The remaining domain space, i.e. volume E, was discretized with unstructured tetrahedral volume meshes.

To determine the effect of mesh size on the simulation results, four meshing schemes with varying mesh sizes have been applied on the model. These are summarized in the following Table 7.2. The size of the quadrilateral surface meshes on the curved surfaces of volume A will follow the default size automatically calculated by FLUENT itself.

Table 7.2: Mesh schemes applied to model

Scheme	Volume A	Volume B	Volume C	Volume D	Volume E	Total mesh cells
1	Hexa (Size 30 mm)	Hexa (Size 30 mm)	Hexa (Size 30 mm)	Hexa (Size 30 mm)	Tetra (Size 50 mm)	128,174 cells
2	Hexa (Size 20 mm)	Hexa (Size 20 mm)	Hexa (Size 20 mm)	Hexa (Size 20 mm)	Tetra (Size 40 mm)	277,079 cells
3	Hexa (Size 15 mm)	Hexa (Size 15 mm)	Hexa (Size 15 mm)	Hexa (Size 15 mm)	Tetra (Size 30 mm)	570,450 cells
4	Hexa (Size 10 mm)	Hexa (Size 10 mm)	Hexa (Size 10 mm)	Hexa (Size 10 mm)	Tetra (Size 25 mm)	1,203,238 cells

An example of a meshed geometry is illustrated in Fig. 7.5 for mesh Scheme 2.

With the mesh files exported from GAMBIT into FLUENT, the velocity field for each case was solved for an inlet air mass flow rate of 0.335 kgs^{-1} (corresponding to $0.283 \text{ m}^3\text{s}^{-1}$ [$600 \text{ ft}^3\text{min}^{-1}$] at 20°C). The standard k - e turbulence model was also set with the default values for the constants in the model [118]. A first-order upwind discretization scheme was used for momentum, k and e , with SIMPLE pressure-velocity coupling. The convergence criterion was set at 10^{-6} .

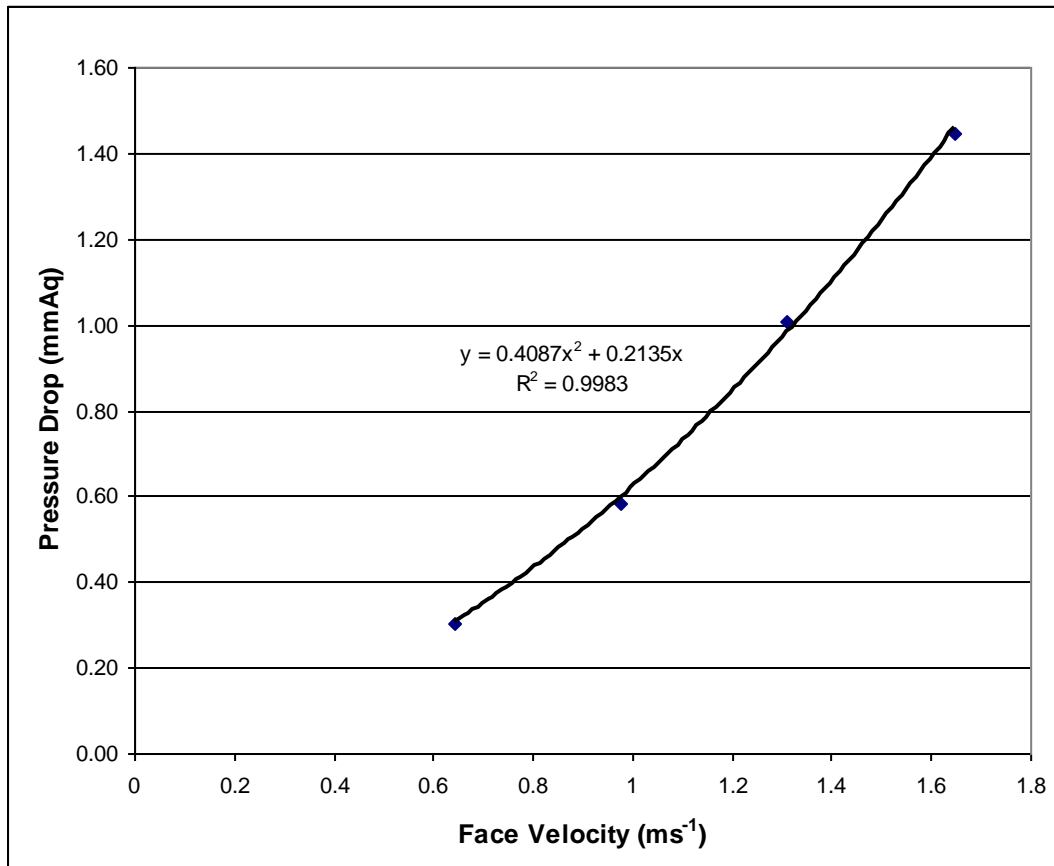


Fig. 7.3: Experimental data of air pressure drop through fin-tube coil

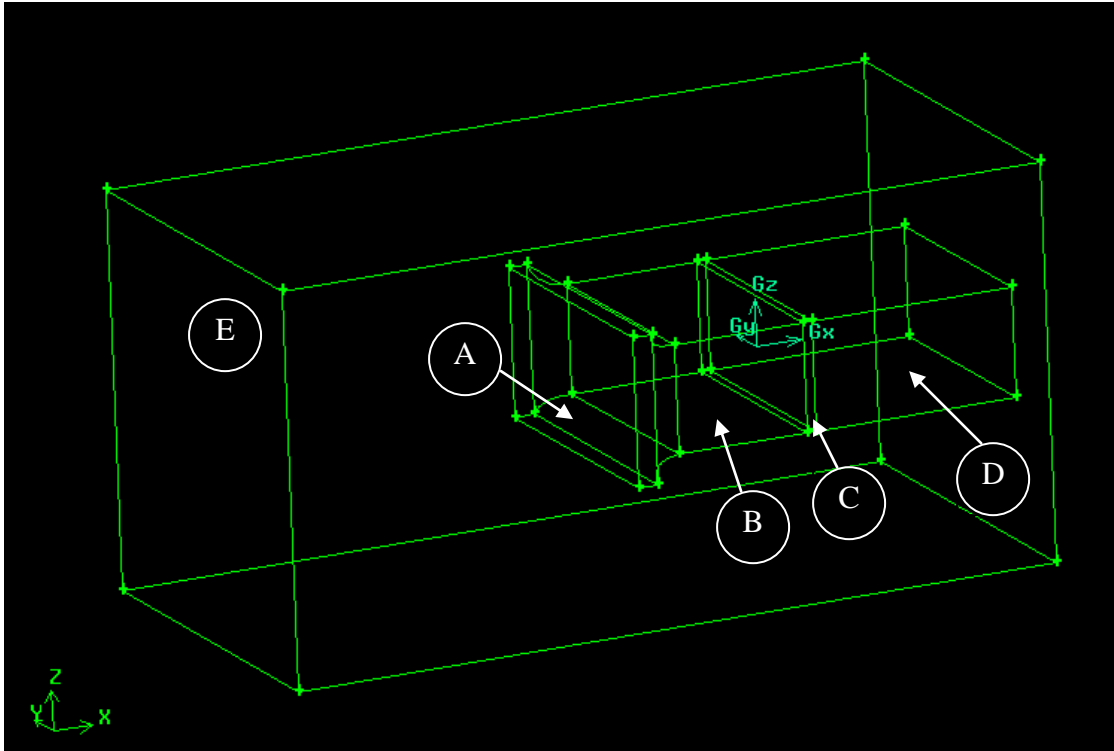


Fig. 7.4: Demarcation of distinct volumes in the numerical model

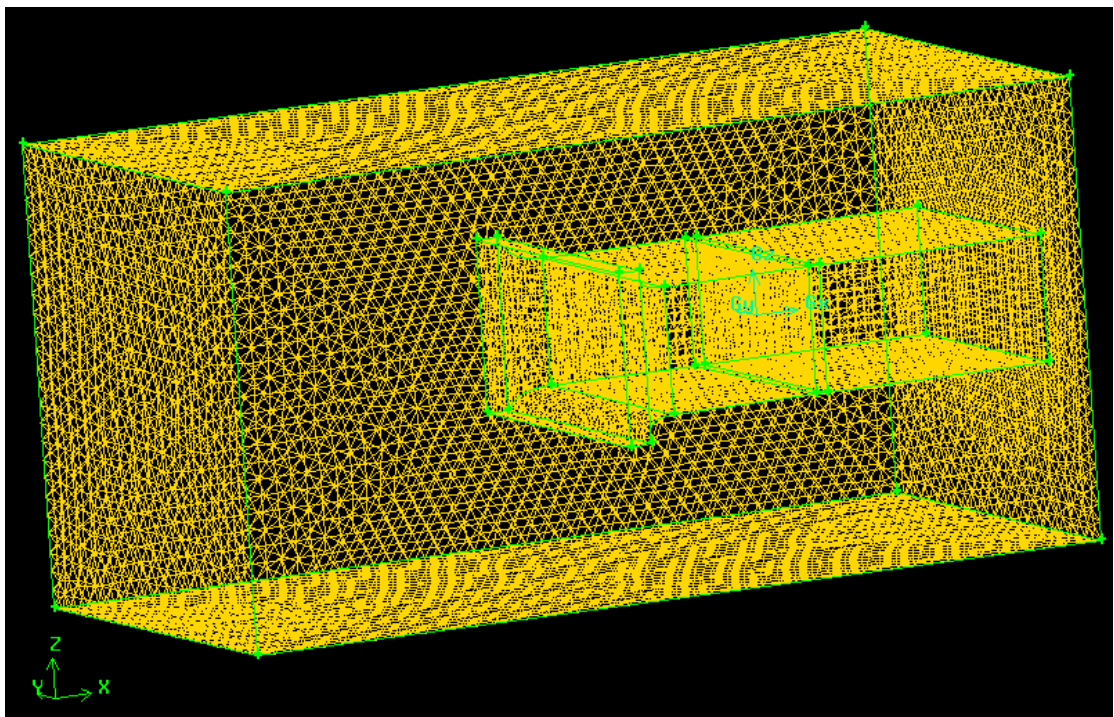


Fig. 7.5: Meshed geometry with Scheme 2

The computational time taken for convergence for each mesh scheme is shown in Table 7.3. The computation was performed on a desktop computer with the following specifications: INTEL *i5* CPU, 2.67 GHz clock speed, 3.49GB RAM and with 1TB HDD. It is clear from the results that scheme 4 takes the longest time to solve due to the largest number of cell elements. Fig. 7.6 illustrates an example of the velocity contours obtained along the center plane of the test duct for the case of mesh scheme 2. The velocity contours on the inlet coil face area are also shown in the same figure.

Table 7.3: Convergence time required for different mesh schemes

Mesh scheme	Convergence time
1	1 hour
2	6 hours
3	13 hours
4	> 1 day

As a comparison, the simulated velocity data on the inlet coil face area for all four mesh schemes, along the z -axis ($y = 0$), are plotted together, as shown in Fig. 7.7. As expected, the velocity on the duct wall is zero due to the no-slip boundary condition. With mesh scheme 1, a flat velocity profile is obtained which coincides with the theoretical average face velocity of 1.72 ms^{-1} at the same mass flow rate. The other three finer mesh schemes (i.e. scheme 2, 3 and 4) exhibit curved profiles where at distances further away from the wall, the velocity gradually increases until a maximum is reached along the duct centerline. Such curved velocity profiles are expected due to the shear stresses along the wall, which are similar to the parabolic-like profiles observed with flows in circular pipes.

It is evident from the results that the velocity profiles for mesh schemes 2, 3 and 4 are very nearly identical. The variation in the velocities between scheme 2 and 3 is approximately 0.5% whereas the difference between scheme 2 and 4 is about 1%. In view of the small differences in the velocities and higher computational effort required with the finer meshes, scheme 2 is chosen for further simulation work without significant impact on the accuracy of the results.

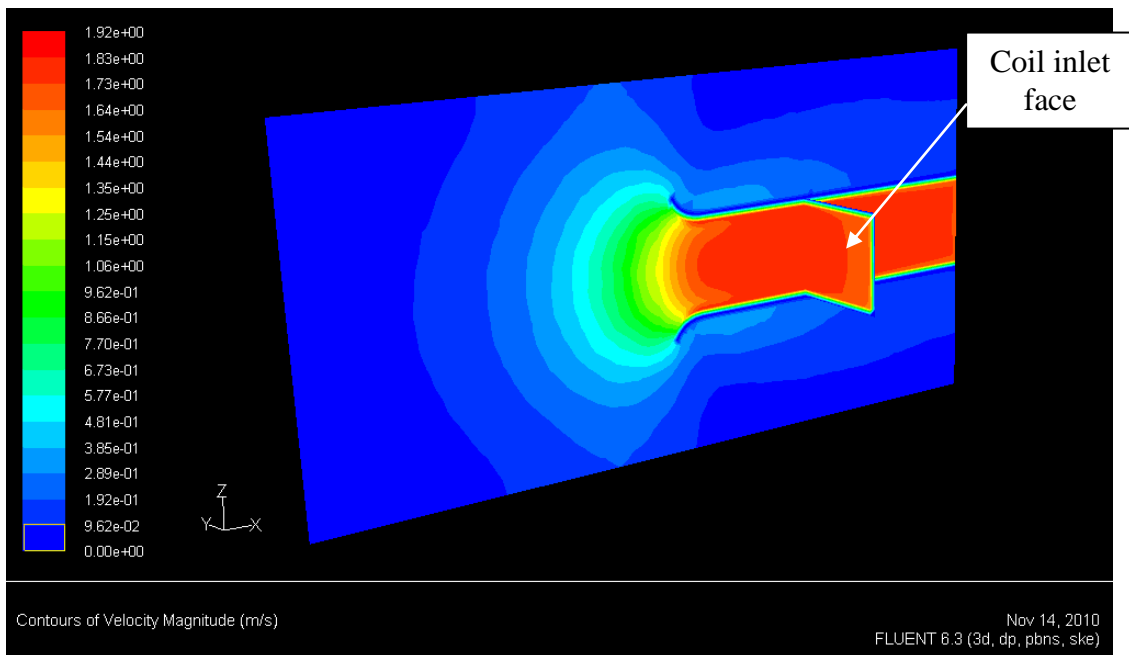


Fig. 7.6: Velocity contours for mesh Scheme 2

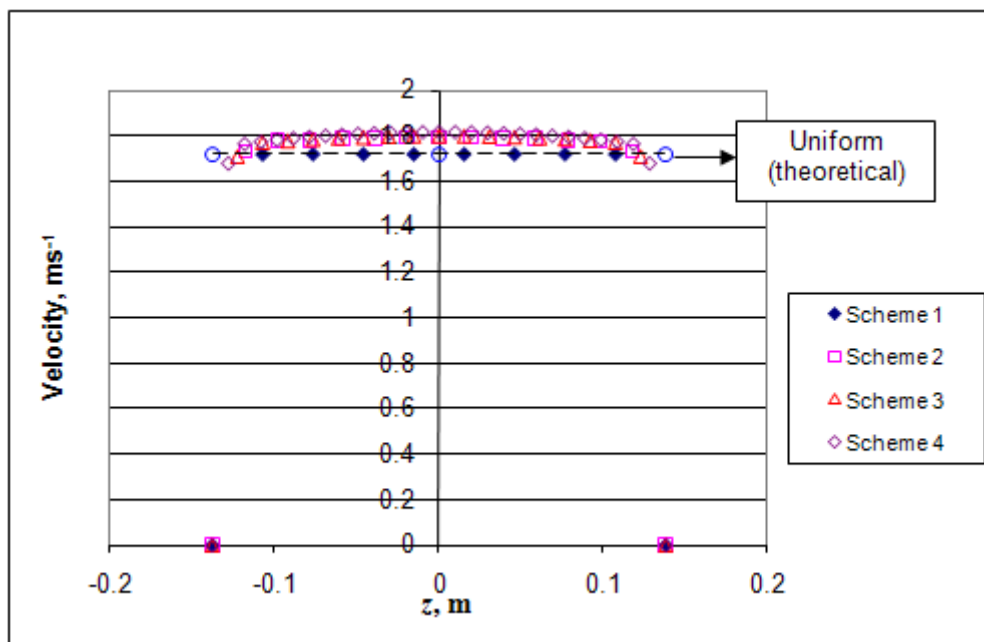


Fig. 7.7: Simulated velocity profile along z -axis ($y = 0$)

7.7 Change of turbulence model

It has been pointed out by Versteeg and Malalasekera [118] that the renormalized RNG k - ϵ model could give better performance than the standard k - ϵ model due to the sensitization of the turbulence dissipation equation to the magnitude of strain in the flow, e.g. along the walls of bounded flows. In view of that, the simulation of the model was repeated by changing the turbulence model in FLUENT to RNG k - ϵ and the results compared with the standard model.

The simulation was performed on the model meshed with scheme 2 for the same air mass flow rate of 0.335 kgs^{-1} . The results of this comparison are shown in Fig. 7.8 which gives the velocity plots, for both turbulence models, on the inlet coil face area along the y -axis ($z = 0$).

It can be seen from the plot that the RNG k - ϵ model has resulted in slightly higher velocities near the center of the duct, i.e. with a difference of approximately 2.3%. The data are comparable near the walls of the duct. In other words, the RNG k - ϵ turbulence model has a small impact on the results of the simulation. However, the convergence time for the solution to reach the same convergence criteria of 10^{-6} was faster, i.e. 4 hours. In view of the small differences in the results, and a lower computation cost, the RNG k - ϵ model has been selected for further simulation work.

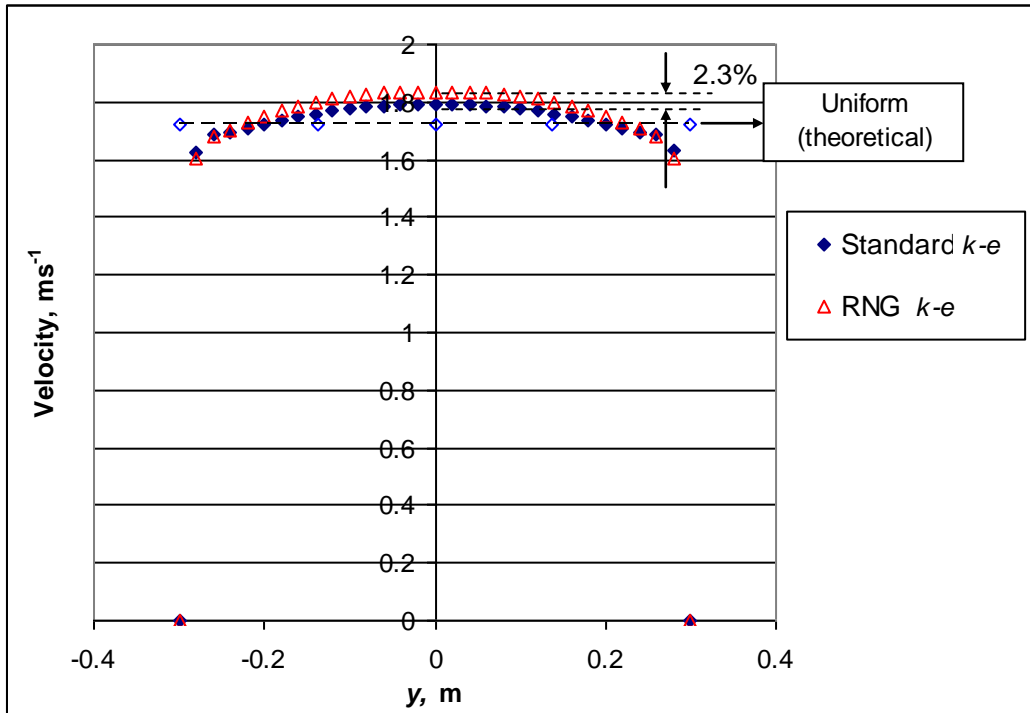


Fig. 7.8: Comparison between turbulence models

7.8 Effect of domain size

The simulation performed in the previous sections was done with a fixed domain size of 2m x 1m x 1m along the x -, y - and z -directions, respectively. To investigate the effect of the domain size on the simulation results, the calculation was repeated by changing the domain dimensions. However, the model of the test duct within the domain was not changed. The same meshing scheme 2 was also applied for the whole model. Table 7.4 summarizes the dimensions of the domain and the corresponding number of cell elements.

The results of the simulation are compared in the following Fig. 7.9 where the velocity profiles on the inlet coil face area, along the y -axis ($z = 0$), are plotted. It is clearly seen that the results are again nearly identical among the different domain sizes. The larger domain size has no significant effect on the results of the simulation. Since a larger computational domain requires a longer convergence time, the smallest Domain 1 has been selected for further simulation work.

Table 7.4: Summary of domain sizes compared

Domain	Domain size	Total mesh cells
1	2m x 1m x 1m	277,079
2	2.2m x 1m x 1m	313,256
3	2.4m x 1m x 1m	333,171
4	2m x 1.2m x 1.2m	370,377
5	2m x 1.5m x 1.5m	588,884

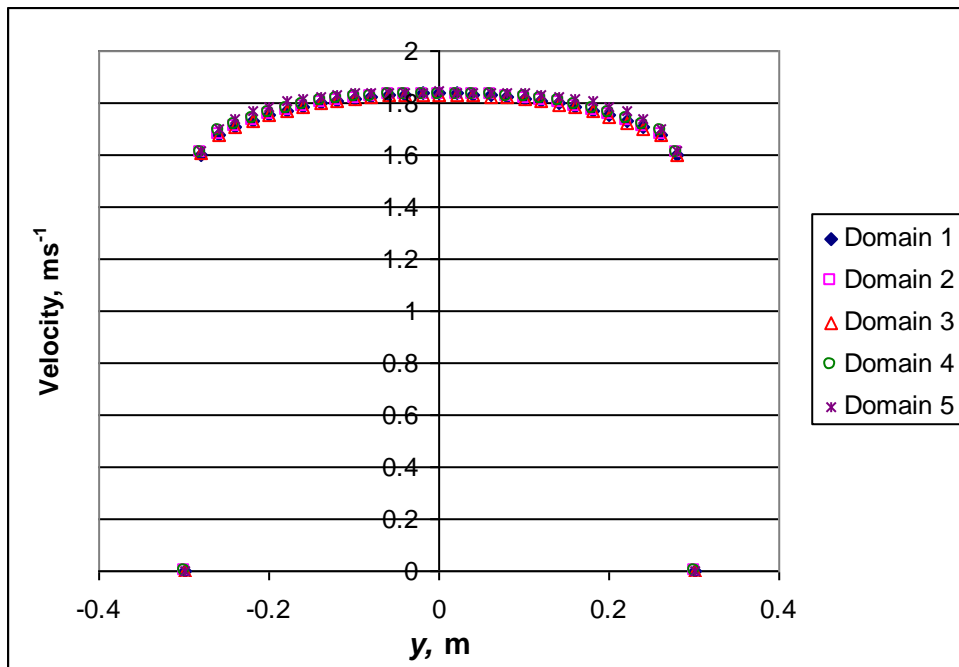


Fig. 7.9: Effect of domain size

7.9 Velocity vectors at the bell-mouth

From the results of the velocity data obtained, the flow behaviour through the inlet bell-mouth is examined with a velocity vector plot through the centerline of the duct. As explained in Chapter 6, the purpose of the bell-mouth is to prevent flow separation at the duct inlet. The simulation has indeed shown the effectiveness of the bell-mouth as can be seen from the vector plot in Fig. 7.10 which illustrates the convergent flow as air is drawn from the domain. No recirculation flows can be seen along the wall of the bell-mouth for the air flow with Reynolds number of approximately 43,000. Consequently, the velocity vectors are seen parallel to each other as the air enters the heat exchanger.

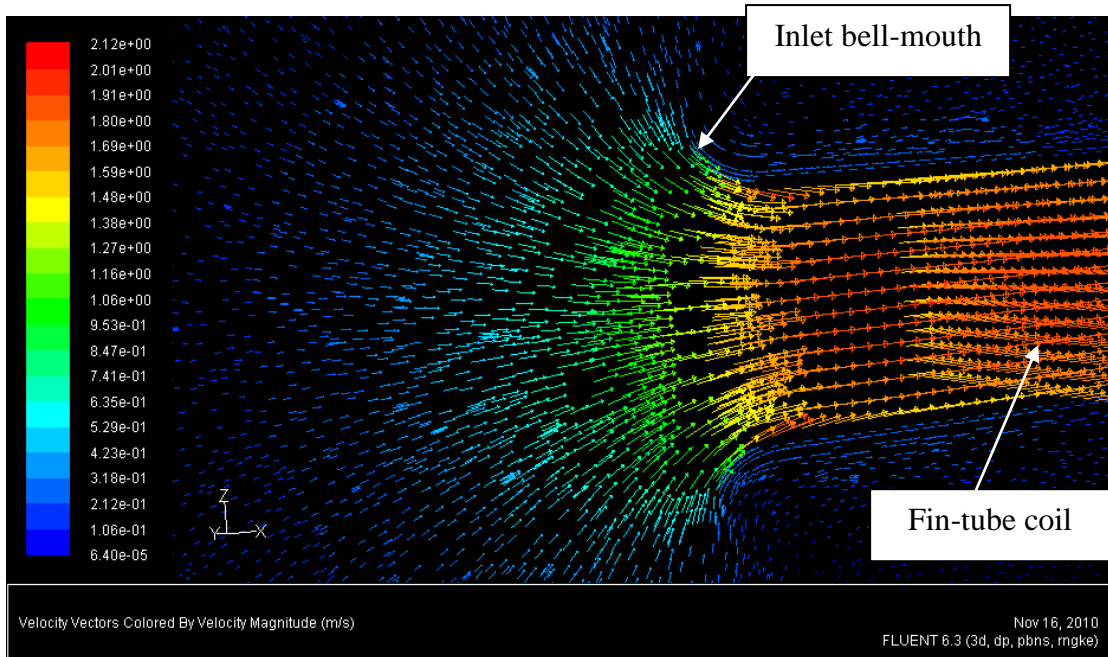


Fig. 7.10: Velocity vector plot along the duct centerline (Domain size 1 and mesh scheme 2; solution obtained with 1st order upwind discretization and with RNG *k-e* turbulence model)

7.10 Simulation of flow maldistribution

To simulate the case of flow maldistribution, the model in GAMBIT was modified by adding wall surfaces on the coil inlet face area which effectively blocked air from going through certain regions of the porous media. This would be similar to the paper block method used during the experiment, as described in Chapter 6, to measure the magnitude of thermal degradation. For this simulation study, the patterns of paper block chosen from the list shown in Fig. 6.18 were Set ①, ② and ④.

Fig. 7.11 illustrates the model generated for blockage pattern Set ④. The no-slip wall boundary condition was set in FLUENT for these additional surfaces on the coil. With the other boundary conditions remaining unchanged, the simulation was then repeated, with an air mass flow rate of 0.376 kgs^{-1} , corresponding to $0.330 \text{ m}^3\text{s}^{-1}$ ($700 \text{ ft}^3\text{min}^{-1}$) at 30°C to determine the maldistributed velocity profile on the fin-tube coil. Following the observations from the previous simulation with uniform distribution, domain size 1 and meshing scheme 2 were chosen for the simulation. The RNG $k\text{-}\epsilon$ was also used as the turbulence model.

Fig. 7.12 (a), (b) and (c) show the simulated velocity contours on a horizontal plane through the center of the duct model for Set ①, ② and ④, respectively. The insets in each of these figures illustrate the blockages imposed on the coil, which corresponds to Fig. 6.18. The results clearly show the flow being diverted away from the imposed blockages.

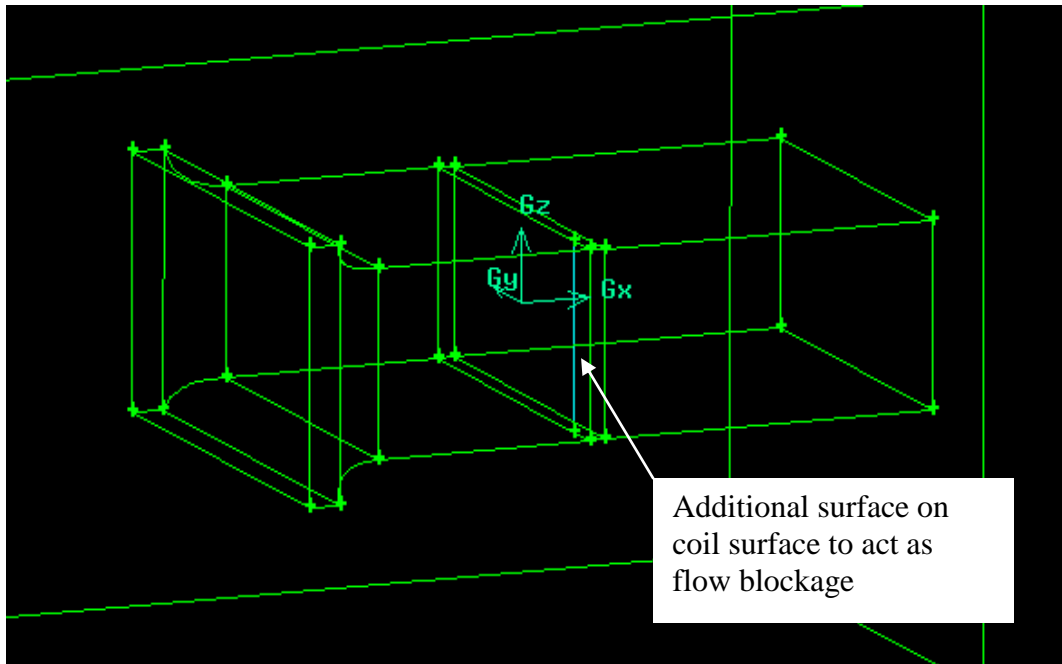
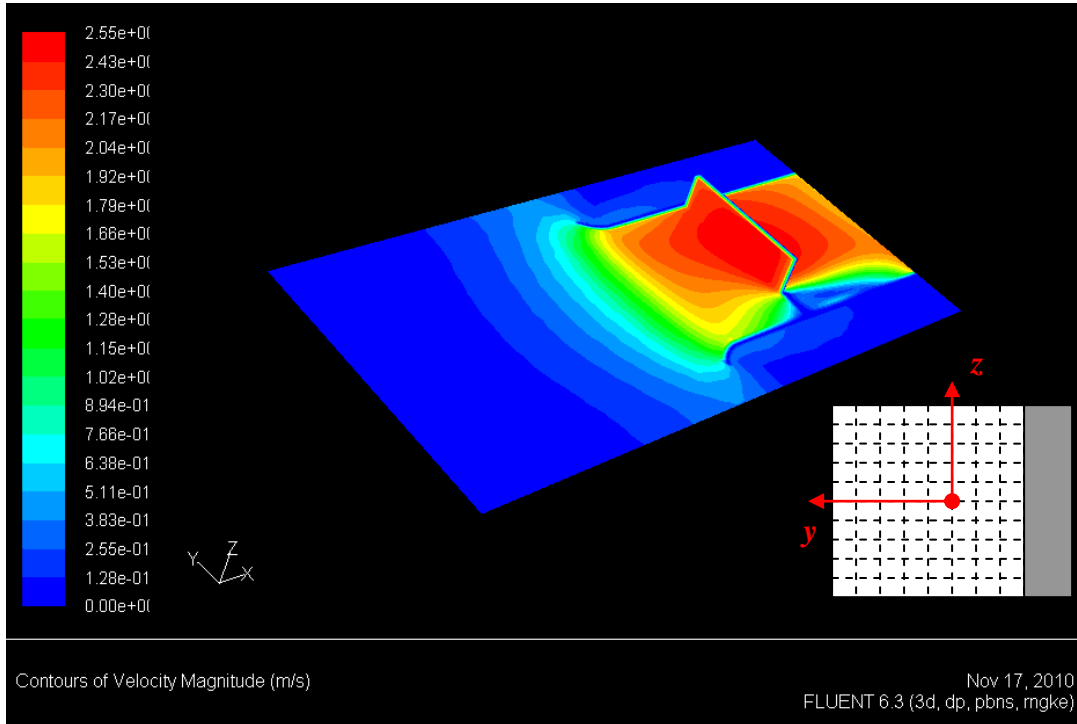
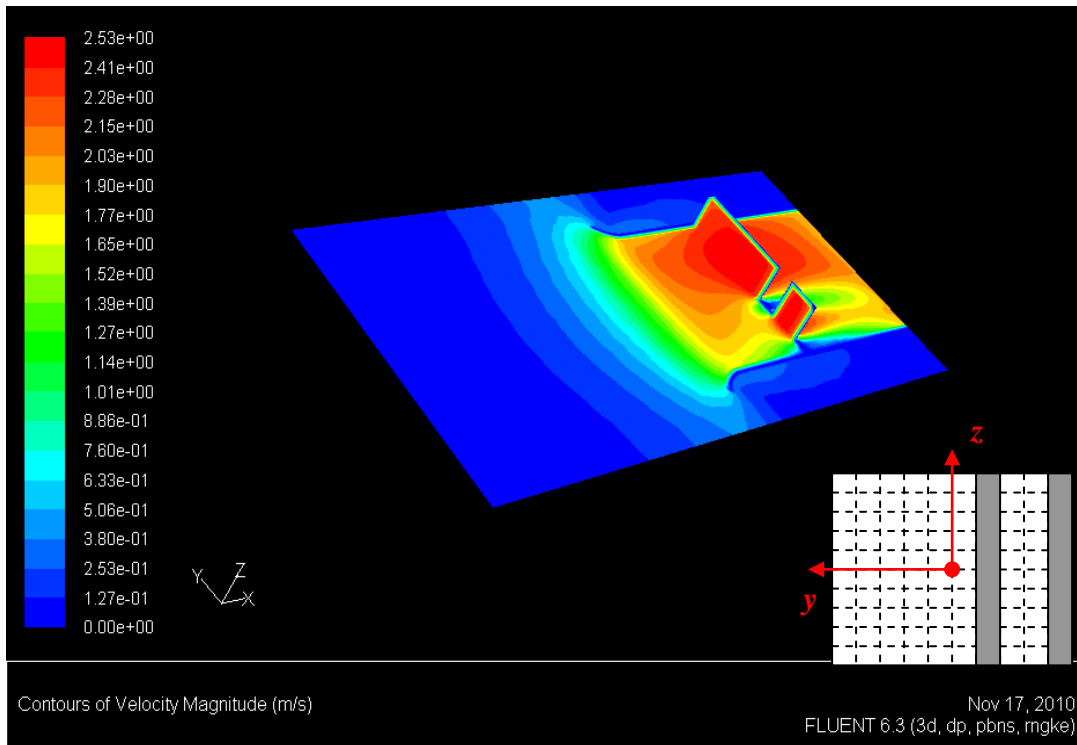


Fig. 7.11: Model generated in GAMBIT for flow blockage pattern Set ④



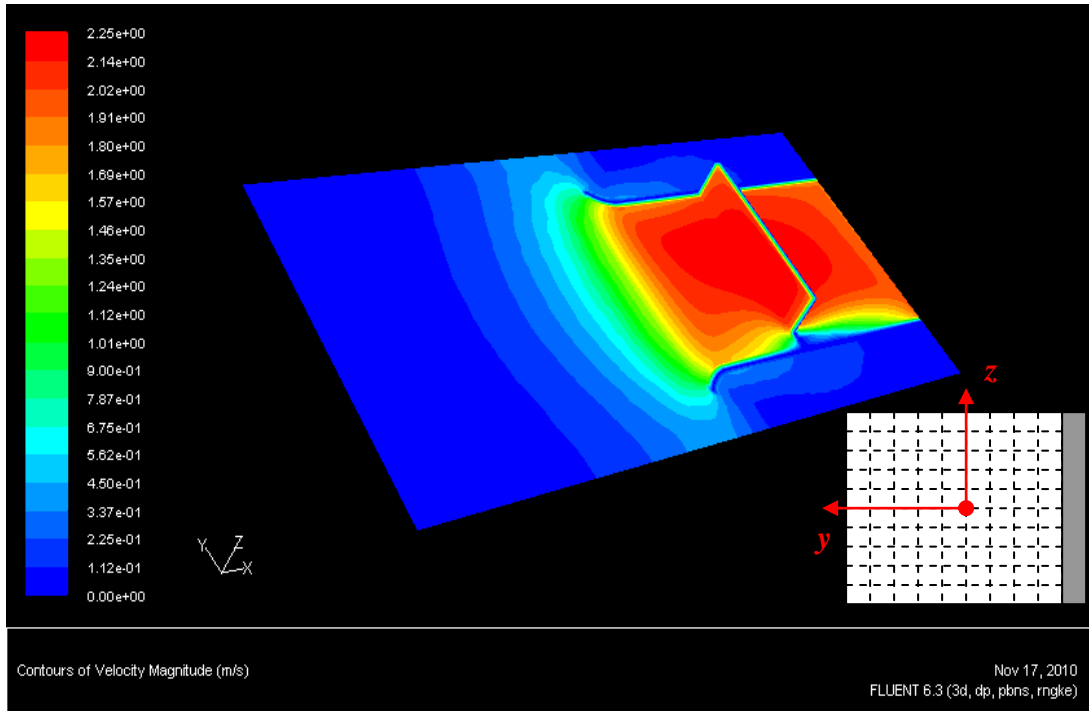
(a)



(b)

Fig. 7.12: Simulated velocity contours for flow maldistribution:

(a) Profile Set ① (b) Profile Set ②



(c)

Fig. 7.12: Simulated velocity contours for flow maldistribution (continued):

(c) Profile Set ④

To verify these simulation results, comparisons have been made with the measured inlet velocity data obtained from the experiments described in Chapter 6 for these maldistribution profiles. These are illustrated in Fig. 7.13, 7.14 and 7.15 for Set ①, ② and ④, respectively where the velocities on the coil inlet face area, along the y -axis ($z = 0$), are compared. It can be seen from the parity plot of Fig. 7.16 that there is a good agreement between the simulation and experimental data where more than 90% of the data points fall within $\pm 8\%$. Among these three set of results, the mean deviation is calculated to be 4%. From this, it can be concluded that the CFD simulation model for flow maldistribution has been validated.

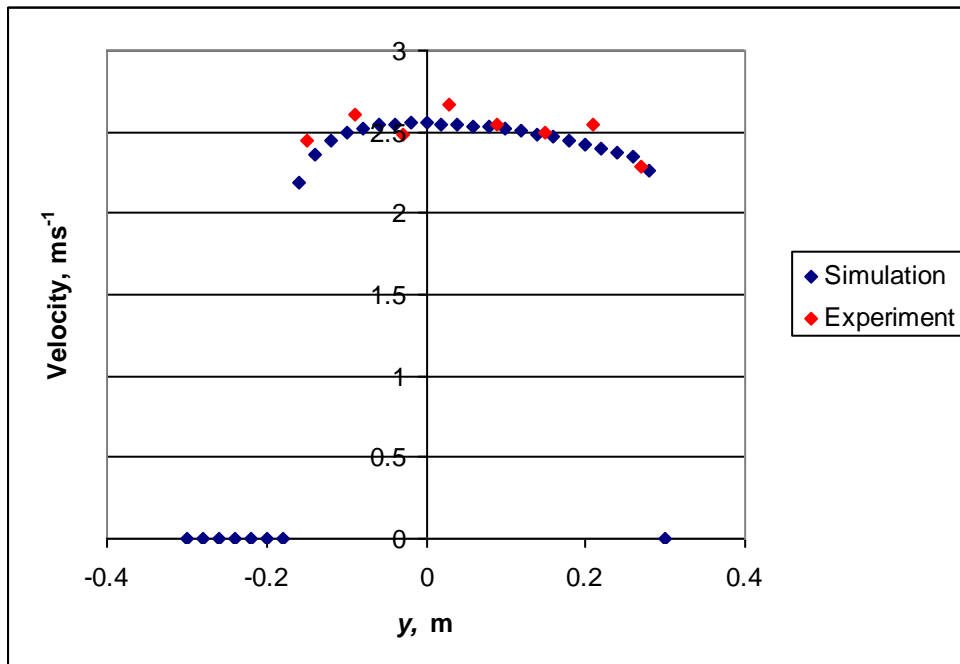


Fig. 7.13: Comparison with experimental data for Profile Set ①

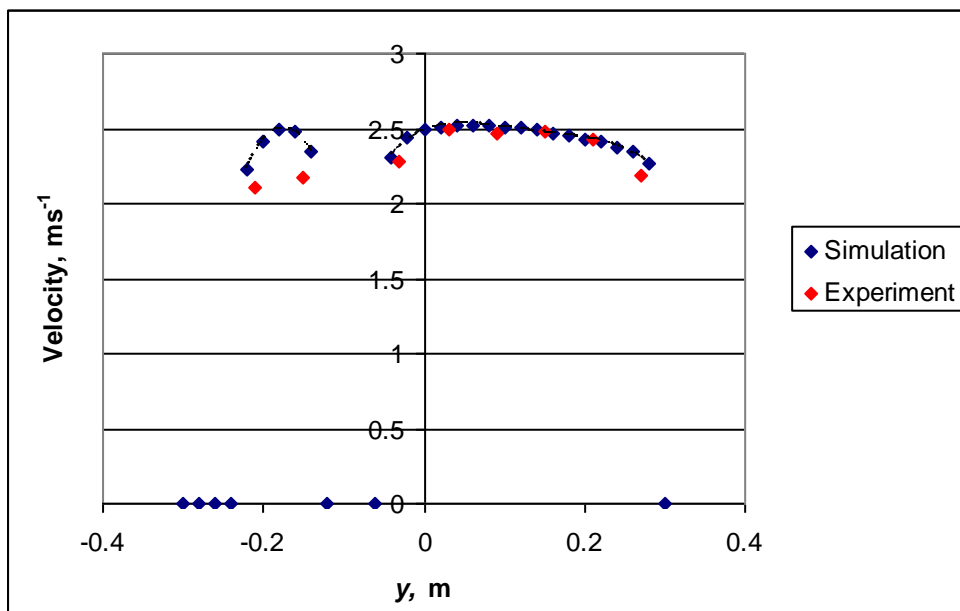


Fig. 7.14: Comparison with experimental data for Profile Set ②

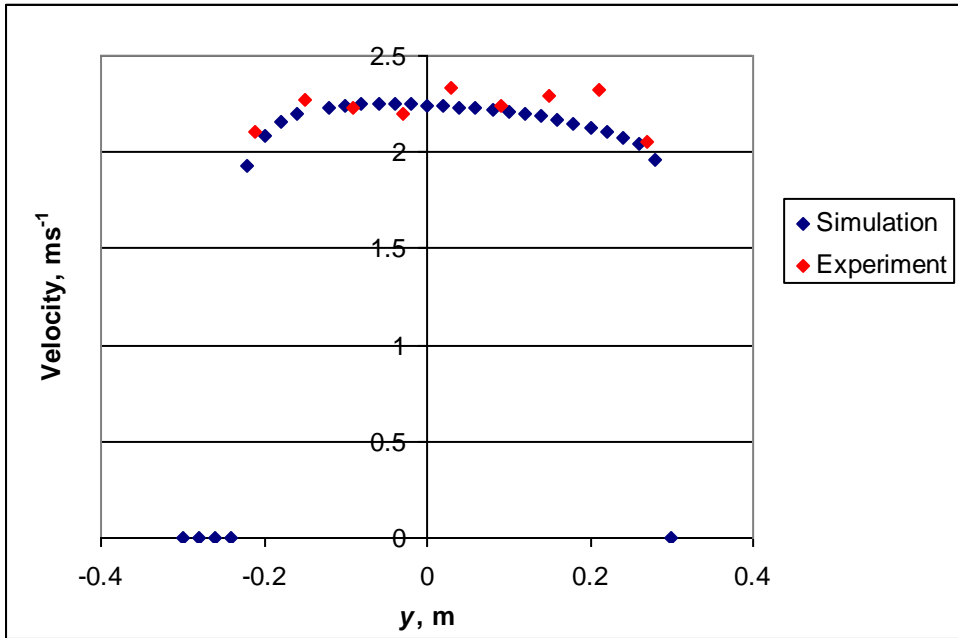


Fig. 7.15: Comparison with experimental data for Profile Set ④

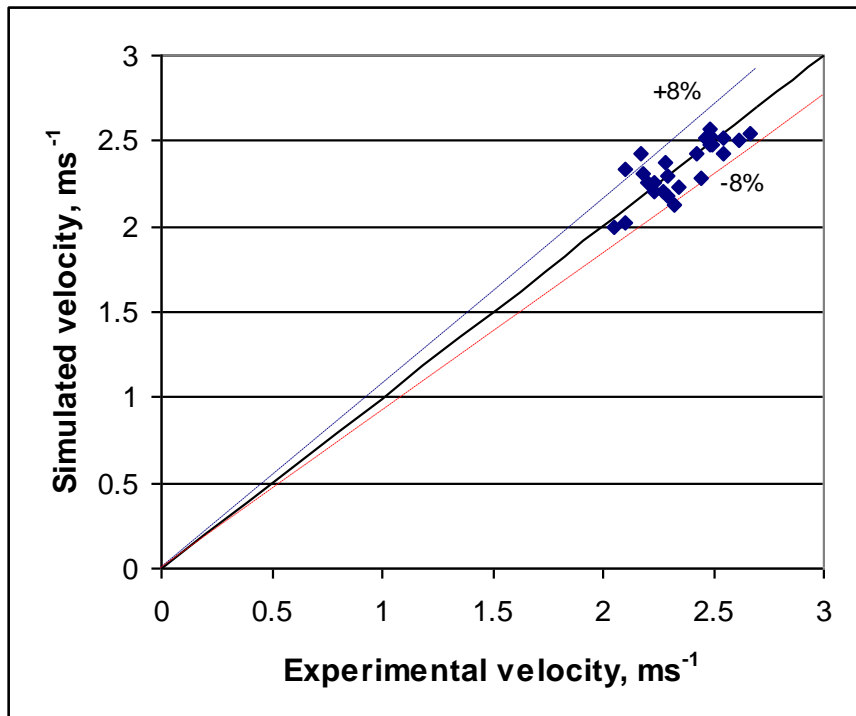


Fig. 7.16: Parity plot comparing simulated and experimental velocity data

With the model validated, the simulated results of the velocity profile could now be used to predict the thermal performance degradation. From the individual simulated node velocities on the coil face area, the normalized profile was calculated, from which the statistical moments were determined. The thermal degradation factor, D , could then be calculated by means of correlation equations (5.11) or (5.13), or by inputting the normalized velocities directly into the discretization procedure described in Chapter 4.

However, it was noted that the nodes on the coil face area in the simulation model formed a 29 x 13 grid instead of the 10 x 10 size used in the previous analysis. As an example, the statistical moments calculated from the simulation grid for maldistribution Profile ② are shown in the following Table 7.5. For comparison purpose, the moments from the corresponding 10 x 10 experimental grid are also tabulated together. The data show a good agreement for the standard deviation and skew between the two, i.e. the simulation has given a correct representation of the actual maldistribution imposed on the coil. In addition, the results in Table 4.2 have already shown the independence of the analysis from the computation grid size.

Table 7.5: Comparison between simulated and experimental normalized moments for maldistribution Profile②

	Numerical simulation (29 x 13 grid)	Experimental data (10 x 10 grid)
Mean	1.00	1.00
Standard deviation	0.515	0.508
Skew	-1.422	-1.452

The CFD simulation could then be repeated for other coil geometries, e.g. for different fin pitches and number of tube rows. For each configuration, the pressure drop characteristics must be known so that the equivalent porous media resistances could be determined. In general, smaller fin pitches and deeper coils have higher pressure drops. Fig. 7.17 shows experimental pressure drop data for two other coils as compared to the single row coil described in Fig. 7.3.

The simulation could also be repeated to determine the velocity distribution profile caused by other flow blockage patterns. These patterns could represent the blockages or flow diversions found in actual applications of the fin-tube heat exchanger. Some examples are illustrated in Fig. 7.18. In any case, the statistical moments would be determined from the simulated velocity profile to predict the thermal degradation factor.

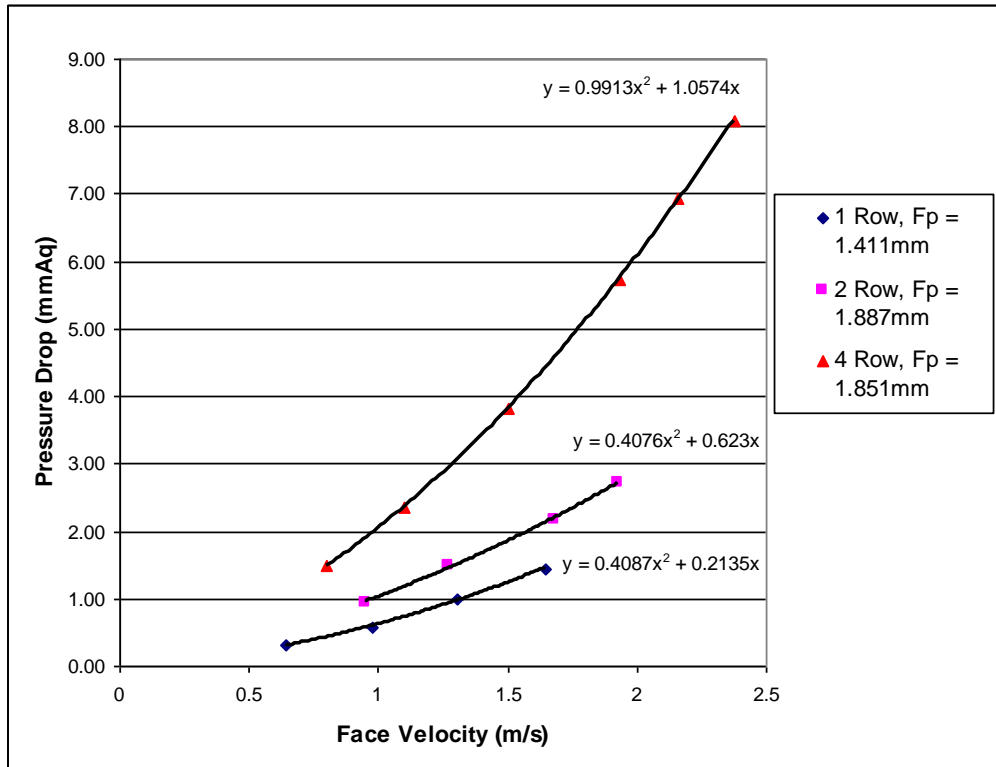


Fig. 7.17: Experimental pressure drop data for other coil configurations

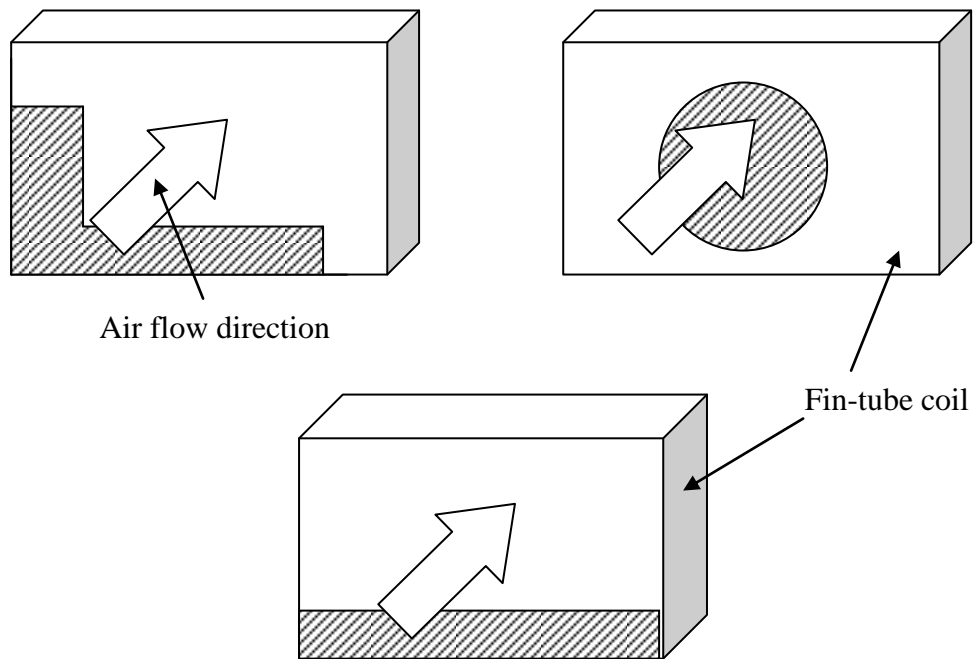


Fig. 7.18: Examples of other flow blockage patterns (shaded)

7.11 Simulation of thermal performance

The simulations described in the previous sections were done without solving the energy equation (7.9). In the work described in this section, the energy equation was switched on, which allowed the solution of the temperature distribution as air flowed through the hot fin-tube coil. Inasmuch as the solution of the velocity field would be sufficient to predict the heat exchanger thermal degradation performance, knowledge of the temperature field would be useful for two reasons:

1. The temperature distribution would enable identification of any hot-spots (or cold-spots) downstream of the heat exchanger. These temperature limits could be used to check the operability of certain components located in the downstream flow. For example, motors and electronic PCBs should not operate beyond the maximum permissible ambient temperature specified by the manufacturers.
2. The leaving air temperature would allow the heat exchanger heating capacity to be calculated. Hence, the CFD thermal simulation could be an alternative method to determine the thermal degradation effect due to flow maldistribution.

However, the porous media model in FLUENT does not have the capability of simulating convective heat transfer as air flows through it. Therefore, in order to facilitate such simulation studies, the fin-tube coil was represented instead with the user-defined Heat Exchanger Model available in FLUENT [121].

7.11.1 Settings in Heat Exchanger Model

In the Heat Exchanger Model, the convective heat transfer characteristics of the coil is described with the heat exchanger effectiveness, ε . A list of effectiveness values has been established, with the aid of the j -factor correlation equation (6.13), at different magnitudes of air inlet face velocity, V_f , for the single row fin-tube coil studied in this work. These values are plotted as shown in Fig. 7.19 and entered into the model in FLUENT.

The pressure drop through the heat exchanger core is characterized in the Heat Exchanger Model with the friction factor, f [122]:

$$f = \frac{A_c}{A_o} \frac{v_{in}}{v_m} \left[\frac{2\Delta p}{G_a^2 v_{in}} - (K_c + 1 - \sigma_r^2) + (1 - \sigma_r^2 - K_e) \frac{v_{out}}{v_{in}} - 2 \left(\frac{v_{out}}{v_{in}} - 1 \right) \right] \quad (7.15)$$

where K_c = entrance loss coefficient due to abrupt contraction and K_e = exit loss coefficient due to abrupt expansion. σ_r is the ratio of the heat exchanger minimum flow area to the face area while A_c is the minimum cross-section flow area. The mean air specific volume, v_m , is calculated as the average between the inlet and outlet, i.e.

$$v_m = \frac{1}{2}(v_{in} + v_{out}) \quad (7.16)$$

By using the same experimental data for the fin-tube coil as shown in Fig. 7.3, the friction factor was calculated and plotted against the Reynolds number, Re_{Dh} , for the maximum velocity at the minimum flow area, V_{max} , i.e.

$$Re_{Dh} = \frac{\rho_a V_{max} D_h}{\mu_m} \quad (7.17)$$

The maximum velocity was calculated as:

$$V_{max} = \frac{V_f}{\sigma_r} \quad (7.18)$$

while the hydraulic diameter, D_h , was calculated with the following equation [119]:

$$D_h = \frac{4A_c L}{A_o} \quad (7.19)$$

where L is the flow length.

The loss coefficients have been adjusted to match the viscous (R_μ) and inertia (R_I) resistances determined earlier as the porous media equivalent characteristics. The values for these coefficients were determined to be $K_c = 0.195$ and $K_e = 0.02$.

With these, the friction factor was calculated and plotted against Re_{Dh} . A power exponent relationship was used to fit the data, as indicated on Fig. 7.20. Both the coefficient and exponent from this equation were then entered into the Heat Exchanger Model in FLUENT.

From the geometry of the fin-tube heat exchanger, the following parameters were also specified in the model:

- Minimum flow to face area ratio (σ_r) = 0.558
- Gas-side (i.e. air-side) surface area = 4.331 m²
- Minimum cross-section flow area = 0.0795 m²

In the model, air was considered as the primary fluid while water was the auxiliary fluid. The heat exchanger itself was split into several discrete macros which were constructed based on the specified number of passes, number of macro rows per pass and number of macro columns per pass for the auxiliary flow. For consistency with the single row coil studied earlier, 10 passes were specified with 10 rows per pass and 1 column per pass. The following Fig. 7.21(a) illustrates the 10 x 10 x 1 macros built. The origin of the Cartesian coordinate system was at the center of the coil. The water direction in the tubes was set along the y -direction while the pass-to-pass direction was in the z -direction. Consequently, the water flowed in an upward serpentine circuit in the model as shown in Fig. 7.21(b).

In the simulation, the air temperature in the domain was set at 303K (30°C) while the inlet water temperature was 323K (50°C). The air and water mass flow rates were 0.376 kgs⁻¹ and 0.3 kgs⁻¹ (i.e. water volume flow rate of 1.1 m³hr⁻¹ at 50°C), respectively.

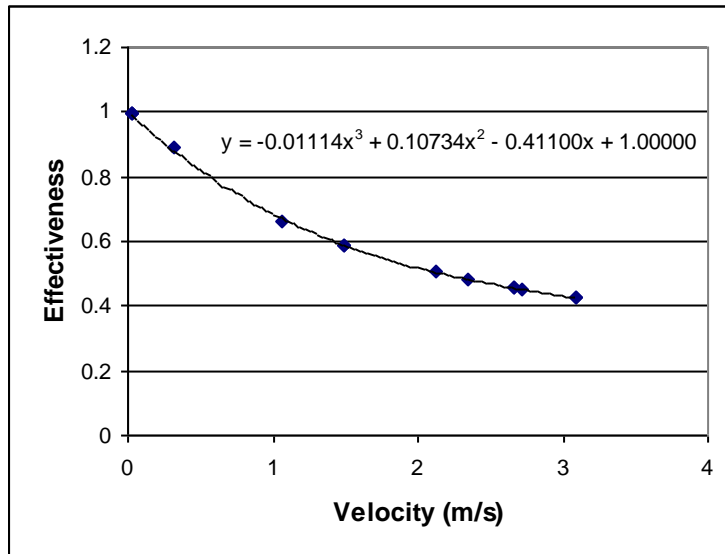


Fig. 7.19: Effectiveness of fin-tube coil

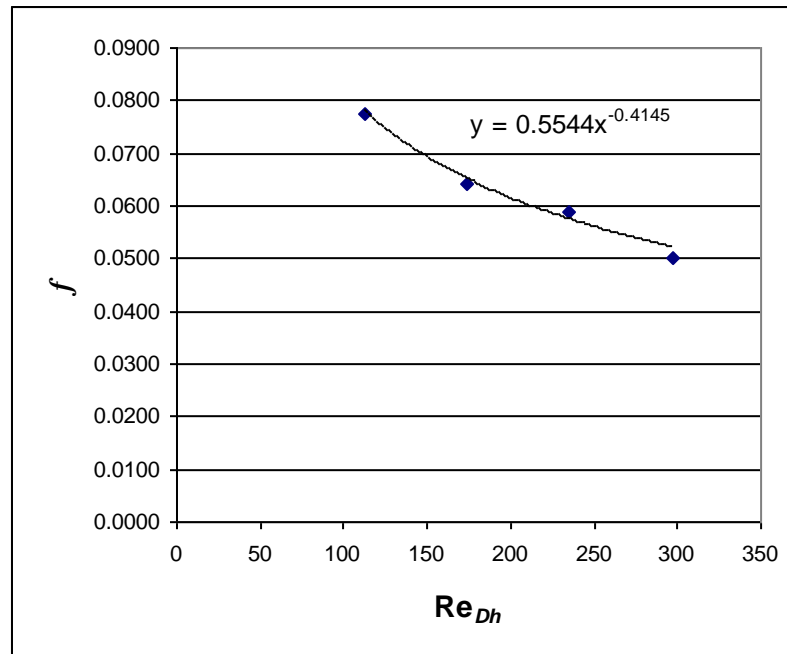


Fig. 7.20: Plot of friction factor vs. Re_{Dh}

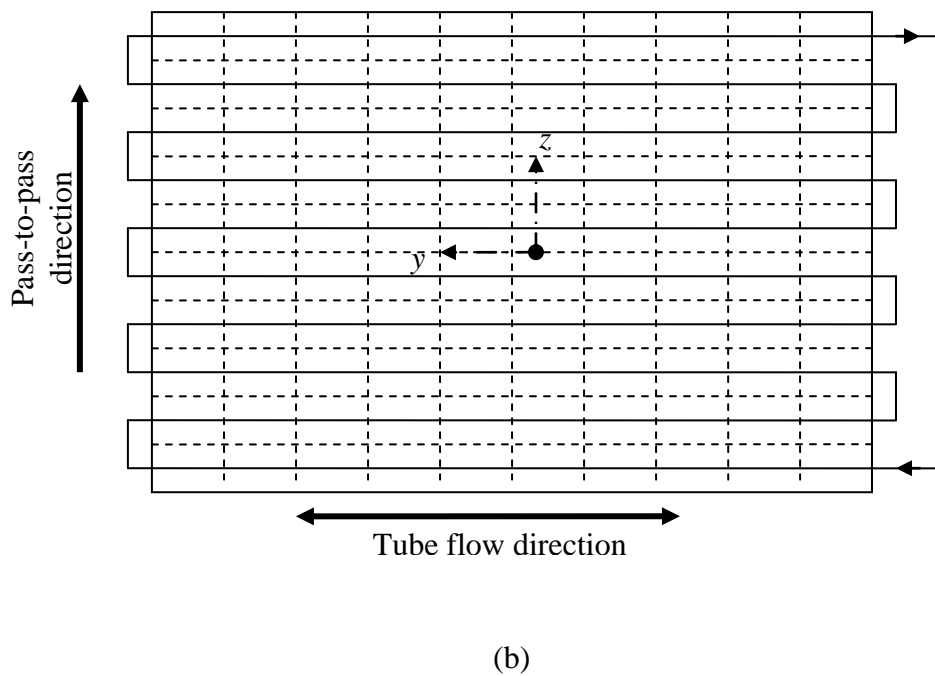
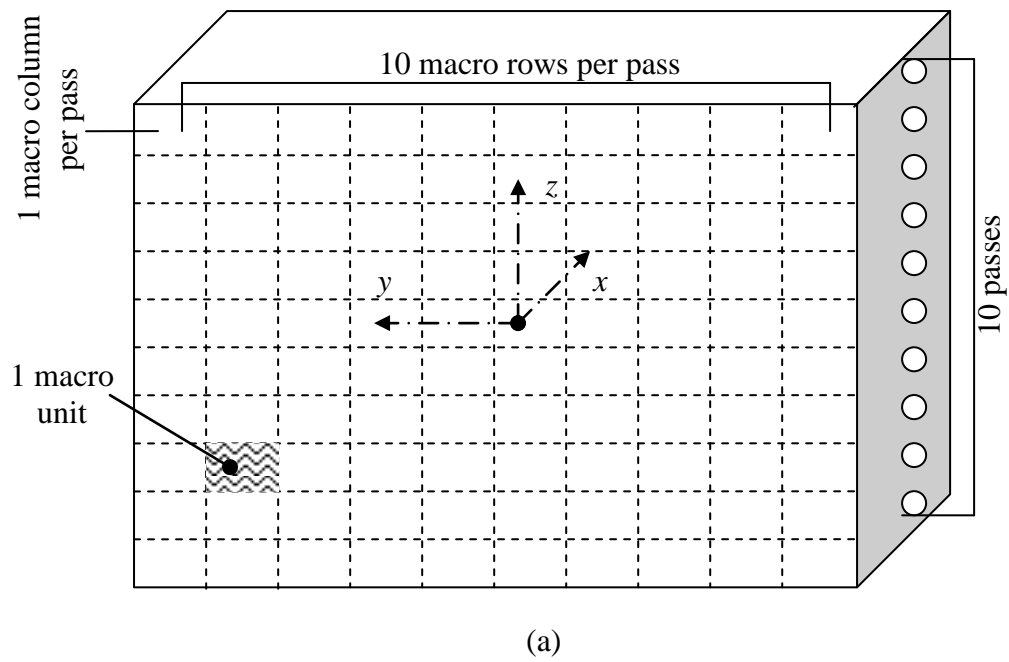


Fig. 7.21: 10 x 10 x 1 macros set in Heat Exchanger Model (a) Illustration of macro row and macro pass (b) Illustration of flow direction in the model

7.11.2 Results of simulation

The thermal performance simulation was performed for both uniform and maldistributed flows. For the case of maldistributed flows, Profile Set ①, ②, ③ and ④ were chosen for the simulation.

The same set of boundary conditions and turbulence model were also used for the thermal simulation. Similarly, the same convergence criterion of 10^{-6} was set for continuity, momentum, turbulence $k-e$ and energy. A second-order discretization scheme was used in the energy equation for enhanced accuracy of the temperature results while the first-order was maintained for continuity and momentum.

The result of the leaving air temperature from the coil surface for uniform distribution is shown in Fig. 7.22. It can be clearly seen that the temperature is the highest near the duct walls which have low or zero air velocities. This is further illustrated with a temperature plot along the y -axis centerline of the duct ($z = 0$) as shown in Fig. 7.23 which shows a non-symmetrical profile. This is due to the reducing water temperature as it flows along the serpentine tube circuit.

The simulation results for maldistribution Profile Set ①, ② and ④ are shown in the following Fig. 7.24, 7.25 and 7.26. From the data, the mass-averaged temperatures of air leaving the coil for each case have been calculated and are tabulated in Table 7.6. The thermal degradation factor, D , is then estimated with the following equation for all maldistribution profiles, which are also summarized in the same table:

$$D = \frac{(T_{a,out,u} - T_{a,in}) - (T_{a,out,m} - T_{a,in})}{(T_{a,out,u} - T_{a,in})} \quad (7.20)$$

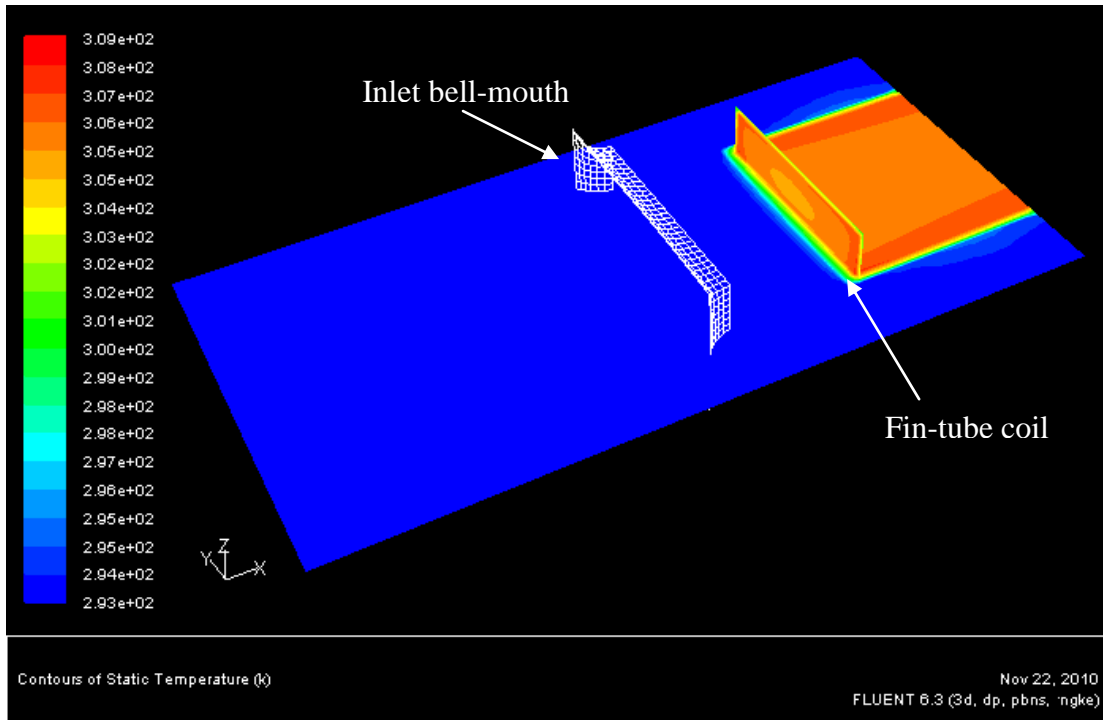


Fig. 7.22: Temperature contour of leaving air for uniform flow distribution

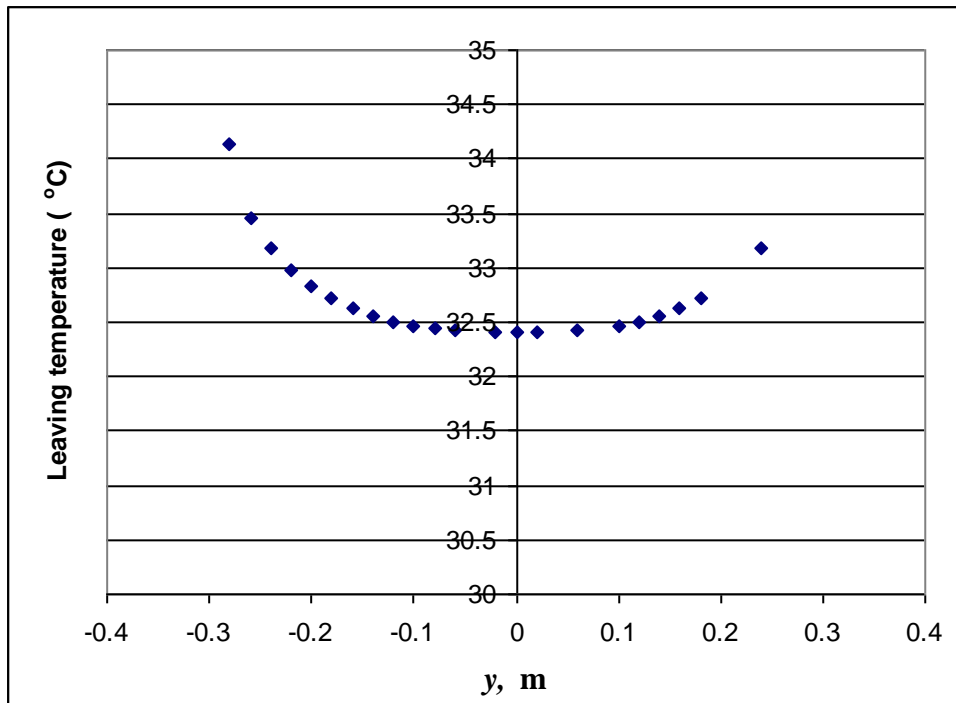


Fig. 7.23: Temperature plot along the y-axis at z = 0 (Uniform flow distribution)

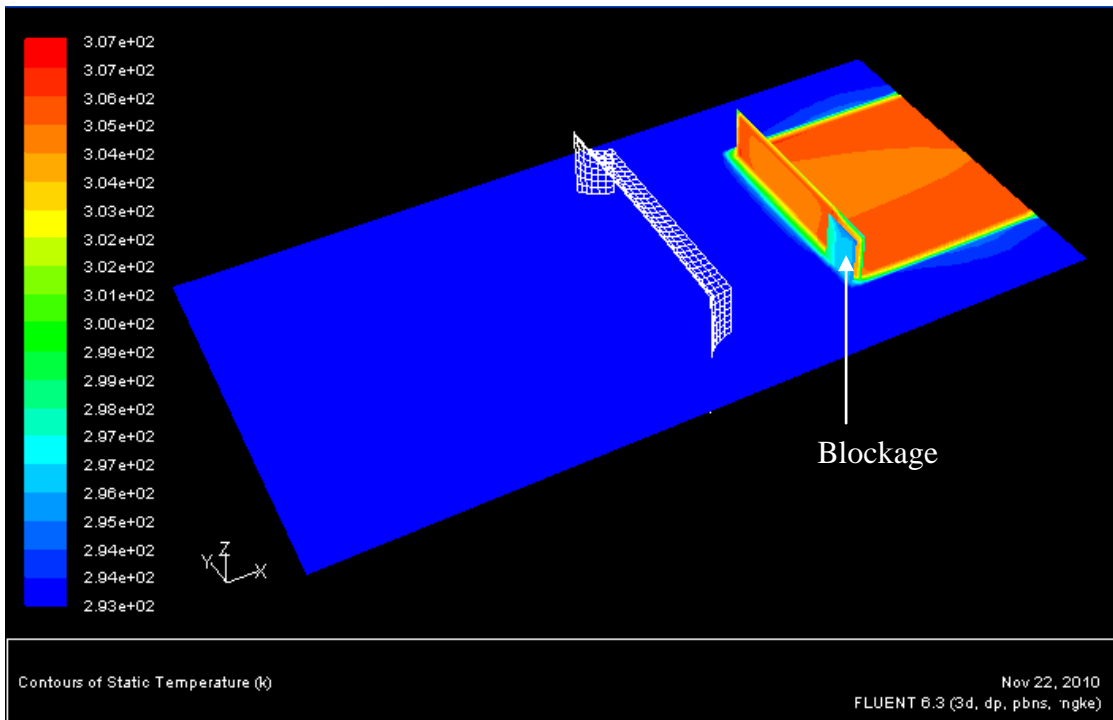


Fig. 7.24: Temperature contour for maldistribution Profile ①

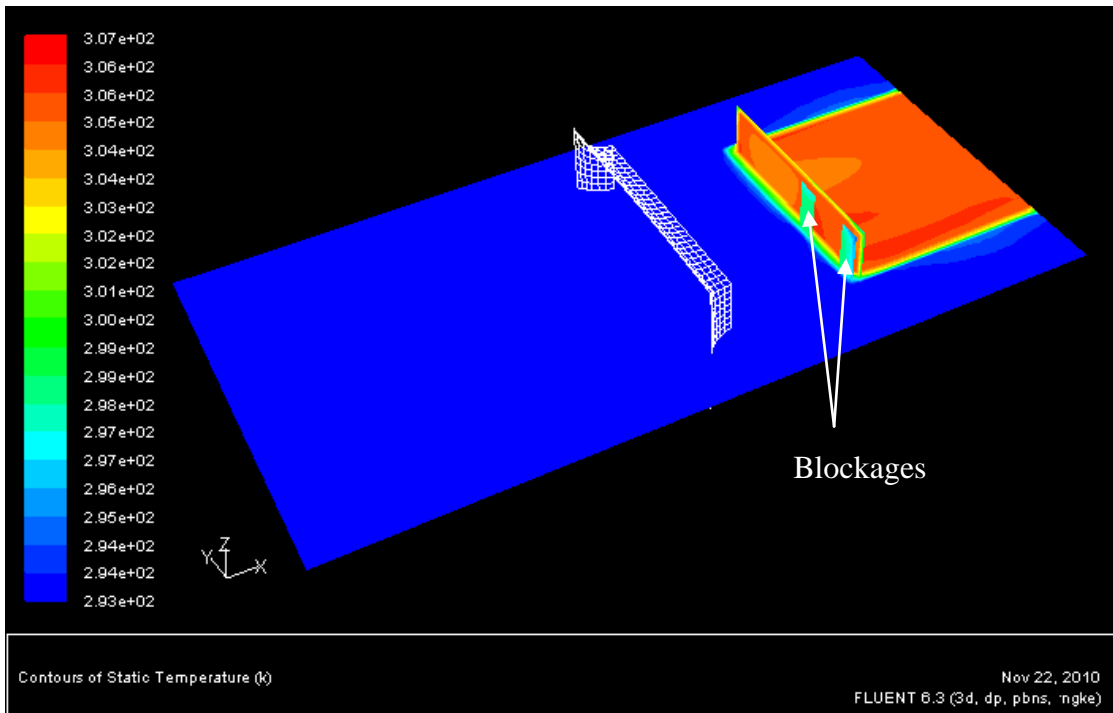


Fig. 7.25: Temperature contour for maldistribution Profile ②

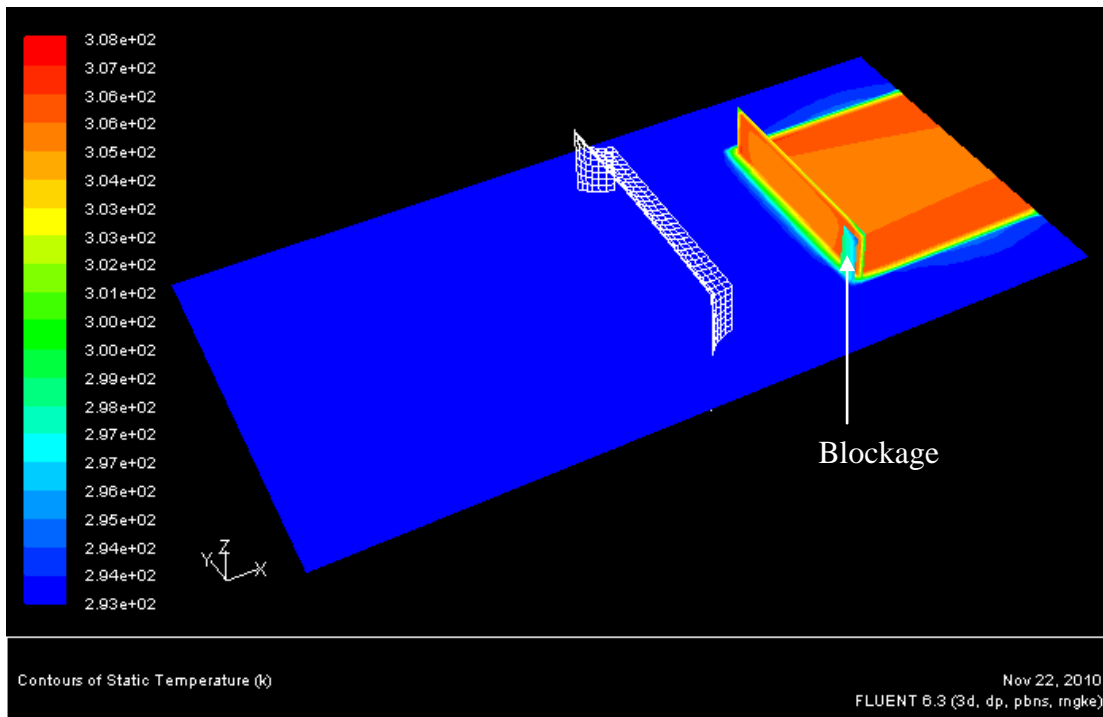


Fig. 7.26: Temperature contour for maldistribution Profile ④

Table 7.6: Results of simulated outlet air temperature and D

	Mass-average $T_{a,out}$, K	D , %
Uniform	312.2	-
Profile ①	311.4	8.7%
Profile ②	311.4	8.7%
Profile ③	311.6	6.5%
Profile ④	311.8	4.3%

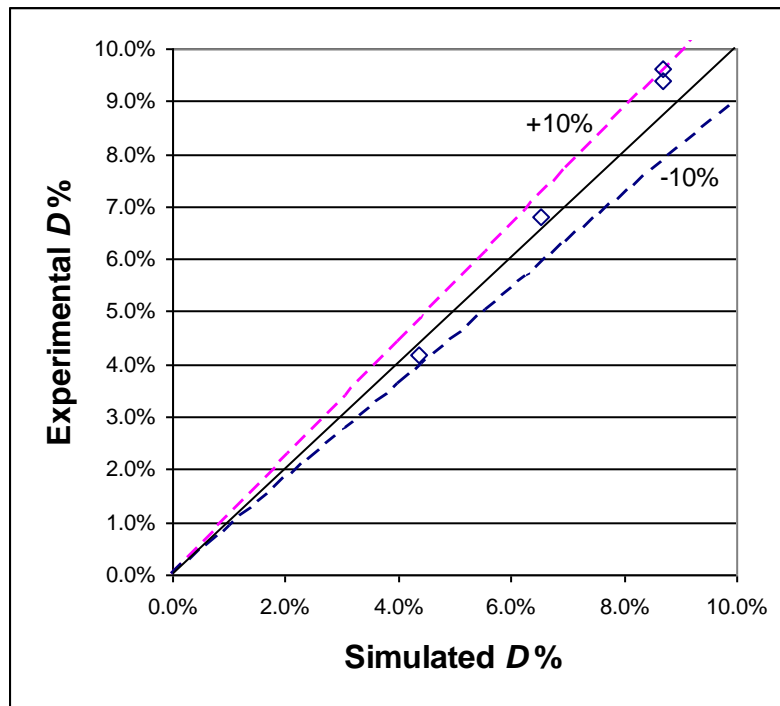


Fig. 7.27: Comparison between simulated and experimental D

These simulated values of D are then compared with the corresponding experimental results reported in Chapter 6. This comparison is shown in Fig. 7.27. It is evident from the comparison that the simulation and experimental methods have good agreement with each other, within $\pm 10\%$, in determining the magnitude of D for the maldistribution problem. With this, it is concluded that the CFD simulation method with the Heat Exchanger Model has been validated.

Subsequent to this, the simulation was then repeated for fin-tube coils with multiple tube rows. To do this, the heat exchanger is modeled by splitting the multiple rows coil into individual single row coils. The FLUENT Heat Exchanger Model is then applied to each of these single row coils. For the study, two-row and four-row coils were modeled. Fig. 7.28 illustrates an example of the four-row coil used in the simulation. In the model, the air exiting the upstream row became the inlet condition to the subsequent row.

The simulation for the multiple tube rows was performed with the same fluid inlet temperatures and boundary conditions used previously. The mass-averaged leaving air temperature was obtained for both uniform and maldistributed cases (i.e. Profile ①, ② and ④) and D calculated with equation (7.20). The simulation results were then compared with calculation results from the discretization technique described in Chapter 4, where the measured velocity profiles on the coil were used. This comparison is shown in the parity plot of Fig. 7.29. A similar agreement within $\pm 10\%$ is seen from this plot.

Hence, the agreement of all these results has demonstrated the possibility of using CFD simulation to predict the thermal performance degradation due to flow maldistribution. Such simulations can be done for any geometrical specifications of the heat exchanger and for any design layout of the exchanger with respect to other components, so long as the convective and pressure drop characteristics of the exchanger are known beforehand.

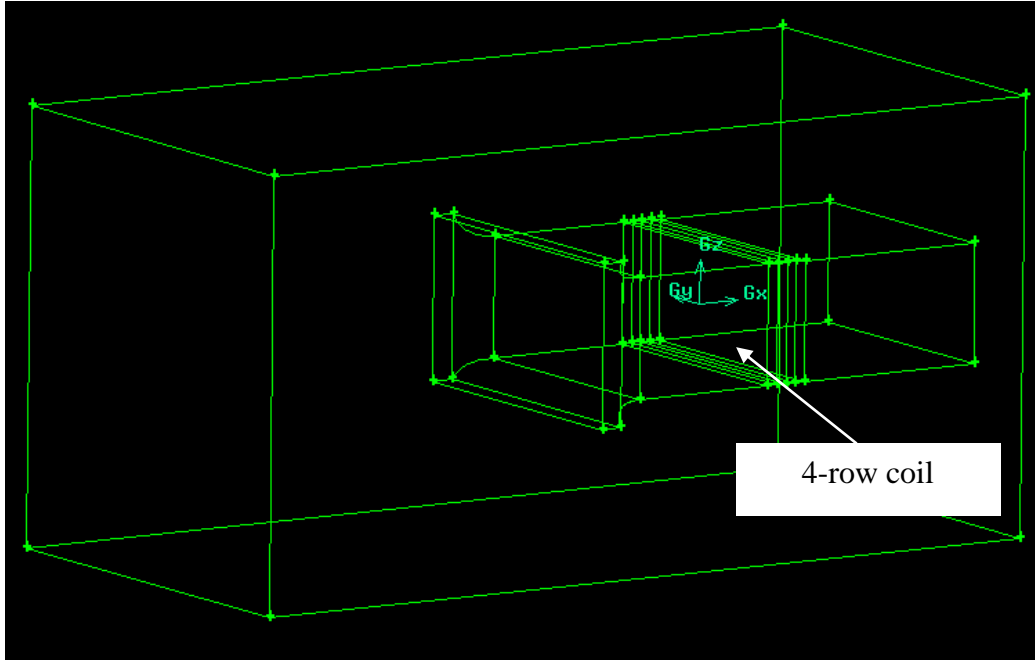


Fig. 7.28: Model of test duct with 4-row fin-tube coil

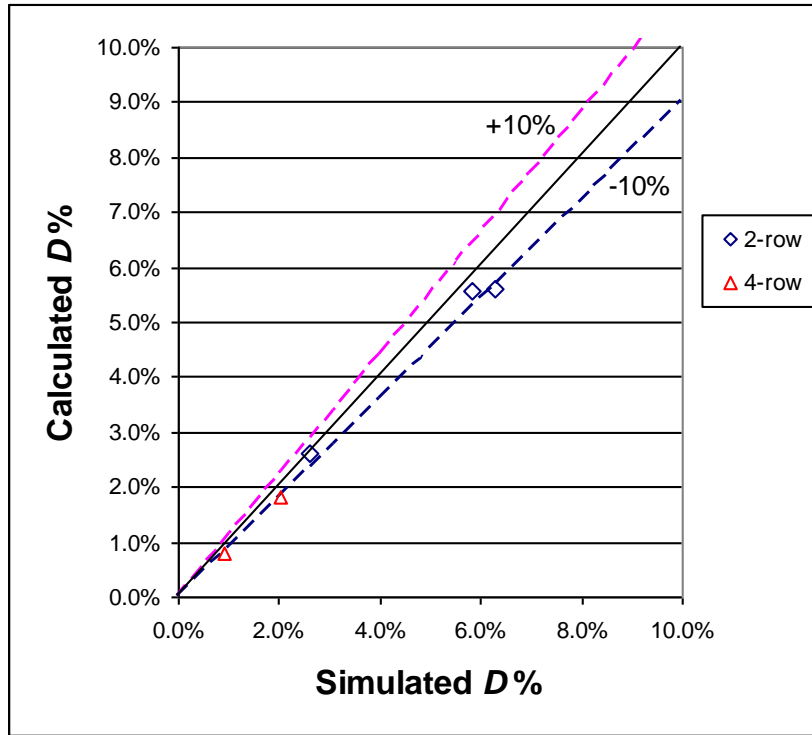


Fig. 7.29: Parity plot between simulated and calculated D for 2-row and 4-row coils

7.12 Summary

The work presented in this section has shown the applicability of CFD simulation to predict the thermal performance degradation of a fin-tube heat exchanger. The commercial CFD code, FLUENT, has been used for the study. Essentially, there are two possible ways this can be done:

- a) The continuity and momentum equations are solved to determine the velocity flow field on the heat exchanger. The normalized statistical moments are computed from the profile and inputted into the thermal degradation factor, D , correlation equation. Alternatively, the computed node velocities of the profile are used in the discretized calculation procedure to determine the magnitude of D . The results of the simulation have shown a good agreement within $\pm 10\%$, with a mean deviation of 4%, between the simulation and actual experimental data for the maldistributed velocity profile.
- b) By solving the energy equation simultaneously with the continuity and momentum equations in the simulation, the temperature field of the heat exchanger is obtained from the simulation. From the computed leaving air temperature and known inlet temperature, the magnitude of D can be calculated. The results have shown good agreement of the simulation with both experimental and analytical data within $\pm 10\%$.

In comparison, the first method is easier to implement where the convective heat transfer characteristics of the fin-tube coil is not required to be known. The convergence time for this method is also faster since there is less number of equations to be solved.

In short, CFD simulation is a useful tool for the analysis of flow maldistribution on fin-tube heat exchangers. The results of the simulation would enable the design of the exchanger to be improved and optimized without the need for expensive experimentation.

CHAPTER 8

CONCLUSION

8.1 Review of findings

The research has established the relationship between the thermal performance degradation of a heat exchanger arising from flow maldistribution and the four statistical moments of probability density function for the maldistribution profile. A novel mathematical derivation, based on the Taylor series expansion of the governing equation for convective heat transfer, i.e. Newton's law of cooling, and core fluid pressure drop, has shown the dominant effect of the mean and standard deviation of the maldistribution on performance degradation. These represent the first and second moments of the probability density function. The third moment, i.e. skew, was shown to have declining influence on the performance degradation while the fourth moment, kurtosis, was found to have insignificant effect.

The magnitude of thermal performance degradation was quantified with the degradation factor, D . With the aid of a discretization calculation technique, the D factor for a single row fin-tube heat exchanger was calculated for a range of maldistribution moments. By normalizing the moments with the mean, it was shown that D varies to the cube of NTU and normalized standard deviation. D also varies linearly with the normalized skew for standard deviation lower than 0.40, but varies to the square of normalized skew at higher standard deviations.

In addition, the analysis has revealed the dependence of D on the relative magnitudes of the external and internal thermal resistances. This was represented with the ratio of external to internal heat transfer coefficients, R . The thermal performance degradation D was observed to vary to the square of R . In general, higher external heat transfer coefficients tend to sensitize the exchanger surfaces to maldistribution effects, i.e. to increase the magnitude of D . However, higher internal heat transfer

coefficients tend to offset the external degradation effects as the heat transfer through the tube walls increases.

With these findings, the first objective of this research has been achieved. A full physical understanding of the effects of the moments on the thermal performance of fin-tube heat exchangers has been obtained and quantified. This work has also been the first to account for the contribution of higher moments, i.e. skew and kurtosis, to the maldistribution problem.

To achieve the second research objective, the effects of typical fin-tube heat exchanger geometrical parameters on D have also been investigated. These include the number of tube rows, fin pitch, tube pitch, tube diameter and fin surface pattern. The results have clearly indicated the significance of the number of tube rows and fin pattern on the magnitude of D . In as much as the other parameters have weak or insignificant effects, the trend of the data show that the parameter which increases the external heat transfer coefficient results in an increase of D due to the sensitization of the surfaces to maldistribution effects.

With all these effects identified and quantified, a set of new correlation equations has been developed based on the observed trends, to calculate the D factor for a known combination of maldistribution moments and heat exchanger geometry. These equations have also been the first set of comprehensive correlations developed which allow the prediction of performance degradation for any maldistribution profile. However, the correlations are only valid for a specific type of fin surface pattern, i.e. wavy fins. New correlations must be formulated for other patterns, for example, louvered and slot fins. With the same methodology, specific correlations may be developed for other types of heat exchangers.

To validate the analysis methodology and correlations, a series of experiments has been performed where the heat transfer degradation and maldistribution moments were measured. With a good coherence of $\pm 10\%$ between the experimental and calculation results, and the corresponding $\pm 15\%$ agreement between experiment data and correlation predictions, the third research objective has been achieved. A better coherence with the correlation would be possible by including the weaker geometrical

parameters into the equation, though these would result in a more complicated form of correlation.

The primary motivation for developing such correlations was to have a design tool which would enable the optimization of thermal performance by changing the layout design of the fin-tube coil. The relative positioning of the coil with respect to other components in a system, whether upstream or downstream of the air flow, could be changed to give a flow maldistribution with lowest possible standard deviation and highest skew. However, it was also pointed out that this must be done in conjunction with an analysis of the increase in fluid pressure drop. From the perspective of hydraulic performance degradation, the maldistribution should have the lowest possible skew. Therefore, there would be an optimum skew where a maximum ratio of heating capacity to the pumping power, Q/P_w would occur, as shown in Fig. 3.11. This optimum performance would then contribute to higher system energy efficiencies.

To this end, Computational Fluid Dynamics (CFD) simulation would be useful to determine the maldistributed velocity profiles on the exchanger coil. The extracted moments from the simulation results could be used to calculate the magnitude of D . Alternatively, the value of D could be calculated directly from the simulated entering and leaving air temperatures. With this method, the design of the heat exchanger could be repeated many times with different layouts without the need for expensive prototyping and experimentation.

To demonstrate the above, a numerical simulation of the experimental test set-up was performed by using the commercial CFD code FLUENT. A good agreement within $\pm 8\%$ was obtained between the simulated and experimental maldistributed velocity profiles. Similarly, a good agreement with $\pm 10\%$ was obtained between the simulated and experimental values of D . Essentially, the good agreement among the three; analytical, experimental and simulation methods in the study, has confirmed the validity of the analysis methodology for this research.

In short, the fundamental research done in this work has provided the solution to an engineering problem commonly faced by the HVAC and automotive industries.

The correlations developed allow a quick method to estimate the heat exchanger performance degradation once the maldistribution profile is known. This method can be easily adopted and applied by the industry in their design work to improve the energy efficiency of their products.

8.2 Recommendations for future research

The study in this research was conducted based upon an assumption of constant tube wall temperature in the heat exchanger. In actual applications, this assumption rarely occurs. Therefore, to be more realistic, the analysis of the maldistribution problem could be extended to study the effects of varying temperature on the fin surfaces. To do this, the inlet and outlet fluid temperatures in the tube for each discrete coil element must be calculated and the effect on D determined.

Similarly, the inlet air temperature was held constant during the analysis. The calculation of the D factor could be repeated by imposing a maldistributed temperature profile simultaneously with the maldistributed flow velocity. In other words, a combined maldistribution analysis could be performed in future research work. Obviously, corresponding experimentation must be done to validate the findings. However, the challenge would be in generating the non-uniform air temperature profile during the experiment.

The experimentation was also done by imposing flow blockages on the fin-tube coil inlet face area which created discontinuous velocity maldistribution profiles. In actual applications, the flow maldistribution profile would be continuous. Therefore, further work could be done by repeating the experimentation with the blockages located at some distances upstream or downstream of the heat exchanger to simulate continuous non-uniform profiles. The validity of the developed correlations could then be checked for such situations.

The research presented in this thesis has only dealt with the degradation of heat exchanger thermal performance. The degradation of hydraulic performance was not evaluated and quantified in detail. Hence, future research could also look into

developing similar correlation equations to predict the pumping power penalty factor, P_p , for a range of statistical moments and coil geometry.

Lastly, the maldistribution in the tube-side of the heat exchanger could also be studied in future research. The same analysis approach could be used to evaluate the influence of statistical moments for the tube-side maldistribution. Furthermore, the combined effect of both air-side and tube-side maldistributions could be studied since maldistributions in both fluid streams of the exchanger would occur in actual applications.

With these recommendations, a full understanding of the maldistribution problem in heat exchangers would be achieved. These findings would be useful for designers to optimize the performance of any heat exchanger and with any maldistribution profile. For practical implementation, CFD should be used to simulate and extract the maldistribution statistical moments for analysis of the degradation effect.

REFERENCES

- [1] U.S. Energy Information Administration. (2009, September). Country Analysis Briefs: Malaysia. [Online]. Available:
<http://www.eia.doe.gov/emeu/cabs/Malaysia/Full.html>
Date last accessed: 6th June 2011
- [2] A. Zain-Ahmed. Contemporary Issues in Energy and Buildings in Malaysia: Focus on R&D and Policies, presented at *SENVAR +ISESEE 2008*. [Online]. Available:
<http://www.scribd.com/doc/13455256/CONTEMPORARY-ISSUES-IN-ENERGY-AND-BUILDINGS-IN-MALAYSIA-FOCUS-ON-RD-AND-POLICIES>
Date last accessed: 7th June 2011
- [3] L. Perez-Lombard, J. Ortiz, C. Pout, “A Review on Buildings Energy Consumption Information,” *Energy & Buildings*, vol. 40, pp. 394-398, 2008
- [4] J. H. Wood, G. R. Long, D. F. Morehouse, U.S. Energy Information Administration. (2004, August). Long-term World Oil Supply Scenarios: The Future is neither as Bleak or Rosy as Some Assert. [Online]. Available:
http://www.eia.doe.gov/pub/oil_gas/petroleum/feature_articles/2004/worldoilsupply/oilsupply04.html
Date last accessed: 6th June 2011
- [5] U.S. Energy Information Administration. (2009, September). NYMEX Futures Prices. [Online]. Available:
http://tonto.eia.doe.gov/dnav/pet/pet_pri_fut_s1_d.htm
Date last accessed: 14th June 2011
- [6] EUR-Lex. (1992, September). Council Directive 92/75/EEC on the Indication by Labelling and Standard Product Information of the Consumption of Energy and Other Resources by Household Appliances. [Online]. Available:
<http://eur-lex.europa.eu/LexUriServ/LexUriServ.do?uri=CELEX:31992L0075:EN:NOT>

Date last accessed: 6th June 2011

- [7] Department of Climate Change and Energy Efficiency, Australia. (2009, October). Requirements for Air Conditioners - Program Overview and Test Procedures. [Online]. Available: <http://www.energyrating.gov.au/rac1.html>

Date last accessed: 14th June 2011

- [8] Asia-Pacific Economic Corporation, Energy Standard Information System. (2010, July). The Hong Kong Mandatory Energy Efficiency Labelling Scheme (EELS) for Room Air-conditioners. [Online]. Available: <http://www.apec-esis.org/>

Date last accessed: 14th June 2011

- [9] Government of Singapore. (2008, January). Environmental Protection and Management Act (Chapter 94A, Section 77), Environmental Protection and Management (Energy Conservation) Regulation. [Online]. Available: <http://app2.nea.gov.sg/data/cmsresource/20090316653072840750.pdf>

Date last accessed: 14th June 2011

- [10] Malaysian Green Technology Corporation. (2010). Energy Rating & Labelling. [Online]. Available: <http://www.ptm.org.my/index.php/energy/energy-efficiency/energy-rating-labelling.html>

Date last accessed: 14th June 2011

- [11] A. C. Mueller., “Effects of Some Types of Maldistribution on the Performance of Heat Exchangers,” *Heat Transfer Eng.*, vol. 8, no. 2, pp. 75-86, 1987
- [12] A. C. Mueller, J. P. Chiou, “Review of Various Types of Flow Maldistribution in Heat Exchangers,” *Heat Transfer Eng.*, vol. 9, no. 2, pp. 36-50, 1988
- [13] A. M. Whistler, “Effect of Leakage around Cross-baffles in a Heat Exchanger,” *Pet. Refiner*, vol. 26, no. 10, pp. 114-118, 1947
- [14] T. Tinker, “Shell Side Characteristics of Shell and Tube Heat Exchangers,” in *ASME-IME 1st Int. Heat Transfer Conf.*, London, 1951, pp. 89-116
- [15] H. Gotoda, S. Izumi, “A Modern Condenser Design,” in *Proc. Inst. Marine Eng.*, 1977, pp. 253-273

- [16] J. P. Chiou, "Thermal Performance Deterioration in Crossflow Heat Exchanger due to the Flow Nonuniformity," *ASME Journal of Heat Transfer*, vol. 100, pp. 580-587, 1978
- [17] J. P. Chiou, "The Effect of Nonuniformities of Inlet Temperatures of Both Fluids on the Thermal Performance of a Crossflow Heat Exchanger," ASME Paper no. 82-WA/HT-42, 1982
- [18] C. H. Ranganayakulu, K. N. Seetharamu, K. V. Sreevatsan, "The Effects of Inlet Fluid Flow Non-uniformity on Thermal Performance and Pressure Drops in Cross-flow Plate-Fin Compact Heat Exchangers," *Int. J. Heat and Mass Transfer*, vol. 40, no. 1, pp. 27-38, 1987
- [19] R. J. Berryman, C. M. B. Russell, "The Effect of Maldistribution of Air Flow on Air-cooled Heat Exchanger Performance," in: *Maldistribution of Flow and Its Effect on Heat Exchanger Performance*, vol. 75, J. B. Kitto and J. M. Robertson, Eds. New York, ASME, 1987, pp. 19-23
- [20] M. K. Bassiouny, H. Martin, "Flow Distribution and Pressure Drop in Plate Heat Exchangers – I U-type Arrangement," *Chem. Eng. Science*, vol. 39, no. 4, pp. 693-700, 1984
- [21] E. M. Sparrow, R. Ruiz, "Effect of Blockage-induced Flow Maldistribution on the Heat Transfer and Pressure Drop in a Tube Bank," *Trans. of ASME, Ser. C, J. Heat Transfer*, vol. 104, pp. 691-699, 1982
- [22] E. M. Sparrow, Y. S. Berman, "Heat Exchanger Situated Downstream of a Right-angle Bend," *Int. J. Heat and Mass Transfer*, vol. 27, no. 9, pp. 1649-1657, 1984
- [23] J. B. Kitto, J. M. Robertson, "Effect of Maldistribution of Flow on Heat Transfer Equipment Performance," *Heat Transfer Eng.*, vol. 10, no. 1, pp. 18-25, 1989
- [24] A. L. London, "Laminar Flow Gas Turbine Regenerators – The Influence of Manufacturing Tolerances," *ASME J. Engineering for Power*, vol. 92, pp. 46-56, 1970
- [25] J. R. Mondt, "Effects of Nonuniform Passages on Deepfold Heat Exchanger Performance," *ASME J. Engineering for Power*, vol. 99, pp. 657-663, 1977

- [26] R. K. Shah, A. L. London, "Effects of Nonuniform Passages on Compact Heat Exchanger Performance," *ASME J. Engineering for Power*, vol. 102, pp. 653-659, 1980
- [27] T. J. Fagan, "The Effects of Air Flow Mal-distributions on Air-to-Refrigerant Heat Exchanger Performance," *ASHRAE Trans.*, vol. 86, no. 2, pp. 699-713, 1980
- [28] J. P. Chiou, "The Effect of the Air Flow Nonuniformity on the Thermal Performance of Automobile Air Conditioning Condenser," *SAE Trans.*, Article no. 830542, 1984
- [29] J. P. Chiou, "The Effect of the Air Flow Nonuniformity on the Thermal Performance of Evaporator of Automobile Air Conditioning System," *SAE Trans.*, Article no. 840381, 1984
- [30] J. P. Chiou, "The Combined Effects of Maldistributions of the Inlet Air Temperature and the Induced Flow Nonuniformity on the Performances of Radiator, Heater and Oil Cooler," *SAE Trans.*, Article no. 850037, 1985
- [31] F. Kondo, Y. Aoki, "Prediction Method on Effect of Thermal Performance of Heat Exchanger due to Non-uniform Air Flow Distribution," *SAE Trans.*, Article no. 850041, 1986
- [32] P. A. Domanski, "Simulation of an Evaporator with Non-Uniform One-Dimensional Air Distribution," *ASHRAE Trans.*, vol. 97, no. 1, pp. 793-802, 1991
- [33] Lee, P. A. Domanski, "Impact of Air and Refrigerant Mal-distributions on the Performance of Finned-tube Evaporators with R-22 and R-407C," The Air-Conditioning and Refrigeration Technology Institute, Final Rep. ARTI MCLR Project Number 665-54500, July 1997
- [34] J. Lee, Y. C. Kwon, M. H. Kim, "An Improved Method for Analyzing a Fin and Tube Evaporator Containing a Zeotropic Mixture Refrigerant with Air Mal-distribution," *Int. J. Refrigeration*, vol. 60, pp. 707 - 720, 2003
- [35] L. L. Shao, L. Yang, C. L. Zhang, B. Gu, "Numerical Modeling of Serpentine Microchannel Condenser," *Int. J. Refrigeration*, vol. 32, pp. 1162-1172, 2009

- [36] M. Chwalowski, D. A. Didion, P. A. Domanski, "Verification of Evaporator Computer Models and Analysis Performance of an Evaporator Coil," *ASHRAE Trans.*, vol. 95, no. 2, pp. 1229-1236, 1989
- [37] D. J. Timoney, P. J. Foley, "Some Effects of Air Flow Mal-distribution on Performance of a Compact Evaporator with R134A," *Heat Recovery Systems & CHP*, vol. 14, no. 5, pp. 517-523, 1994
- [38] A. D. Ryan, D. J. Timoney, "Measured and Predicted Effects of Air Flow Non-uniformity on Thermal Performance of an R-134a Evaporator," *SAE Trans.*, Article no. 970831, 1997
- [39] M. G. Beiler, D. G. Kroger, "Thermal Performance Reduction in Air-cooled Heat Exchangers Due to Nonuniform Flow and Temperature Distributions," *Heat Transfer Eng.*, vol. 17, no. 1, pp. 82-92, 1996
- [40] E. S. Kirby, C. W. Bullard, W. E. Dunn, "Effect of Air Flow Non-uniformity on Evaporator Performance," *ASHRAE Trans.*, vol. 104, no. 2, pp. 755 - 762, 1998
- [41] J. M. Choi, W. V. Payne, P. A. Domanski, "Effects of Non-uniform Refrigerant and Air Flow Distributions on Finned-tube Evaporator Performance," presented at the 21st Int. Congr. Refrigeration, Washington D.C., 2003, Paper no. ICR0040
- [42] W. V. Payne, P. A. Domanski, "Potential Benefits of Smart Refrigerant Distributors," The Air-Conditioning and Refrigeration Technology Institute, Final Rep. ARTI-21CR/610-20050-01, 2003
- [43] A. A. Aganda, J. E. R. Coney, P. E. Farrant, C. G. W. Sheppard, T. Wongwuttanasatian, "A Comparison of the Predicted and Experimental Heat Transfer Performance of a Finned Tube Evaporator," *App. Thermal Eng.*, vol. 20, pp. 499-513, 2000
- [44] A. A. Aganda, J. E. R. Coney, C. G. W. Sheppard, "Airflow Maldistribution and the Performance of a Packaged Air Conditioning Unit Evaporator," *App. Thermal Eng.*, vol. 20, pp. 515-528, 2000
- [45] A. Elgowainy, "Effect of Airflow Mal-distribution on Pressure Drop and Thermal Performance of Heat Exchangers in Residential Heat Pump Systems," *ASHRAE Trans.*, vol. 109, no. 2, Article no. 4629, 2003

- [46] N. Chen, L. Xu, H. D. Feng, C. G. Yang, "Performance Investigation of a Finned Tube Evaporator under the Oblique Frontal Air Velocity Distribution," *App. Thermal Eng.*, vol. 25, pp. 113-125, 2005
- [47] J. Y. Gong, T. Gao, X. L. Yuan, D. Huang, "Effects of Air Flow Maldistribution on Refrigeration System Dynamics of an Air Source Heat Pump Chiller under Frosting Conditions," *Energy Conversion and Management*, vol. 49, pp. 1645-1651, 2008
- [48] J. S. McDonald, K. Y. Eng, "Tube Side Flow Distribution Effects on Heat Exchanger Performance," *Chem. Eng. Progr. Symp. Ser.*, vol. 59, pp. 11-17, 1963
- [49] T. J. Rabas, "The Effect of Tube-side Maldistribution on the Thermal Performance of Condensers Used in Multistage Flash Distillation Plants," *Desalination*, vol. 55, pp. 515-528, 1985
- [50] A. J. Jiao, R. Zhang, S. K. Jeong, "Experimental Investigation of Header Configuration on Flow Maldistribution in Plate-fin Heat Exchanger," *App Thermal Eng.*, vol. 23, pp. 1235-1246, 2003
- [51] A. J. Jiao, Y. Z. Li, C. Z. Chen, "Experimental Investigation on Fluid Flow Maldistribution in Plate-fin Heat Exchangers," *Heat Transfer Eng.*, vol. 24, no. 4, pp. 25-31, 2003
- [52] A. J. Jiao, S. W. Baek, "Effect of Distributor Configuration on Flow Maldistribution in Plate-fin Heat Exchangers," *Heat Transfer Eng.*, vol. 26, no. 4, pp. 19-25, 2005
- [53] S. Vist, "Two-phase Refrigerant Distribution in Round Tube Manifolds," *ASHRAE Trans.*, vol. 110, no. 1, pp. 307-317, 2004
- [54] Y. H. Hwang, D. H. Jin, R. Radermacher, "Refrigerant Distribution in Minichannel Evaporator Manifolds," *HVAC&R Research*, Vol. 13, no. 4, pp. 543-555, 2007
- [55] M. Ahmad, G. Berthoud, P. Mercier, "General Characteristics of Two-phase Flow Distribution in a Compact Heat Exchanger," *Int. J. Heat and Mass Transfer*, vol. 52, pp. 442-450, 2009

- [56] M. A. Habib, R. Ben-Mansour, S. A. M. Said, M. S. Al-Qahtani, J. J. Al-Bagawi, K. M. Al-Mansour, "Evaluation of Flow Maldistribution in Air-cooled Heat Exchangers," *Computers & Fluids*, vol. 38, pp. 677-690, 2009
- [57] L. Shiek Ismail, C. Ranganayakulu, R. K. Shah, "Numerical Study of Flow Patterns of Compact Plate-fin Heat Exchangers and Generation of Design Data for Offset and Wavy Fins," *Int. J. Heat and Mass Transfer*, vol. 52, pp. 3972-3983, 2009
- [58] J. Wen, Y. Z. Li, "Study of Flow Distribution and its Improvement on the Header of Plate-fin Heat Exchanger," *Cryogenics*, vol. 44, pp. 823-831, 2004
- [59] L. L. Shao, L. Yang, C. L. Zhang, "Comparison of Heat Pump Performance using Fin-and-tube and Microchannel Heat Exchangers Under Frost Conditions," *App. Energy*, vol. 87, pp. 1187-1197, 2010
- [60] M. Tierney, A. Nasr, G. Quarini, "The Use of Proprietary Computational Fluid Dynamics Codes for Flows in Annular Packed Beds," *Separation and Purification Tech.*, vol. 13, pp. 97-107, 1998
- [61] Y. Jiang, M. H. Al-Dahhan, M. P. Dudukovic, "Statistical Characterization of Macroscale Multiphase Flow Textures in Trickle Beds," *Chem. Eng. Science*, vol. 56, pp. 1647-1656, 2001
- [62] J. Wen, Y. Z. Li, A. M. Zhou, K. Zhang, J. Wang, "PIV Experimental Investigation of Entrance Configuration on Flow Maldistribution in Plate-fin Heat Exchanger," *Cryogenics*, vol. 46, pp. 37-48, 2006
- [63] T. J. Rabas, "The Effect of Nonuniform Inlet Flow and Temperature Distributions on the Thermal Performance of Air-cooled Condensers," in: *Maldistribution of Flow and Its Effect on Heat Exchanger Performance*, vol. 75, J. B. Kitto and J. M. Robertson, Eds. New York, ASME, 1987, pp. 29-35
- [64] Z. G. Xu, D. H. T. Gotham, M. W. Collins, J. E. R. Coney, C. G. W. Sheppard, S. Merdjani, "A Numerical and Experimental Study of Turbulent Flow through the Evaporator Coil in an Air-conditioning Unit," *Int. J. Refrigeration*, vol. 19, no. 6, pp. 369-381, 1996
- [65] H. S. Kou, P. Yuan, "Thermal Performance of Crossflow Heat Exchanger with Nonuniform Inlet Temperatures," *Int. Comm. Heat and Mass Transfer*, vol. 24, no. 3, pp. 357-370, 1997

- [66] E. B. Ratts, "Investigation of Flow Maldistribution in a Concentric-tube, Counterflow, Laminar Heat Exchanger," *Heat Transfer Eng.*, vol. 19, no. 3, pp. 65-75, 1998
- [67] C. J. Meyer, D. G. Kroger, "Plenum Chamber Flow Losses in Forced Draught Air-cooled Heat Exchangers," *App. Thermal Eng.*, vol. 18, pp. 875-893, 1998
- [68] S. Lalot, P. Florent, S. K. Lang, A. E. Bergles, "Flow Maldistribution in Heat Exchangers," *App. Thermal Eng.*, vol. 19, pp. 847-863, 1999
- [69] C. H. Ranganayakulu, K. N. Seetharamu, "The Combined Effects of Longitudinal Heat Conduction, Flow Nonuniformity and Temperature Nonuniformity in Crossflow Plate-fin Heat Exchangers," *Int. Comm. Heat and Mass Transfer*, vol. 26, no. 5, pp. 669-678, 1999
- [70] P. Yuan, "Effect of Inlet Flow Maldistribution on the Thermal Performance of a Three-fluid Crossflow Heat Exchanger," *Int. J. Heat and Mass Transfer*, vol. 46, pp. 3777-3787, 2003
- [71] B. P. Rao, S. K. Das, "Effect of Flow Distribution to the Channels on the Thermal Performance of the Multipass Plate Heat Exchangers," *Heat Transfer Eng.*, vol. 25, no. 8, pp. 48-59, 2004
- [72] B. P. Rao, B. Sunden, S. K. Das. "An Experimental and Theoretical Investigation of the Effect of Flow Maldistribution on the Thermal Performance of Plate Heat Exchangers," *ASME J. Heat Transfer*, vol. 127, pp. 332-342, 2005
- [73] C. T'Joen, M. D. Paepe, F. Vanhee, "Heat Exchanger Behavior in Non-Uniform Flow," *Exp. Heat Transfer*, vol. 19, pp. 281-296, 2006
- [74] M. Mishra, P. K. Das, S. Sarangi, "Effect of Temperature and Flow Nonuniformity on Transient Behaviour of Crossflow Heat Exchanger," *Int. J. Heat and Mass Transfer*, vol. 51, pp. 2583-2592, 2008
- [75] E. Kreysiz, "Data Analysis. Probability Theory," in *Advanced Engineering Mathematics*, 8th Ed., Hoboken, New Jersey: Wiley, 1999, pp. 1069
- [76] J. K. Patel, C. H. Kapadia, D. B. Owen, "Moments, Cumulants, and Generating Functions" in *Handbook of Statistical Distributions*, 1st Ed., New York: Marcel, 1976, pp. 1-5
- [77] R. E. Walpole, R. H. Myers, "Random Variables," in *Probability and Statistics for Engineers and Scientists*, 2nd Ed., New York: Macmillian, 1978, pp. 65-66

- [78] NIST/SEMATECH. (2010, June). e-Handbook of Statistical Methods. [Online]. Available:
<http://www.itl.nist.gov/div898/handbook/eda/section3/eda35b.htm>
 Date last accessed: 14th June 2011
- [79] D. J. Sheskin, “Introduction” in Handbook of Parametric and Nonparametric Statistical Procedures, 4th Ed., Boca Raton: CRC, 2007, pp. 1-29
- [80] W. H. Rohsenow, J. P. Hartnett, Y. I. Cho, “Forced Convection, Internal Flow in Ducts,” in Handbook of Heat Transfer, 3rd Ed., New York: McGraw Hill, 1998, pp. 5.22 - 5.26
- [81] O. A. Jaramillo, M. A. Borja, “Wind Speed Analysis in La Ventosa, Mexico: A Bimodal Probability Distribution Case,” *Renewable Energy*, vol. 29, pp. 1613-1630, 2004
- [82] C. C. Wang, J. Y. Jang, N. F. Chiou, “Technical Note: A Heat Transfer and Friction Correlation for Wavy Fin-and-tube Heat Exchangers,” *Int. J. Heat and Mass Transfer*, vol.42, pp. 1919-1924, 1999
- [83] F. C. McQuiston, J. D. Parker, J. D. Spitler, “Extended Surface Heat Exchangers,” in Heating, Ventilating and Air-conditioning: Analysis and Design”, 6th Ed., Hoboken, New Jersey: Wiley, 2005, pp. 486-492
- [84] F. P. Incropera, D. P. DeWitt, “Heat Exchangers”, in Introduction to Heat Transfer, 4th Ed., New York: Wiley, 2002, pp. 625-629
- [85] American Society of Heating, Refrigerating and Air-conditioning Engineers, “Psychrometrics”, in Handbook - Fundamentals, Atlanta: ASHRAE, 2009, pp. 1.1-1.9, 30.63
- [86] M. Hazewinkel. (2002). Encyclopaedia of Mathematics. Springer-Verlag. [Online] Available: <http://eom.springer.de/>
 Date last accessed: 14th June 2011
- [87] E. W. Weisstein. (2010). Continuous Distribution. Wolfram Mathworld. [Online]. Available:
<http://mathworld.wolfram.com/ContinuousDistribution.html>
 Date last accessed: 14th June 2011
- [88] A. Azzalini, A. Capitanio, “Statistical applications of the multivariate skew-normal distribution,” *J. Royal Statistical Soc., Ser. B*, vol. 61, pp. 579-602, 1999

- [89] M. Abramowitz, I. A. Stegun, "Probability Functions," in Handbook of Mathematical Functions with Formulas, Graphs and Mathematical Tables, 10th Printing, Washington D.C.: National Bureau of Standards, U. S. Department of Commerce, 1972, pp. 925-943
- [90] NIST, Statistical Engineering Division. (2007). Kumaraswamy Probability Density Function. [Online]. Available: <http://www.itl.nist.gov/div898/software/dataplot/refman2/auxillar/kumpdf.htm>
Date last accessed: 14th June 2011
- [91] G. N. Xie, Q. W. Wang, B. Sunden, "Parametric Study and Multiple Correlations on Air-side Heat Transfer and Friction Characteristics of Fin-and-tube Heat Exchangers with Large Number of Large-Diameter Tube Rows," *App. Thermal Eng.*, vol. 29, pp. 1-16, 2009
- [92] N. H. Kim, J. H. Yun, R. L. Webb, "Heat Transfer and Friction Correlations for Wavy Plate Fin-and-tube Heat Exchangers," *ASME J. Heat Transfer*, vol. 119, pp. 560-567, 1997
- [93] C. C. Wang, C. J. Lee, C. T. Chang, S. P. Lin, "Heat Transfer and Friction Correlation for Compact Louvered Fin-and-Tube Heat Exchangers," *Int. J. Heat and Mass Transfer*, vol. 42, pp. 1945-1956, 1999
- [94] D. G. Rich, "The Effect of the Number of Tube Rows on Heat Transfer Performance of Smooth Plate Fin-and-tube Heat Exchangers," *ASHRAE Trans.*, vol. 81, pp. 307-317, 1975
- [95] C. C. Wang, W. L. Fu, C. T. Chang, "Heat Transfer and Friction Characteristics of Typical Wavy Fin-and-tube Heat Exchangers," *Exp. Thermal and Fluid Science*, vol. 14, pp. 174-186, 1997
- [96] C. C. Wang, K. Y. Chi, "Heat Transfer and Friction Characteristics of Plain Fin-and-Tube Heat Exchangers, Part 1: New Experimental Data," *Int. J. Heat and Mass Transfer*, vol. 43, pp. 2681-2691, 2000
- [97] Oakland Engineering. (2010). Datafit version 9.0. [Online]. Available: <http://oakdaleengr.com/>
Date last accessed: 10th June 2011

- [98] P. A. Domanski, D. Yashar., M. S. Kim, “Performance of a Finned-Tube Evaporator Optimized for Different Refrigerants and its Effect on System Efficiency,” *Int. J. Refrigeration*, vol. 28, pp. 820-827, 2005
- [99] H. B. Jiang, V. Aute, R. Radermacher R., “CoilDesigner - A General-Purpose Simulation and Design Tool for Air-to-Refrigerant Heat Exchangers,” *Int. J. Refrigeration*, vol. 29, pp. 601-610, 2006
- [100] X. Jia, C. P. Tso, P. Jolly, Y. W. Wong, “Distributed Steady and Dynamic Modelling of Dry Expansion Evaporators,” *Int. J. Refrigeration*, vol. 22, pp. 126-136, 1999
- [101] R. K. Shah, D. P. Sekulic, “Surface Basic Heat Transfer and Flow Friction Characteristics,” in *Fundamentals of Heat Exchanger Design*, 1st Ed., Hoboken, New Jersey: Wiley, 2003, pp. 450-452
- [102] *Standard Method for Temperature Measurement*, ANSI/ASHRAE 41.1-1986 (RA 91), 1991
- [103] *Methods of Testing Forced Circulation Air Cooling and Air Heating Coils*, ASHRAE 33-1978, 1978
- [104] *Methods of Testing for Rating Heat-Operated Unitary Air-conditioning Equipment for Cooling*, ANSI/ASHRAE 40-1980 (RA 92), 1992
- [105] R. A. Bowman, A. C. Mueller and W. M. Nagle, “Mean Temperature Difference in Design,” *Trans. ASME*, vol. 62, pp. 283–294, 1940
- [106] R. H. Perry, D. Green, “Perry’s Chemical Engineers’ Handbook”, 6th Ed., Singapore: McGraw-Hill, 1984, pp. 5.10-5.11
- [107] E. Caffagni, P. Levoni, M. Pirracini, A. Muscio, M. A. Corticelli, G. Z. Barozzi, “Thermographic Analysis of Flow Distribution in Compact Heat Exchangers for a Formula 1 Car,” *Infrared Physics & Tech.*, vol. 49, pp. 321-326, 2007
- [108] S. J. Kline, F. A. McClintok, “Describing Uncertainties in Single-Sample Experiments,” *Mech. Eng.*, vol. 75, pp. 3-8, 1953
- [109] United Kingdom Accreditation Service. (2007). *M3003, The Expression of Uncertainty and Confidence in Measurement*, 2nd Ed. [Online]. Available: <http://www.ukas.com/library/Technical-Information/Pubs-Technical-Articles/Pubs-List/M3003.pdf>
Date last accessed: 14th June 2011

- [110] A. Erek, B. Ozerdam, L. Bilir, Z. Ilken, “Effect of Geometrical Parameters on Heat Transfer and Pressure Drop Characteristics of Plate Fin and Tube Heat Exchangers,” *App. Thermal Eng.*, vol. 25, pp. 2421-2431, 2005
- [111] H. M. Sahin, A. R. Dal, E. Baysal, “3-D Numerical Study on the Correlation Between Variable Inclined Fin Angles and Thermal Behaviour in Plate Fin-tube Heat Exchanger,” *App. Thermal Eng.*, vol. 27, pp. 1806-1816, 2007
- [112] R. Barrajo-Pelaez, J. Ortega-Casanova, J. M. Cejudo-Lopez, “A Three-Dimensional Numerical Study and Comparison Between the Air Side Model and the Air/Water Side Model of a Plain Fin-and-tube Heat Exchanger,” *App. Thermal Eng.*, vol. 30, pp. 1608-1615, 2010
- [113] F. Moukalled, S. Verma, M. Darwish, “The Use of CFD for Predicting and Optimizing the Performance of Air Conditioning Equipment,” *Int. J. Heat and Mass Transfer*, vol. 54, pp. 549-563, 2011
- [114] N. B. P. Reddy, P. R. M. Rao, “Convergence Effect on the Flow Resistance in Porous Media,” *J. Inst. Eng. (India) – Civil Eng.*, vol. 85, pp. 36-43, 2004
- [115] A. M. Hayes, J. A. Khan, A. H. Shaaban, I. G. Spearing, “The Thermal Modeling of a Matrix Heat Exchanger Using a Porous Medium and the Thermal Non-equilibrium Model,” *Int. J. Thermal Sciences*, vol. 47, pp. 1306-1315, 2008
- [116] H. K. Versteeg, W. Malalasekera, “Conservation Laws of Fluid Motion and Boundary Conditions,” in *An Introduction to Computational Fluid Dynamics: The Finite Volume Method*, 2nd Ed., Harlow, UK: Pearson, 2007, pp. 9-24
- [117] E. Carluccio, G. Starace, A. Ficarella, D. Laforgia, “Numerical Analysis of a Cross-flow Compact Heat Exchanger for Vehicle Applications,” *App. Thermal Eng.*, vol. 25, pp. 1995-2013, 2005
- [118] H. K. Versteeg, W. Malalasekera, “Turbulence and its Modelling,” in *An Introduction to Computational Fluid Dynamics: The Finite Volume Method*, 2nd Ed., Harlow, UK: Pearson, 2007, pp. 72- 80, 87-88
- [119] B. R. Munson, D. F. Young, T. H. Okiishi, “Appendix B: Physical Properties of Fluids” in *Fundamentals of Fluid Mechanics*, 4th Ed., Hoboken: John Wiley, 2002, pp. 833

- [120] ANSYS FLUENT. (2007). Flow through Porous Media - Flow Lab 1.2.
[Online]. Available:
http://www.philonnet.gr/downloads/ansys/flowlab/porous_tutorial.pdf
Date last accessed: 14th June 2011
- [121] ANSYS FLUENT. (2006). FLUENT 6.3 User Guide, 7.25.2: Heat Exchanger Model Theory. [Online]. Available:
<http://my.fit.edu/itresources/manuals/fluent6.3/help/html/ug/node297.htm>
Date last accessed: 14th June 2011
- [122] W. M. Kays, A. L. London, "Heat Exchanger Thermal and Pressure-Drop Design," in Compact Heat Exchangers, 3rd Ed., New York: McGraw-Hill, 1984, pp. 36

LIST OF PUBLICATIONS

Journal papers

1. **W. M. Chin**, V. R. Raghavan, “On the Adverse Influence of Higher Statistical Moments of Flow Maldistribution on the Performance of a Heat Exchanger”, *International Journal of Thermal Sciences*, Vol. 50, Issue 4, 581-591, April 2011
2. **W. M. Chin**, V. R. Raghavan, “The Influence of the Moments of Probability Density Function for Flow Maldistribution on the Thermal Performance of a Fin-tube Heat Exchanger”, *International Journal of Thermal Sciences*, **doi: 0.1016/j.ijthermalsci.2011.04.014**, 2011
3. **W. M. Chin**, V. R. Raghavan, “Effect of the Moments of Probability Density Function for Non-uniform Air Flow Distribution on the Hydraulic Performance of a Fin-tube Heat Exchanger”, *Journal of Applied Sciences*, **doi: 10.3923/jas.2011**, 2011

Conference papers

1. **W. M. Chin**, V. R. Raghavan, “Effect of Non-uniform Distribution of Flow on the Performance of Fin-tube Heat Exchangers”, *National Postgraduate Conference (NPC)*, Universiti Teknologi Petronas, March 2009
2. **W. M. Chin**, V. R. Raghavan, “Effect of the Moments of Probability Density Function for Non-Uniform Air Flow Distribution on the Hydraulic Performance of a Fin-Tube Heat Exchanger”, *International Conference on Plant Equipment and Reliability (ICPER)*, Kuala Lumpur, June 2010.

APPENDIX A
HEAT TRANSFER COLBURN j -FACTOR CORRELATION

The air-side Colburn j -factor for a fin surface is defined as:

$$j = \frac{Nu_a}{Re_{D_c} Pr_a^{1/3}} \quad (A-1)$$

where

Nu_a is the air-side Nusselt number

Re_{D_c} is the air-side Reynolds number based on the fin collar diameter (D_c)

Pr_a is the air-side Prandtl number

For the wavy corrugated fin used in this study, the correlation developed by Wang et al. [81] was used to evaluate the j -factor. This correlation is re-produced here as follows:

$$j = 0.324 Re_{D_c}^{J1} \left(\frac{F_p}{X_l} \right)^{J2} (\tan \theta)^{J3} \left(\frac{X_l}{X_t} \right)^{J4} N_r^{0.428} \quad (A-2)$$

where

$$J1 = -0.229 + 0.115 \left(\frac{F_p}{D_c} \right)^{0.6} \left(\frac{X_l}{D_h} \right)^{0.54} N_r^{-0.284} \ln(0.5 \tan \theta) \quad (A-3)$$

$$J2 = -0.251 + \frac{0.232 N_r^{1.37}}{(\ln(Re_{D_c}) - 2.303)} \quad (A-4)$$

$$J3 = -0.439 \left(\frac{F_p}{D_h} \right)^{0.09} \left(\frac{X_l}{X_t} \right)^{-1.75} N_r^{-0.93} \quad (A-5)$$

$$J4 = 0.502(\ln(Re_{D_c}) - 2.54) \quad (A-6)$$

In the equations above, F_p is the fin pitch, D_h is the hydraulic diameter, X_l is the longitudinal tube pitch and X_t is the traverse tube pitch. The fin has a corrugation angle, θ , of 20° .

APPENDIX B

LIST OF CONTINUOUS PROBABILITY DENSITY FUNCTIONS

Other than the Normal distribution described in Chapter 4, the following probability density functions have been used in this work to generate maldistribution profiles:

1) **Weibull distribution** (with 2 parameters k and λ)

$$P(x; k, \lambda) = \frac{k}{\lambda} \left(\frac{x}{\lambda} \right)^{k-1} e^{-(x/\lambda)^k} \quad (\text{B-1})$$

$$\text{Mean, } \mu = \lambda \Gamma \left(1 + \frac{1}{k} \right) \quad (\text{B-2})$$

$$\text{Variance, } \sigma^2 = \lambda^2 \Gamma \left(1 + \frac{2}{k} \right) - \mu^2 \quad (\text{B-3})$$

$$\text{Skew, } \gamma = \frac{\Gamma \left(1 + \frac{3}{k} \right) \lambda^3 - 3\mu\sigma^2 - \mu^3}{\sigma^3} \quad (\text{B-4})$$

$$\text{Kurtosis, } \kappa = \frac{\lambda^4 \Gamma \left(1 + \frac{4}{k} \right) - 4\gamma\sigma^3\mu - 6\mu^2\sigma^2 - \mu^4}{\sigma^4} \quad (\text{B-5})$$

2) **Pearson Type VII distribution** (with skew = 0)

$$P(x) = \frac{1}{\alpha B \left(m - \frac{1}{2}, \frac{1}{2} \right)} \left[1 + \left(\frac{x - \mu}{\alpha} \right)^2 \right]^{-m} \quad (\text{B-6})$$

where

$$B(x, y) \text{ is the Beta function; i.e. } B(x, y) = \frac{\Gamma(x)\Gamma(y)}{\Gamma(x+y)} \quad (\text{B-7})$$

$$\alpha = \sigma \sqrt{2m - 3} \quad (\text{B-8})$$

with

$$m = \frac{5}{2} + \frac{3}{\kappa} \quad (\text{B-9})$$

3) **Beta distribution** (with 2 parameters α and β)

$$P(x) = \frac{x^{\alpha-1}(1-x)^{\beta-1}}{B(\alpha, \beta)} \quad (\text{B-10})$$

where $B(x,y)$ is the Beta function defined in equation (B-7)

$$\text{Mean, } \mu = \frac{\alpha}{\alpha + \beta} \quad (\text{B-11})$$

$$\text{Variance, } \sigma^2 = \frac{\alpha\beta}{(\alpha + \beta)^2(\alpha + \beta + 1)} \quad (\text{B-12})$$

$$\text{Skew, } \gamma = \frac{2(\beta - \alpha)\sqrt{\alpha + \beta + 1}}{(\alpha + \beta + 2)\sqrt{\alpha\beta}} \quad (\text{B-13})$$

$$\text{Kurtosis, } \kappa = 6 \frac{\alpha^3 - \alpha^2(2\beta - 1) + \beta^2(\beta + 1) - 2\alpha\beta(\beta + 2)}{\alpha\beta(\alpha + \beta + 2)(\alpha + \beta + 3)} \quad (\text{B-14})$$

This distribution will have negative skews when $\beta < \alpha$.

4) **Exponential distribution** (with 1 parameter λ)

$$P(x) = \lambda e^{-\lambda x} \quad (\text{B-15})$$

$$\text{Mean, } \mu = \frac{1}{\lambda} \quad (\text{B-16})$$

$$\text{Variance, } \sigma^2 = \frac{1}{\lambda^2} \quad (\text{B-17})$$

Skew is fixed at 2, and kurtosis is also fixed at 6

5) **Log-normal distribution**

$$P(x) = \frac{1}{x\sigma\sqrt{2\pi}} \exp\left[-\frac{(\ln(x) - \mu)^2}{2\sigma^2}\right] \quad (\text{B-18})$$

$$\text{Mean, } \mu = e^{\mu + \sigma^2/2} \quad (\text{B-19})$$

$$\text{Variance, } \sigma^2 = (e^{\sigma^2} - 1)e^{2\mu + \sigma^2} \quad (\text{B-20})$$

$$\text{Skew, } \gamma = (e^{\sigma^2} + 2)\sqrt{e^{\sigma^2} - 1} \quad (\text{B-21})$$

$$\text{Kurtosis, } \kappa = e^{4\sigma^2} + 2e^{3\sigma^2} + 3e^{2\sigma^2} - 6 \quad (\text{B-22})$$

6) **Chi distribution** (with parameter k)

$$P(x) = \frac{2^{1-k/2} x^{k-1} e^{-x^2/2}}{\Gamma(k/2)} \quad (\text{B-23})$$

$$\text{Mean, } \mu = \sqrt{2} \frac{\Gamma((k+1)/2)}{\Gamma(k/2)} \quad (\text{B-24})$$

$$\text{Variance, } \sigma^2 = k - \mu^2 \quad (\text{B-25})$$

$$\text{Skew, } \gamma = \frac{\mu}{\sigma^3} (1 - 2\sigma^2) \quad (\text{B-26})$$

$$\text{Kurtosis, } \kappa = \frac{2}{\sigma^2} (1 - \mu\sigma\gamma - \sigma^2) \quad (\text{B-27})$$

7) **Inverse Gaussian distribution** (with parameter λ and mean μ)

$$P(x) = \left[\frac{\lambda}{2\pi x^3} \right]^{1/2} \exp \frac{-\lambda(x-\mu)^2}{2\mu^2 x} \quad (\text{B-28})$$

$$\text{Variance, } \sigma^2 = \frac{\mu^3}{\lambda} \quad (\text{B-29})$$

$$\text{Skew, } \gamma = 3 \left(\frac{\mu}{\lambda} \right)^{1/2} \quad (\text{B-30})$$

$$\text{Kurtosis, } \kappa = \frac{15\mu}{\lambda} \quad (\text{B-31})$$

8) **Pareto distribution** (with parameters k and x_m)

$$P(x) = \frac{kx_m^k}{x^{k+1}} \quad (\text{B-32})$$

$$\text{Mean, } \mu = \frac{kx_m}{k-1} \quad (\text{B-33})$$

$$\text{Variance, } \sigma^2 = \frac{x_m^2 k}{(k-1)(k-2)} \text{ for } k > 2 \quad (\text{B-34})$$

$$\text{Skew, } \gamma = \frac{2(1+k)}{k-3} \sqrt{\frac{k-2}{k}} \text{ for } k > 3 \quad (\text{B-35})$$

$$\text{Kurtosis, } \kappa = \frac{6(k^3 + k^2 - 6k - 2)}{k(k-3)(k-4)} \text{ for } k > 4 \quad (\text{B-36})$$

8) **Skew normal distribution** (with parameter α and location ξ, ω)

$$P(x) = 2\phi(x)\Phi(\alpha x) \quad (\text{B-37})$$

where

$$\phi(x) = \frac{1}{\omega\sqrt{2\pi}} \exp\left(-\frac{(x-\xi)^2}{2\omega^2}\right) \quad (\text{B-38})$$

$$\Phi(\alpha x) = \frac{1}{2} \left[1 + \operatorname{erf}\left(\frac{\alpha(x-\xi)}{\omega\sqrt{2}}\right) \right] \quad (\text{B-39})$$

with $\operatorname{erf}(x)$ as the error function

$$\text{Mean, } \mu = \xi + \omega\delta\sqrt{\frac{2}{\pi}} \quad (\text{B-40})$$

$$\text{Variance, } \sigma^2 = \omega^2 \left(1 - \frac{2\delta^2}{\pi} \right) \quad (\text{B-41})$$

$$\text{Skew, } \gamma = \frac{4-\pi}{2} \frac{(\delta\sqrt{2/\pi})^3}{(1-2\delta^2/\pi)^{3/2}} \quad (\text{B-42})$$

$$\text{Kurtosis, } \kappa = 2(\pi-3) \frac{(\delta\sqrt{2/\pi})^4}{(1-2\delta^2/\pi)^2} \quad (\text{B-43})$$

with

$$\delta = \frac{\alpha}{\sqrt{1+\alpha^2}} \quad (\text{B-44})$$

9) **Raised cosine distribution** (with parameter α and mean μ)

$$P(x) = \frac{1}{2s} \left[1 + \cos\left(\frac{x-\mu}{s}\pi\right) \right] \quad (\text{B-45})$$

$$\text{Variance, } \sigma^2 = \alpha^2 \left(\frac{1}{3} - \frac{2}{\pi^2} \right) \quad (\text{B-46})$$

Skew = 0

$$\text{Kurtosis, } \kappa = \frac{6(90-\pi^4)}{5(\pi^2-6)^2} \quad (\text{B-47})$$

10) **Wigner semi-circle distribution** (with parameter R)

$$P(x) = \frac{2}{\pi R^2} \sqrt{R^2 - x^2} \quad (\text{B-48})$$

Mean = 0

$$\text{Variance, } \sigma^2 = \frac{R^2}{4} \quad (\text{B-49})$$

Skew = 0

$$\text{Kurtosis, } \kappa = \ln(\pi R) - \frac{1}{2} \quad (\text{B-50})$$

11) **Kumaraswamy distribution** (with parameter a and b)

$$P(x) = abx^{a-1} (1 - x^a)^{b-1} \quad (\text{B-51})$$

$$\text{Mean, } \mu = \frac{b\Gamma(1+1/a)\Gamma(b)}{\Gamma(1+1/a+b)} \quad (\text{B-52})$$

All three variance, skew and kurtosis are too complicated to have an analytical form. These are calculated from the generated data of equation (B-51).

Note:

In some of the distributions above, the **Gamma function**, $\Gamma(x)$ is used. This function is defined, for any real number z , as:

$$\Gamma(z) = \int_0^{\infty} t^{z-1} e^{-t} dt \quad (\text{B-53})$$

For this work, a numerical integration procedure is used to evaluate this equation.

APPENDIX C
SPECIFICATIONS OF FLOW NOZZLES

The specified dimensions of flow nozzles used to measure air flow rates are given in the ASHRAE Standard 40-1980 (RA 92) [104], as shown in the following Fig. C.1. Clause 9.3.2 of the standard has stated that when nozzles are constructed according to the specified dimensions, they may be used without calibration.

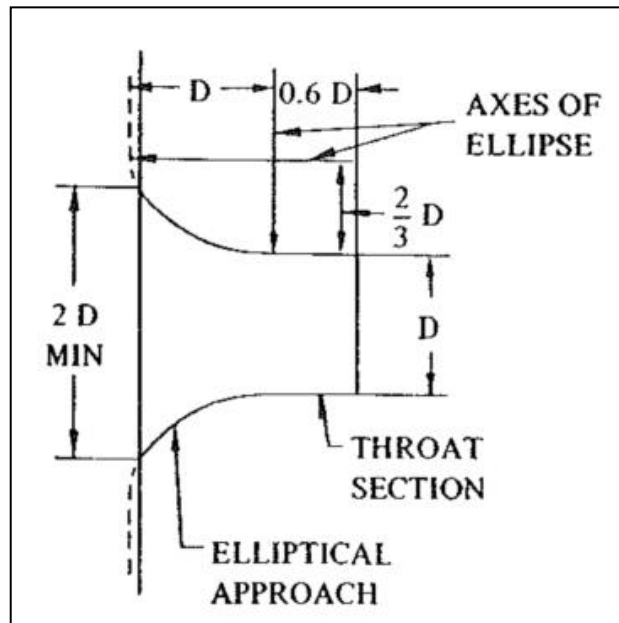


Fig. C.1: Flow-measuring nozzle